Flexoelectric and Dielectric Phenomena in Helicoidal Liquid Crystals

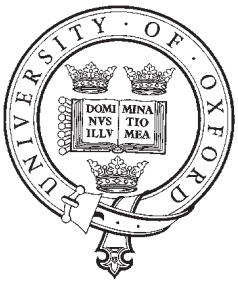

Benjamin I. Outram

Linacre College

University of Oxford

A thesis submitted for the degree of

Doctor of Philosophy

Trinity 2013

FLEXOELECTRIC AND DIELECTRIC PHENOMENA IN HELICOIDAL LIQUID CRYSTALS

Submitted for the degree of Doctor of Philosophy

Benjamin I. Outram, Linacre College, Trinity 2013

The unique features of flexoelectric and dielectric effects are investigated, and exploited for a variety of functions, in a wide range of helicoidal liquid crystal systems, including non-chiral, cholesteric and blue phases.

Electrooptic techniques are developed to measure flexoelectric parameters in non-chiral and cholesteric liquid crystals using twisted nematic and Grandjean geometries respectively. A crystal rotation method, and using a lock-in amplifier, is used to enable the measurement of a very small e/K of 0.011 $\mathrm{CN^{-1}m^{-1}}$.

Enhancement in chiral-flexoelectric switching is demonstrated theoretically in liquid crystals with negative dielectric anisotropy and in systems in which the pitch is constrained to be other than the natural pitch.

A methodological framework for inducing stable Uniform Lying Helix alignment is developed based on weak homeotropic alignment conditions and a method to bias the helicoidal axis orientation; a series of approaches within this framework are demonstrated, including nano-grooved interfaces, periodic boundaries conditions, in-plane fields, and mould-templated micro-channels. The latter approach is potentially commercially viable for sub-millisecond electrooptic technology.

The contribution to a cholesteric material's effective dielectric permittivity of flexoelectric polarization is formulated, and an ability to switch a cholesteric between Grandjean and lying-helix configurations based on the dispersion in the flexoelectric polarization and resultant relaxation in dielectric properties is demonstrated. The flexoelectric contribution to dielectric permittivity is exploited to enable switching in bistable reflective displays and alignment of the Uniform Lying Helix.

The existence of a flexoelectric contribution to Kerr switching in blue phases is demonstrated, and a semi-empirical model for the effect is developed. The effect is the first known example of a non-polar flexoelectrooptic effect. Independent flexoelectric and dielectric contributions to Kerr switching in blue phases are measured experimentally by measuring the induced birefringence as a function of driving frequency in flexoelectric- and dielectric-dominated wide-temperature-range blue phase materials.

Acknowledgements

Foremost I would like to thank my supervisor, Professor Steve Elston, for his kind and expert guidance. Problems seem to dissolve away when looked upon with Steve's eyes. Thanks also to Peter Raynes, and my industrial supervisors Rachel Tuffin and David Wilkes. I would also like to thank Merck for the supply of liquid crystal material, and the EPSRC and Merck for financial support through a CASE award. I am grateful to collaborators at Merck, Simon Siemianowski, Ben Snow and Rachel Tuffin, for their hospitality while hosting me at Merck. I would like to thank collaborators at Feng Chia University, Hui-Yu Chen and her students, both for the supply of blue phase liquid crystals, and for their kind hospitality during my visit to Taiwan. I would like to thank collaborators in Cambridge, especially Flynn Castles, for the supply of blue phase materials and for useful discussions. Further, I would like to thank the liquid crystal community, with special thanks to Ingo Dierking, Helen Gleeson, Graham Renwick, Oliver Coles, Aurore Gandubert, Patrick Salter, Philip Benzie, Daniel Corbett, and Giovanni Carbone. Finally, a big thank you to my parents.

Contents

0.1 Conferences Attended

[1] 2010 16$^{\text{th}}$ Merck CASE conference, Southampton, England, 19–20 April, oral presentation "Investigating the effect of in-plane electric fields on twisted nematic structures using periodic electrodes".

[2] 2010 25$^{\text{th}}$ British Liquid Crystal Society (BLCS) Annual Meeting, Hull, England, 29–31 March, poster "Investigating the effect of in-plane electric fields on twisted nematic structures using periodic electrodes".

[3] 2010 Liquid Crystal Workshop: Recent developments in the analysis and modelling of liquid crystals, Hull, March.

[4] 2011 17$^{\text{th}}$ Merck CASE conference, Southampton, England, 9–10 May, oral presentation "A novel method for measuring the flexoelastic ratio of liquid crystals".

[5] 2011 British Liquid Crystal Society (BLCS) conference, Nottingham, England, 18–20 April, poster "Measurement of the flexoelectric effect using the crystal rotation method".

[6] 2011 2$^{\text{nd}}$ International Symposium on liquid crystals: Science and Technology (LCST2011), Changzhou, China, 17–19 July, oral presentation "A novel method for measuring the difference in flexoelectric coefficients of liquid crystals".

[7] 2012 26$^{\text{th}}$ British Liquid Crystal Society (BLCS) Annual Meeting, Strathclyde, Scotland, 2–4 April, oral presentation "Flexoelectric and dielectric in-plane switching behaviour of Grandjean liquid crystal structures".

[8] 2012 18$^{\text{th}}$ Merck CASE Conference, Southampton, England, oral presentation "Flexoelectric and dielectric in-plane switching behaviour of Grandjean liquid crystal structures".

[9] 2012 1$^{\text{st}}$ Oxford Photonics Day, Oxford, England, 18 April.

[10] 2012 SID conference: One-day technical meeting and Chapter AGM: UK Display Innovations, Cambridge, England, 26 April.

[11] 2012 Royal Society Theo Murphy International Scientific Meeting: New frontiers in anisotropic fluid-particle composites, Milton Keynes, England, 28–29 June.

[12] 2012 24$^{\text{th}}$ International Liquid Crystal Conference (ILCC), Meinz, Germany, 19–24 August, oral presentation "Flexoelectric and Dielectric Behaviour of Conventional and Bimesogenic Chiral Doped Liquid Crystals".

[13] 2012 13$^{\text{th}}$ International Symposium on Colloidal and Molecular Electrooptics (ELOPTO 2012), Ghent, Belgium, September 2–5, oral presentation "Flexo-electrooptic behaviour of helical liquid crystals over a wide pitch range".

[14] 2012 Oxford Photonics Day 2012: 2$^{\text{nd}}$ photonics day, Oxford, England, 27 September, oral presentation "Switching behaviour in ultra-fast next-gen chiral flexoelectrooptic technologies".

[15] 2013 27$^{\text{th}}$ British Liquid Crystal Society (BLCS) Annual Meeting, Cambridge, England, 25–27 March, oral presentation "New Approaches to Uniform Lying Helix Alignment".

0.2 Publications

[1] B. I. Outram and S. J. Elston. A novel method for measuring the difference in flexoelectric coefficients of nematic liquid crystals. *Solid State Phenomena*, 118:26–32, 2012. 2nd International Symposium on Liquid Crystals: Science and Technology, Changzhou, China, 2011.

[2] B. I. Outram and S. J. Elston. Determination of flexoelectric coefficients in nematic liquid crystals using the crystal rotation method. *Liquid Crystals*, 39(2):149–156, 2012.

[3] B. I. Outram. The 26th British Liquid Crystal Society annual meeting 2012, Glasgow. *Liquid Crystals*, 21(3):66–70, 2012.

[4] B. I. Outram and S. J. Elston. Flexoelectric and dielectric in-plane switching behaviour of Grandjean liquid-crystal structures. *Europhysics Letters*, 99(3):37007, 2012.

[5] B. I. Outram and S. J. Elston. Spontaneous and stable uniform lying helix liquid-crystal alignment. *Journal of Applied Physics*, 113(4):043103, 2013.

[6] B. I. Outram, S. J. Elston, R. Tuffin, S. Siemianowski, and B. Snow. The use of mould-templated surface structures for high-quality uniform-lying-helix liquid-crystal alignment *Journal of Applied Physics*, 113:213111, 2013.

[7] B. I. Outram, S. J. Elston. Patent: Control of state switching in helicoidal liquid crystal systems using flexoelectric dispersion *Patent Pending*, 2013.

[8] B. I. Outram, S. J. Elston. Dielectric enhancement of chiral flexoelectro-optic switching *Accepted by Liquid Crystals*, 2013.

[9] B. I. Outram, S. J. Elston. Frequency dependent dielectric contribution of flexoelectricity allowing control of state switching in helicoidal liquid crystals *Physical Review E* 88(1): 012506, 2013.

[10] B. I. Outram, S. J. Elston, F. Castles, H. Coles, H.-Y. Chen, S.-F. Lu. Non-polar flexoelectrooptic effect in blue phase liquid crystals *Submitted to Physical Review Letters*, 2013.

[11] B. I. Outram, S. J. Elston. Dual-frequency bistable reflective cholesteric liquid crystal displays based on chiral-flexoelectric polarisation dispersion *Journal of Applied Physics*, 114(8):083113, 2013.

[12] B. I. Outram, S. J. Elston. Alignment of cholesteric liquid crystals using the macroscopic flexoelectric polarization contribution to dielectric properties *Applied Physics Letters*, 103(141111), 2013.

0.3 Extended Abstract

Chapter 1: Introduction to Key Concepts — This thesis is concerned with dielectric and flexoelectric electrooptic phenomena in helicoidal liquid crystal systems and their use in material characterisation and technology. Chapter 1 explores key concepts in liquid crystals that will be required by the non-specialist to understand the work to follow, including an introduction to the liquid crystal phase, the continuum theory of liquid crystals including elastic, electric, flexoelectric and optical properties of liquid crystals, analytical approaches to modelling distortions in chiral liquid crystals, and some comment on numerical methods and types of liquid crystal display.

Chapter 2: Measurement of Flexoelectricity — Techniques to measure flexoelectric properties are investigated in both chiral and non-chiral geometries. Analytical and numerical models of dielectric and flexoelectric switching in cholesteric liquid-crystal structures with in-plane switching (IPS) electric fields are employed to analyse angle-of-incidence-dependent transmission of Grandjean structures. Adoption of a perturbative driving regime, and measurement of both 1^{st} and 2^{nd} harmonic transmission amplitudes, allows the detailed and simultaneous measurement of distortions arising from both flexoelectric and dielectric interactions, at electric fields as little as 0.01 $\text{V}\mu\text{m}^{-1}$. The method is applied to measure the flexoelectric parameter $(e_1 - e_3)/(K_1 + K_3)$ and the dielectric distortion parameter $\Delta\varepsilon/K_2$ in E7 liquid crystal and a bimesogen mixture MDA-1245 optimised for the chiral-flexoelectrooptic effect, and the method is extended using a quarter-wave plate to enhance the sensitivity in cases where the birefringence of the device is small. The extended method is used to measure a value of $(e_1 - e_3)/(K_1 + K_3)$ as small as 0.011 $\text{CN}^{-1}\text{m}^{-1}$.

A crystal rotation method is further employed to measure $e_1 - e_3$ in non-chiral liquid crystals using a Twisted Nematic (TN) cell with in-plane electric fields. The method mitigates the static changes in the internal electric field due to the influence of charge carriers by determining the field implicitly from electrooptic data.

Chapter 3: Enhancement of Flexoelectric Switching — The chiral flexoelectro-optic effect is a candidate for realising sub-millisecond electro-optic technologies. Two approaches to enhancing the switching are discussed. The effect of the dielectric distortion on flexoelectric switching in cholesteric liquid crystals is investigated for cases where the liquid crystal has both positive and negative dielectric anisotropy. An experimental technique to measure the influence of the dielectric distortion on the flexoelectric switching is developed, and the theoretical framework is found to be consistent for a chiral nematic mixture E7+3.5%R5011. The optimal liquid-crystal parameters to best exploit the effect are explored, and an enhancement in the flexoelectric switching angle of up to a degree is demonstrated numerically.

A second approach is described that exploits the elastic energy in systems where the pitch is constrained to be other than the natural pitch of the cholesteric liquid crystal. An analytical expression for the flexoelectric tilt is derived in the general case that the constrained and natural pitch are not equal. It is found that by constraining a cholesteric material to have a pitch that is shorter than the natural pitch, an enhancement of up to 2.3 times can be achieved theoretically. The likelihood of realising this level of enhancement experimentally is considered, given the requirement of a polymer network to provide the pitch constraint and the resultant effect this may have on the switching.

Chapter 4: Uniform Lying Helix Alignment — The Uniform Lying Helix (ULH) architecture provides a sub-millisecond in-plane rotation of the optic axis with the application of a transverse field, vital for the next generation of liquid crystal displays. The salient chal-

lenge is the alignment quality of the ULH. Here, a methodological framework is developed for successful formation of the ULH, that relies on the use of a weak homeotropic alignment condition, which destabilises the Grandjean alignment relative to the ULH alignment, in conjunction with an agent that breaks the degeneracy in the uniform lying helicoidal axis orientation. Within this framework, a series of techniques are demonstrated, including the use of nano-grooved surface profiles, in-plane electric fields, periodic boundary conditions and micron-scale polymer channels fabricated using a mould-templating technique. The latter approach is found to produce the best quality alignment, and is suggested as a commercially viable technology. It is demonstrated experimentally and theoretically that the helicoidal axis aligns parallel to the channels in these devices.

Chapter 5: Flexoelectric Polarization Dispersion — The contribution of flexoelectric polarisation to the dielectric susceptibility in helicoidal liquid crystals is formulated for the static equilibrium case, and further in the case of a time-varying field. A dispersion of the dielectric permittivity due to the frequency response of flexoelectric switching is described. The special case of a negative dielectric anisotropy nematic material is considered and experimentally shown to agree with the analytical theory. It is further demonstrated how relaxation of the flexoelectric contribution to the dielectric tensor in this special case can be exploited to switch between states in cholesteric liquid crystal structures by altering the applied time-dependent field amplitude, if $\Delta\varepsilon < 0$ and $\frac{(e_1-e_3)^2}{(K_1+K_3)} > -\Delta\varepsilon\varepsilon_0$. Consequentially, a new and versatile mechanism for driving between states in liquid crystal systems is demonstrated.

The switching mechanism is applied to develop a reflective cholesteric display device. Flexoelectric polarisation allows the device to be switched into a weakly-scattering focal-conic state at low frequencies, while at higher frequencies, the device is driven into the reflective Grandjean state. The non-conventional dual-frequency effect allows driving between states in both directions. The cross-over frequency can be as low as 200 Hz, orders of magnitude smaller than other dual-frequency effects. Devices of various reflective colours are demonstrated, and have favourable contrast ratios, viewing angles, and switching behaviours at room temperature. The technique potentially affords a greater flexibility in surface alignment conditions, driving schemes, material parameters and use of polymer networks in cholesteric devices than other switching methods. Finally, the implications of the switching technique for other liquid crystal technologies are commented upon.

Chapter 6: Dielectric and Flexoelectric Kerr Effects in Blue Phases — The Kerr effect in blue phase liquid crystals (BPLCs) could enable a variety of next-generation electro-optic devices. The effect has until now been considered as being due only to the dielectric effect. However, here it is demonstrated that both flexoelectric and dielectric effects contribute to Kerr switching in BPLCs by comparing wide-temperature-range BPLCs without polymer stabilisation having either dominant flexoelectric or dielectric field interactions. It is demonstrated experimentally that the flexoelectric and dielectric Kerr contributions can act together or against each other, depending on the sign of the dielectric anisotropy, leading to a suggestion for the engineering of Kerr-effect blue phase materials. Using dimensional considerations, a semi-analytical approximation to the contribution to the Kerr switching in blue phases due to flexoelectricity is developed. Geometric factors relating analytical approximations of the flexoelectric and dielectric contributions to Kerr switching in blue phases to experimentally measured values are determined, and shown to be similar in magnitude in both cases. The wide-temperature range blue phase materials used are commented upon, whose properties are drastically different from one another, having been developed independently using different approaches.

Chapter 1

Introduction to Key Concepts

1.1 Liquid Crystals

1.1.1 The Nematic Phase

In the case that constituent molecules of a fluid material are anisotropic, either prolate or oblate, then the molecular symmetry can become manifest at the macroscopic scale to produce what are known as nematic liquid crystal phases. These are thermodynamically stable phases that occur within a temperature range between an isotropic liquid and a crystalline solid, and although they are fluid, they can have a variety of orientational and sometimes positional order and associated anisotropic physical properties. The least ordered and most common liquid crystal mesophase used in technology is the thermotropic calamitic nematic phase, which consists of prolate molecules. The nematic phase is characterised by having orientational order but no positional order, as illustrated in fig. 1.1.

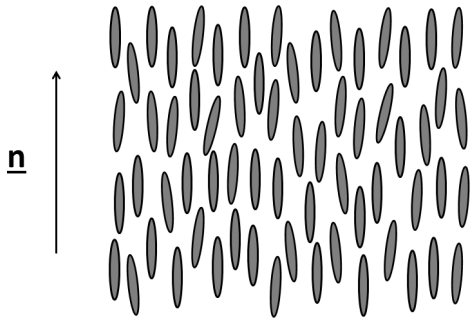

Figure 1.1: Molecules in a calamitic nematic. The average orientation of the molecules is given by the director $\hat{\mathbf{n}}$.

To describe such a phase, we can ignore individual molecular motions and instead adopt

a set of macroscopic parameters. The nematic director, denoted $\hat{\mathbf{n}}$, is a unit vector oriented parallel to the average axis of molecules in a local region, or alternatively, the time-averaged axis of a single molecule. The macroscopic order parameter, S, characterises something like the variance of the orientations of molecules with respect to the director. For a uniaxial nematic, S is quantified by the mean of the second Legendre polynomial, P_2,

$$S = \langle P_2(\cos\theta) \rangle = \langle \frac{3}{2}\cos^2\theta - \frac{1}{2} \rangle \tag{1.1}$$

where θ is the angle of a molecule with respect to the local director $\hat{\mathbf{n}}$. The cosine function produces the desired symmetry, and the coefficients allow the order parameter to take a value of $S = 0$ for the isotropic case, and $S = 1$ where all molecules are aligned without deviation from the director. For nematic liquid crystals S is somewhere between 0 and 1 and varies with temperature.

1.1.2 A Liquid Crystal Cell

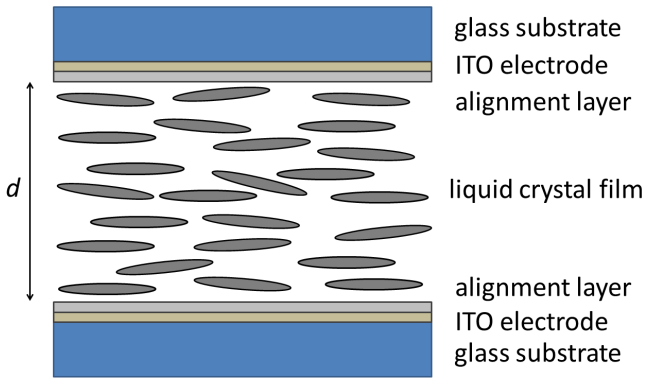

Figure 1.2: This illustration is not to scale. A liquid crystal cell is a composite structure consisting of a liquid crystal film of thickness d confined between glass substrates that have been treated with transparent conducting electrodes and alignment layers. The illustration here represents a planar liquid crystal alignment.

The nematic phase's fluidity and anisotropy make is suitable for a variety of different technological applications. In order to utilise the liquid crystal, it is normally filled into a

'cell', that is, two glass substrates separated by a small distance, d, such that a thin film of liquid crystal is formed, as illustrated in figure 1.2. The film thickness is determined by the cell thickness, and is usually between 2 and 10 µm, depending on the application. This thickness is often controlled using spacer particles of known diameter or another spacing material. The substrate surfaces are usually treated with a variety of additional functional layers. A transparent conducting medium, such as indium tin oxide (ITO) can be used to apply voltages across the cell, and an alignment layer can be used control the director orientation at each surface interface.

1.2 Elastic Properties

1.2.1 Bulk Elastic Energy

The equilibrium state for a nematic liquid crystal is where the director orientation is invariant in space, i.e. the liquid crystal has a uniform director field. Distortions in the director field have an elastic energy cost, the magnitude of which is dependent on the type of distortion and varies from one liquid crystal to another. A macroscopic continuum model has developed over time which has proven highly successful at modelling the behaviour of liquid crystals. Still one of the best and most lucid descriptions of the basic continuum model for elastic energy is the original paper by Frank, whose Frank elastic energy equation is ubiquitous in the field of liquid crystal science [1]. The paper discusses elastic energy in terms of possible types of director distortion away from being uniform, and then considers energy-degenerate transformations that are inherent to the nematic symmetry to reduce the elastic energy expression to key coordinate-independent energy terms.

The result of the process is that elastic energy in nematic liquid crystals can be described by a combination of three distortions: splay, twist and bend. Mathematically, these distortions are related to the director by $[\nabla \cdot \hat{\mathbf{n}}]$, $[\hat{\mathbf{n}} \cdot (\nabla \times \hat{\mathbf{n}})]$, and $[\hat{\mathbf{n}} \times (\nabla \times \hat{\mathbf{n}})]$ respectively, and are illustrated in fig. 1.3.

An elastic energy density per unit volume of the system is given by the Frank-Oseen

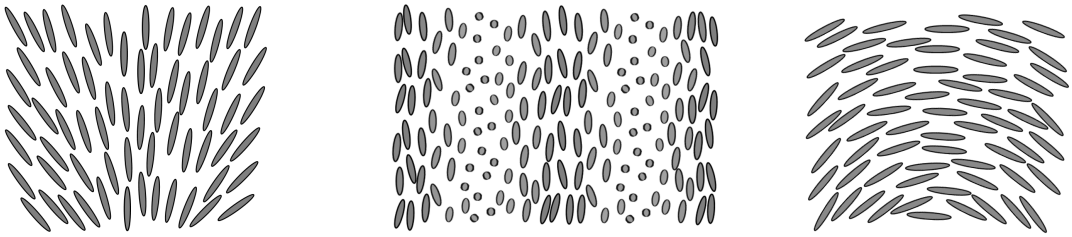

Figure 1.3: Illustration of splay $[\nabla \cdot \hat{\mathbf{n}}]$ (left), twist $[\hat{\mathbf{n}} \cdot (\nabla \times \hat{\mathbf{n}})]$ (center) and bend $[\hat{\mathbf{n}} \times (\nabla \times \hat{\mathbf{n}})]$ (right) distortions of the director field.

elastic free energy [1],

$$\begin{aligned} f_{\text{elastic}}(\hat{\mathbf{n}}) &= f_{\text{splay}}(\hat{\mathbf{n}}) + f_{\text{twist}}(\hat{\mathbf{n}}) + f_{\text{bend}}(\hat{\mathbf{n}}) \\ &= \frac{1}{2}K_1[\nabla \cdot \hat{\mathbf{n}}]^2 + \frac{1}{2}K_2[\hat{\mathbf{n}} \cdot (\nabla \times \hat{\mathbf{n}})]^2 + \frac{1}{2}K_3[\hat{\mathbf{n}} \times (\nabla \times \hat{\mathbf{n}})]^2 \end{aligned} \tag{1.2}$$

which relates the different kinds of distortion to their elastic potential energy. The coefficients K_1, K_2 and K_3 are usually of the order of 10 pN, but their relative magnitudes vary from one material to another, and indeed are important design parameters in many liquid crystal systems. K_2 is usually smaller than K_1 and K_3.

There is another important elastic constant that Frank identified, but that is not often considered. K_{24} is called the 'saddle splay' elastic energy term, and is usually omitted from considerations of the elastic energy when the director is continuous, because it can be shown mathematically to be only important at surface interfaces or near defects. However, at an interface between a liquid crystal and a surface, the most common approach to model the energy is by using a separate surface energy term, which will be described presently.

1.2.2 Surface Energy

Depending on the treatment of the surface substrates within a cell, it is possible to allow for a variety of liquid crystal alignments to be energetically favoured. A polymer layer such as polyimide or poly-vinyl alcohol, after rubbing with a textile cloth, can orient molecules at the interface with the rubbing direction. If both substrate surfaces are treated in this way, and the cell is constructed such that the rubbing directions are parallel, then a nematic

will form planar alignment, so called because the molecules are in the plane of the cell (see figure 1.2). In contrast, a surfactant treatment such as natural egg lecithin will favour molecular orientations normal to the surface, called homeotropic or perpendicular alignment. To produce an alignment condition, a solution of polymer or surfactant is usually pipetted onto a glass substrate and subsequently spun at about 3000 rpm in order to achieve a uniform thickness. Liquid crystal alignment is notoriously sensitive to differences in cleaning and processes, and in the literature is sometimes referred to as an 'art' [2, 3]. A good reference is the 1982 review on the subject by Jacques Cognard [3].

Using a simple model for homeotropic anchoring, for example, we can describe the energy per unit area of the liquid crystal in contact with a surface as,

$$W_{\text{surface}} = \frac{W_0}{2}\left(1 - (\hat{\mathbf{n}} \cdot \hat{\mathbf{s}})^2\right) \tag{1.3}$$

where W_0 is the surface anchoring strength, $\hat{\mathbf{n}}$ is the unit magnitude director, and $\hat{\mathbf{s}}$ is a unit vector normal to the surface. Notice that in this expression, the surface energy is minimised if $\hat{\mathbf{n}} \cdot \hat{\mathbf{s}}$ is zero, i.e. if the director is normal to the surface interface. The surface anchoring strength depends on the type of alignment used. Rubbed poly-vinyl alcohol, for example, produces an anchoring strength of around 3 mJm^{-2}, but lecithin is approximately 1000 times weaker. We will see this expression used in chapter 4, where we will see that surface interactions must be carefully considered in liquid crystal technologies.

1.3 Electric Properties

1.3.1 Dielectric Energy

In order to understand and model how a liquid crystal responds to electric fields, we must first consider its electric susceptibility. From this we can define the electric displacement, whose integral with respect to the electric field is the dielectric energy. Because liquid crystals are anisotropic, we will see that the energy depends on the angle between the director and the field, and this means that electric fields can be used to align the liquid crystal detector, which we will see exploited in subsequent sections.

Liquid crystals are dielectric materials, that is, under the application of a field, electric polarization occurs that acts to reduce the energy of the system by reducing the electric flux. Nematic liquid crystals in general have different susceptibilities parallel and perpendicular to the director, and so we must express the susceptibility with a tensor,

$$\chi_e = \begin{bmatrix} \chi_\perp & 0 & 0 \\ 0 & \chi_\perp & 0 \\ 0 & 0 & \chi_\parallel \end{bmatrix} \tag{1.4}$$

where $\chi_\perp$ and $\chi_\parallel$ are the susceptibilities perpendicular and parallel to a director aligned along an arbitrary z-axis. Now, we can express the polarization as,

$$\mathbf{P} = \varepsilon_0 \chi_e \mathbf{E} \tag{1.5}$$

The polarization is therefore also a tensor, and a consequence of the anisotropy is that the polarization is in general not parallel to the field direction. The electric displacement can thus be defined,

$$\mathbf{D} = \varepsilon_0 \mathbf{E} + \mathbf{P} = \varepsilon_0 (\mathbf{I} + \chi_e)\mathbf{E} = \varepsilon_0 \varepsilon_r \mathbf{E} \tag{1.6}$$

where $\mathbf{I}$ is the identity matrix (multiplying a tensor by the identity matrix leaves the tensor unchanged), and we have defined the relative permittivity ε_r, which is also a tensor. Writing this in full, we have,

$$\mathbf{D} = \varepsilon_0 \begin{bmatrix} \varepsilon_\perp & 0 & 0 \\ 0 & \varepsilon_\perp & 0 \\ 0 & 0 & \varepsilon_\parallel \end{bmatrix} \begin{bmatrix} E_x \\ E_y \\ E_z \end{bmatrix} \tag{1.7}$$

which can be written,

$$\mathbf{D} = \varepsilon_0 \left(\varepsilon_\perp \begin{bmatrix} 1 & 0 & 0 \\ 0 & 1 & 0 \\ 0 & 0 & 1 \end{bmatrix} \begin{bmatrix} E_x \\ E_y \\ E_z \end{bmatrix} + \begin{bmatrix} 0 & 0 & 0 \\ 0 & 0 & 0 \\ 0 & 0 & \Delta\varepsilon \end{bmatrix} \begin{bmatrix} E_x \\ E_y \\ E_z \end{bmatrix} \right) \tag{1.8}$$

which, because $\hat{\mathbf{n}} = (0, 0, 1)$, can be written simply,

$$\mathbf{D} = \varepsilon_0 \varepsilon_\perp \mathbf{E} + \varepsilon_0 \Delta\varepsilon (\hat{\mathbf{n}} \cdot \mathbf{E}) \hat{\mathbf{n}} \tag{1.9}$$

where $\Delta\varepsilon = \varepsilon_\parallel - \varepsilon_\perp$ and is called the dielectric anisotropy. The dielectric anisotropy varies from one material to another, and is an important design parameter for different applications. The common liquid crystal E7 has $\Delta\varepsilon = 13.7$, bimesogenic mixtures often have $\Delta\varepsilon \approx 0$, and the negative material MLC-7029 has $\Delta\varepsilon = -3.7$.

To obtain the dielectric energy, we must evaluate,

$$f_{\text{dielectric}} = -\int_0^{\mathbf{E}} \mathbf{D}.\mathrm{d}\mathbf{E} \tag{1.10}$$

and thus the dielectric energy is,

$$f_{\text{dielectric}} = -\frac{1}{2}\varepsilon_0\varepsilon_\perp E^2 - \frac{1}{2}\varepsilon_0\Delta\varepsilon(\hat{\mathbf{n}}\cdot\mathbf{E})^2 \tag{1.11}$$

Note that only the second term is dependent upon the director orientation, and therefore the first term is usually omitted when expressing the free energy. The free energy can therefore be simply expressed as,

$$f_{\text{dielectric}} = -\frac{1}{2}\Delta\varepsilon\varepsilon_0(\hat{\mathbf{n}}\cdot\mathbf{E})^2 \tag{1.12}$$

From this we see that the dielectric free energy is minimised when the director is parallel to the field for positive dielectric anisotropy, and perpendicular to the field for negative dielectric anisotropy. This result means that an electric field can potentially be used to reorient the liquid crystal director, if doing so will result in a smaller total free energy. In this thesis, the 'dielectric effect' will be used to refer to the reorientational torque on the director due to the coupling of the dielectric anisotropy to the field.

1.3.2 Dispersion

The dielectric susceptibility of a material is a measure of the dipole moment induced per unit volume per unit electric field. In liquid crystals there are several contributing phenomena; primarily an induced molecular dipole and an induced population bias in the orientations of permanent molecular dipoles. There is a correlation between the mobilities of molecular dipole reorientations and the time-dependence of macroscopic induced electric polarization [4, 5, 6], and this means that the dielectric susceptibility is dependent on field frequency. The frequency-dependent dielectric constant undergoes drops in magnitude, known as a 'relaxations', that are centred on characteristic frequencies associated with the time dependence of particular contributions to the susceptibility. Relaxation in the dielectric constant as a function of frequency is also known as dispersion, and will be discussed in detail in chapter 5.

1.3.3 Capacitance

A liquid crystal cell comprising a liquid crystal layer sandwiched between two conducting electrodes acts as a capacitor, with a capacitance given by,

$$C = \varepsilon_r \varepsilon_0 \frac{A}{d} \tag{1.13}$$

where A is the area of the cell, d the cell thickness and ε_r the relative permittivity of the dielectric medium within the cell. The relative permittivity of the liquid crystal can be determined by measuring the cell's capacitance before and after the cell is filled. Since the permittivity of air is approximately the same as free space, we have,

$$\varepsilon_r = \frac{C_{\text{filled}}}{C_{\text{empty}}} \tag{1.14}$$

Hence, by repeating the procedure for planar and homeotropically aligned cells, one can determine the parallel and perpendicular components of the liquid crystal dielectric permittivity.

Capacitance measurements can reveal other properties of liquid crystals and are an important tool in liquid crystal research. Most commonly, capacitance is measured as a function of the applied voltage, which can be used to measure elastic properties (see for example reference [7]). Further, capacitance can be measured as a function of frequency, and this allows for the study of dielectric relaxation phenomena in liquid crystals (and indeed dielectric media in general). This technique will be used in chapter 5, where a novel dielectric dispersion effect in liquid crystals is exploited to switch between states in a reflective liquid crystal display technology.

1.3.4 Flexoelectricity

Although liquid-crystal molecules have different components of a permanent dipole moment parallel and perpendicular to the molecular axis, in the absence of an electric field or bulk distortion, there is no net polarization in the nematic phase. This is because the equilibrium thermodynamic distribution of molecular orientations has rotational symmetry

about the director and is invariant under the inversion transformation $\hat{\mathbf{n}} \leftrightarrow -\hat{\mathbf{n}}$, which provides the necessary nematic uniaxial symmetry. However, when an electric field is applied, the equilibrium distribution is disturbed and a bulk net polarization is induced. As we saw in §1.3.1, the resulting coupling to the induced polarization leads to reorienting torque due to the anisotropy in the polarizability, which is referred to as the 'dielectric effect'.

However, the coupling between electric fields and director-reorienting torques is further complicated by an effect called flexoelectricity, which was first described by Meyer in 1969 [8]. If liquid crystal molecules have shape anisotropy, for example the molecules are bent (banana shaped) or wider at one end (pear shaped), then a field-induced population bias in molecular orientations reduces the molecular packing efficiency, at a cost to the free energy. This cost in energy effectively reduces the material's polarizability and the resultant dielectric torque on the molecules [9, 10]. However, the liquid crystal can mitigate the reduced packing efficiency by forming spontaneous curvature distortion and as a result, there is a coupling between electric fields and director curvature distortions.

Reciprocally, if a curvature distortion is present, a spontaneous population bias in dipole orientations occurs that results in electric polarization, as illustrated by figures 1.4 and 1.5. This polarization produces an internal field at a free energy cost, that effectively increases the material's elastic constant. This effect has been expounded by Helfrich [9].

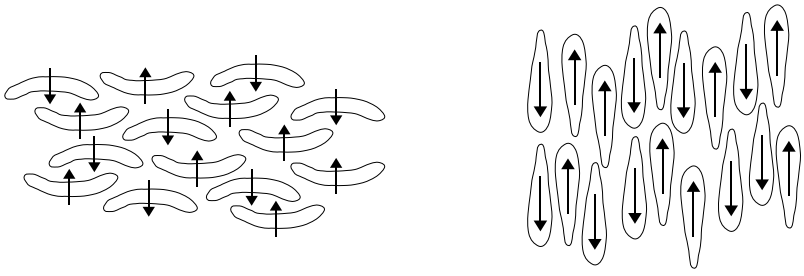

Figure 1.4: Banana shaped and pear shaped molecules pack closely when there is no net polarization. Molecular dipole moments are represented by arrows.

The free energy associated with flexoelectric polarization can be expressed as,

$$f_{\text{flexo}}(\hat{\mathbf{n}}) = -\mathbf{P}_{\text{flexo}} \cdot \mathbf{E} \tag{1.15}$$

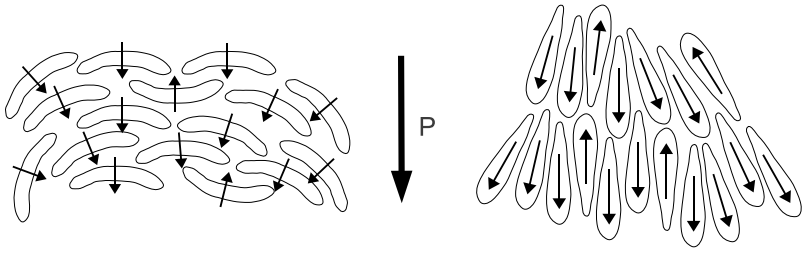

Figure 1.5: A bend or splay distortion breaks the symmetry of dipole moment orientations and gives rise to a flexoelectric polarization.

where $\mathbf{P}_{\text{flexo}}$ is given by,

$$\mathbf{P}_{\text{flexo}} = e_1\hat{\mathbf{n}}(\nabla\cdot\hat{\mathbf{n}}) + e_3(\nabla\times\hat{\mathbf{n}})\times\hat{\mathbf{n}} \tag{1.16}$$

where e_1 and e_3 are the bend and splay flexoelectric coefficients in the original Meyer sign convention for flexoelectric polarization [8]. Putting this together with the elastic and dielectric free energy contributions gives an expression for the total free energy density,

$$\begin{aligned} F(\hat{\mathbf{n}}) =& \frac{1}{2}K_1[\nabla\cdot\hat{\mathbf{n}}]^2 + \frac{1}{2}K_2[\hat{\mathbf{n}}\cdot(\nabla\times\hat{\mathbf{n}}) + q]^2 + \frac{1}{2}K_3[\hat{\mathbf{n}}\times(\nabla\times\hat{\mathbf{n}})]^2 \\ & - \frac{1}{2}\varepsilon_0\Delta\varepsilon(\hat{\mathbf{n}}\cdot\mathbf{E})^2 - \left[e_1\hat{\mathbf{n}}(\nabla\cdot\hat{\mathbf{n}}) + e_3(\nabla\times\hat{\mathbf{n}})\times\hat{\mathbf{n}}\right]\cdot\mathbf{E} \end{aligned} \tag{1.17}$$

With this single expression, one can model very accurately a large variety of device behaviours, and derive useful analytical expressions for many specific distortions, as we will see in subsequent sections. Note that the flexoelectric contribution is dependent on the field and is therefore dependent on the sign of the field, however, the dielectric contribution is dependent on the square of the field, and is therefore independent of the sign of the field. This will become an important distinction later on.

Finally, the flexoelectric effect can be expressed also in terms of the resultant torque on the director [11, 12, 13]. The flexoelectric torque can be expressed $(\hat{\mathbf{n}}\times\mathbf{h}_{\mathbf{flexo}})$ where,

$$\mathbf{h}_{\text{flexo}} = (e_1 - e_3)\big(\mathbf{E}(\nabla\cdot\hat{\mathbf{n}}) - (\nabla\otimes\hat{\mathbf{n}})\mathbf{E}\big) - (e_1 + e_3)(\hat{\mathbf{n}}\cdot\nabla)\mathbf{E} \tag{1.18}$$

and is the flexoelectric contribution to the molecular field. The molecular field describes the change in the energy of the system for changes in director orientation. By representing

flexoelectricity in this way we see that the flexoelectric interaction is split into a part that depends upon field gradients in which $e_1 + e_3$ is important (sometimes called gradient flexoelectricity), and a part that depends on the field magnitude in which $e_1 - e_3$ is important. We will see in chapter 2 that the measurement of e_1 or e_3 individually is very difficult, and in general the approach is to measure combinations of either $e_1 + e_3$ or $e_1 - e_3$.

1.4 Optical Properties

The anisotropic nature of liquid crystals gives them birefringence, and the ability to control the optic-axis orientation using electric fields is convenient for electro-optic technology. Here are presented some important concepts to understand the subsequent work.

1.4.1 Polarization and Birefringence

The refractive index n of a non-magnetic material is related to its relative dielectric permittivity ε_r via,

$$n = \sqrt{\varepsilon_r} \tag{1.19}$$

Since the dielectric permittivity is frequency dependent, it is different at optical frequencies than at the voltage frequencies that are used to drive liquid crystal devices. There are also dispersion phenomena within the range of optical frequencies, and therefore the refractive index varies with the wavelength of light.

Because liquid crystal materials are anisotropic, they are in general also birefringent. Birefringence is characterised by the difference in refractive indices parallel and perpendicular to the optic axis, $\Delta n = n_{\mathrm{e}} - n_{\mathrm{o}}$. Polarization components of light travelling parallel and perpendicular to the optic axis travel at different velocities through the liquid crystal, resulting in a phase lag between the polarization components that changes the light's polarization state.

Consider an electromagnetic wave with angular frequency ω, and wavevector k_0, propagating in the z direction in free space having equal components of its electric field **E** in

both x and y directions, described by,

$$E_x(z,t) = E_0 \cos(k_0 z - \omega t) \tag{1.20}$$

$$E_y(z,t) = E_0 \cos(k_0 z - \omega t + \delta) \tag{1.21}$$

where E_0 is a field amplitude and δ is equivalent to a difference in phase between the x and y field components. In the case where $\delta = n\pi$ where $n = 0, 1, 2\ldots$, the wave is said to be linearly polarized, because the field vector stays in the same plane through time and space. If the waves are perfectly out of phase, i.e. $\delta = \frac{\pi}{2}$, then the wave is said to be circularly polarized, and the field vector rotates about the *z*-axis through space and time. In any other case, the wave is said to be elliptically polarized.

In a dielectric medium, the permittivity is different from that of free space, and this means that the wavevector k in the medium changes proportional to the refractive index. A wave propagating in the z direction through a birefringent material whose optic axis is in the y direction, will have x and y components of the electric field affected by different refractive indices corresponding to those perpendicular and parallel to the optic axis;

$$E_x(z,t) = E_0 \cos(n_\perp k_0 z - \omega t) \tag{1.22}$$

$$E_y(z,t) = E_0 \cos(n_\parallel k_0 z - \omega t) \tag{1.23}$$

which can be rewritten as,

$$E_x(z,t) = E_0 \cos(n_\perp k_0 z - \omega t) \tag{1.24}$$

$$E_y(z,t) = E_0 \cos(n_\perp k_0 z - \omega t + \Delta n k_0 z) \tag{1.25}$$

i.e. as the wave propagates through the birefringent material, the phase difference between the wave's x and y field components (the phase retardation) changes by an amount,

$$\delta = \Delta n k_0 z \tag{1.26}$$

thereby altering the polarisation state of the wave.

Here we have considered light incident normal to the optical axis, however, in many situations we would like to know the refractive index experienced when the light is not normal to the optical axis. The ordinary and extra-ordinary waves (those parallel and perpendicular to the optic axis respectively) travelling though a uniaxial medium experience a refractive index given by $n = n_{\mathrm{o}}$ for the ordinary component and,

$$n = \left(\frac{\cos^2 \phi}{n_{\mathrm{o}}^2} + \frac{\sin^2 \phi}{n_{\mathrm{e}}^2} \right)^{-\frac{1}{2}} \tag{1.27}$$

for the extraordinary component, where ϕ is the angle between the optic axis and the direction of light propagation. Note that at $\phi = 0$, the refractive index for both ordinary and extraordinary components are equal to n_{o}, and at $\phi = \pi/2$, the extraordinary component has $n = n_{\mathrm{e}}$ as expected. For a more detailed description of the propagation of light through uniaxial media, see Yeh and Gu [14].

1.4.2 Jones Matrices

When dealing with the propagation of light through birefringent media, it is often convenient to exploit a matrix formulation of polarization states. All polarization states can be expressed in terms of a 2-by-1 complex column vector representing x- and y-components of the E-field. The phase of the component is given by the inverse-tangent of the real and imaginary parts, while the amplitude is simply the magnitude of the complex number. For example, linear and circular polarization states can be described by,

$$\text{linear} = \frac{1}{\sqrt{2}} \begin{bmatrix} 1 \\ -1 \end{bmatrix} \qquad \text{circular} = \frac{1}{\sqrt{2}} \begin{bmatrix} 1 \\ i \end{bmatrix} \tag{1.28}$$

Here, the factor $1/\sqrt{2}$ gives the vector a magnitude of 1. Note in the case of a linear state, both components are real and therefore represent components that are in phase. In contrast, the circular polarization state is represented by x- and y-components being out of phase by $\pi/2$. A further feature of this representation is that any polarization state can be described by the linear superposition of two orthogonal components, which means that one can always transform a given polarization state in order to describe it in terms of components parallel and perpendicular to a given coordinate axis.

This kind of representation is powerful for calculating polarization states after light has passed through various optical elements. Optical elements such as polarizers, birefringent slabs (wave plates), and rotation transformations can be described by 2-by-2 matrices. Multiplying these matrices with the polarization state vector yields the transmitted polarization state. For example, consider a linear polarizer that completely attenuates the y-component of E-field, acting on the circular polarization state described in equation 1.28. The state can be calculated by,

$$\begin{bmatrix} 1 & 0 \\ 0 & 0 \end{bmatrix} \frac{1}{\sqrt{2}} \begin{bmatrix} 1 \\ i \end{bmatrix} = \frac{1}{\sqrt{2}} \begin{bmatrix} 1 \\ 0 \end{bmatrix} \tag{1.29}$$

in which the 2-by-2 matrix is the linear polarizer. Note the transmitted polarization state becomes a linear polarization state.

Often, one wants to know the transmission amplitude of light passing through a wave plate situated between orthogonally arranged (crossed) polarizers, whose optic axis makes an angle $\pi/4$ with the first polarizer. This situation represents many involving a liquid crystal that is uniformly aligned and observed between crossed polarizers, either in a display, a polarizing microscope, or with a laser and photo diode. The problem can be expressed in terms of Jones matrices,

$$\begin{bmatrix} 0 & 0 \\ 0 & 1 \end{bmatrix} \begin{bmatrix} \cos(\delta/2) & -i\sin(\delta/2) \\ -i\sin(\delta/2) & \cos(\delta/2) \end{bmatrix} \frac{1}{\sqrt{2}} \begin{bmatrix} 1 \\ 0 \end{bmatrix} = \frac{1}{\sqrt{2}} \begin{bmatrix} 0 \\ -i\sin\delta/2 \end{bmatrix} \tag{1.30}$$

where the second matrix represents a wave plate with a phase retardation δ given by,

$$\delta = \frac{2\pi\Delta n d}{\lambda} \tag{1.31}$$

where d is the thickness of the wave plate and λ is the wavelength of incident light. The resultant transmission amplitude is calculated by multiplying the resultant polarization vector by its complex conjugate, giving,

$$T = \frac{\sin^2(\delta/2)}{2} \tag{1.32}$$

Note that Jones matrices are not, in general, commutable, and so the order of optical components in an experiment is often crucial to the behaviour of the transmitted light.

Finally, a couple of precautions should be observed when using Jones matrices. Jones matrices model only the forward propagating wave, and cannot deal with reflected components. Further, Jones matrices do not accommodate variations in the optic axis or birefringence of dielectric media in directions perpendicular to the light propagation vector. In order to take account of reflected components and more complicated geometries, a more advanced model must be employed. For example, the 4-by-4 Berreman matrix method takes into account more components and can model a larger variety of situations [15]. We will see in subsequent chapters that the Berreman method will be necessary to model device optics accurately in many of the experiments in this thesis, however for a detailed discussion, please refer to references [15, 16, 17].

1.5 Chirality in Liquid Crystals

1.5.1 Spontaneous Helicity

A liquid crystal mixture comprised of mirror-symmetric or racemic molecules has a minimum elastic energy when the director is uniform. However, if the molecules are chiral, or a chiral dopant is added, the mirror symmetry is broken resulting in a tendency for the director to rotate through space to form a helicoidal structure. Such a material is often called a cholesteric. The director of a cholesteric material whose helicoidal axis lies along the z-axis, as illustrated in figure 1.6, can be described by,

$$\hat{\mathbf{n}} = \begin{bmatrix} \cos\theta \\ \sin\theta \\ 0 \end{bmatrix} \tag{1.33}$$

The natural twist can be accounted for in the elastic continuum model by modifying the 'twist' elastic energy term in equation 1.2 such that,

$$f_{\text{twist}}(\hat{\mathbf{n}}) = \frac{1}{2} K_2 [\hat{\mathbf{n}} \cdot (\nabla \times \hat{\mathbf{n}}) + q]^2 \tag{1.34}$$

where q is the chirality (or wavenumber of the unconstrained helical twist) of the liquid crystal material, given by,

$$q = \frac{2\pi}{P} \tag{1.35}$$

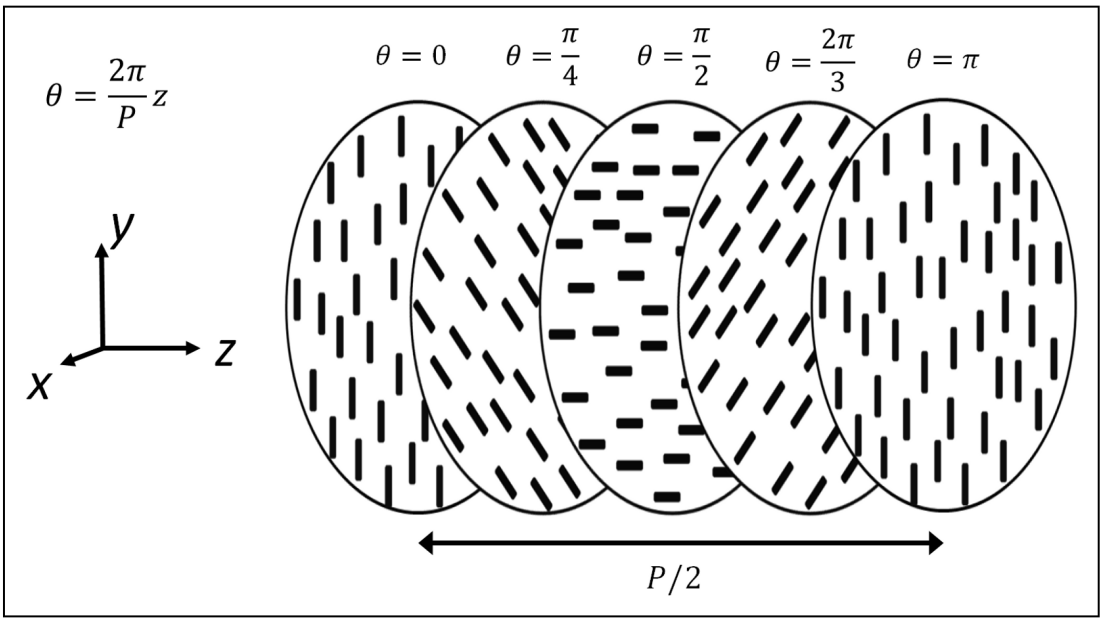

Figure 1.6: The presence of chiral asymmetry results in a spontaneous helicoidal director structure in which the director rotates in space.

where P is the natural pitch of the material or the distance over which the director rotates about the helicoidal axis by 2π. Due to the uniaxial nematic symmetry, the cholesteric structure is periodic over a distance $P/2$.

The pitch is controlled primarily by the concentration of chiral additive. Many chiral additives have been designed to maximise the induced chirality with the minimum concentration, in order to reduce the effect on other properties such as phase transition temperatures. The dopant's helical twisting power (HTP) is defined as,

$$\mathrm{HTP} = \frac{1}{P \times \mathrm{concentration}} \tag{1.36}$$

although the twisting power also depends on the host liquid crystal. A high-HTP material R5011, which is used often in this thesis, has a HTP of $\approx 1 \times 10^8$ m^{-1}.

For many applications, it is useful to be able to align the cholesteric axis in a variety of orientations with respect to a liquid crystal cell. Planar alignment will favour a state with the helicoidal axis perpendicular to the glass substrates, often called Grandjean alignment [18] (and sometimes Uniform Standing Helix (USH) alignment [19]). Through a variety of processes, a state in which the helicoidal axis is in the plane of the cell can be obtained,

either in a uniform direction, called Uniform Lying Helix (ULH) alignment [20], or randomly oriented, sometimes called focal conic alignment. The alignment of in-plane states, and especially the Uniform Lying Helix state, is the subject of chapter 4. Polarizing optical microscope pictures of the different alignment textures are shown in §1.6.3.

1.5.2 Blue Phases

In some cases, where the pitch of the cholesteric material is small ($\lesssim 500$ nm), there exist one or more of what are known as blue phases, in the temperature region between the isotropic and cholesteric phase. Three thermodynamically stable blue phases are known to exist; BPI, BPII and BPIII, in order of increasing temperature (see figure 1.7) [21, 22]. Whilst in the cholesteric phase the director twists uniformly in a single direction along the helicoidal axis, the blue phases consist of arrangements of cylinders in which the director twists in a radial direction from the cylinder centre. These arrangements are not topologically compatible with a continuous director structure, and as a result a network of non-continuous line-defects in the director field occur. BPI and BPII have body-centred cubic and simple cubic symmetry of the director structure, while BPIII is amorphous. A visual representation of the cubic phases can be found, for example, in reference [23].

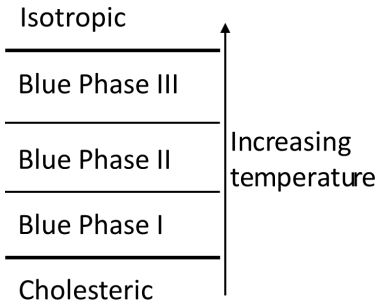

Figure 1.7: The phase sequence in chiral nematic materials that exhibit all three known blue phases. Not all materials exhibit all the phases.

When first discovered, the blue phases were only found to exist in a very narrow temperature range (less than 2°C) [24]. However, recent developments have widened this temperature range, in some cases to over 40°C for pure materials [25] and even greater in polymer stabilised structures [26]. These developments have given blue phases potential application

and have allowed their electrooptic characteristics to be more easily examined, which will be the subject of chapter 6.

1.6 Chiral Liquid Crystal Optics

This thesis is concerned with the exploration and exploitation of the surprising variety of optical and electro-optical behaviours of helicoidal liquid crystals. In this section is presented a brief overview of key optical behaviours of these structures, and includes a description of particular geometries and technologies that exploit them. The particular optical behaviour of a cholesteric material is dependent primarily on the ratio of the pitch to the wavelength of light within the liquid crystal, nP/λ, and here, three special regimes are dealt with in turn.

As noted above, when a cholesteric liquid crystal is aligned with its helicoidal axis uniformly perpendicular to bounding cell substrate surfaces, it is called Grandjean alignment. The transmission of such a device as a function of the incident wavelength is shown in figure 1.8. The behaviour of the transmission as a function of wavelength can be split broadly into three regimes: where the wavelength is much shorter than the pitch, called the wave-guide or Maugin regime; where the wavelength is about the same as the pitch, called selective reflection or the Bragg regime; and where the wavelength is much longer than the pitch, called the circular birefringence regime.

1.6.1 Maugin Regime

In the case that $\lambda \ll nP$, then a cholesteric layer will guide the light polarization state about the helix axis. Consequently, liquid crystals in the so-called Mauguin regime with multiple pitches have extremely large optical rotations.

A useful example of the Mauguin regime is the Twisted Nematic (TN) cell, in which the surfaces are treated with planar alignment layers that have been rubbed at 90° to each other. When filled with a nematic with a pitch much greater than the cell thickness, the liquid crystal will form a 90° twist. Linearly polarized light that is incident with its field vector

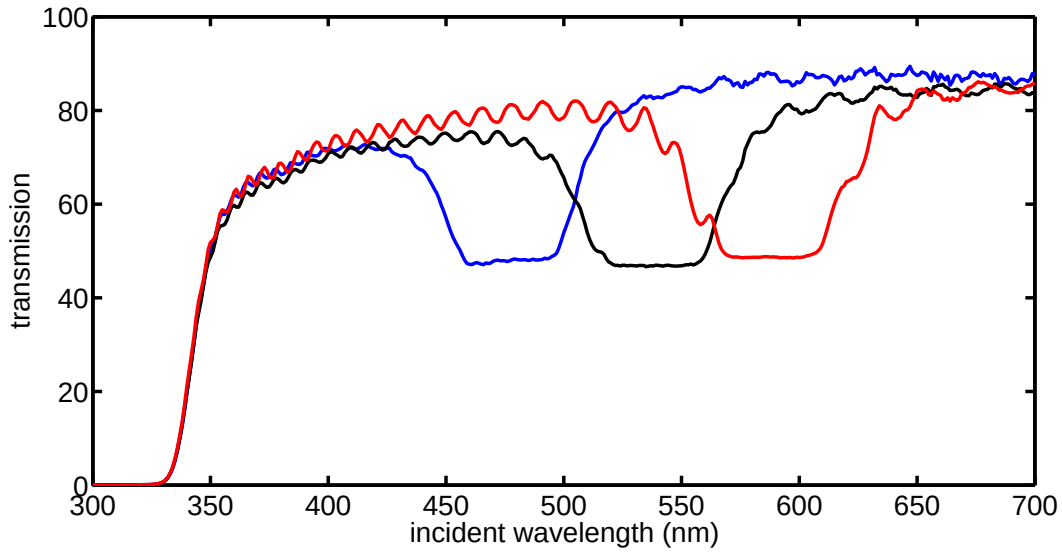

Figure 1.8: Transmission is shown as a function of wavelength for Grandjean cells containing cholesteric materials of three different pitches. At UV wavelengths, the glass in the cell is greatly absorbing. Bragg reflection bands are evident, whose positions are related to the cholesteric pitch by equation 1.37. At longer wavelengths, the cell is highly transmissive in the circular birefringence regime.

parallel to one of the rubbing directions will be guided about the helix axis so that linearly polarized light with its **E** field vector at 90° to that of the incident light's field vector will emerge.

To produce an electrooptic display using the TN, the 90° twisted structure is placed between parallel polarizers as shown in figure 1.9. The polarization state of light travelling through the first polarizer is rotated by 90° due to the liquid crystal twist, and is therefore attenuated by the analyser, producing an opaque state. If a sufficient voltage is applied then the liquid crystal director becomes homeotropic, thereby destroying the twisted structure and allowing the light to pass through to produce a highly-transmitting display state.

1.6.2 Bragg Regime

In the case that $n_{\mathrm{e}}P > \lambda > n_{\mathrm{o}}P$, for light propagating parallel to the helicoidal axis there is a selective Bragg reflection of circularly polarized light that is of the same handedness as the twist of the cholesteric, while the other circularly polarized component of the light

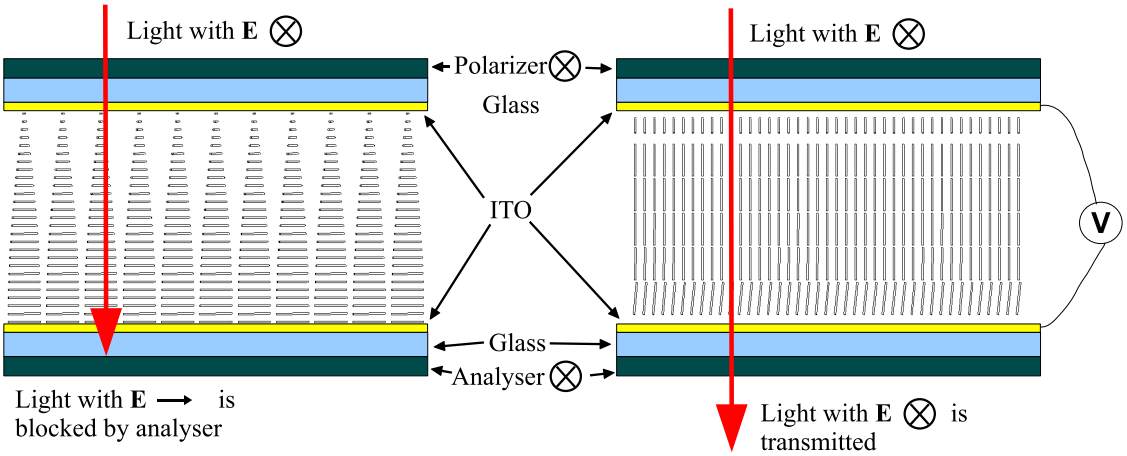

Figure 1.9: Illustration of the TN liquid crystal display mode. (left) Surface conditions impose a 90° rotation of the director across the device. Linear polarized light is guided by 90° and blocked by a second, parallel analyser. (right) A voltage applied across the device causes the director to become homeotropic; the liquid crystal no longer rotates the polarization state, and the light is transmitted. Hence, the transmission is electrically controllable.

is transmitted. The reflection occurs because the helical structure is a periodic dielectric interface that promotes the constructive interference of reflected components, resulting in a photonic band-gap that prevents the propagation of light. The structure can therefore be described as a one-dimensional photonic crystal for a particular circular polarization. The centre of the Bragg band-gap corresponds to,

$$\lambda_{\text{Bragg}} = \frac{P}{2}\left(n_{\text{e}} + n_{\text{o}}\right) \tag{1.37}$$

If the refractive indices are known, measuring the transmission spectrum and observing the midpoint in the Bragg reflection band is a standard method for determining the cholesteric pitch P [27].

The Bragg Regime has also been successfully exploited as a reflective display technology [28, 29, 30], which will be discussed in detail in chapter 5 where a cholesteric material is used to produce a reflective display. In the Grandjean state, wavelengths that coincide with the Bragg reflection band that are of the same handedness as the cholesteric helicoid are reflected to produce a bright reflective state. One or more processes are then used to create a transmitting state in which the helicoidal axis is parallel to the cell. The Bragg

regime has also been exploited for mirrorless liquid crystal band-edge lasing [31, 32]. The unique properties of cholesteric liquid crystals potentially allow for the electric control of lasing wavelengths [33, 34].

1.6.3 Circular Regime

In the case that $\lambda \gg nP$, then the light will not be guided. Instead, the cholesteric material becomes optically uniaxial with a negative birefringence and with the optic axis parallel to the helicoidal axis [35]. Because the liquid crystal contains chiral compounds, the material in this regime also exhibits optical activity, with a specific rotatory power given by,

$$\rho = \frac{\pi n^2 (\Delta n)^2 P^3}{4\lambda^4} \tag{1.38}$$

as given in reference [14]. Optical polarizing micrographs of such a material, whose pitch is much less than optical wavelengths, are shown in figure 1.10. Note that the term 'texture' refers to the appearance of a particular liquid crystal state under polarizing optical microscopy.

The refractive index component perpendicular to the helicoidal axis is given by,

$$n_2 = \sqrt{\frac{\varepsilon_\perp + \varepsilon_\parallel}{2}} \tag{1.39}$$

such that the cholesteric has refractive index components given by,

$$\begin{bmatrix} n_1 \\ n_2 \end{bmatrix} = \begin{bmatrix} n_{\mathrm{o}} \\ \sqrt{\frac{1}{2}(n_e^2 + n_o^2)} \end{bmatrix} \tag{1.40}$$

where n_1 and n_2 are the refractive index components parallel and perpendicular to the helicoidal axis respectively.

One can simply represent the optics by considering the cholesteric as a uniaxial material with a negative birefringence. Using a Jones matrix approach, as we saw in §1.4.2, one can then calculate the transmission between crossed polarizers for a Uniform Lying Helix device, which is given by,

$$T = \frac{1}{2}\sin^2(2\chi)\sin^2\left(\frac{\pi \Delta n_{\text{effective}} d}{\lambda}\right) \tag{1.41}$$

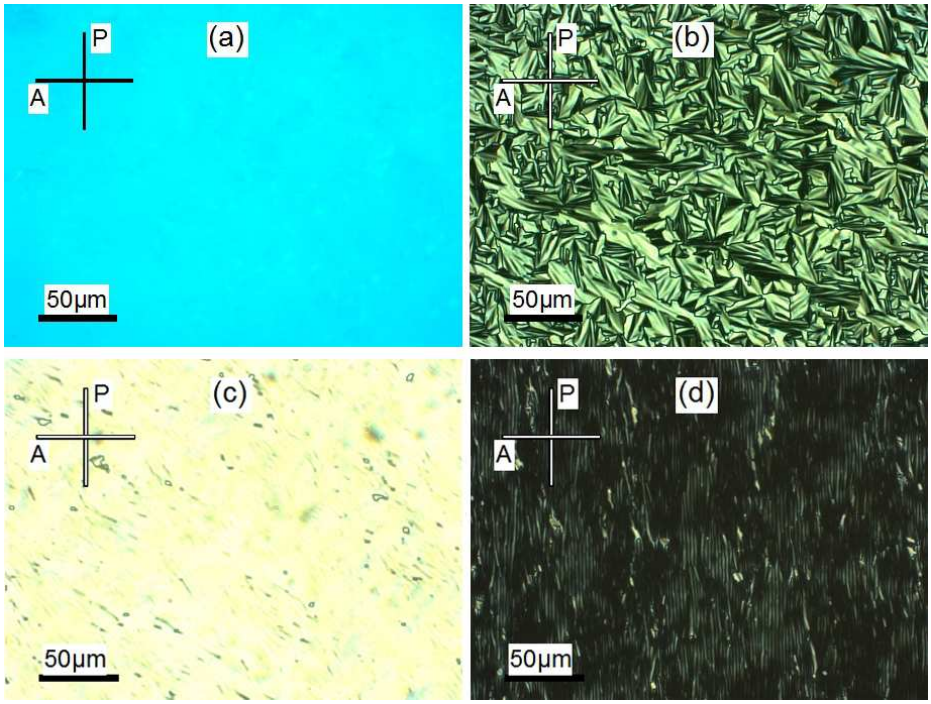

Figure 1.10: Polarizing optical microscope photographs of liquid crystal textures in which the cholesteric has a $nP \ll \lambda$. (a) The Grandjean texture, in which the helicoidal axis is oriented normal to the cell. The texture appears blue due to the optical rotatory power of the material, which rotates shorter blue wavelengths more than longer red ones as per equation 1.38. (b) The focal conic texture, in which the helicoidal axis forms small, randomly oriented domains of uniform orientation. (c) and (d) show the Uniform Lying Helix (ULH) texture, in which the helicoidal axis is uniformly aligned in the plane of the cell at an angle of $\chi = \pi/4$ and $\chi = 0$ to the polarizer respectively. The transmission depends upon χ as per equation 1.41.

where χ is the angle that the material's optic axis makes with the polarizer, d is the thickness of the liquid crystal layer, λ is the wavelength of incident light and $\Delta n_{\text{effective}} = n_1 - n_2$ and is the effective birefringence of the cholesteric. The factor $1/2$ accounts for unpolarized incident light.

Determining the Optic Axis of a ULH structure

From equation 1.41, we can see that the transmission is degenerate under the transformation $\chi \to \chi + \pi/2$. It can therefore be difficult to know the optic axis, and therefore helicoidal axis, orientation within a device. A useful method for determining the orientation is to position the ULH between crossed polarizers in series with a thin (2µm) homeotropically

aligned cell. At normal incidence, the homeotropically aligned cell has no effective birefringence, however, as it is rotated out of the plane of the polarizers and ULH device, about an axis at 45 degrees to the polarizers, its effective birefringence increases. The ULH optic axis can be determined by considering that the transmission of this system is given by,

$$T = \frac{1}{2}\sin^2(2\chi)\sin^2\left(\frac{\pi\Delta n_{\text{effective}}d}{\lambda} + \frac{\pi\Delta n_{\text{H}}d}{\lambda\sin\alpha}\right) \tag{1.42}$$

where n_{H} is the effective birefringence of the homeotropic device, given by,

$$\Delta n_{\text{H}} = \left(\frac{\cos^2\alpha}{n_{\text{o}}^2} + \frac{\sin^2\alpha}{n_{\text{e}}^2}\right)^{-\frac{1}{2}} - n_{\text{o}} \tag{1.43}$$

and α here is the angle that the optic axis of the homeotropic device makes with the normal to the ULH device and polarizers. As the homeotropic device is rotated out of the plane, the retardation will either add or subtract from the ULH retardation, and whether there is an increase or decrease in the resultant transmission reveals the ULH optic axis.

The regime where $\lambda \gg nP$ has potential application in a variety of fast-switching electrooptic technologies, as will be discussed in subsequent chapters.

1.6.4 Optics of the Blue Phases

Blue phase materials in which $\lambda \gg nP$ are optically isotropic due to their cubic or amorphous symmetry, and exhibit optical rotatory powers much smaller than their cholesteric counterparts [21]. In the case where $\lambda \approx nP$, Bragg reflections occur in BPI and BPII, in a close analogue to the cholesteric phase. While the cholesteric phase reflects in only a single direction, however, the cubic symmetry of the blue phases make them three-dimensional photonic crystals that reflect light incident from all directions. The optics and electrooptics of blue phases, as well as their application potential, will be discussed in more detail in chapter 6.

In short pitch liquid crystals in which blue phases exist, it is sometimes difficult to distinguish between Grandjean and blue phases using a polarizing microscope, as both appear optically isotropic. One way to distinguish easily between them is to tilt the cell. If the liquid crystal is in the Grandjean alignment, then tilting the cell will result in some

effective birefringence and light leakage through crossed polarizers. For the blue phase however, which has no birefringence, no such light leakage will occur.

1.7 Dielectric Effects in Chiral Systems

The dielectric interaction produces a quadratic electrooptic (Kerr) effect in blue phase systems, and a Kerr-type induced biaxiality in the cholesteric phase, which will be discussed in the next section. Dielectric interactions can also be used to reorient the helicoidal axis, which will be described in §1.7.2, and at larger field strengths, the dielectric interaction unwinds the helix completely, which will be discussed in §1.7.3. The exploitation of each of these processes in technology will also be commented on. The flexoelectric effect in cholesteric liquid crystals is dealt with separately in §1.8.1.

1.7.1 In-Plane Distortion

In a cholesteric material that is subject to a field applied perpendicular to the helicoidal axis, there will be a torque that distorts the director towards alignment parallel or perpendicular to the field in the plane in which the directors are uniform. In this section, the amplitude of the in-plane distortion that arises due to this torque is determined, following the derivation in the publication by the present author [36].

In order to deal with field effects in cholesteric liquid crystal systems, it is useful to express the elastic and dielectric energy from equations 1.2 and 1.12 in terms of the in-plane angle of the director. Consider an ideal cholesteric structure, whose pitch is constrained such that $P = P_0$, where P_0 is the natural pitch, and whose helicoidal axis is parallel to the z-axis. The director is given by,

$$\hat{\mathbf{n}} = \begin{bmatrix} n_x \\ n_y \\ n_z \end{bmatrix} = \begin{bmatrix} \cos\theta \\ \sin\theta \\ 0 \end{bmatrix} \tag{1.44}$$

where the twist component of the undistorted cholesteric director $\theta(z) = qz$. The free energy of the system is given by,

$$F(\hat{\mathbf{n}}) = f_{\text{elastic}} + f_{\text{dielectric}} \tag{1.45}$$

where,

$$f_{\text{elastic}} = \frac{1}{2}K_1[\nabla \cdot \hat{\mathbf{n}}]^2 + \frac{1}{2}K_2[\hat{\mathbf{n}} \cdot (\nabla \times \hat{\mathbf{n}}) + q]^2 + \frac{1}{2}K_3[\hat{\mathbf{n}} \times (\nabla \times \hat{\mathbf{n}})]^2 \tag{1.46}$$

$$f_{\text{dielectric}} = -\frac{1}{2}\Delta\varepsilon\varepsilon_0(\hat{\mathbf{n}} \cdot \mathbf{E})^2 \tag{1.47}$$

as was described in §1.2 and §1.3 on elastic and electric properties of nematics in equations 1.2 and 1.12. If we apply a field such that $\mathbf{E} = E_x\hat{\mathrm{x}}$, substituting our expression for $\hat{\mathbf{n}}$ from equation 1.44 into equations 1.46 and 1.47, we get,

$$f_{\text{elastic}} = \frac{1}{2}K_2\left(\frac{\partial\theta}{\partial z} - q\right)^2 \tag{1.48}$$

$$f_{\text{dielectric}} = -\frac{1}{2}\Delta\varepsilon\varepsilon_0 E_x^2 \sin^2\theta \tag{1.49}$$

because θ is a function of only z. If the field amplitude is small, we can assume that the dielectric interaction causes a perturbation to θ such that,

$$\theta(z) = qz + \theta_0 \sin(2qz) \tag{1.50}$$

where θ_0 is the twist distortion perturbation amplitude. This gives,

$$\frac{\partial\theta}{\partial z} = q + 2q\theta_0 \cos(2qz) \tag{1.51}$$

We would like to know an expression for θ_0, which we will find by minimising the total energy with respect to θ_0. In order to do this we must first find a form of $F(\hat{\mathbf{n}})$ that can be integrated over a pitch length to find the total energy. Let us first consider the elastic energy. Substituting $\partial\theta/\partial z$ from equation 1.51 into 1.48 we have,

$$f_{\text{elastic}} = \frac{1}{2}K_2\left(4q^2\theta_0^2\cos^2(2qz)\right) \tag{1.52}$$

and using a double-angle identity, we can write,

$$f_{\text{elastic}} = \frac{1}{2}K_2\left(2q^2\theta_0^2(1 + \cos(4qz))\right) \tag{1.53}$$

Now let us consider the dielectric energy. Substituting θ from 1.50 into 1.49, we have,

$$f_{\text{dielectric}} = -\frac{1}{2}\Delta\varepsilon\varepsilon_0 E^2 \sin^2\left(qz + \theta_0 \sin(2qz)\right) \tag{1.54}$$

Again using a double-angle identity, we can write,

$$f_{\text{dielectric}} = -\frac{1}{4}\Delta\varepsilon\varepsilon_0 E^2 \left(1 - \cos\left(2qz + 2\theta_0 \sin(2qz)\right)\right) \tag{1.55}$$

Now using the following identity,

$$\cos(A + B) = \cos(A)\cos(B) - \sin(A)\sin(B) \tag{1.56}$$

we can write,

$$f_{\text{dielectric}} = -\frac{1}{4}\Delta\varepsilon\varepsilon_0 E^2 \left(1 - \cos(2qz)\cos\left(2\theta_0 \sin(2qz)\right) + \sin(2qz)\sin\left(2\theta_0 \sin(2qz)\right)\right) \tag{1.57}$$

If we take the approximation that θ_0 is small, we can then write,

$$f_{\text{dielectric}} = -\frac{1}{4}\Delta\varepsilon\varepsilon_0 E^2 \left(1 - \cos(2qz) + 2\theta_0 \sin^2(2qz)\right) \tag{1.58}$$

and using a double-angle identity a final time we have,

$$f_{\text{dielectric}} = -\frac{1}{4}\Delta\varepsilon\varepsilon_0 E^2 \left(1 + \theta_0 - \cos(2qz) - \cos(4qz)\right) \tag{1.59}$$

Now in order to calculate the total energy, we must integrate the energy density over a half pitch repeating unit of the structure, $P/2 = \pi/q$. Any $\cos$ and $\sin$ terms integrate to zero, and we have,

$$\begin{aligned} \int_0^{\pi/q} F(\hat{\mathbf{n}})dz &= \int_0^{\pi/q} f_{\text{elastic}} + f_{\text{dielectric}} dz \\ &= \frac{\pi}{q}\left(K_2 q^2 \theta_0^2 - \frac{1}{4}\Delta\varepsilon\varepsilon_0 E^2(1 + \theta_0)\right) \end{aligned} \tag{1.60}$$

Now, minimising with respect to θ_0 we have,

$$\frac{\partial}{\partial\theta_0}\int_0^{\pi/q} F(\hat{\mathbf{n}})dz = 2K_2 q^2\theta_0 - \frac{1}{4}\Delta\varepsilon\varepsilon_0 E^2 = 0 \tag{1.61}$$

which can be rearranged for θ_0 to get,

$$\theta_0(E) = \frac{\Delta\varepsilon\varepsilon_0}{8K_2 q^2}E^2 \tag{1.62}$$

The twist distortion perturbation amplitude for a common liquid crystal E7 with a pitch of 250 nm and with a field of 1 V μm^{-1} is calculated using this expression to be 0.2 degrees.

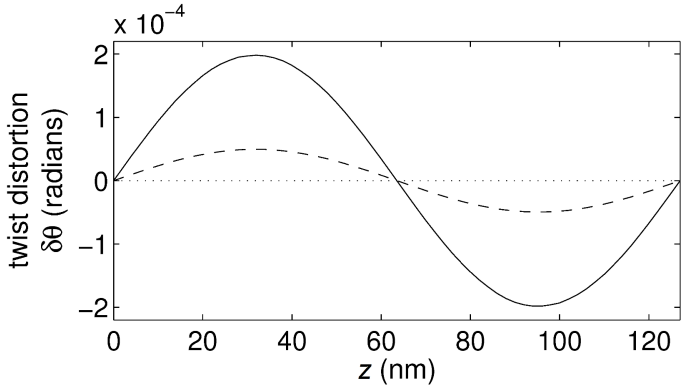

Figure 1.11: Simulated twist distortion about the helicoidal axis ($\delta\theta = \theta(z) - qz$ from equation 1.63) for a 180° segment of pitch 250 nm, with the application of 0 Vμm^{-1} (dotted), 0.1 Vμm^{-1} (dashed) and 0.2 Vμm^{-1} (solid line).

Finally, θ_0 is substituted back into equation 1.50 to obtain an expression for the equilibrium twist component of the director,

$$\theta(z) \approx qz + \frac{\Delta\varepsilon\varepsilon_0}{8K_2q^2}E^2 \sin(2qz) \tag{1.63}$$

The twist distortion of the director due to the dielectric interaction in a 180° single repeating unit with a field perpendicular to the helix axis is shown in figure 1.11 for common cholesteric liquid crystal parameters.

As was described in §1.6.3, a Grandjean structure whose pitch is short relative to the wavelength of light acts as an optically anisotropic homogeneous layer whose optic axis coincides with the helicoidal axis. The twist distortion due to the dielectric interaction induces optical biaxiality, i.e. breaks the uniaxial optical symmetry of the cholesteric such that the material has three refractive indices corresponding to three orthogonal directions. The effective biaxial refractive index components of a short pitch cholesteric can be determined by considering the average of the perpendicular and parallel components of the permittivity, and the corresponding local ordinary and extraordinary refractive indices, n_o and n_e, over one pitch length. Hence, we have effective biaxial refractive index components,

$$\begin{bmatrix} n_1 \\ n_2 \\ n_3 \end{bmatrix} = \begin{bmatrix} \sqrt{\langle n_\mathrm{e}^2 \cos^2\theta + n_\mathrm{o}^2 \sin^2\theta \rangle} \\ \sqrt{\langle n_\mathrm{e}^2 \sin^2\theta + n_\mathrm{o}^2 \cos^2\theta \rangle} \\ n_\mathrm{o} \end{bmatrix} \tag{1.64}$$

where n_1, n_2 and n_3 are the refractive indices corresponding to x-, y- and z-axes respectively. As we saw in the derivation from equation 1.54 to 1.59, the average of $\sin^2\theta$, and following a similar process $\cos^2\theta$, where θ is given by equation 1.50, can be shown to be,

$$\langle \sin^2\theta \rangle \approx \frac{1}{2}(1+\theta_0)$$
$$\langle \cos^2\theta \rangle \approx \frac{1}{2}(1-\theta_0) \tag{1.65}$$

Substituting these into 1.64 and rearranging, we can write,

$$\begin{bmatrix} n_1 \\ n_2 \\ n_3 \end{bmatrix} = \begin{bmatrix} \sqrt{\frac{n_e^2+n_o^2}{2}}\sqrt{1-\theta_0\left(\frac{n_e^2-n_o^2}{n_e^2+n_o^2}\right)} \\ \sqrt{\frac{n_e^2+n_o^2}{2}}\sqrt{1+\theta_0\left(\frac{n_e^2-n_o^2}{n_e^2+n_o^2}\right)} \\ n_o \end{bmatrix} \tag{1.66}$$

where θ_0 is as in equation 1.62.

The resultant biaxial refractive index components can be used with numerical Jones or Berreman optics to determine transmission characteristics. We will see in chapter 2 how this can be used to measure $\Delta\varepsilon/K_2$. Note that θ_0 is dependent upon E^2 and induced optical biaxiality is therefore a Kerr-type effect. Interestingly, this effect in cholesteric liquid crystals has been proposed as a display technology [37, 38]. The Kerr effect is defined as E^2-dependent field-induced birefringence, and Kerr effects are also important in blue-phase liquid crystals, which will be discussed in chapter 6.

1.7.2 Dielectric Helix Reorientation

In the above derivation of the twist distortion, we considered the case where the field is applied perpendicular to the helix. However, there are a number of other dielectric effects that we should consider and that have been exploited in display technology, including the dielectric effect on the helicoidal axis orientation.

For a material with $\Delta\varepsilon > 0$, the dielectric energy is minimised when the director is parallel to an applied field, and $\hat{\mathbf{n}} \cdot \mathbf{E} = 1$, as we saw in §1.3.1. In the case of an undistorted cholesteric material, the director can never be uniformly parallel to the field. However, the dielectric energy is minimum where as much of the director is parallel to the field

as possible, which occurs then the helicoidal axis is perpendicular to the field. We can determine the difference in energy between cases where the helicoidal axis is parallel and perpendicular to the field by considering the dielectric energy from §1.3.1, which is given by,

$$f_{\text{dielectric}} = -\frac{1}{2}\Delta\varepsilon\varepsilon_0(\hat{\mathbf{n}}\cdot\mathbf{E})^2 \tag{1.67}$$

Let us allow $\mathbf{E} = E_x\hat{\mathbf{x}}$. For the case that the helicoidal axis is parallel to the field, $n_x = 0$ and therefore $f_{\text{dielectric}} = 0$. On the other hand, if the field is perpendicular to the helicoidal axis, such that, for example, $n_x = \cos(qz)$, then the dielectric energy becomes,

$$f_{\text{dielectric}} = -\frac{1}{2}\Delta\varepsilon\varepsilon_0\cos^2(qz)E_x^2 \tag{1.68}$$

Averaging over a half pitch repeating unit of the helicoid, we can take $\langle\cos^2(qz)\rangle = 1/2$, and so the energy becomes simply,

$$f_{\text{dielectric}} = -\frac{1}{4}\Delta\varepsilon\varepsilon_0 E_x^2 \tag{1.69}$$

Hence, we have quantified the difference in energy between the two cases. If the liquid crystal is not otherwise confined, then a reorienting torque due to the dielectric effect will align the helicoidal axis perpendicular to the field in the case of a positive dielectric anisotropy. We will see in chapter 4 that this effect has been used to align cholesteric liquid crystals.

In the case of a negative dielectric anisotropy, $\Delta\varepsilon < 0$, then the difference in energy between the two alignment cases is reversed, such that the helicoidal axis will align parallel to the field. This has also been used to align liquid crystals, as we will discuss in chapter 4 on alignment of the Uniform Lying Helix, and also in chapter 5 where the dielectric effect is exploited with a negative dielectric anisotropy to align a Grandjean geometry to create a reflective display.

In this section, we have described how the dielectric interaction can cause a reorienting torque in cholesteric materials by considering a case in which the pitch is fixed. However, in the next section the dielectric interaction's influence on the pitch is considered.

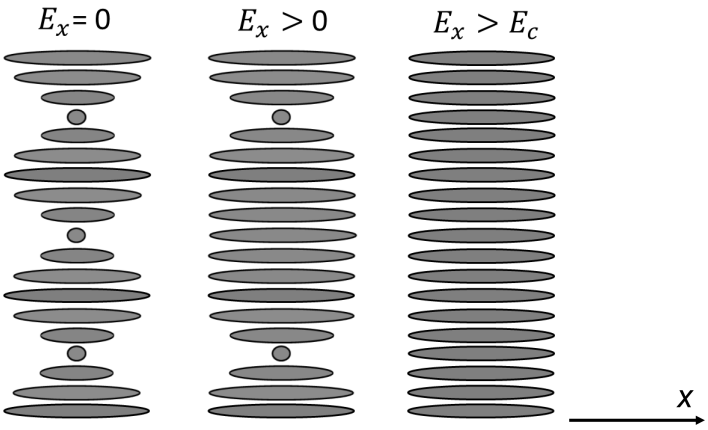

Figure 1.12: Illustration of helix unwinding for a positive dielectric anisotropy cholesteric material having a field applied perpendicular to the helix. The pitch of the material increases with increasing field, before becoming completely unwound for fields above a critical field E_c.

1.7.3 Dielectric Helix Unwinding

We have so far considered a fixed-pitch cholesteric having non-zero dielectric anisotropy in the presence of an electric field. However, if one allows the pitch to vary in order to minimise the free energy, then the pitch increases to allow a greater degree of director alignment parallel to the field. At a critical field, the helix completely unwinds to become uniformly parallel to the field, as illustrated in figure 1.12. This critical field can be calculated by considering the free energy equation in a similar fashion to the approach used in §1.7.1, and was independently derived by Meyer and de Gennes [39, 40] to be,

$$E_c = \frac{\pi^2}{P_0}\sqrt{\frac{K_2}{\Delta\varepsilon\varepsilon_0}} \tag{1.70}$$

where P_0 here is the natural helicoidal pitch.

Helix unwinding is used in several reflective cholesteric display technologies [30, 28], which are further discussed in chapter 5. Essentially, the dielectric effect is used to orient a cholesteric with positive dielectric anisotropy with the helicoidal axis perpendicular to the cell to achieve a first display state. A second state can then be accessed via the application of a large field, which completely unwinds the helix. On removal of the field from the unwound state, depending on the surface alignment used, the liquid crystal then relaxes to

the Grandjean state, thereby allowing the switching between two different states [41, 42, 43, 44, 45, 46].

1.8 Flexoelectricity in Chiral Systems

In §1.3.4 we saw that molecular shape anisotropy results in a coupling between director curvature distortions and electric polarization; a phenomenon called flexoelectricity. In this section, we will see how flexoelectric polarization in chiral systems couples to electric field components perpendicular to the helicoidal axis to produce a rotation of the director about the field direction. We will then look at some potential technologies that exploit the effect.

1.8.1 The Chiral Flexoelectric Effect

From §1.3.4, recall that flexoelectric polarization is given by,

$$\mathbf{P}_{\text{flexo}} = e_1\hat{\mathbf{n}}(\nabla \cdot \hat{\mathbf{n}}) + e_3(\nabla \times \hat{\mathbf{n}}) \times \hat{\mathbf{n}} \tag{1.71}$$

which gives the relationship between bend and splay distortions and electric polarization. In the case of a uniform field, and provided that $e_1 \neq e_3$, the flexoelectric polarization can be maximised by forming a periodic splay-bend combined distortion, as illustrated in figure 1.13.

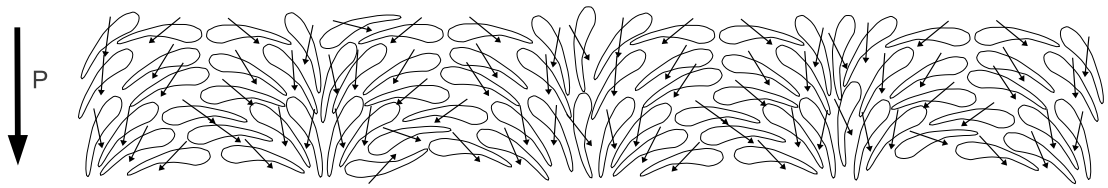

Figure 1.13: Tear shaped molecules have the greatest flexoelectric polarization when in this periodic spay-bend distortion.

In a chiral nematic at equilibrium with no applied fields or polarization, there is a natural twist distortion that results in a periodic helicoidal director structure, as illustrated in the left of figure 1.14. The planes perpendicular to the helicoidal axis contain a uniform director

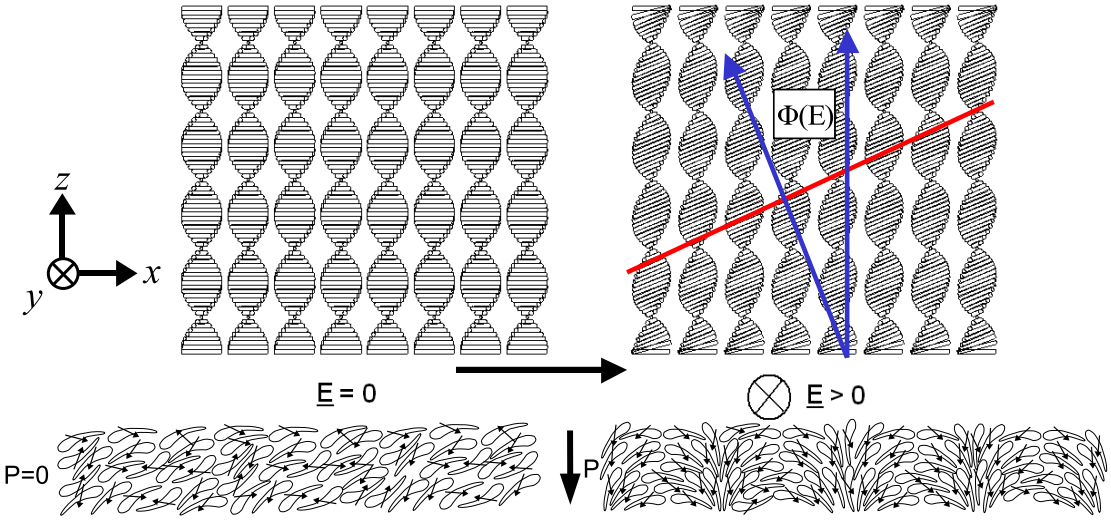

Figure 1.14: A Bouligand plane in the tilted helix structure shows the splay-bend distortion that couples to a field via the flexoelectric effect. At zero field, there is no splay or bend distortion.

orientation. However, if the director is tilted about an axis perpendicular to the helicoidal axis, then planes containing the director exhibit the periodic splay-bend structure that we encountered in figure 1.13, and therefore contain flexoelectric polarization. The period of the splay-bend is given by

$$P_{\text{splay-bend}} = \frac{P}{\sin\phi} \tag{1.72}$$

where P is the cholesteric pitch and ϕ is the director tilt angle as defined in the right of figure 1.14. Note that for $\phi = \pi/2$, $P_{\text{splay-bend}} = P$ and the structure is pure splay-bend with no twist at all. The periodic splay-bend that arises within the plane that is at an angle ϕ to the helicoidal axis was first noted by Bouligand, and is therefore known as a Bouligand plane [47].

Now, while tilting the director results in some flexoelectric polarization and therefore sets up an internal electric field, by the converse process, such a tilt can be induced by the application of a field perpendicular to the helicoidal axis. The resultant tilt angle ϕ is a balance between the elastic and flexoelectric free energy. A full analytical treatment of this effect was first developed by Patel and Meyer [48, 49, 50] and further developed by

Rudquist [51] to include the dynamics.

1.8.2 Flexoelectric Tilt Angle

Here we follow the derivation by Rudquist of the tilt in the director of a cholesteric liquid crystal due to flexoelectricity [51, 52]. The method describes the director in terms of a spherical coordinate system, uses this director in the free energy expression for liquid crystal elastic and flexoelectric energy from equation 1.17, averages this energy over a repeating unit of the cholesteric structure to determine the relative total energy, and then minimises this total energy with respect to the flexoelectric tilt angle ϕ. The dynamics are then also considered.

Consider the axis and director field in figure 1.14. The director for the undistorted helix $\hat{\mathbf{n}}$ is described by,

$$\hat{\mathbf{n}} = \begin{bmatrix} n_x \\ n_y \\ n_z \end{bmatrix} = \begin{bmatrix} \cos qz \\ \sin qz \\ 0 \end{bmatrix} \tag{1.73}$$

In the case where there is no flexoelectric tilt. If we allow for a tilt ϕ about the y-axis and assume a fixed pitch, this is modified to,

$$\hat{\mathbf{n}} = \begin{bmatrix} n_x \\ n_y \\ n_z \end{bmatrix} = \begin{bmatrix} \cos qz \cos\phi \\ \sin qz \\ -\cos qz \sin\phi \end{bmatrix} \tag{1.74}$$

By using these components of $\hat{\mathbf{n}}$ in the free energy expression given in equation 1.17, and omitting the dielectric energy term, we get,

$$F = \frac{1}{2}K_1 q^2 \sin^2 qz \sin^2\phi + \frac{1}{2}K_2 q^2 (1-\cos\phi)^2 + \frac{1}{2}K_3(q^2 \cos^2 qz \sin^2\phi)$$
$$-E(e_1 q \sin^2 qz \sin\phi - e_3 \cos^2 qz \sin\phi) \tag{1.75}$$

where $E = E_y$. Since we want to know the tilt angle ϕ when the total free energy of the whole system is minimum, we average over a whole number of pitches using the fact that,

$$\langle \sin^2 qz \rangle = \langle \cos^2 qz \rangle = \frac{1}{2} \tag{1.76}$$

and so the average energy volume density is,

$$\langle F \rangle = \frac{1}{4}(K_1 + K_3) q^2 \sin^2\phi + \frac{1}{2}K_2 q^2 (1-\cos\phi)^2 - \frac{1}{2}(e_1 - e_3) E q \sin\phi \tag{1.77}$$

In order to determine the value of ϕ that minimises the total energy (assuming a fixed q), we take the differential and minimise by setting equal to zero,

$$\frac{\partial\langle F\rangle}{\partial\phi} = \frac{1}{2}(K_1 - 2K_2 + K_3)q^2 \sin\phi\cos\phi + K_2 q^2 \sin\phi - \frac{1}{2}(e_1 - e_3)Eq\cos\phi = 0 \quad (1.78)$$

which can be rearranged for $\tan\phi$,

$$\tan\phi = \frac{e_1 - e_3}{2K_2 q}E - \frac{K_1 - 2K_2 + K_3}{2K_2}\sin\phi \quad (1.79)$$

Finally, for small angles, we can approximate and simplify the expression for the tilt angle,

$$\phi(E) = \frac{e_1 - e_3}{K_1 + K_3}\frac{E}{q} \quad (1.80)$$

and this is sometimes expressed as,

$$\phi = \frac{e}{Kq}E \quad (1.81)$$

where $e = \frac{1}{2}(e_1 - e_3)$ and $K = \frac{1}{2}(K_1 + K_3)$. $\frac{e}{K}$ is called the flexoelastic ratio, and is considered a figure of merit in the production of materials designed to have optimal chiral flexoelectric switching properties.

We can see that the flexoelectric tilt angle is proportional to both the field E and the difference in flexoelectric coefficients, $e_1 - e_3$. This is in contrast to the amplitude of the twist distortion due to the dielectric effect that we derived in §1.7.1 which is proportional to E^2. In the next section, the dynamics of the chiral flexoelectric effect are considered.

1.8.3 Characteristic Time

Liquid crystal's are viscous fluids, and therefore a transition from an undistorted state to a distorted state with the application of a field takes a characteristic time. The liquid crystal is an over-damped linear system, and we might imagine that the characteristic time is dependent upon the damping (viscosity), the elastic constant, and the characteristic length scale of the distortion. In liquid crystal devices, all of these are important design parameters. In particular, the characteristic length scale of the flexoelectric distortion in chiral nematics depends on the pitch, which means that devices that exploit chiral flexoelectricity can have

much faster response times than devices exploiting non-chiral systems, whose characteristic length scale is usually the device thickness. Here, we follow the derivation by Rudquist for the dynamics of the chiral flexoelectric effect.

The dynamics of the flexoelectric effect in cholesteric liquid crystals can be formulated by considering that in an over-damped linear system, the rate of change of a variable, for example the flexoelectric tilt angle ϕ, is proportional to the rate of change of energy f with respect to that variable, i.e.,

$$\frac{\partial \phi}{\partial t} = -\frac{1}{\gamma}\frac{\partial f}{\partial \phi} \tag{1.82}$$

where γ is a damping coefficient that corresponds to the liquid crystal viscosity. Taking the previous expression for $\partial f/\partial \phi$ of our system from equation 1.78, we find that the above expression becomes,

$$-\gamma\frac{\partial \phi}{\partial t} = \frac{1}{2}(K_1 + K_3)q^2\phi - \frac{1}{2}(e_1 - e_3)qE \tag{1.83}$$

This equation has the step-response solution,

$$\phi(t) = \phi_0(1 - e^{-\frac{t}{\tau}}) \tag{1.84}$$

where $\phi(t)$ is the tilt angle as a function of time, ϕ_0 is the equilibrium value of the flexoelectric tilt angle given by,

$$\phi_0(E) = \frac{e_1 - e_3}{K_1 + K_3}\frac{E}{q} \tag{1.85}$$

and τ is the characteristic time given by,

$$\tau = \frac{2\gamma}{(K_1 + K_3)q^2} \tag{1.86}$$

where γ is a viscosity. The characteristic time τ corresponds to the time taken for the tilt angle to reach within $1/e$ of the equilibrium value, and is proportional to P^2. Hence, the response time is heavily dependent on the pitch. A typical material used in the work presented in this thesis, E7 doped with 3.5% of a high twisting power chiral dopant R5011, has a pitch of 250 nm, $K_1 + K_3 = 27$ pN, and a characteristic time of $\tau \sim 60$ µs, which gives a viscosity $\gamma \sim 0.3$ Pa.s. In comparison, a device that switches a non-chiral material in a typical cell

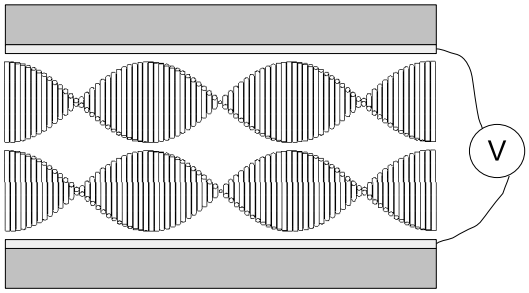

Figure 1.15: Illustration of a Uniform Lying Helix (ULH) cell. The cell is treated to encourage a short-pitch cholesteric to align with the helicoidal axis in the plane of the cell. Transparent conducting electrodes are coated on the glass to allow the application of an electric field perpendicular to the helicoidal axis to produce a flexoelectrically driven rotation of the optical axis.

of thickness equal to 4 µm, would have a characteristic switching time of ~ 5 ms; over one hundred times slower. For this reason, electrooptic technologies that exploit fast-switching cholesteric liquid crystals have been hotly researched and developed. In the next section, we consider such an electrooptic device.

1.8.4 The Chiral Flexoelectro-optic Effect

Uniform Lying Helix

In §1.8.1, we discussed how a field applied perpendicular to the helicoidal axis of a cholesteric material will rotate the director about the field direction due the coupling of the field with flexoelectric polarization. For a material in which $nP \ll \lambda$, this manifests as a rotation of the optic axis of the material.

Figure 1.15 shows a Uniform Lying Helix (ULH) arrangement [20], in which the helicoidal axis of a short-pitch cholesteric is aligned uniform and perpendicular to glass cell substrates. Transparent conducting electrodes on the top and bottom substrate surfaces are used to apply a voltage across the liquid crystal. The resultant structure acts as a wave plate whose optic axis orientation can be controlled electrically via the flexoelectric effect. When placed between crossed polarizers, the transmission is given by

$$T = \frac{1}{2}\sin^2(2\chi \pm 2\phi)\sin^2\left(\frac{\pi\Delta n_{\text{effective}}d}{\lambda}\right) \tag{1.87}$$

where, as before, the flexoelectric tilt angle is given by,

$$\phi = \frac{e_1 - e_3}{K_1 + K_3}\frac{E}{q} \tag{1.88}$$

The transmission behaviour is illustrated in figure 1.16. For a given $\frac{\Delta n_{\text{effective}} d}{\lambda}$, the max-

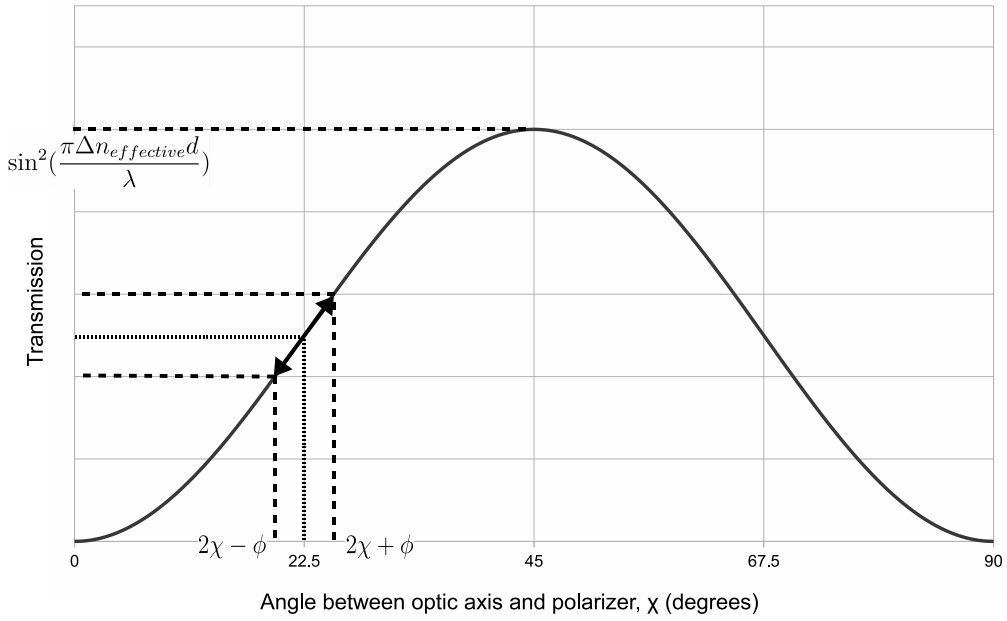

Figure 1.16: The transmission of a ULH device between crossed polarizers. The ULH cell acts as a wave plate whose optic axis makes an angle $\chi + \phi$. The maximum transmitted intensity occurs at $\chi + \phi = 45°$ and is equal to $\frac{1}{2}\sin^2(\frac{\pi \Delta n_{\text{effective}} d}{\lambda})$ as per equation 1.87

imum transmitted intensity occurs where the optic axis is at 45° to the polarizer, with the greatest light modulation due to the flexoelectric tilt at $\chi = 22.5°$. For small flexoelectric tilt angles, the transmission is modulated proportional to the applied voltage. By measuring the tilt-angle as a function of voltage, one can therefore calculate particular flexoelectric properties of the liquid crystal, as will be discussed in chapter 2.

The linear electrooptic effect produced by the ULH has several desirable properties from a display engineering perspective [53, 54, 55, 56, 57, 42]. The effect is very fast, because $\tau \propto P^2$ (from equation 1.86). Short pitches can therefore offer characteristic switching times of the order of tens of microseconds. The chiral flexoelectrooptic effect in

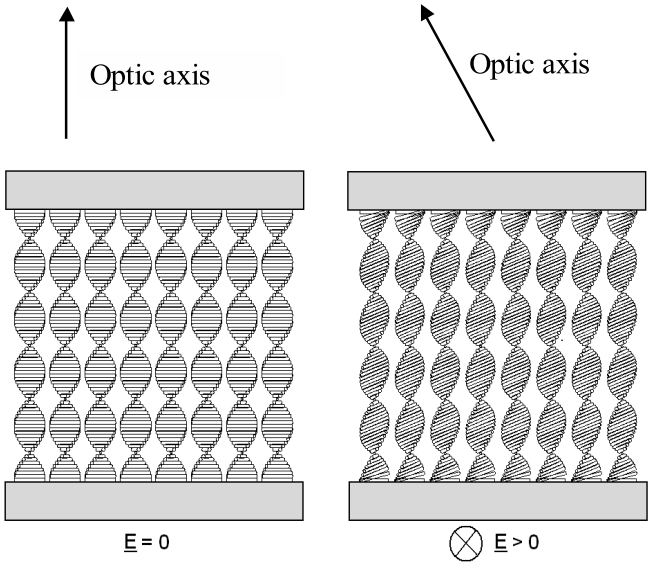

Figure 1.17: Illustration of the Grandjean alignment and flexoelectric tilt. If the pitch is much shorter than the wavelength, then the macroscopic optic axis tilts with the flexoelectric tilt angle, thereby producing an effective birefringence.

the ULH geometry is also effected by a voltage applied across the cell, unlike some in-plane switching geometries that rely on patterned electrodes that are more expensive to produce. The primary problem with the ULH as a technology at present is that the ULH is difficult to align uniformly, and as will be discussed in chapter 4, imperfections in the alignment of the ULH cause a problem for the device contrast. One solution has been to avoid the ULH altogether by exploiting instead a Grandjean geometry, also known as the Uniform Standing Helix [58, 19].

Uniform Standing Helix

The Uniform Standing Helix (USH) arrangement, also known as Grandjean alignment [18], was introduced in §1.5.1, and is related to the ULH, however the helicoidal axis is oriented normal to the plane of the cell, rather than in the plane of the cell. The arrangement forms spontaneously in cells with planar surface alignment layers. If electrodes are arranged on the surface of one substrate such that they can create a field in the plane of the device, then the applied field will again be perpendicular to the helicoidal axis and flexoelectric tilt will be induced (see figure 1.17). If this device is placed between crossed polarizers under the

condition that the pitch is much shorter than optical wavelengths, then in the field off state it will appear black if viewed at normal incidence. With an applied field, the optic axis, which is initially parallel to the helix axis, will tilt and therefore provide an effective birefringence across the layer and the transmission will again follow equation 1.87. The USH therefore has the potential to be exploited for electrooptic technology [19].

1.9 Types of Liquid Crystal Display

We have already looked at two examples of liquid crystal display devices. Firstly, in §1.6.1 the Twisted Nematic was described, which is still used in many display applications including computer monitors and small information displays on, for example, calculators and microwave ovens. Secondly, the Uniform Lying Helix was introduced in §1.8.4, which although not yet commercially exploited, could improve on many aspects of existing technology. This latter technology will be studied in further detail in subsequent chapters, especially in chapter 4, which is concerned with the unresolved issue of ULH alignment. In chapter 5, we will also look at Bragg-reflecting cholesteric technologies that are in commercial production and describe a method based on flexoelectricity that provides a new way to switch between stable states in such devices. Finally, in chapter 6 blue phase liquid crystal display technology will also briefly be touched upon.

There are many different liquid crystal display technologies on the market and in development, however this section will describe briefly the two most ubiquitous transmissive display technologies available today, and some notes on electronic driving schemes and optical compensation films.

1.9.1 Vertically Aligned Nematic

The Vertically Aligned Nematic (VAN) technology incorporates a homeotropic alignment configuration with a material in which $\Delta\varepsilon < 0$. The cell has no effective birefringence when there is no field applied, owing to the homeotropic alignment, and between crossed polarizers exhibits zero transmission at normal incidence. The top and bottom substrates

are treated so as to allow a voltage to be applied across the liquid crystal layer. As the field increases, the liquid crystal director reorients perpendicular to the field, in order to minimise the dielectric energy given by

$$f_{\text{dielectric}} = -\frac{1}{2}\Delta\varepsilon\varepsilon_0(\hat{\mathbf{n}} \cdot \mathrm{E}) \tag{1.89}$$

In so doing, the effective birefringence across the liquid crystal device increases, and results in a transmission between crossed polarizers (assuming the tilt is at 45 degrees to the polarizer), according to

$$T = \frac{1}{2}\sin^2\delta \tag{1.90}$$

where δ is the phase retardation of the layer. If the layer and material birefringence are chosen correctly, then a phase retardation of $\pi/2$ can be produced, thereby maximising the possible transmission contrast between off and on states.

Devices made using the VAN architecture have minimum switching times of the order of milliseconds. The switching time is controlled by the device thickness, viscosity and elastic parameters of the liquid crystal.

1.9.2 In-Plane Switching

In-plane switching (IPS) technology uses a different approach. A cell is constructed with a liquid crystal with $\Delta\varepsilon > 0$, and with the director homogeneously aligned in the plane of the cell. Electrodes on a single substrate surface, separated by a small distance, are used to apply a field also in the plane of the device, typically at 45 degrees to the equilibrium director orientation at zero field. The field produces a torque on the liquid crystal via the dielectric interaction described in §1.3.1, that reorients the director parallel to the field. The cell is positioned between crossed polarizers, such that the zero-field equilibrium director orientation is parallel to one of the polarizers. The transmission for such a device (assuming that it produces a phase retardation of $\pi/2$ for optimum contrast), is given by

$$T = \frac{1}{2}\sin^2(2\chi) \tag{1.91}$$

where χ is the angle that the optic axis makes with the polarizer. Hence, in the equilibrium state with zero field, the transmission is zero. As a field is introduced, the director is rotated and χ increases thereby increasing the transmission.

A device made using the IPS architecture has a similar response time to the VAN, and is again controlled by the device thickness, liquid crystal viscosity and elastic constants. Devices are often constructed with a patterned alignment structure that alternates the in-plane orientation of the director alignment, in order to improve the off-axis viewing properties of the display.

1.9.3 Thin Film Transistors

Addressing schemes are methods to address and control individual pixels in a liquid crystal display with a voltage in order to facilitate switching. There are many different methods of addressing, which will not be described here. However, it should be understood that the present methods for addressing liquid crystal displays require Thin-Film-Transistors (TFTs) which can hold charge in order to provide a field across a liquid crystal pixel until the pixel is again addressed by a voltage pulse. The use of TFTs has been critical in allowing large arrays of pixels and the size and resolutions of modern displays, however they do put constraints on various aspects of liquid crystal display engineering. The most important is that TFTs cannot sustain high voltages, and so for any new operational liquid crystal mode, full intensity modulation must be achievable at modest addressing voltages, typically less than about 10 V.

1.10 Numerical Methods

The modelling of liquid crystals is a vibrant area of current research, and they are modelled at a variety of levels. In order to predict macroscopic properties of new liquid crystal molecules and mixtures, molecular models are under development [59]. However, for modelling at the level of device behaviour where the macroscopic properties are known, continuum models must be used. These deal with macroscopic quantities such as the director $\hat{\mathbf{n}}$

and flexoelectric, dielectric and elastic constants.

Ericksen-Leslie-Parodi theory [60, 61, 62] is a liquid crystal continuum model which has been successful in modelling device behaviour [63]. This is then used in conjunction with Jones-Matrix [64] or Berreman [15] optics, which were introduced in §1.4.2, in order to simulate measurable quantities such as the transmission through the device. Detailed descriptions of these methods can be found elsewhere [65, 66] but it is appropriate to give a brief qualitative explanation here.

The approach is to first define a coordinate system of the liquid crystal cell. In most literature, the cell plane is defined to be the x, y-plane and z to be the axis normal to the cell surface, although other coordinate systems can be employed depending on the application. An initial director field is then described based on known device properties. This director field is discretised by representing it as a matrix of finite resolution with each element containing director components of the director field. An electric field is also defined. The free energy described by

$$\begin{aligned} F(\hat{\mathbf{n}}) =& \frac{1}{2}K_1[\nabla \cdot \hat{\mathbf{n}}]^2 + \frac{1}{2}K_2[\hat{\mathbf{n}} \cdot (\nabla \times \hat{\mathbf{n}}) + q]^2 + \frac{1}{2}K_3[\hat{\mathbf{n}} \times (\nabla \times \hat{\mathbf{n}})]^2 \\ & - \frac{1}{2}\varepsilon_0 \Delta\varepsilon(\hat{\mathbf{n}} \cdot \mathbf{E})^2 - \left[e_1 \hat{\mathbf{n}}(\nabla \cdot \hat{\mathbf{n}}) + e_3(\nabla \times \hat{\mathbf{n}}) \times \hat{\mathbf{n}}\right] \cdot \mathbf{E} \end{aligned} \tag{1.92}$$

(see the end of §1.3.4) which considers bulk elastic, dielectric and flexoelectric energy, is then used in conjunction with appropriate surface energy expressions in a Euler-Lagrange energy minimisation routine. The routine is based on the Euler-Lagrange equation given by, (in one dimension)

$$\frac{\partial f}{\partial \theta} - \frac{\partial}{\partial x}\left(\frac{\partial f}{\partial\left(\frac{\partial \theta}{\partial x}\right)}\right) = 0 \tag{1.93}$$

which gives a set of functions that correspond to the minimum energy solutions to a general function $\theta(x)$.

Finite difference approximations are used to calculate director field differentials at elements in the director field matrix for use within the equations. A resultant torque on the director field is calculated for each matrix point, and the director is adjusted by an amount proportional to the torque and a 'time step' parameter. At each stage the electric field is cal-

culated based on the current director field, the dielectric and flexoelectric properties and the applied voltage for use in the next iteration. This process is repeated until there is negligible change in the director field with further iteration.

Once a director field has been simulated, either Jones or Berreman optics are employed. The director structure is divided into a finite number of birefringent slices. The corresponding Jones or Berreman matrices for the slices are then used with an input polarization matrix to calculate transmission properties. Jones optics cannot take into account reflections, but is useful for simulations of transmission at normal incidence to the cell. Berreman optics takes account of reflected light components, and can be used to simulate off-axis transmissions, however, the method is more complicated to implement and requires greater computational resources.

This method is useful for director fields that are topologically continuous. However, the behaviour of defects in the liquid crystal director field is not adequately represented. At defect sites, the order parameter changes, and the energies of the distortions at these points are therefore not well approximated by a standard continuum approach, because the continuum theory does not account for changes in the elastic properties under these conditions. However, modelling the behaviour and free energies associated with defects has been attempted through the use of Q-tensor models, which includes the order parameter and its relation to distortions [67, 68].

1.11 Conclusion

In this chapter, the fundamental concepts required to understand the chapters that follow have been described. The nematic phase and its elastic, electric and optical properties have been described using a continuum approach. Chiral liquid crystals, their behaviour in electric fields, and their electrooptic behaviours have also been introduced, and we have discussed some of their applications.

This thesis is concerned with the study and utilisation of these behaviours in helicoidal liquid crystal systems for the purposes of measurement and in engineering novel function-

alities for technological application. As such, each chapter describes a key problem for helicoidal liquid crystal technology and tackles it by developing techniques for exploiting the electrical, elastic and optical properties of helicoidal liquid crystals. In the next chapter, the problem of measurement of flexoelectricity is discussed, both in chiral and non-chiral liquid crystal systems, which is an important capability in the development and optimisation of materials for flexoelectric technology, and for materials research in general.

Chapter 2

Measurement of Flexoelectricity

2.1 Introduction

The current generation of liquid crystal displays almost exclusively utilise Twisted Nematic, Vertically Aligned Nematic (VAN), or In-Plane Switching (IPS) technologies, which were introduced in the last chapter. While having enjoyed widespread success over the last few decades, the next generation of displays will demand functionalities impossible with these technologies. A key limitation is the transmission modulation switching time, which is fundamentally limited by device thickness, liquid crystal viscosity, and elastic constants. Significantly improved switching times would enable a variety of new display functionalities.

Currently, each display pixel is divided into three primary-colour sub-pixels. A colour filter is placed over each sub-pixel, which is illuminated from behind by a white light source. As a consequence, most of the incident light's power is attenuated in the filter. Furthermore, the spacial resolution of the sub-pixels must be three times that of the display. However, an alternative method is to temporally, rather than spatially, modulate the primary colour transmission intensities; a method called field-sequential colour. The white back-light is replaced by one that cycles through red, green and blue (RGB) primary colours, thereby saving the energy that was previously attenuated by colour filters (a critical advantage in mobile devices). Furthermore, since only a single pixel is required to modulate all primary colours, the displayed image resolution is improved. The range of colours (known as the colour gamut) could also be improved by selecting a larger number of back-illuminating

colours, without jeopardising the spatial resolution of the image. Although field-sequential systems improve energy efficiency and resolution, they rely on fast switching to prevent the spatial separation of colours when moving ones eye across the screen [69]. Spatial separation of colours is sometimes apparent in projectors that use field-sequential systems.

The proliferation of 3D display technology could also be boosted using field-sequential technology. Current technologies often require the user to wear special glasses. These systems work in one of two ways. In one system, each display pixel is split further into two sub-pixels, corresponding to left- and right- eyes. The left/right sub-pixels are covered in polarizers that attenuate orthogonal circular polarization states, that match corresponding polarizers in the lenses of glasses covering the correct left or right eye of the user. In this way, only one of the left/right sub-pixels is visible by each eye, thereby enabling a stereoscopic 3D image. Problems with this system are the same as those encountered with the primary colour filter system: there is an attenuation loss in the polarizing filters, and a reduction in the image resolution, as two sub-pixels are required for each display pixel. The second system uses a field sequential approach, in which the left and right images are temporally interlaced. Known as 'active' 3D, glasses worn by the users contain electro-optic liquid crystal light shutters that attenuate the image intended for the opposite eye. Again, due to the limited speed of liquid crystal devices, there is the potential for left/right image cross-talk (which produces what is known as a 'ghosting' artefact) [70], and due to the limited frame rate that is possible with current systems, users often report viewing discomfort [71].

Auto-stereoscopic systems (i.e. without the need for glasses) are an emerging technology. Faster sequential-transmission systems offer a solution to providing unique images for the eyes of one or potentially multiple users in succession. There have also been systems developed to accommodate multiple focal planes, which provide a more realistic illusion of depth [72]. Faster liquid crystal devices allow more information to be projected to the user, enabling functionalities that were impossible before. Apart from displays, there are a variety of other electrooptic applications that require fast modulation times, including wireless

and fibre-optic communications, imaging and photonics. Fast liquid crystal technologies are therefore of critical importance.

The chiral flexoelectro-optic effect, which was introduced in §1.8.4, offers the potential to improve switching times by one or more orders of magnitude. However, there are a number of issues preventing the commercialisation of the technology. The development of bimesogenic liquid crystals and their mixtures, which are optimised for flexoelectric switching, has allowed optic-axis rotation angles of $\pm 22.5^\circ$ (and in some cases $\pm 45^\circ$[73]) [74, 56, 75, 76, 57]. Full transmission modulation is therefore achievable (c.f. equation 1.87), however, bimesogenic mixtures are highly viscous and still require further development. To develop the technology and materials further, tools for studying distortions in cholesteric structures are required. Therefore, the first part of this chapter describes a new technique that is highly sensitive to electro-elastic parameters, including the flexoelastic ratio introduced in chapter 1, and the 'dielectro-elastic' ratio $\Delta\varepsilon\varepsilon_0/K_2$.

While methods to measure flexoelectric, dielectric and elastic parameters in cholesteric systems are of great importance, there has also been interest in methods that utilise non-chiral systems. Chiral dopants can alter the properties of a mixture, potentially including flexoelectric parameters [77]. High twisting power dopants have allowed measurements of flexoelectric parameters using cholesteric systems with only small concentrations of chiral dopant, and suggest that flexoelectric parameters are negligibly dependent on chirality itself [77], at least in nematic materials such as E7, although measurements in non-chiral systems have large associated error. However, interest in measurements of flexoelectricity in non-chiral systems has been sparked by the investigation of bent-core materials, which exhibit unusual flexoelectric and other properties and form spontaneous chiral domains even when the mixtures themselves have no chiral molecules [78, 79, 80, 81, 82]. The literature has not discussed the influence of chiral dopants on the nematic phases of bent-core materials. It has been suggested that the inclusion of chiral dopants into these mixtures may obscure unique behaviour of the enantiomerically symmetric materials, and so methods for measuring flexoelectric parameters that rely on chiral materials may be inappropriate [83]. The

second part of this chapter is therefore concerned with the measurement of flexoelectricity in non-chiral systems. The specifics of chiral and non-chiral systems demand different experimental approaches, and in the rest of §2.1, a couple of preliminary concepts are commented upon.

2.1.1 Flexoelectric Torque

As was introduced in chapter 1, flexoelectricity can be conveniently described in terms of the resultant torque on the director field, $\hat{\mathbf{n}} \times \mathbf{h}_{\text{flexo}}$, where,

$$\mathbf{h}_{\text{flexo}} = (e_1 - e_3)\big(\mathbf{E}(\nabla \cdot \hat{\mathbf{n}}) - (\nabla \otimes \hat{\mathbf{n}})\mathbf{E}\big) - (e_1 + e_3)(\hat{\mathbf{n}} \cdot \nabla)\mathbf{E} \tag{2.1}$$

This groups the flexoelectric coefficients into terms associated with homogeneous and gradient electric fields [11]. Experiments are usually designed to measure either $e_1 - e_3$ or $e_1 + e_3$. In all the geometries considered in the present chapter, and indeed in this thesis, the homogeneous field regime is dealt with, where $e_1 - e_3$ is important.

2.1.2 Field Frequency and Charge Carriers

Methods to measure flexoelectricity are numerous. Some early studies tried to measure the flexoelectric polarization indirectly by measuring the effect on distortions caused by magnetic fields [84], or directly under forced mechanical distortions [85] (which has also been more recently attempted [86]). These methods often produce measurements that are not consistent with one another or with more recent methods (the latter case differing by three orders of magnitude). In the last decade however, the literature has converged almost unanimously on electrooptic techniques in one of two regimes; with either AC or quasi-DC electric fields. Which driving frequency is employed depends upon the characteristic switching time of the cell, given by,

$$\tau = \frac{\gamma l^2}{\pi^2 K} \tag{2.2}$$

where γ is a viscosity, K is an elastic parameter and l is a characteristic length-scale of the distortion. For non-chiral or weakly chiral geometries including the Twisted Nematic (TN)

and Hybrid Aligned Nematic (HAN), this characteristic length-scale is the device thickness (with $\tau \sim$ milliseconds). However, for chiral systems this length-scale is half the pitch of the material, which can be an order of magnitude or more smaller than the cell thickness (with $\tau \sim$ tens of microseconds).

Charge carriers can migrate in DC fields and alter the field environment [87]. Therefore, if a low or quasi-DC driving frequency is used, the effect of charge carriers on the field must be taken into account when measuring flexoelectricity. The consequence for the measurement of flexoelectricity in non-chiral systems will be discussed in the second part of the present chapter. Further, it will be discussed in chapter 5 that charge carriers play a major role at frequencies well below 500 Hz, where their influence becomes apparent in capacitance measurements and must be accounted for.

In the case of highly chiral systems however, which is the subject of the next section, the liquid crystal can be studied using field frequencies where charge carriers have a negligible influence on the internal field strength.

2.2 Chiral Systems: Uniform Lying Helix Method

The most common method to measure $e_1 - e_3$ is to align liquid crystal in the quasi-stable ULH texture and analyse transmission between crossed polarizers [48, 73, 49, 50, 51, 88, 75, 89]. The flexoelectric parameter, $e_1 - e_3$, can be determined by measuring the rotation in the optical axis of the cell as a function of the applied voltage using the formula,

$$T = \frac{1}{2}\sin^2(2\chi \pm 2\phi)\sin^2\left(\frac{\pi\Delta n_{\text{effective}}d}{\lambda}\right) \tag{2.3}$$

where,

$$\phi(E) = \frac{e_1 - e_3}{K_1 + K_3}\frac{V}{qd} \tag{2.4}$$

where V is the applied voltage amplitude, and d is the device thickness (see §1.8.2 for a derivation). To determine the optic axis rotation, which corresponds to the flexoelectric tilt angle ϕ, a ULH device is prepared by capillary filling the material to be studied into a cell containing transparent conducting electrodes on top and bottom substrates. To illustrate,

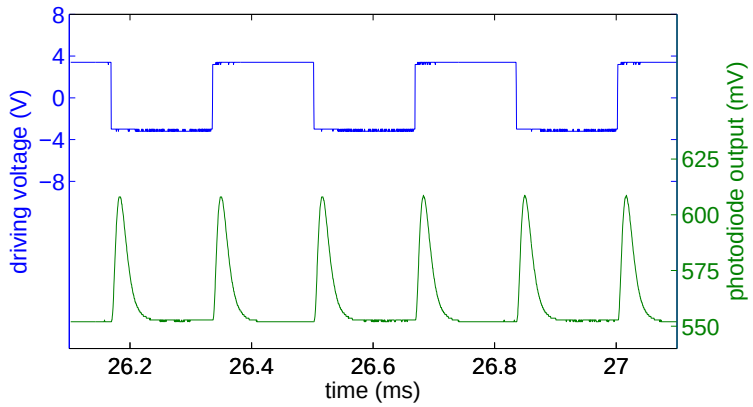

Figure 2.1: A typical photo diode output for a ULH device observed with a polarizing microscope having its optic axis at 45 degrees to the polarizer and being driven by a square-wave voltage. The transmission of the device is independent of the polarity of the field, c.f. figure 1.16.

here an example of a chiral liquid crystal mixture E7 with 3.5 wt% of chiral dopant R5011 is used, which results in a cholesteric with a pitch of 250 nm, in a cell where $d = 5$ µm. A ULH texture forms spontaneous on cooling from the isotropic to the nematic phase under the application of a 70 Hz square-wave voltage of approximately 20 V_{rms}.

A square-wave voltage of a period substantially longer than the characteristic flexoelectric switching time is applied to the cell, and the device observed between crossed polarizers using a polarizing microscope fitted with a photo diode. The cell is first rotated such that the helicoidal axis is at approximately 45 degrees to the polarizer, which corresponds to a maximum transmission amplitude (see figure 1.16). The cell's orientation is then refined such that the photo diode response is symmetric for both positive and negative voltage amplitudes, as shown in figure 2.1. The cell is then rotated by 22.5 degrees, at which point the flexoelectric effect will have an approximately linear electrooptic response, and the transmission will depend on the field polarity, as shown in figure 2.2 (left) (see again figure 1.16). The cell is then rotated, such that the transmission for the negative voltage takes the value that the transmission for the positive voltage was before the rotation, as in figure 2.2 (right). This rotation, corresponding to 2ϕ, is recorded and the measurement is repeated for a series of voltage amplitudes.

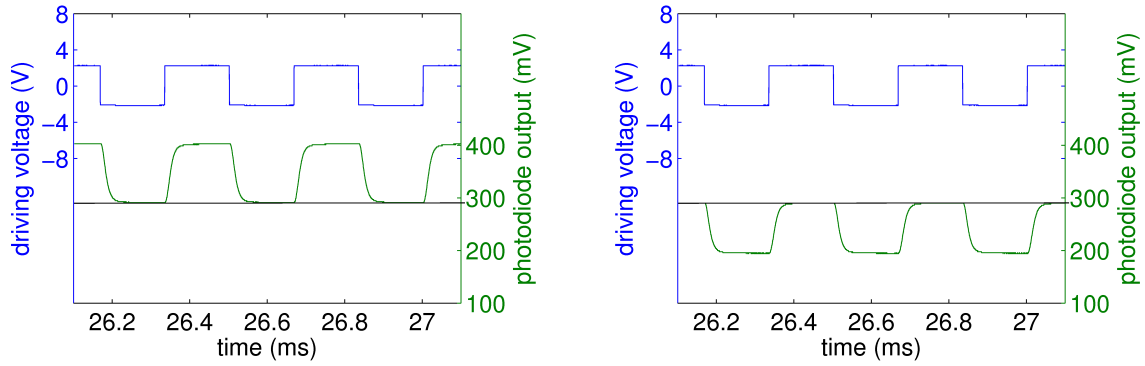

Figure 2.2: (left) A typical photo diode response to a ULH device with its optic axis at 22.5 degrees observed through a polarizing microscope. (right) To measure the the flexoelectric tilt angle ϕ, the cell is rotated such that the transmission amplitude changes by an amount corresponding to the peak-to-peak amplitude of the signal when at 22.5 degrees.

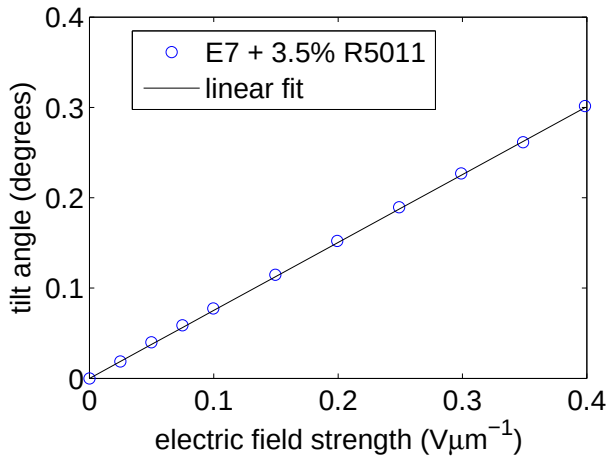

Figure 2.3: Flexoelectric tilt angle as a function of field strength, used to determine the flexoelastic ratio e/K.

The measured tilt angle is plotted and shows a linear increase with the applied voltage in figure 2.3. From the slope of the line, which is equal to $\phi d/V$, the flexoelastic parameter can be determined by rearranging equation 2.4 to give

$$\frac{e_1 - e_3}{K_1 + K_3} = \frac{\phi d}{V} q \tag{2.5}$$

where $q = 2\pi/P$. In this case, the flexoelastic ratio e/K for E7+3.5%R5011 is determined to be 0.45 $\mathrm{Cm^{-1}N^{-1}}$.

Usually this method, as has been done here, relies on Patel and Meyer's analytic small-angle approximation to the flexoelectric tilt in which is inherent the assumption that the flexoelectric effect is large in relation to the dielectric effect, and that the structure is an ideal and unconstrained helicoid (see §1.8.2) [48, 49, 50, 51]. For small fields, this is a good approximation. Castles has shown that the method, when executed with care, can be used to deduce the flexoelectric parameter $e_1 - e_3$ with an uncertainty as small as 2% [89]. However, it is difficult to analyse flexoelectric and dielectric effects independently. Furthermore, the measurement of $e_1 - e_3$ may not be accurate because the topological incompatibility of the structure with homogeneous surface alignment layers distorts the structure from being ideal, and because of the difficulty of forming homogeneous ULH textures. In particular, for materials that have small or negative dielectric anisotropy, forming the ULH using conventional methods is sometimes not possible[1]. For these reasons, the following section describes a new method that instead utilises a Grandjean arrangement, which is inherently stable and uniform in cells with planar alignment. An in-plane field is applied, and a lock-in amplifier and a rotation method are used to extract information about both flexoelectric and dielectric distortions. The method is then extended to enhance the sensitivity by using a quarter-wave plate.

[1] A method for ULH alignment that does not depend on the application of fields is used in §4.4.2 to measure flexoelectric properties of a negative dielectric anisotropy liquid crystal MLC-7029 using a ULH method.

2.3 Chiral Systems: Grandjean Rotation Method

In chapter 1, analytical models of the optics of the flexoelectric effect were described. The flexoelectric effect causes a tilt in the optic axis of a short-pitch cholesteric that is proportional to E (see §1.8.4), and the dielectric distortion causes an in-plane distortion resulting in optical biaxiality that is proportional to E^2 (see §1.7.1). In this study, these analytical models are employed to analyse angle-of-incidence-dependent transmission of Grandjean structures with in-plane electric fields. The stable Grandjean structure has the advantage of being uniform and compatible with homogeneous alignment layers. It is also a structure of particular technological interest in both flexoelectric and dielectric driving regimes [19, 37, 38]. Adoption of a perturbative driving regime, and measurement of both 1^{st} and 2^{nd} harmonic transmission amplitudes relative to a sinusoidal driving field, allows the detailed and simultaneous measurement of distortions arising from both flexoelectric and dielectric interactions, at electric fields as little as 0.01 $\text{V}\mu\text{m}^{-1}$. The method is applied to measure the flexoelectric parameter $(e_1 - e_3)/(K_1 + K_3)$ and the dielectric distortion parameter $\Delta\varepsilon/K_2$ in E7 liquid crystal and a bimesogen mixture MDA-1245 optimised for the chiral-flexoelectrooptic effect. The method is then extended to increase the sensitivity in systems with small birefringence by using a quarter-wave plate (QWP), and used to measure these parameters in a material with an extra-ordinarily small flexoelastic parameter of 0.011 $\text{CN}^{-1}\text{m}^{-1}$.

2.3.1 Device Preparation

E7 liquid crystal is doped with 3.5% by weight of commercially available chiral dopant R5011 from Merck. The resultant mixture has a cholesteric pitch of 250 nm, as measured using a spectrometer (method described in §1.6.2). This mixture is capillary filled in the isotropic phase into an 8 µm spaced, anti-parallel aligned cell that uses 1 mm thick glass, and allowed to form a Grandjean texture. To produce a uniform electric field, a 2 mm gap is etched into an indium-tin-oxide layer on one of the substrate surfaces. The large electrode gap relative to the cell thickness ensures field uniformity in the region onto which the laser

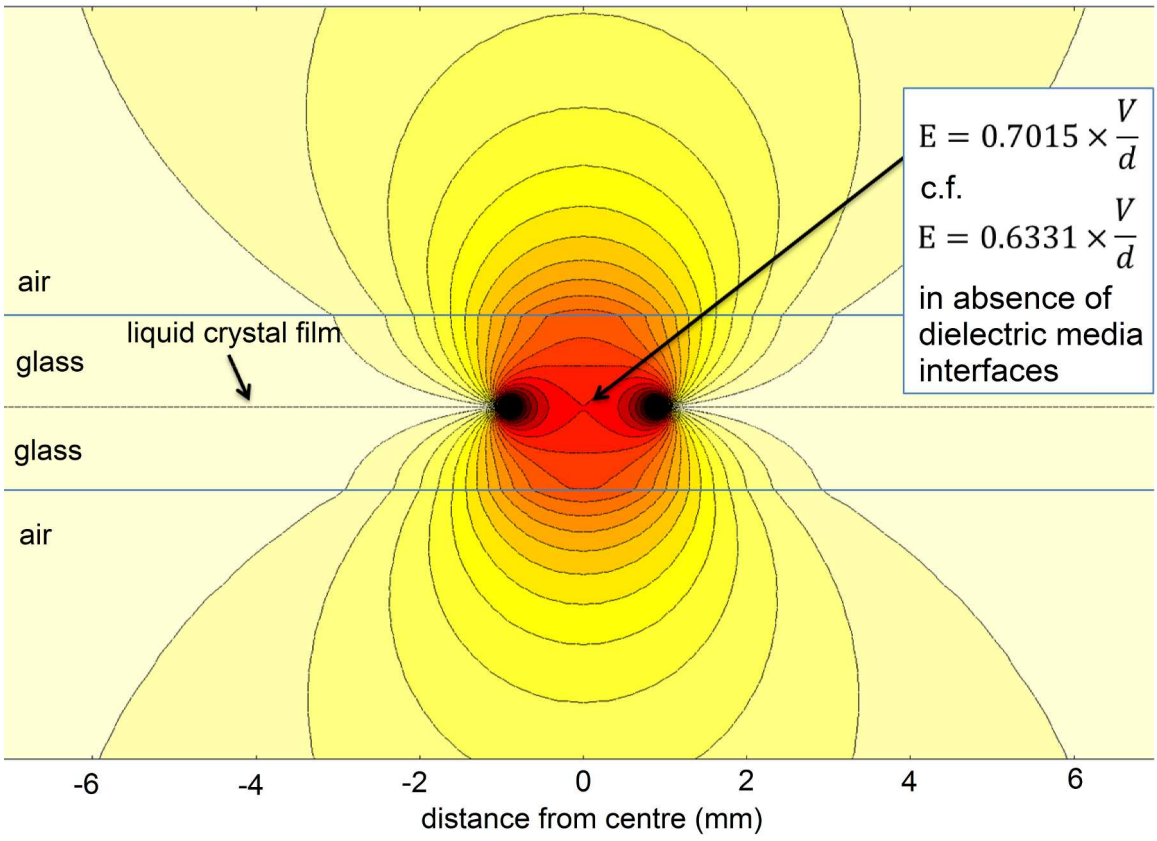

Figure 2.4: A numerical simulation of the electrostatics of an 8 µm thick liquid crystal device. The simulation shows a cross-section through the device, which has a potential difference between electrodes separated by 2 mm on the bottom substrate surface.

is incident, and the cell's surface alignment is parallel to the applied field direction.

2.3.2 Modelling the Electric Field

At frequencies of 1 kHz or greater, the effect of charge carriers can be neglected, and the electric-field strength is determined by the device geometry and dielectric properties. The electric field between parallel-plate electrodes separated by a distance d is V/d, where V is the potential difference between electrodes. It can be shown that for the field between two thin in-plane electrodes this modifies to,

$$E_z(\text{thin electrodes}) = \frac{2}{\pi}\frac{V}{d} = 0.6366 \times \frac{V}{d} \tag{2.6}$$

However, the presence of liquid-crystal and glass dielectric layers enhances the field.

To determine the internal field strength, a finite-element package, COMSOL Multi-

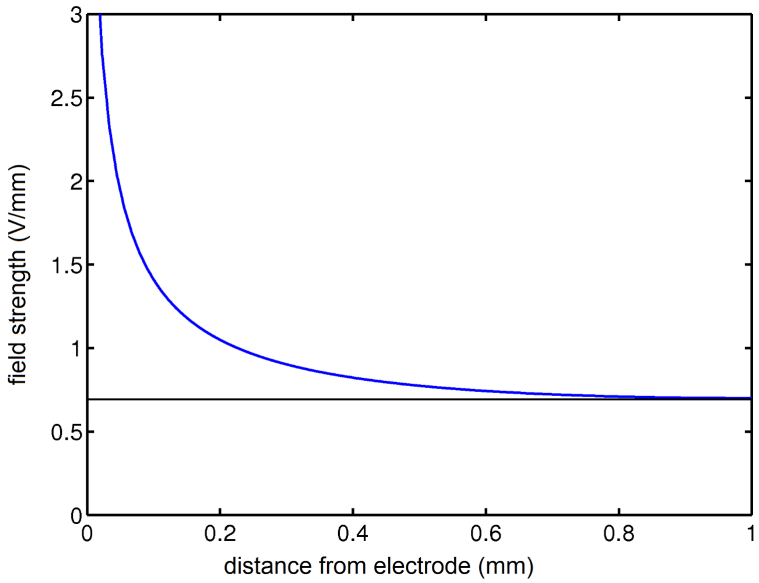

Figure 2.5: The simulated electric field is plotted as a function of distance away from the electrode edge across the electrode gap, using the simulated data also used in figure 2.4. There is a potential difference of 2 V between the electrodes in the simulation. Although the field is very large and non-uniform near the electrode edges, there is a high degree of field uniformity around the centre of the electrode gap.

physics, was used to model field behaviour in the environment of liquid-crystal-glass and glass-air interfaces. In this model, the cholesteric material was treated as a uniform uniaxial anisotropic dielectric medium, with dielectric constants estimated based on known dielectric properties of analogous liquid-crystal mixtures. The simulated static field is shown in figure 2.4. The simulation shows that the field is affected by the presence of the dielectric interfaces, and for the device described, the simulation suggests a field of,

$$E_z \simeq 0.7015 \times \frac{V}{d} \tag{2.7}$$

at the centre of the electrode gap. Further, figure 2.5 shows the field strength as a function of distance away from the electrode edge. Although the field increases rapidly towards the electrode edge, in the region of interest at 1 mm away from the electrode in the centre of the electrode gap, the field has a high degree of uniformity. Not shown, the simulation also suggests that the field does not vary significantly across the cell thickness in the region of interest.

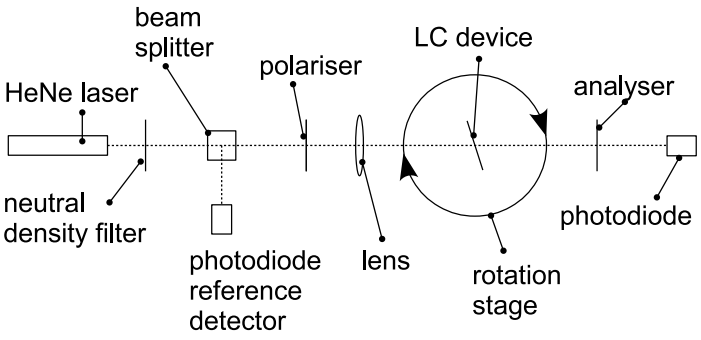

Figure 2.6: A schematic representation of the Grandjean rotation experiment. The arrangement allows the measurement of the transmission between crossed polarizers as a function of angle of incidence.

2.3.3 The Crystal Rotation Method

Here, a Grandjean cell with in-plane electrodes is utilised with a crystal-rotation method. The method measures the transmission of a device as a function of angle of incidence and is very sensitive to out-of-plane rotations in the optic axis of a device. For this reason, it has previously been used in several liquid crystal applications. For example, Baur *et al* used the crystal rotation method to measure surface pretilt angles in liquid-crystal devices to an accuracy of 0.1°[90]. The method is also employed in the measurement of flexoelectricity in DC driven TN cells with in-plane fields in work contributing to this thesis [91, 92], which will be described in §2.4. In an IPS Grandjean geometry, the crystal rotation method is sensitive to the out-of-plane rotation in the optic axis resulting from the flexoelectric interaction, and can therefore be used to study flexoelectric behaviour.

A schematic of the experimental arrangement is shown in figure 2.6. The cell is placed in the path of a 633-nm-wavelength Helium-Neon (HeNe) laser between crossed polarizers on a computer-controlled rotation stage. A lens weakly focuses the laser to a 50 µm spot and a photo diode detects the light intensity after the analyser.

The liquid crystal device is arranged on the rotation stage so that the planar surface alignment and applied field are parallel to the rotation axis and perpendicular to the plane defined by the incident laser beam and the cell normal (the plane of incidence). Referring to the geometry illustrated in figure 2.7, the device is mounted so that the axis of rotation is

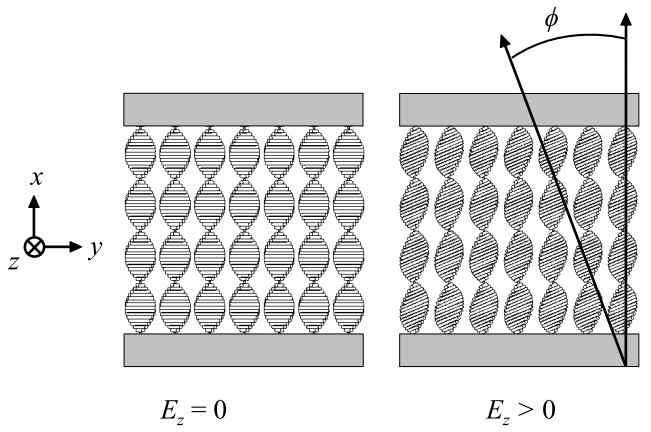

Figure 2.7: An illustration of the chiral-flexoelectric effect in a Grandjean cell. The flexoelectric tilt ϕ is a rotation of the director about the applied in-plane field direction.

the z-axis. Flexoelectric tilt is therefore in the plane of incidence, resulting in a maximum change in the transmission between crossed polarizers when a field is applied. The crossed polarizers are at 45 degrees to the plane of incidence. This ensures a maximum change in transmission because the projection of the optic axis onto the polarizer always makes an angle of 45 degrees to the polarizer axis as the device is rotated.

2.3.4 Electro-optic Measurements

Studying Response to Sine-Modulated Fields

As described in §1.6.3, the Grandjean device acts as a uniaxial birefringent slab, with the optic axis normal to the cell. As was described in §1.4, the transmission of such a device with zero applied field has transmission between crossed polarizers given by,

$$T = \sin^2\left(\frac{\pi \Delta n_{\text{effective}} d}{\lambda \cos\alpha}\right) \tag{2.8}$$

where $n_{\text{effective}}$ is the angle-of-incidence dependent effective birefringence of the Grandjean device, given by,

$$\Delta n_{\text{effective}} = \left(\frac{\cos^2(\alpha+\phi)}{n_1^2} + \frac{\sin^2(\alpha+\phi)}{n_2^2}\right)^{-\frac{1}{2}} - n_1 \tag{2.9}$$

and α here is the angle of incidence of light onto the device, n_1 and n_2 are the effective refractive indices perpendicular and parallel to the helicoidal axis as defined by equation

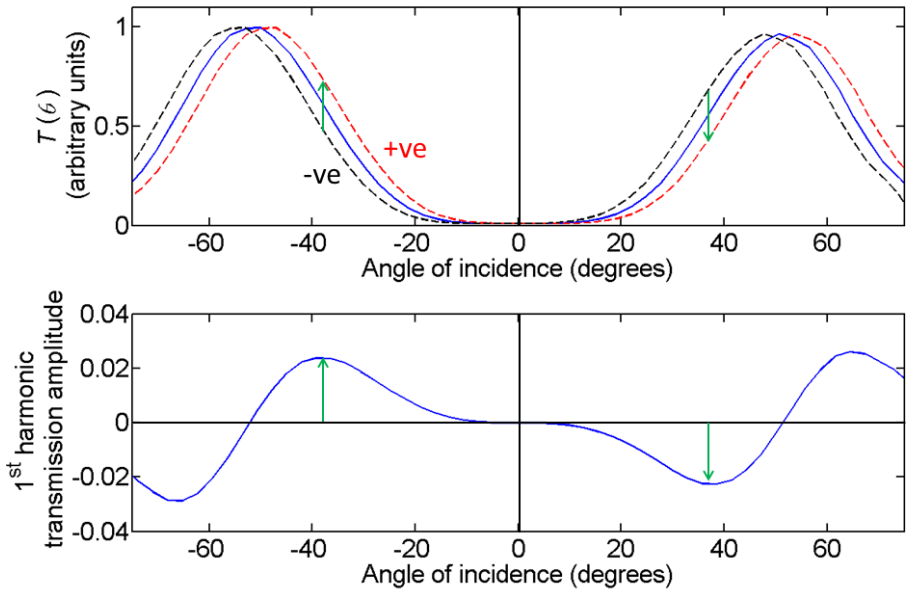

Figure 2.8: (top) An illustration of the transmission as a function of angle of incidence for a Grandjean device placed between crossed polarizers. At normal incidence the transmission is close to zero, because the optic axis of the material is parallel to the incident light. As the angle of incidence increases, the transmission increases as the effective birefringence of the device increases. Under the application of positive and negative electric fields, the incident angle dependent transmission shifts due to the flexoelectric tilt in the optic axis of the device. The shift in the curve shown here is exaggerated for illustrative purposes. (bottom) Under the application of field of the form $E = E_0 \sin(\omega t)$, the transmission amplitude at an angular frequency of ω (the 1^{st} harmonic) can be measured, and gives a direct measure of the change in the transmission due to the flexoelectric tilt in the optic axis.

1.40 in chapter 1, and ϕ is the tilt in the optic axis due to flexoelectricity. At normal incidence, $\alpha = 0$ and therefore $\Delta n_{\text{effective}} = 0$ and $T = 0$. As α increases, the transmission increases, as illustrated in figure 2.8 (top), which shows transmission of the Grandjean device between crossed polarizers as a function of angle of incidence.

Under the application of a field, the optic axis tilts due to flexoelectricity. This tilt shifts the symmetry axis of the transmission as a function of angle of incidence, as is illustrated, again, in figure 2.8 (top). By measuring this shift, one can therefore determine ϕ and, using equation 2.5, therefore determine $(e_1 - e_3)/(K_1 + K_3)$. In order to measure precisely the shift in the symmetry axis, and to avoid the influence of ions, a sine-modulated field with a

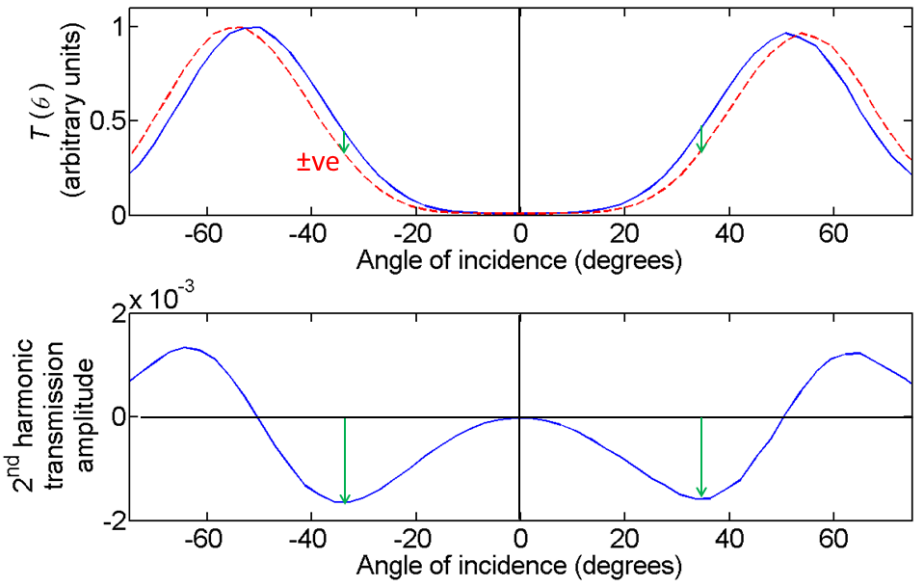

Figure 2.9: (top) The transmission as a function of the angle of incidence of a Grandjean device between crossed polarizers is shown. With the application of a field, the dielectric interaction causes director distortion that is the same for positive and negative electric fields. The effect on the transmission as a function of angle of incidence is illustrated (red dashed line). The shift shown in the transmission as a function of angle of incidence has again been exaggerated for illustrative purposes. (bottom) The 2^{nd} harmonic transmission measures the shift in the transmission that depends on E^2.

frequency greater than 500 Hz is applied to the cell, and the amplitude of the photo-diode response at the same frequency is measured using a lock-in amplifier. The amplitude of the 1^{st} harmonic at a particular angle of incidence depends on the difference in the transmission between positive and negative applied fields, as illustrated in figure 2.8.

As mentioned earlier, the dielectric distortion causes an in-plane distortion resulting in optical biaxiality that is proportional to E^2 (see §1.7.1). The effect of this on the angle dependent transmission is shown in figure 2.9. Since the dielectric interaction depends on E^2, the response is the same for both positive and negative applied fields. For a field of amplitude E_0 described by

$$E = E_0 \sin(\omega t) \tag{2.10}$$

the response is therefore expected to have the form,

$$\begin{aligned} T &= T_0 \sin^2(\omega t) \\ &= \frac{T_0}{2}(1 - \cos(2\omega t)) \end{aligned} \tag{2.11}$$

Hence, the 2$^{\text{nd}}$ harmonic, which is the component of the photo diode response at twice the driving frequency, is sensitive to the in-plane distortion due to the dielectric interaction.

The 2$^{\text{nd}}$ harmonic response, however, is also influenced by flexoelectricity. Some 2$^{\text{nd}}$ harmonic response occurs due to the flexoelectric tilt in the helicoidal axis if the transmission at that point is not in the linear part of the angle-dependent transmission curve. In materials with very small $\Delta\varepsilon$, the flexoelectric contribution can dominate and make measurement of the dielectric distortion less sensitive.

Response Time

By applying a small-amplitude square wave to the Grandjean cell, the characteristic response time can be measured by determining the time for the response to reach within $1/e$ of the final value after a field-polarity inversion. A small amplitude ensures that we are in a linear regime. For E7 at room temperature with 250 nm pitch, this characteristic time is 60 µs, and for MDA-1245 at 37°C with 290 nm pitch it is 1.4 ms.

Care should be taken to scale correctly between lock-in amplifier output and the transmission modulation. The finite switching time of the liquid crystal means that under a constantly changing field, the director will never reach equilibrium. The amplitude of the response will therefore be reduced. For a sinusoidal driving voltage of angular frequency ω and a characteristic switching time of the liquid crystal τ, the amplitude is reduced such that

$$V = V_0 \frac{1}{\sqrt{1 + \omega^2 \tau^2}} \tag{2.12}$$

where V is the photo diode output voltage amplitude and V_0 is the output in the limit $\omega\tau \to 0$. For E7 the switching time of 60 µs is small relative to the characteristic time of the harmonic, and so this effect is small. For example, if driving with a frequency of 1 kHz, the

second harmonic has $\omega = 6300$ s^{-1}, and so $V/V_0 = 1.07$. However, MDA-1245 is more viscous and consequently this effect is much greater. For MDA-1245 driven at 513 Hz, having $\tau = 1.4$ ms, for the second harmonic, $V/V_0 = 8.9$.

Fresnel Reflections at Glass-Air Interfaces

So far we have neglected to consider the effect on the transmission of reflections at the air-glass interfaces of the cell. Rather than include the air-glass interfaces in the Berreman numerical optics simulation, here, the Fresnel equations are instead used to calculate the transmitted amplitude as a function of angle of incidence at these interfaces. The simulated transmission in the data presented in the next section has been modified to account for this effect.

2.3.5 Results and Discussion

Figure 2.10 (top left) shows experimental field-off angle-dependent transmission along with analytical- and numerical-model simulations for E7 + 3.5 w.t.% R5011. Parameters used in fitting are summarised in table 2.1. At normal incidence there is a small transmission due to the optical rotation of the chiral Grandjean structure (measured to be $5°$), which is not present in the analytical model. This is because the analytical model treats the cholesteric as an optically uniaxial medium, without taking account of the optical activity of the cholesteric material (see §1.6.3). The field-off transmission is used to determine Δnd where $\Delta n = n_{\mathrm{e}} - n_{\mathrm{o}}$, by changing this parameter in the model until the output of the model is consistent with the experimental incident-angle-dependent transmission.

The fitting was done manually (i.e. without an automated fitting routine). The transmission as a function of angle of incidence is first used to determine the device thickness d, by varying this parameter in the simulation until the transmission produced by the model is as close as possible to the experimental transmission. Once d is determined, electro-elastic parameters e/K and $\Delta\varepsilon/K_2$ can then be included as fitting parameters. Harmonics of the angle-dependent transmission relative to the driving voltage, which are sensitive to changes in the electro-elastic parameters, can be extracted from the simulation using finite differ-

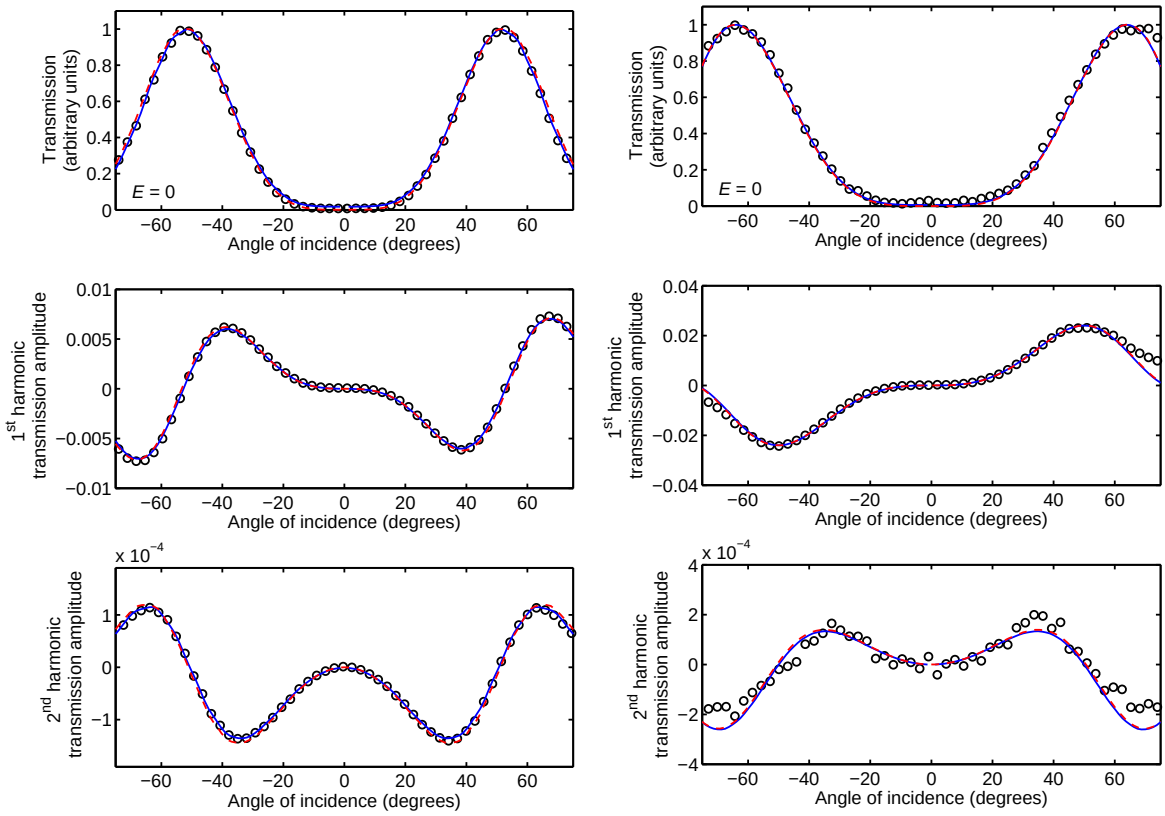

Figure 2.10: The normalised transmission (top), 1st harmonic transmission amplitude (centre) and 2nd harmonic transmission amplitude (bottom) for E7 + 3.5 w.t.% R5011 (left) and MDA-1245 (right) are shown as a function of angle of incidence. A sample of the data are shown as circles, while the solid blue line shows numerical simulation and the dashed red line shows the analytic approximation using fitting parameters described in the text.

ence approximations to the angle-dependent transmission as a function of voltage. The simulated 1st and 2nd harmonics are determined using the finite-difference approximations given by,

$$T'(E_0) \approx \frac{1}{2}\left(T_{(E=E_0)} - T_{(E=-E_0)}\right) \tag{2.13}$$

and,

$$T''(E_0) \approx \frac{1}{4}\left(T_{(E=E_0)} + T_{(E=-E_0)} - 2T_{(E=0)}\right) \tag{2.14}$$

respectively, where E_0 is the applied field amplitude.

The 1 kHz transmission modulation amplitude under the application of a 1 kHz sine-modulated electric field of amplitude 0.075 Vμm^{-1} is shown as a function of angle of inci-

Table 2.1: Parameters used in analytical and numerical models used with the Grandjean rotation experiment.

Material	Δnd (µm)	$\frac{\Delta\varepsilon}{K_2}$(pN^{-1})	$\frac{e_1-e_3}{K_1+K_3}$ (CN^{-1}m^{-1})	E (Vµm^{-1})	Pitch P (nm)
E7	1.940	2.7	0.45	0.075	250
MDA-1245	1.155	$<$1.5	2.0	0.070	290

dence for E7 + 3.5 w.t.% R5011 in figure 2.10 (centre-left). By introducing the ratio e/K as a fitting parameter, the best fit occurs when $e/K = 0.45 \pm 0.02$ CN^{-1}m^{-1} for E7 + 3.5 w.t.% R5011 at 25°C. This corresponds to a value of $e_1 - e_3$ of 12.2 ± 0.6 pCm^{-1}.

The 2$^{\text{nd}}$ harmonic (the 2 kHz transmission modulation amplitude under the same 0.075 Vµm^{-1} 1 kHz driving field) for E7 + 3.5 w.t.% R5011 is shown in figure 2.10 (bottom-left). In this case, the ratio $\Delta\varepsilon/K_2$, which affects the twist distortion (see equation 1.62), is adopted as a fitting parameter, with a best fit of $\Delta\varepsilon/K_2 = 2.7$ pN^{-1}. Merck (a supplier of E7) has measured $\Delta\varepsilon$ of E7 of 13.7, which, considering the measured value of $\Delta\varepsilon/K_2$ here gives a value of K_2 of 5.1 pN. Merck has measured K_2 independently to be 6.5 pN. The discrepancy between these two measured values for K_2 may be due to differences in temperature when the measurements were taken or variations in the ratios of constituent components of different E7 mixtures.

The same procedure has been used with a bimesogen mixture MDA-1245 (provided by Merck Chemicals Ltd.) that was developed to have large flexoelectric properties and small dielectric anisotropy. Figure 2.10 (right) shows the transmission and 1$^{\text{st}}$ and 2$^{\text{nd}}$ harmonic transmission amplitudes as a function of angle of incidence for MDA-1245. The material displays a pronounced flexoelectric response compared to E7, with e/K of 2.0 ± 0.2 CN^{-1}m^{-1}. Because the dielectric anisotropy is very small, the 2$^{\text{nd}}$ harmonic response at 0.07 Vµm^{-1} is dominated by the flexoelectric response, but is consistent with $\Delta\varepsilon$ being relatively small with an upper bound on $\Delta\varepsilon/K_2$ of 1.5 pN^{-1}.

Hence, analysing the transmission and harmonic components of the transmission of Grandjean cells between crossed polarizers driven with AC field, has enabled the measurement of dielectric and flexoelectric properties of cholesteric liquid crystal materials. In the

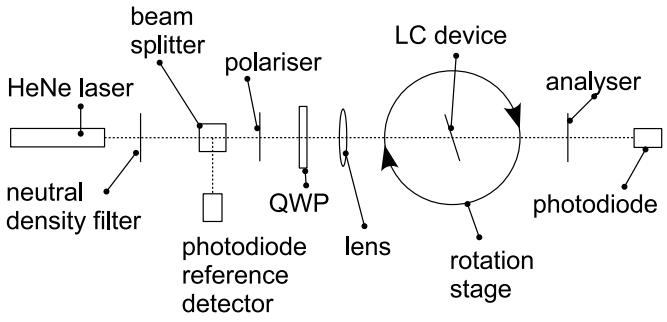

Figure 2.11: The experimental arrangement from figure 2.6 has been modified to include a quarter-wave plate (QWP) before the device. The QWP enhances the sensitivity of the detection of small changes in birefringence.

next section, a modification to the technique is made in order to enhance the sensitivity in devices with very small birefringence.

2.3.6 Enhancing the Sensitivity with a Quarter-Wave Plate

In chapter 6, a study of the dielectric and flexoelectric effects in blue phases will be described in which a material with an extremely small flexoelectric parameter was used, and in a relatively thin cell of 5 µm. The material is a mixture of a nematic host liquid crystal FCU-LCM10 with 21 wt% chiral dopant FCU-NYCL (provided by Feng Chia University, Taiwan). The material's small flexoelectric switching motivated a modification to the Grandjean rotation method in order to increase the sensitivity of measurements in systems where the birefringence of the device is small. In order to be sensitive to small birefringence, a quarter-wave plate can be used [93]. Consider a transmission between crossed polarizers given by,

$$T = \frac{1}{2}\sin^2(\Gamma + \delta) \tag{2.15}$$

where Γ is the retardation due to a wave plate and δ the retardation due to a liquid crystal device (and is assumed to be small). The value of Γ that provides the greatest sensitivity to changes in δ is that where $\partial^2 T/\partial\delta^2 = 0$. Using a double-angle formula and differentiating, we find

$$\frac{\partial^2 T}{\partial \delta^2} = \cos(2\Gamma)\cos(2\delta) + \sin(2\Gamma)\sin(2\delta) = 0 \tag{2.16}$$

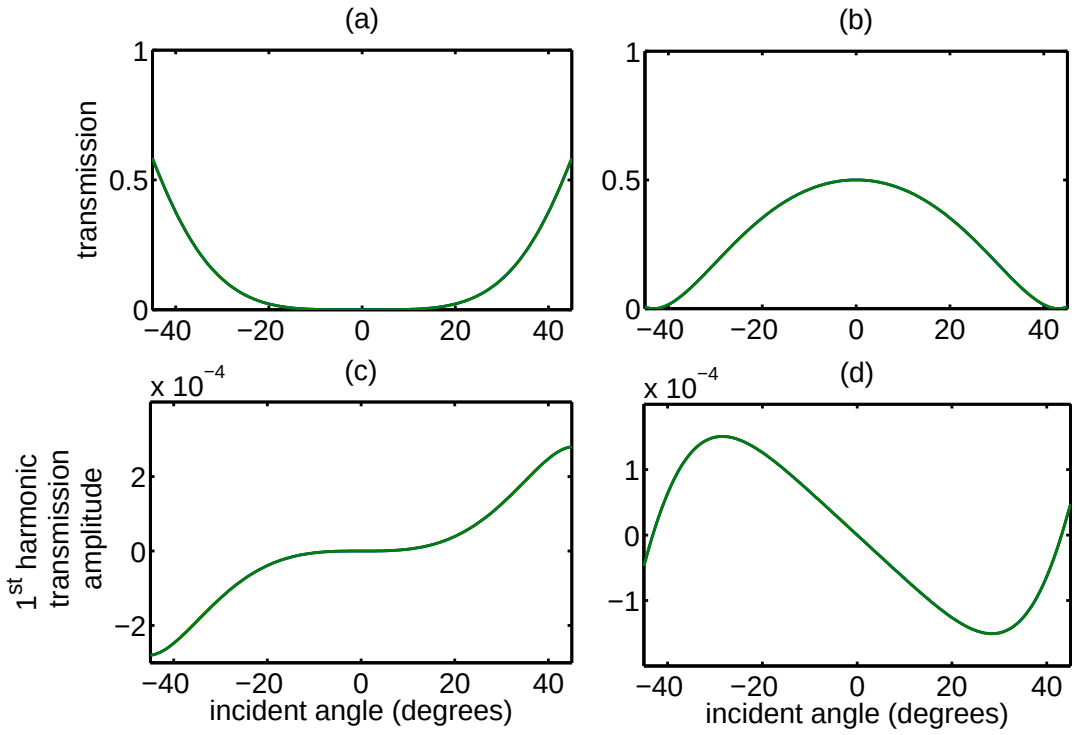

Figure 2.12: Calculated transmission and 1st harmonic transmission amplitude for a thin Grandjean cell observed between crossed polarizers ((a) and (c)) without and ((b) and (d)) with a quarter-wave plate included in the experimental arrangement shown in figure 2.11. The quarter-wave plate enhances the sensitivity in the measurement of changes in birefringence at small angles of incidence in devices with small birefringence, which is apparent by the large slope of the 1st harmonic in (d) compared to (c) at small angles of incidence.

Now, since δ is small, we can write,

$$\cos(2\Gamma) = 0 \tag{2.17}$$

which has the solution that $\Gamma = \pi/2$, which is equal to a quarter-wave. Thus, when a greater sensitivity is required, a quarter-wave plate (which produces the required retardation of $\pi/2$) can be used in the experimental arrangement, as shown in figure 2.11.

Figure 2.12 shows the calculated transmission and 1st harmonic transmission amplitude for a Grandjean device with $P = 250$ nm, $(e_1 - e_3)/(K_1 + K_3)$ = 0.01 CN^{-1}m^{-1}, $d = 5$ µm, $\Delta n = 0.1$ and where $\lambda = 633$ nm and $E = 0.2$ Vµm^{-1}, in the experimental arrangement in figure 2.11, without (left) and with (right) a quarter-wave plate. The glass-air interfaces have not been considered in the calculations of the transmission or 1st harmonic in this case. Figure 2.12 (a) shows the transmission of the device with no quarter-wave plate.

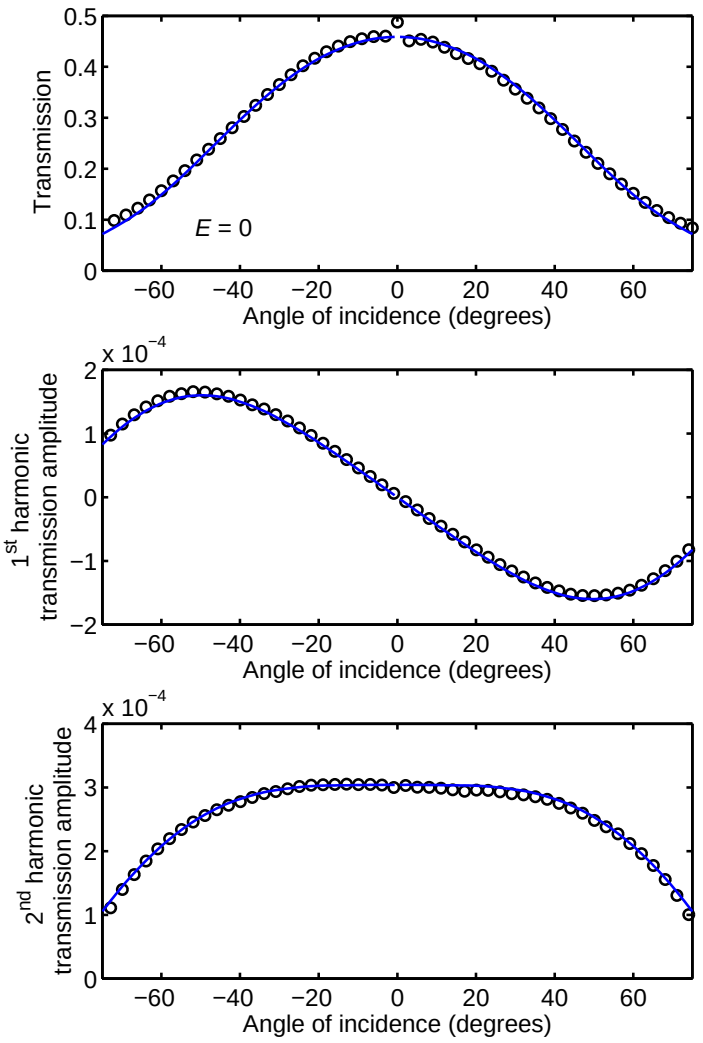

Figure 2.13: The transmission (top), 1st harmonic transmission amplitude (centre) and 2nd harmonic transmission amplitude (bottom) for FCU-LCM10+21wt%FCU-NYCL are shown as a function of angle of incidence. A sample of the data are shown as circles, while the solid blue line shows the numerical simulation. The experimental arrangement used includes a quarter-wave plate to improve the sensitivity.

There is no transmission at normal incidence, because the light propagates parallel to the optic axis of the cholesteric. Because the device is relatively thin, and the birefringence is small, the transmission does not reach a maximum at larger angles. The 1st harmonic for the same device, also with no quarter-wave plate, is shown in figure 2.12 (c). The harmonic shows little change as a function of angle of incidence between -20 and 20 degrees. On

the other hand, figure 2.12 (b) shows the transmission with a quarter-wave plate included. The transmission is 0.5 at normal incidence. Small changes in birefringence cause a larger change in the transmission, which is demonstrated by the 1$^{\text{st}}$ harmonic of the quarter-wave plate case shown in 2.12 (d). The slope of the 1$^{\text{st}}$ harmonic response with respect to angle of incidence is much greater between -20 and 20 degrees than in the case without a quarter-wave plate. Crucially, this feature allows less uncertainty in the parameters of the model that best fits the experimental data, allowing a more precise measurement in this case.

A similar procedure to that described in §2.3.4 is undertaken, utilising a lock-in amplifier and measuring 1$^{\text{st}}$ and 2$^{\text{nd}}$ harmonic components of the transmission as a function of angle of incidence of Grandjean-aligned cells, which for FCU-LCM10+21wt%FCU-NYCL at room temperature are shown in figure 2.13. The numerical fits allow the flexoelastic and dielectro-elastic ratios to be determined. In this case, $e/K = 11 \pm 0.6$ mCN^{-1}m^{-1} and $\Delta\varepsilon/K_2 = 0.8 \pm 0.04$ pN^{-1}. Thus, using this method has allowed the measurement of a flexoelastic ratio as small as 0.01 CN^{-1}m^{-1}

2.3.7 Grandjean Rotation Method Conclusion

A new technique for measuring the flexoelastic parameter e/K, and the parameter $\Delta\varepsilon/K_2$, has been developed by considering the influence of flexoelectric and dielectric distortions on the transmission of short pitch Grandjean-aligned liquid crystal devices as a function of angle of incidence between crossed polarizers. Including a quarter-wave plate in the apparatus can enhance the sensitivity in cases where the device has a small birefringence. The technique is sensitive enough to allow the measurement of e/K as small as 0.01 CN^{-1}m^{-1}, at fields as small as 0.01 Vμm^{-1}, making the technique a powerful tool for probing chiral flexoelectric switching behaviour and measuring important characteristics of elastic, flexoelectric and dielectric liquid-crystal properties. In the next section, a related crystal rotation method is adopted to measure flexoelectricity in achiral systems.

2.4 Achiral Systems: Twisted Nematic Rotation Method

As was discussed in the introduction to this chapter, there has been recent interest in the measurement of flexoelectricity in some unique non-chiral (or achiral) systems. However, non-chiral systems respond slowly to electric fields, and so flexoelectrooptic switching can only be achieved with low field frequencies. This can cause migration of charge carriers within the device and this introduces uncertainty in the resultant internal field strength [94]. The influence of charge carriers on the internal field strength may vary with applied voltage and over the duration of the experimental measurement.

Low frequency or DC fields have been used in a variety of non-chiral systems to measure flexoelectricity although it is rare that the effect of charge carriers is taken into account. A widely cited method by Dozov [95, 96, 97], involving DC in-plane fields in a HAN geometry, is subject to this problem. Prost *et al* also used a non-chiral method involving a homeotropically aligned liquid-crystal phase grating [98], and flexoelectrooptic studies of TN structures have been conducted using a variety of methods [99, 100]. Measurements of $e_1 - e_3$ are often inconsistent between different quasi-DC experiments, casting doubt on the reliability of these methods.

The method presented here utilises the TN IPS (field in plane of device) geometry, and is an attempt to overcome the difficulties of ionic influence by simultaneously studying in-plane and out-of-plane distortions in the helicoidal structure, in analogy to the Grandjean crystal rotation technique in the previous section. Like the Grandjean structure, the TN has a helicoidal director structure whose axis is normal to the cell substrates. The most important difference between the Grandjean and TN crystal rotation methods is that the in-plane rotation of the director, rather than being used to measure the dielectric properties of the liquid crystal, is instead used to determine the internal field, and the dielectric properties of the liquid crystal must therefore be measured independently. By studying the in-plane distortion, which is the result of the dielectric interaction, one can deduce the internal field strength if the dielectric anisotropy of the liquid crystal is known. The out-of-plane distortion, which is due to the flexoelectric interaction, can then be used to measure the flex-

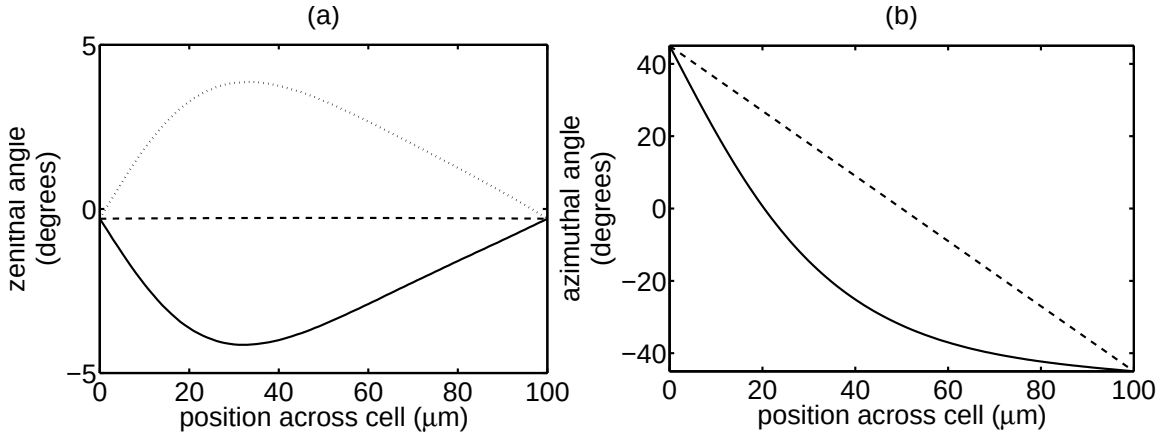

Figure 2.14: Simulated zenithal and azimuthal components of the liquid-crystal director as a function of the z-axis through the thickness of the cell at applied fields of 0 (dashed), $+10$ (solid line) and -10 (dotted) Vmm^{-1} for a 100 μm cell with a small surface pretilt angle, filled with E7 liquid crystal. The flexoelectric difference, $e_1 - e_3$, is set to 10 pCm^{-1}. At zero applied field there is no zenithal tilt in the director, and the azimuthal angle varies linearly from 45 to –45 degrees for the TN. As a field is applied, there is induced a zenithal tilt, the sign of which is dependent on the field direction, and there is a change to the azimuthal component distribution with respect to the z-axis due to the dielectric interaction.

oelectric properties of the liquid crystal once the internal field has been determined from the dielectric interaction. In this way, the field is known intrinsically from the electro-optic data, and the effect of ionic impurities on the field strength are, in principle, therefore taken into account. Another major difference between the Grandjean and TN methods is the use of a quasi-DC field, which means that lock-in amplifier techniques to measure harmonic components are inappropriate.

2.4.1 TN Measurements

Figure 2.14 shows simulated zenithal and azimuthal liquid crystal director angles across a 100 μm thick 90 degree TN cell filled with E7 liquid crystal, with strong surface anchoring conditions in the cases where in-plane electric fields of 0, $+10$ Vmm^{-1} and -10 Vmm^{-1} are applied parallel to the orientation of the director at one cell surface. The zenithal angle is defined as the out of plane tilt in the director about the applied field direction, and the azimuthal angle is defined as the angle the director makes about the helicoidal axis, which here is parallel to the z-axis. The director structure in these cases is also illustrated in figure

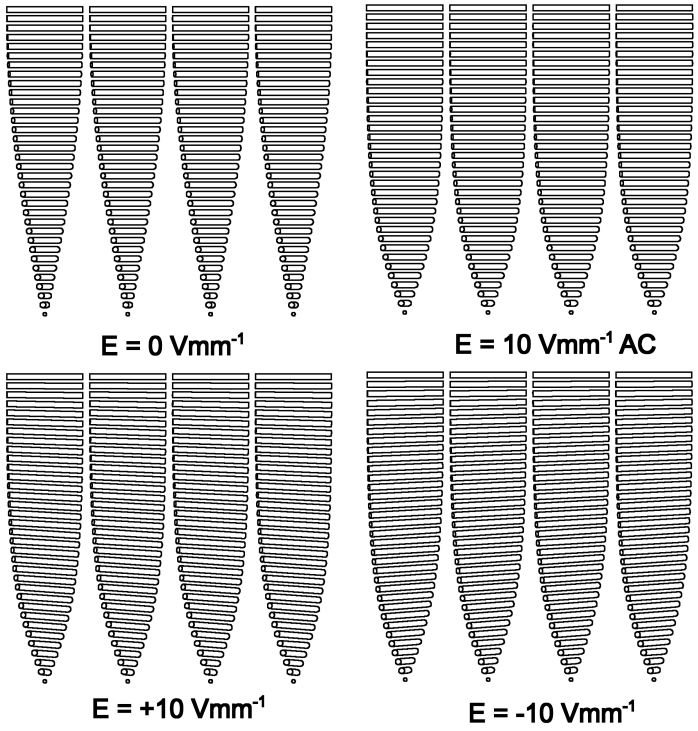

Figure 2.15: The simulated director structure of a TN cell is shown under the application of DC and AC fields. An AC field results in a dielectrically-induced in-plane distortion of the director. In the case of a DC field, there is an additional field-polarity dependent tilt in the director due to flexoelectricity.

2.15. The numerical simulation uses a single-dimensional minimisation of the liquid-crystal free energy,

$$\begin{aligned} F(\hat{\mathbf{n}}) =& \frac{1}{2}K_1[\nabla\cdot\hat{\mathbf{n}}]^2 + \frac{1}{2}K_2[\hat{\mathbf{n}}\cdot(\nabla\times\hat{\mathbf{n}}) + q]^2 + \frac{1}{2}K_3[\hat{\mathbf{n}}\times(\nabla\times\hat{\mathbf{n}})]^2 \\ & - \frac{1}{2}\varepsilon_0\Delta\varepsilon(\hat{\mathbf{n}}\cdot\mathbf{E})^2 - \left[e_1\hat{\mathbf{n}}(\nabla\cdot\hat{\mathbf{n}}) + e_3(\nabla\times\hat{\mathbf{n}})\times\hat{\mathbf{n}}\right]\cdot\mathbf{E} \end{aligned} \tag{2.18}$$

which was first given in §1.3.4. The dielectric interaction causes the director through the device to rotate solely azimuthally to maximise $\hat{\mathbf{n}}\cdot\mathbf{E}$. The flexoelectric interaction on the other hand causes a zenithal tilt of the director out of the plane of the cell, which is analogous to the flexoelectric tilt in the chiral-flexoelectric effect, and reverses with a reversal of the field direction, as is illustrated by figures 2.14 and 2.15. At the surfaces of the cell, there is no tilt due to the strong planar anchoring condition, but the tilt is larger towards the centre of the cell thickness. It has also been shown that the zenithal flexoelectric tilt of the director

structure has a negligible effect on the azimuthal dielectric distortion [100]. In principle the cell's internal field strength should be determinable independent of flexoelectric effects by measuring this azimuthal dielectric distortion using electrooptic techniques [99].

Ewings *et al* [99] analysed the transmission of a TN IPS device between crossed polarizers at two oblique angles of incidence as a function of applied voltage. The electric field was assumed to vary in proportion to the applied voltage, and the constant of proportionality and the parameter $e_1 - e_3$ were determined by comparing the transmission at different voltages with a numerical simulation. They reported $e_1 - e_3$ for E7 to be 9.3 $\pm$ 0.3 pCm^{-1}, although this was revised to 12.1 $\pm$ 1.0 pCm^{-1} in a later paper using a similar method [101]. A second method, by Tidey *et al* [100], again used the TN IPS geometry but analysed the conoscopic transmission at discrete applied voltages. Here, the field was again assumed to vary in proportion to the applied voltage, and the constant of proportionality was determined using conoscopic images taken with the application of a 1 KHz Alternating Current (AC) field, which couples only to the dielectric interaction. A Direct Current (DC) field was then used to determine $e_1 - e_3$ for E7 to be 9 $\pm$ 1 pCm^{-1}.

The switching time is slow for TN devices, of the order of seconds for a 50 µm thick cell. In order to circumvent the uncertainty of the field due to ion migration, rather than relying on knowledge of the device geometry and the voltage applied, as is the case in the ULH method, Ewings attempted to determine the internal field implicitly from transmission data, by observing the effect of the in-plane distortion due to the dielectric effect on the transmission. However, Ewings makes the assumption that the influence of charge carriers on the proportionality between the applied voltage and the internal field is constant. This may well not be the case. Tidey's conoscopic technique [100] does not consider the influence of charge carriers.

2.4.2 Crystal Rotation Method in TN Devices

In the technique developed in the present study, incident angle-dependent transmission of the TN IPS geometry is measured using a crystal rotation method. By measuring the trans-

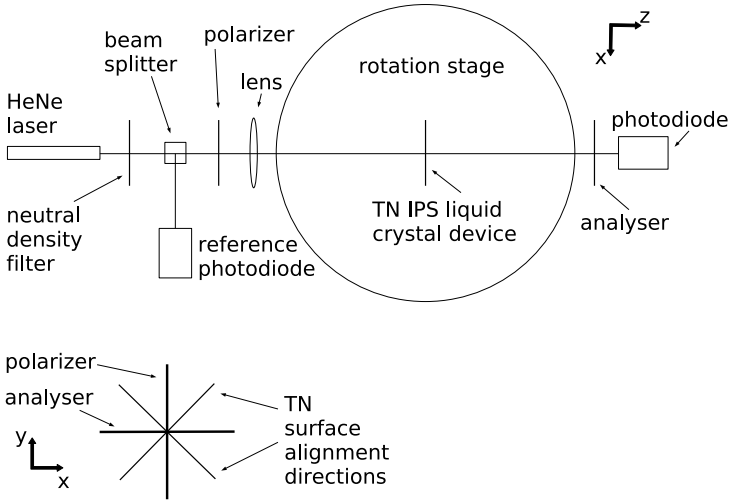

Figure 2.16: A schematic of the experimental arrangement. A TN IPS device is placed on a rotation stage such that its transmission can be measured as the angle of incidence varies. The orientations of the polarizers and the surface planar alignment treatment directions are also shown. A right-handed coordinate system is in use, and the z-axis is defined as the axis normal to the cell, and the coordinate system is defined in relation to the cell's frame of reference.

mission as a function of angle of incidence over a wide range of angles, there is less possibility of degeneracy between the output of models with different sets of parameters, than in an experiment at which only two angles of incidence are chosen. Rather than using multiple voltages, and assuming that the field is proportional to the voltage applied, here, a single voltage magnitude is chosen and the device behaviour is observed as a function of angle of incidence. As mentioned before, the crystal rotation method is routinely used to measure small surface-induced director tilt-angles in homogeneous liquid-crystal cells with a precision of 0.1 degrees, and has been extended to TN cells [90], but up until now it has not been used to measure flexoelectricity in TN devices.

In the work by Baur *et al* [90], antiparallel-planar and TN liquid-crystal devices are rotated between crossed polarizers, such that the angle at which light travelling normal to the polarizers is incident on the device, θ, will vary. The experimental arrangement shown in figure 2.16 can be used to measure the transmission as a function of angle of incidence. The rotation stage allows the angle of incidence to be controlled. The transmission, T, in TN devices varies symmetrically about an angle θ_x, where there is the greatest difference

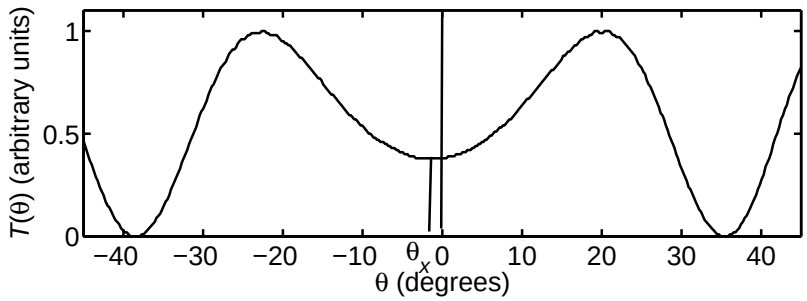

Figure 2.17: Simulated transmission through crossed polarizers as a function of the angle of incidence, θ, for a 10 µm thick TN cell filled with E7 liquid crystal in the experimental arrangement shown in figure 2.16. The symmetry point corresponds to θ_x, and can be used to determine the surface induced pretilt.

in optical path length between the ordinary and extraordinary rays (figure 2.17). This angle is related to the surface-induced zenithal tilt angle, α_0, of the liquid crystal director, which remains constant from one surface to the other throughout the cell. Numerical methods are required to determine α_0 from θ_x. The high precision with which θ_x can be determined makes this a very precise method for measuring α_0, which is equal to the surface pretilt angle of the alignment layers.

Baur points out that the axis of rotation of the device must be chosen correctly in order for θ_x to be found [90]. The TN geometry, should be rotated about an axis normal to the plane defined by the light incident on the device and the director at the centre of the cell. The cell should be placed between crossed polarizers whose polarization directions are parallel and normal to this plane. This is so that the light is incident and propagates through the liquid crystal at 45 degrees to the optic axis for maximum transmission modulation as a function of angle of incidence.

Figure 2.18 shows the simulated transmission as a function of the angle of incidence, $T(\theta)$, through a 100 µm thick TN cell filled with E7 under the application of electric fields of strength (a) 0Vmm^{-1}, (b) 10Vmm^{-1} AC, (c) $+10\text{Vmm}^{-1}$ and (d) -10Vmm^{-1}, where, for the DC field cases, $e_1 - e_3$ is set to 10 pCm^{-1}. The switch-on time for such a cell is of the order of a second, and so an AC field whose polarity switches significantly faster than once a second, for example a field frequency of 100 Hz, will couple to the field-

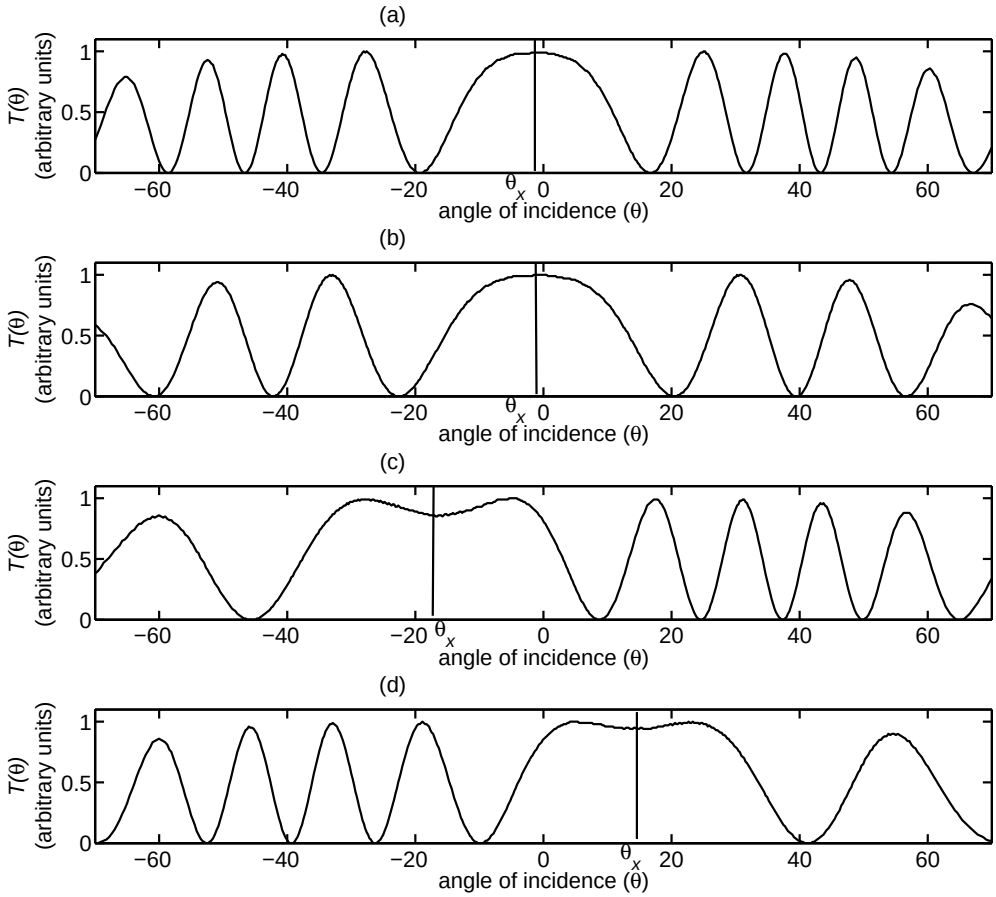

Figure 2.18: Simulated transmission as a function of the angle of incidence, $T(\theta)$, through a 100 μm thick TN cell filled with E7 with an applied in-plane field of (a) 0Vmm^{-1}, (b) 10Vmm^{-1} AC, (c) $+10\text{Vmm}^{-1}$ and (d) -10Vmm^{-1}.

polarity-independent dielectric interaction but not the field-polarity-dependent flexoelectric interaction. This case is simulated by switching off the flexoelectric effect in the model and is shown in figure 2.18 (b). The simulation uses a numerical minimisation of the free energy given in Equation 2.18 to model the director structure (see §1.10), in conjunction with 4-by-4 Berreman optics [15] to simulate transmission (see §1.4.2).

Using the simulation, it is possible to change the strength of the dielectric and flexoelectric interaction independently in order to understand the resultant effect on $T(\theta)$. The strength of the flexoelectric interaction — dependent on E and therefore field-polarity dependent — influences the zenithal tilt of the director and therefore shifts $T(\theta)$ in the θ-axis,

effectively changing θ_x. The strength of the dielectric interaction on the other hand — dependent on E^2 and therefore field-polarity independent — scales $T(\theta)$ in the θ-axis, increasing the angle between the first transmission minima on each side of the symmetry point, rather than significantly changing θ_x. In this way, the influence of the dielectric and flexoelectric interactions are decoupled and can be determined separately. For greatest sensitivity to both E and $e_1 - e_3$, one must choose the appropriate field to apply. Since the strengths of the flexoelectric and dielectric interaction are linearly and quadratically field-dependent respectively, there is an optimal field strength where the interactions are similar in magnitude, and can be determined with the greatest degree of certainty. If the field strength is too small, the dielectric interaction is small and its measurement less precise. Too large however, and the dielectric interaction inhibits the flexoelectric tilt, reducing the precision of the tilt measurement. 10 Vmm^{-1} is found numerically to be optimum for the device modelled in figure 2.18, where there is the greatest sensitivity to both flexoelectric and dielectric interactions.

Having found the optimal field strength that allows the best compromise between sensitivity to flexoelectric and dielectric distortions, this can be used as the basis for choosing what voltage to apply. Then, the strengths of the flexoelectric and dielectric interactions can be determined by altering the parameters E and $e_1 - e_3$ in the model until the simulated transmission is as close to the data as possible.

2.4.3 Experimental

The transmission as a function of the angle of incidence, $T(\theta)$, can be measured using the experimental arrangement shown in figure 2.16. In a similar arrangement to that used in the Grandjean rotation method in §2.3, a TN cell is mounted on a computer-controlled rotation-stage between crossed polarizers which allows control of the angle of incidence of a laser on the cell. Crossed polarizers are set perpendicular and parallel to the plane of incidence, while the TN cell is mounted with its surface alignment at 45 degrees to the x- and y-axes, such that the liquid crystal director in the centre of the TN cell is parallel to

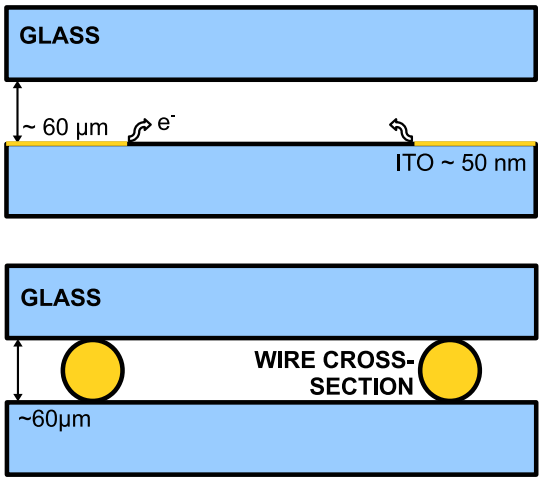

Figure 2.19: An illustration of the two electrode structures. ITO electrodes produce larger field strengths near electrode edges, which may result in an enhancement of the influence of ions on the internal field strength.

the incident plane. The laser passes through a beam-splitter to provide a reference signal. To ensure that a region is probed over which the device thickness, liquid crystal alignment and electric field are uniform, a lens is used to weakly focus the beam to a diameter of approximately 50 µm at the cell. In order to create a TN alignment, the cell is constructed from glass substrates that are treated with a unidirectionally rubbed PVA layer, which is known to produce low pretilt angles [3]. 32 µm PET-plastic spacer material is used to set the cell thickness. Electrodes were produced in two different ways. In the first experiment, a 4 mm channel is etched into Indium Tin Oxide (ITO) treated glass. The wideness of the electrode gap relative to the cell thickness ensures a uniform field distribution (as was discussed in §2.3). In the second experiment, circular cross-section wire was used. The regions near ITO electrode edges have high field strengths. These high field regions may enhance the influence of ions on the internal field, possibly by injecting ions into the liquid crystal [102], which is undesirable. By using a circular cross-section electrode in the form of thin wires, it was thought that this influence may be reduced (see figure 2.19).

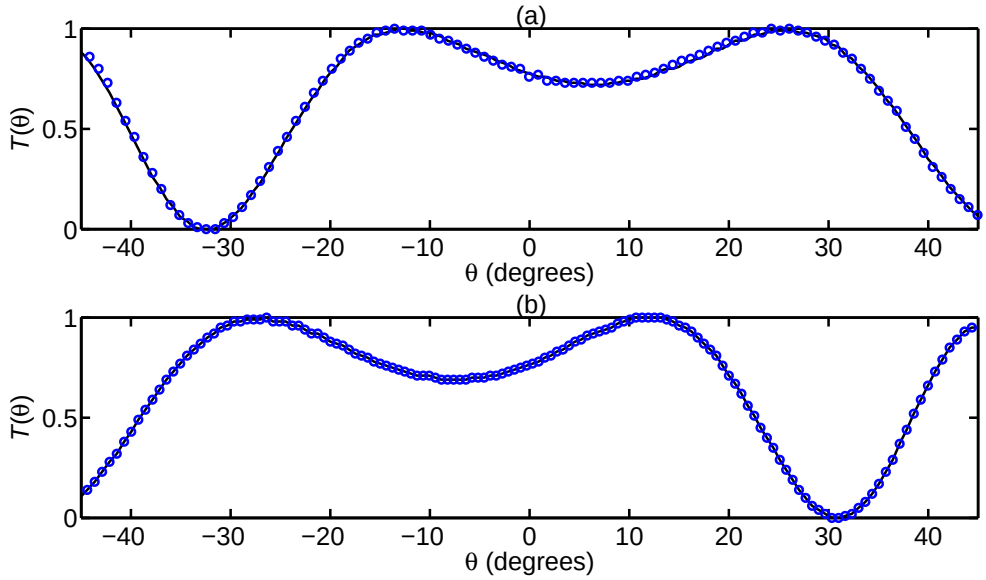

Figure 2.20: The measured angle-dependent transmission of a TN cell filled with E7 in the case where (a) a positive field is applied using ITO electrodes and, (b) a negative field is applied. A sample of the measurements are shown as circles, and the best-fit theoretical angle-dependent transmission is shown as a continuous line. The parameters used in the simulated angle-dependent transmissions are shown in table 2.2.

2.4.4 Results

Figure 2.20 shows experimental incident-angle-dependent transmission, $T(\theta)$, for E7 liquid crystal under the application of positive and negative applied fields for cells with ITO electrodes, and figure 2.21 shows corresponding data for a TN cell containing BL087. The position of the symmetry point, θ_x, of the angle-dependent transmission depends on the magnitude and polarity of the applied field. The dependence on the field polarity is solely due to the flexoelectric effect, which is further evidenced by the fact that under the application of an AC field, $T(\theta)$ does not shift, but only scales in the θ axis such that the first minima on each side of the symmetry point become further apart, as seen in figure 2.21.

As noted above, the large fields at the electrode edges could enhance the ion influence on the field. Therefore, experiments were repeated using circular cross section wire electrodes. The incident-angle-dependent transmission for wire-electrode cells containing E7 and BL087 are shown in figures 2.22 and 2.23 respectively.

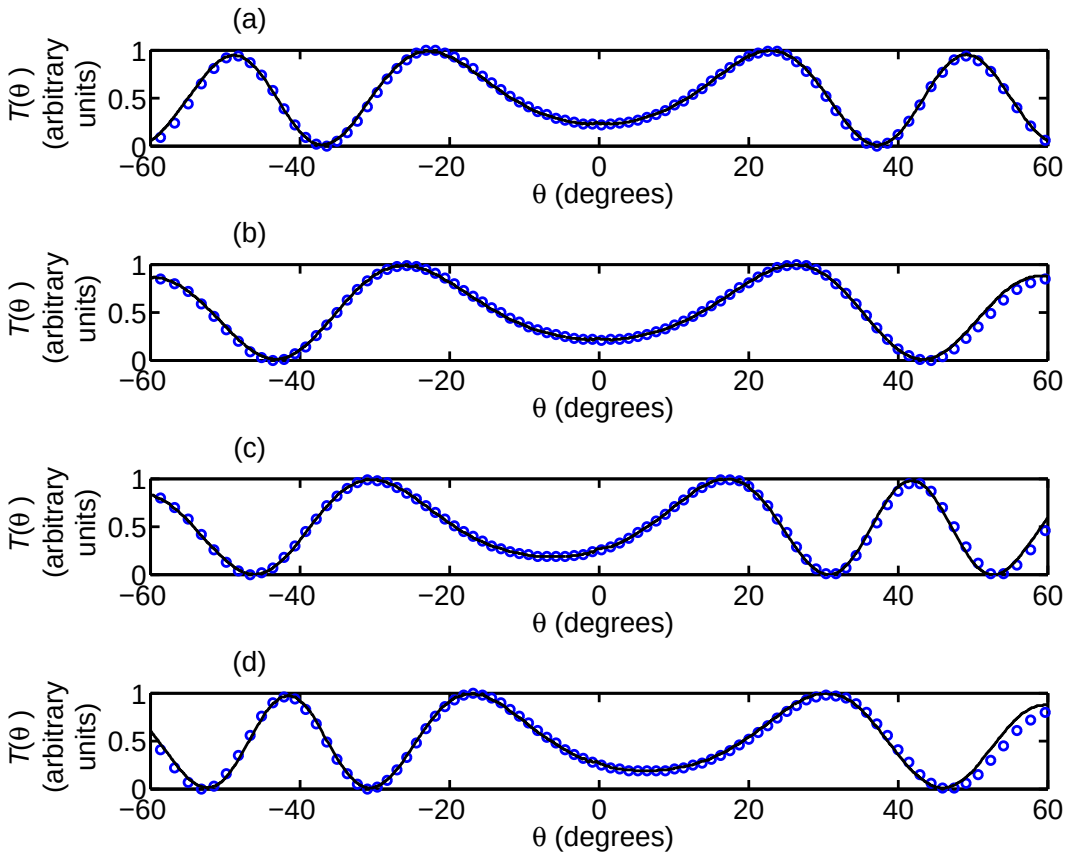

Figure 2.21: Incident-angle-dependent transmission for TN cells containing BL087 with ITO in-plane electrodes with (a) zero field, (b) AC field, (c) negative field, and (d) positive field. Again, circles are measured values and the black continuous line is the numerical simulation. The parameters used for the simulated angle-dependent transmissions using the method described in the text are shown in table 2.2.

A spectrometer that can measure the transmission of the cell at wavelengths in the range of 400 to 800 nm can be used to determine d independently by analysing the fabry-perot fringes in the transmission of an empty cell, where before filling with liquid crystal, the cell gap is assumed to have the dielectric properties of free space. This interferometric method can be used to determine d to a precision of 100 nm, based on how accurately one can measure the positions of Fabry-Perot fringes. However, the incident-angle-dependent transmission of the filled cell with no field applied can also be used to determine the thickness d by including d as a fitting parameter in a numerical simulation and finding the value

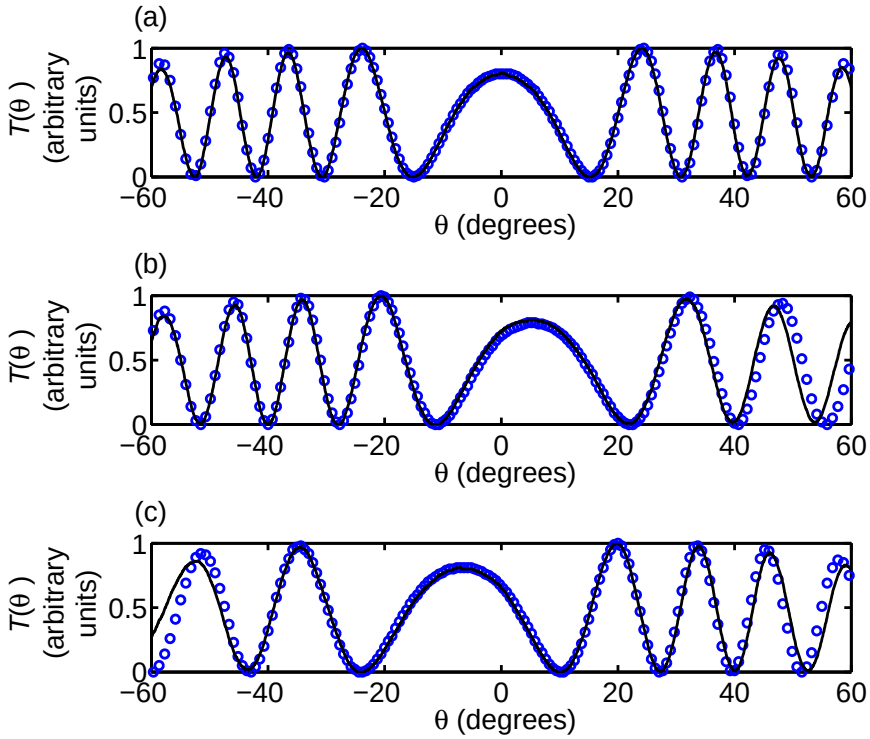

Figure 2.22: Experimental transmission as a function of angle of incidence for a TN cell filled with E7, with applied voltages of (a) 0 V, (b) +40 V and (c) -40 V. In this case, electrodes were made using wire. Again, circles are measured values and the black continuous line is the numerical simulation.

of d that best reproduces the experimental transmission in the case with zero applied field. The best-fit numerical simulation is sensitive to changes in d of 10 nm. Using this latter method for determining d overcomes variation that can arise from its weak dependence on position in the cell, variation by up to 10 nm with temperature fluctuations, and a slight change when filling the cell. However, the transmission depends on the product Δnd, and so using the transmission of the liquid crystal as a function of angle of incidence between crossed polarizers to measure d means that the accuracy of d is limited by the accuracy of Δn (which is also temperature dependent). The incident-angle-dependent transmission of the filled cell with no field applied is also used to determine α_0 (the pretilt angle due to the liquid crystal alignment layer) by adopting α_0 as another fitting parameter.

The parameters d and α_0, once determined, were then kept fixed in further simulations

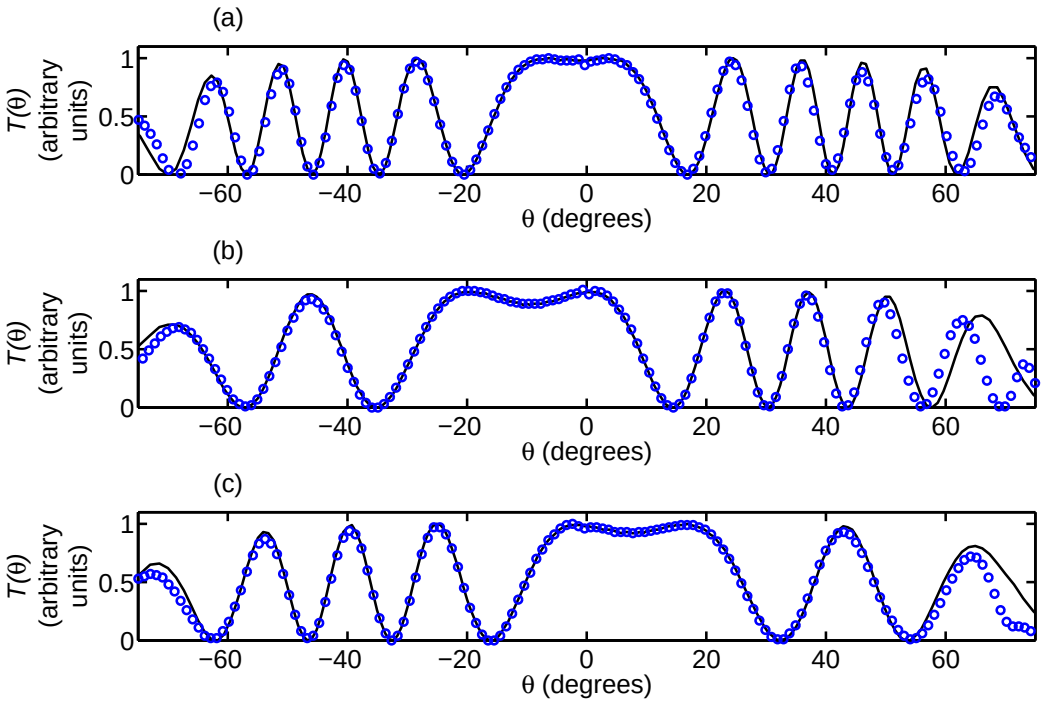

Figure 2.23: Experimental transmission as a function of angle of incidence for a TN cell filled with BL087, with applied voltages of (a) 0 V, (b) +50 V and (c) -50 V. Again, electrodes were made using wire. The parameters used in the simulation (solid line) are used to measure flexoelastic and properties of the material.

where the strength of the flexoelectric and dielectric interactions were allowed to vary in order to best fit the experimental field-on data. The field strength E and flexoelectric parameter $e_1 - e_3$ were then calculated from the best-fit values of the strengths of the two interactions. The values of d, α_0, E and $e_1 - e_3$ for E7 and BL087 determined from this procedure are shown in table 2.2. Values of the dielectric, elastic and refractive index parameters, which are kept constant in the simulations, were supplied by the manufacturer Merck and are also given in table 2.2.

Uncertainty in the values of the elastic constants, dielectric anisotropy and birefringence cause an uncertainty in the measured value of $e_1 - e_3$ due to the dependence of the fitting on these parameters. Using the numerical fitting procedure described, values of these parameters were perturbed in order to determine the corresponding change in the measured value of $e_1 - e_3$. A 5% increase in the values of the elastic constants lead to a similar increase in

Table 2.2: The pretilt angle α_0, thickness d, flexoelectric parameter $e_1 - e_3$, and field strength E that were found by fitting numerical simulations to experimental data for cells filled with E7 and BL087 using ITO electrodes using the procedure described in the text. The values used for the dielectric anisotropy, ordinary and extraordinary refractive indices and elastic constants are also listed.

Parameter description	Symbol	E7	BL087	Unit
Splay elastic coefficient	K_{11}	10.7	12.1	pN
Twist elastic coefficient	K_{22}	6.5	5.9	pN
Bend elastic coefficient	K_{33}	16	23.7	pN
Dielectric anisotropy	$\Delta\epsilon$	13.7	20.5	
Ordinary refractive index	n_{o}	1.52	1.52	
Extraordinary refractive index	n_{e}	1.73	1.74	
Surface induced pretilt angle	α_0	3.6	0.7	mrad
Cell thickness	d	35.8	46.8	μm
Internal electric field strength best-fit value for positive field data	E_{positive}	10.7	8.2	Vmm^{-1}
Internal electric field strength best-fit value for negative field data	E_{negative}	–14.4	–8.2	Vmm^{-1}
Flexoelectric difference best-fit value for positive field data	$e_1 - e_3$	8.4	10.8	pCm^{-1}
Flexoelectric difference best-fit value for negative field data	$e_1 - e_3$	7.2	10.8	pCm^{-1}
Flexoelastic parameter	e/K	0.30	0.31	$\mathrm{Cm}^{-1}\mathrm{N}^{-1}$

the measured $e_1 - e_3$; a 5% increase in the dielectric anisotropy causes a 2.5% increase in the measured $e_1 - e_3$; and an increase in the birefringence by an amount that corresponds to a change in the temperature of 5° causes a change in the measured $e_1 - e_3$ of $\sim 2.5\%$. Combining these errors in quadrature gives an overall uncertainty in $e_1 - e_3$ of $\sim 7.5\%$.

Using ITO electrodes, the result of the numerical data fitting procedure found $e_1 - e_3$ for E7 to be 7.8 ± 1.0 pCm^{-1} and for BL087 to be 10.8 ± 1.0 pCm^{-1} at 25 degrees centigrade. This gives $(e_1 - e_3)/(K_{11} + K_{33})$ — often called e/K and used as a figure-of-merit for materials optimised for the chiral-flexoelectric effect — of 0.30 ± 0.04 $\mathrm{Cm}^{-1}\mathrm{N}^{-1}$ for E7 and 0.31 ± 0.03 $\mathrm{Cm}^{-1}\mathrm{N}^{-1}$ for BL087.

The uncertainty arises from the uncertainty in the values of the physical parameters used in the simulation, and differences between best-fit values of $e_1 - e_3$ obtained from transmission data collected for positive and negative applied electric fields and between multiple

experimental runs. For example, as seen in table 2.2, for E7 the average of the values of $e_1 - e_3$ determined in positive and negative field cases is 7.8 pCm^{-1}, the measured values are approximately 7% to either side of this value. This was found to be typical between multiple experimental runs. If this error is combined in quadrature with the uncertainty of 7.5% due to uncertainty in the values of physical parameters that was mentioned previously, then the total standard error is approximately 10%.

Independent analysis of the incident-angle-dependent transmission of the devices with wire electrodes found values of $e_1 - e_3$ for E7 of 7.2 $\pm$ 1.0 pCm^{-1} and for BL087 of 9.4 $\pm$ 1.0 pCm^{-1} at $25\,^{\circ}\mathrm{C}$. These values are consistent with those found using ITO electrodes, which suggests that if there is a difference in the ionic influence on the measurement, it is not significant within the experimental error. The measurements here using TN crystal rotation methods show inconsistency with measurements using the Grandjean structure in §2.3. This will be further commented on in the next section.

2.4.5 Influence of Ions

Although the internal fields were determined implicitly from the transmission data, it is interesting to compare this with an estimate. One can estimate the field by using the analytical solution for the field half way between two parallel wires that are separated by a distance D and of radius a in free space, with an applied voltage of V given by,

$$E_{\text{freespace}} = \frac{2}{\ln\left(\frac{D-a}{a}\right)} \times \frac{V}{D} \tag{2.19}$$

and for where $D = 4$ mm and $a = 40$ µm,

$$E_{\text{freespace}} \simeq 0.44 \times \frac{V}{D} \tag{2.20}$$

As was seen in numerical simulations of the field in §2.3, dielectric interfaces can enhance the internal field, and a larger value may be expected than that given by equation 2.19, however, in the absence ionic influences, the field would not be expected to be greater than $E = V/D$, which is the case for parallel plate electrodes. If we define a field factor γ, given

by,

$$\gamma = \frac{E_{\text{measured}}}{E_{\text{freespace}}} \tag{2.21}$$

then for the case where $E_{\text{measured}} = E_{\text{freespace}}$ then $\gamma = 1$, and for the case where $E_{\text{measured}} = V/D$, then $\gamma = 2.3$. We may therefore expect that,

$$1 < \gamma < 2.3 \tag{2.22}$$

What is found is that values of γ in the wire-electrode experiments are within the expected range, however there is some variation in the value, which may be indicative of the influence of charge carriers on the internal field strength.

It is interesting to note that there is a greater variation between different experimental runs for E7, which is known to contain a lot of ionic impurities, than for BL087, which is a newer material and is less ionic. Whilst it is thought here that the TN crystal rotation method is robust against the static influence of charge carriers, differences in measured values of $e_1 - e_3$ between different experimental runs may arise from changes in the internal field during the runs, which lasted 4 minutes. A more precise measurement using this method could potentially be made if the data were collected over a shorter time period, which would minimise the change in the internal field during the data collection period. A study of the change in the internal field over time would allow a more suitable time period to be chosen. The value of $e_1 - e_3$ determined in the TN crystal rotation method presented here for E7 is lower than the corresponding value measured by Kischka *et al* [101] using a TN experiment with E7, which may reflect the way in which the field strength was determined and the influence of ions. The value of $e_1 - e_3$ presented here is however consistent with the corresponding conoscopic measurement from Tidey *et al* [100], which reported a value of 9 ± 1 pCm^{-1}.

Curiously, the value of $e_1 - e_3$ determined here with the TN crystal rotation method is inconsistent with the corresponding measurement in the Grandjean geometry in §2.3, which determined $e_1 - e_3$ to be 12.2 ± 0.6 pCm^{-1}. This is in contrast to work by Salter *et al* In a further measurement using a TN experiment similar to the one used by Kischka,

Salter found 12.2 $\pm$ 1.0 pCm^{-1} [77], and in that work, they found consistency between methods using both chiral and non-chiral techniques. It is therefore an open question as to exactly why there is inconsistency between the TN and Grandjean methods presented in this chapter, although as has been suggested, the inconsistency may be explained with a more detailed examination of the influence of ions.

Unfortunately, a detailed study of the influence of ions is outside the scope of this thesis. Ionic behaviours have been extensively studied by measuring the transient current on applying voltages to liquid crystals [103, 104]. These studies have revealed that ions can be injected from electrode edges [102], are often already present in liquid crystal mixtures [105], can stick onto electrodes [106], and that their mobility is coupled to the director orientation [107]. A more detailed consideration of these effects, and possibly monitoring the transient current during flexoelectric measurements, could provide valuable insight and allow a more accurate measurement of flexoelectricity in non-chiral systems.

2.4.6 Final Remarks

It has been demonstrated that the crystal rotation method can be used to measure the difference in flexoelectric parameters $e_1 - e_3$ of nematic liquid crystals in TN cells. The method determines the strength of the dielectric and flexoelectric interactions simultaneously, and therefore allows an independent measure of the internal field. However, the dynamical and hysteretic effects of ions, and other complicated ion behaviour, is probably the cause of variation between experimental runs. Indeed, materials that are known to contain less ions have been found to produce more consistent results. Although flexoelectricity is not expected to vary with chirality [77], here it has been found that the measured values of $e_1 - e_3$ in this study for E7 are significantly smaller than those measured in chiral-doped E7 using the ULH and Grandjean methods described in §2.2 and §2.3 respectively. This discrepancy may also be a result of a naive treatment of ionic effects.

The crystal rotation method used with the TN geometry is most sensitive with materials that exhibit moderate flexoelectric and dielectric field interactions. This is because the

method relies on a similar amount of distortion from each effect in order to measure both the field strength and the flexoelectric distortion simultaneously. This could be a significant limitation, since many materials of interest exhibit very small dielectric anisotropy and large $e_1 - e_3$. However, a reasonable estimate of the flexoelectric properties of low-ionic-content materials could be made by modifying the analysis to allow an estimate of the electric field, rather than determining the field from transmission data. This could be done, for example, by considering the geometry and dielectric properties of the device and solving the electrostatic equations using a numerical modelling package, as was used in §2.3.2 in relation to the Grandjean geometry.

With the increasing demand for field-sequential display technologies that may exploit the chiral-flexoelectrooptic effect, and the interest in non-chiral systems, the development of techniques to measure flexoelectric parameters is of continuing necessity. The TN crystal rotation method provides a unique way to measure $e_1 - e_3$ in non-chiral materials that has benefits over other non-chiral methods, including the possibility of determining the field implicitly from electrooptic data.

2.5 Conclusion

In this chapter, a variety of techniques have been developed for measuring flexoelectric properties of both chiral and non-chiral liquid crystal materials. The Grandjean method described in the first half of this chapter allows the measurement of both flexoelastic and dielectro-elastic properties of cholesteric materials, and the technique is used in later chapters to characterise material parameters. The non-chiral TN method described in the second half has been an attempt to more accurately measure flexoelectric properties in non-chiral systems, by attempting to take into account the effect of ionic impurities on the internal field environment. Particularly with the present interest in spontaneous chirality in bent-core materials, methods to measure properties of non-chiral systems are of particular importance, and the challenge of dealing with ionic content is still pressing.

As will be discussed in the next chapter, the techniques developed here can be exploited

further to look more closely at the details of flexoelectric switching in Grandjean structures. Up until now, the electric field has been kept small in order to minimise non-linear effects that can occur when there are large distortions. In the next chapter, the method is developed further to look at how dielectric distortion can suppress or enhance flexoelectric switching when larger fields are applied.

Chapter 3

Enhancement of Flexoelectric Switching

3.1 Introduction

As was discussed in chapter 1 and the introduction of chapter 2, the chiral flexoelectrooptic effect has potential for use in ultra-fast display technologies. From an engineering perspective, a large rotation in the cholesteric optic axis with a minimum applied field strength is favourable, so that a maximum transmission modulation can be achieved with voltages that are within the range of what can be applied using thin-film transistor technology (≈ 10 V). As was described in §1.8.2, the flexoelectric tilt angle can be approximated by,

$$\phi_0 = \frac{e_1 - e_3}{K_1 + K_3} \frac{P}{2\pi} E \tag{3.1}$$

where e_1 and e_3 are the flexoelectric coefficients as originally defined by Meyer [8], K_1 and K_3 are the splay and bend elastic coefficients, P is the pitch of the cholesteric material, and E is the electric field component perpendicular to the helicoidal axis. Notice that this equation does not depend on either the dielectric anisotropy $\Delta\varepsilon$, or on the twist elastic coefficient K_2. In order to maximise the rotation in the cholesteric optic axis, given by ϕ_0, it can be seen from equation 3.1 that it is desirable either to increase P, or to increase the flexo-elastic ratio $(e_1 - e_3)/(K_1 + K_3)$ of the liquid crystal material. The value of P can in principle be increased arbitrarily by selecting an appropriate chiral dopant concentration, however there are other constraints on this parameter. The pitch should be as small as possible in order to minimise the switching response time, which is proportional to P^2. Another constraint on P from an engineering perspective, is that the material must be in

the ‘circular regime’ (see §1.6.3) so as to not cause unwanted Bragg or diffraction effects. Within the circular regime, the liquid crystal also exhibits optical activity, with an optical rotary power that is proportional to P^3 (see equation 1.38). Optical activity results in light leakage between crossed polarizers, and because optical rotary power is also proportional to λ^{-4}, it is difficult to compensate the rotation for all visible wavelengths. For these reasons, cholesteric materials designed for flexoelectrooptic applications tend to have a pitch less than 300 nm.

Since the pitch is limited by other engineering requirements, the usual method for increasing ϕ_0 is to develop materials with large $(e_1 - e_3)/(K_1 + K_3)$. Materials have been developed that exhibit switching angles at appropriate pitch lengths and field strengths adequate for technological applications [74, 56, 75, 76, 57]. However, these materials include bimesogens, which tend to greatly increase the viscosity and therefore increase the switching time (which is proportional to viscosity). Furthermore, as will be discussed in chapter 4, bimesogenic materials do not respond well to homeotropic alignment conditions, which may be necessary for a commercially viable method to align the uniform lying helix. Methods to enhance the switching capability without increasing the flexo-elastic ratio would therefore allow greater flexibility in material parameters such as the viscosity, allowing improvement in switching time, or would allow flexibility in additional mixture components that are conducive to ULH alignment (which is discussed in chapter 4).

This chapter is concerned with how flexoelectro-optic switching in cholesteric structures can be enhanced without using either P or $(e_1 - e_3)/(K_1 + K_3)$. The derivation of the flexoelectric tilt angle ϕ_0 given in equation 3.1, which was described in §1.8.2, made some assumptions. Firstly, it assumed that $\Delta\varepsilon$ is small, and therefore that the dielectric energy term in the free energy can be ignored. It has been known for some time that a positive dielectric anisotropy suppresses the flexoelectric switching [19], however in §3.2, this behaviour is explored further and it is shown that the dielectric coupling of the field to materials with negative dielectric anisotropy can improve the switching angle. The Grandjean rotation method, described previously in §2.3, is adapted to measure the dielectric

influence on flexoelectric switching, and the technique is applied to a chiral nematic mixture E7+3.5%R5011. The optimal liquid-crystal parameters to best exploit the dielectric enhancement in flexoelectric switching are explored numerically, and a potential enhancement of up to a degree is demonstrated.

Another assumption made in the derivation of ϕ_0 by Rudquist and others, on which the derivation in §1.8.2 is based, is that the pitch is fixed and not free to vary [50, 52]. However, there is no significant difference between the expressions for ϕ_0 that are derived under assumptions of a pitch that is fixed [50, 52] or a pitch that is free to change in order to minimise the total free energy [48], especially for small switching angles, and accommodating a pitch that is free to vary is therefore not considered here.

A final assumption that is made in the derivation of ϕ_0 is that the imposed, fixed pitch is equal to the cholesteric material's natural pitch. In many cases, this assumption is likely to be a fairly good one, however there may be situations in which this is not the case. For example, the pitch of a material is, in general, a function of temperature. If a polymer network is used to stabilise a cholesteric structure at a different temperature to when it is being switched, then the polymer network will impose a pitch that is different from the natural pitch of the liquid crystal. In §3.3, the derivation of ϕ_0 that was presented in §1.8.2 is generalised to the case where the imposed pitch may be different from the natural pitch of the cholesteric. The effect on the flexoelectric switching angle is explored theoretically, and methods to observe or exploit the effect are suggested.

Consider the total free energy, given by,

$$\begin{aligned} F(\hat{\mathbf{n}}) =& \frac{1}{2}K_1[\nabla\cdot\hat{\mathbf{n}}]^2 + \frac{1}{2}K_2[\hat{\mathbf{n}}\cdot(\nabla\times\hat{\mathbf{n}}) + q]^2 + \frac{1}{2}K_3[\hat{\mathbf{n}}\times(\nabla\times\hat{\mathbf{n}})]^2 \\ & - \frac{1}{2}\varepsilon_0\Delta\varepsilon(\hat{\mathbf{n}}\cdot\mathbf{E})^2 - \left[e_1\hat{\mathbf{n}}(\nabla\cdot\hat{\mathbf{n}}) + e_3(\nabla\times\hat{\mathbf{n}})\times\hat{\mathbf{n}}\right]\cdot\mathbf{E} \end{aligned} \tag{3.2}$$

which was first given in §1.3.4. Notice that parameters related to the dielectric and twist-elastic energy terms, $\Delta\varepsilon$ and K_2, are present in this free energy equation but are absent from the common expression of ϕ_0 given in equation 3.1. By considering scenarios in which there is an unusual twist or dielectric energy, however, we will find that these terms do affect flexoelectric tilt, contrary to what is implied by equation 3.1, which does not include

$\Delta\varepsilon$ or K_2. To summarise: in §3.2 the dielectric term in the free energy is considered, in which $\Delta\varepsilon$ is important; and in §3.3 the elastic twist energy term is considered, in which K_2 is important, and it is shown that both can potentially be used to enhance flexoelectric switching.

3.2 Using Negative Dielectric Anisotropy Liquid Crystals

Chiral flexoelectric phenomena, discussed in §1.8.1, have been interesting both from a theoretical perspective, and also for potential electro-optic applications. The recent improvement in flexo-elastic parameters in bimesogenic liquid crystals opens potential not only for the realisation of electro-optic devices that exploit the chiral flexoelectro-optic effect, including displays, but also for studying new electro-optical effects that arise due to an increased parameter space that is physically accessible. As was discussed in the introduction to this chapter, the chiral flexoelectric tilt angle, ϕ_0, is usually given by equation 3.1. While this linear, small-angle approximation is good for many situations, previous assumptions that are common in the literature on chiral flexoelectricity give rise to significant deviations from real behaviour [108]. For example, dielectric and flexoelectric distortions are not, in general, decoupled, with the result that flexoelectric tilt is non-uniform along the helicoidal axis and non-linear with respect to field strength [108, 19]. Materials designed for flexoelectric switching are usually engineered to have small dielectric anisotropy ($\Delta\varepsilon$) to avoid any reduction in flexoelectric tilt due to this coupling [76, 19]. However, negative $\Delta\varepsilon$ materials have not been considered in this context. Here, it is demonstrated numerically that negative anisotropy can lead to an enhanced electro-optic effect in some systems. A numerical simulation is used to model device behaviour, and the model is tested with E7 nematic liquid crystal. Finally, the implications of dielectrically enhanced flexoelectric switching for device applications is commented upon.

3.2.1 Effect of Dielectric Anisotropy

For materials with zero $\Delta\varepsilon$, the flexoelectric tilt angle approximately follows equation 3.1 and is linear with the applied field strength at small angles. The tilt is due to the flexoelectric torque on the director, which results from a reduction in the free energy contribution from flexoelectricity, given by,

$$f_{\text{flexoelectric}} = -(e_1\hat{\mathbf{n}}(\nabla\cdot\hat{\mathbf{n}}) + e_3(\nabla\times\hat{\mathbf{n}})\times\hat{\mathbf{n}})\cdot\mathbf{E} \tag{3.3}$$

where $\hat{\mathbf{n}}$ is the local unit-magnitude director, and $\mathbf{E}$ is a field applied perpendicular to the cholesteric helicoidal axis (see §1.3.4).

The free energy associated with the dielectric coupling to the field is given by,

$$f_{\text{dielectric}} = -\frac{1}{2}\Delta\varepsilon\varepsilon_0(\hat{\mathbf{n}}\cdot\mathbf{E})^2 \tag{3.4}$$

where ε_0 is the permittivity of free space (a derivation is provided in §1.3.1). As was described in detail in §1.7.1, in the case of a non-zero $\Delta\varepsilon$, the dielectric coupling to a field applied perpendicular to the helicoidal axis induces a distortion that causes a rotation of the director about this axis, such that the director will have an angle about the helicoidal axis given by,

$$\theta(z) = qz + \theta_0\sin(2qz) \tag{3.5}$$

where θ_0 is given by,

$$\theta_0(E) = \frac{\Delta\varepsilon\varepsilon_0}{8K_2q^2}E^2 \tag{3.6}$$

and the z-axis is the helicoidal axis (using the coordinate system given in figure 3.1).

The flexoelectric tilt and dielectric distortion in the helicoidal director structure have a negligible influence on each other at small distortion angles. This is demonstrated by the fact that both numerical methods (that take both effects into account simultaneously) and analytical methods (that assume the effects are independent) used in chapter 2 to model the electrooptic behaviour resulting from dielectric and flexoelectric distortions, produce almost identical results at small field strengths where the distortion angles are small. However, at larger distortion angles this is not the case and predictions based on an analytical

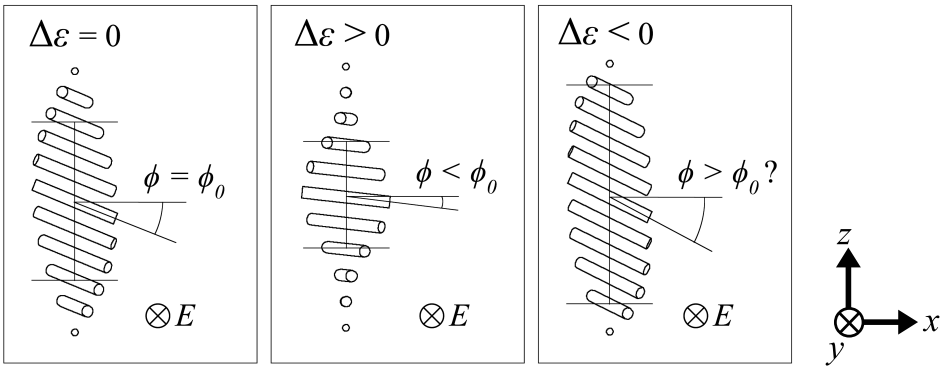

Figure 3.1: The local dielectric anisotropy couples to the field to distort the helix and alter the local effective pitch. This change in pitch in turn couples to the flexoelectric polarization, altering the flexoelectric tilt angle as illustrated. The relative effect of the dielectric distortion on the local effective pitch is illustrated by the lines in the diagram that show the distance between positions along the helicoidal axis about which the director makes an angle of 45° to the direction lateral to the field direction. A positive $\Delta\varepsilon$ reduces the local effective pitch and therefore the flexoelectric tilt angle, as is commonly observed (illustrated in the centre). A negative $\Delta\varepsilon$ material, however, increases the local effective pitch, and in some cases can enhance the tilt angle (illustrated right). Because the tilt is not uniform, the angle ϕ is defined here as the angle the director is deflected about the field direction at the point at which the director is perpendicular to the field. The distortion and tilt angles have been exaggerated for illustrative purposes.

treatment begin to deviate from real device behaviour. Therefore, a numerical approach that can allow for the dielectric, flexoelectric and elastic contributions to the free energy simultaneously, is required to examine behaviour in this regime.

To help understand how the dielectric effect influences the flexoelectric distortion, a schematic representation of a single repeating unit of a cholesteric director structure (half a pitch) is shown in figure 3.1. For materials with positive $\Delta\varepsilon$, the dielectric coupling tends to deflect the director towards being parallel with the field. Note that the pitch of the twisted region effectively becomes smaller in such a situation. From equation 3.1, we can see that for a shorter pitch, we expect a reduced flexoelectric tilt angle, and this is indeed what is observed in this region for positive $\Delta\varepsilon$ materials [108, 19]. However, for a negative $\Delta\varepsilon$ material, the director tends to deflect towards being perpendicular with the field. In this case, the pitch of the twisted region effectively becomes larger, and we may expect an increased flexoelectric tilt in this region with respect to the zero $\Delta\varepsilon$ case. The tilt also becomes non-uniform along the helicoidal axis, and for this reason, the angle ϕ is defined

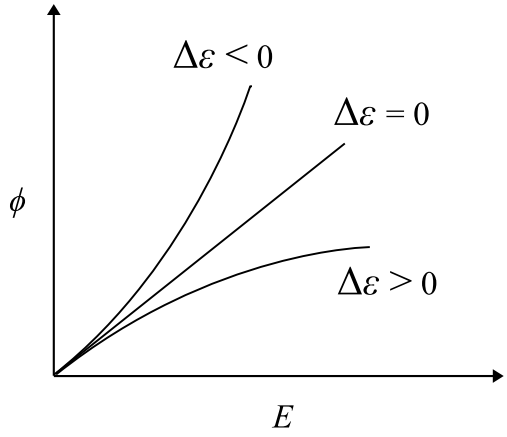

Figure 3.2: An illustration of ϕ as a function of the electric field for cases where the dielectric anisotropy, $\Delta\varepsilon$, is either positive, zero, or negative. In the negative $\Delta\varepsilon$ case, there may be an enhancement of ϕ relative to the zero $\Delta\varepsilon$ case.

here as the angle the director is deflected about the field direction at the point at which the director is perpendicular to the field (see figure 3.1).

Additionally, whereas the flexoelectric coupling and associated distortion is proportional to E (see equation 3.1) the dielectric interaction depends on E^2 (equation 3.4). Therefore the dielectric distortion of the structure and its influence on ϕ is non-linear, and is therefore expected to introduce a non-linear term in $\phi(E)$. The situation is illustrated in figure 3.2. For $\Delta\varepsilon = 0$, $\phi(E)$ is linear. For positive $\Delta\varepsilon$ the dielectric interaction reduces ϕ below this level as the field increases, and for negative $\Delta\varepsilon$ we might expect an increase in ϕ as the field increases (although at larger fields it will still saturate). This potential tilt enhancement could have useful implications for device applications.

3.2.2 Measuring the Dielectric Effect on Flexoelectric Tilt

In order to probe this behaviour experimentally, the incident angle dependent electro-optic behaviour of Grandjean cholesteric structures is studied under the application of a driving field of the form,

$$E = E_0 \sin(2\pi f t) \tag{3.7}$$

where E_0 is the field amplitude and f is the field frequency. The approach was described in the last chapter (§2.3) where it was used to determine both out-of-plane linear flexoelectric

and in-plane quadratic dielectric electrically induced distortions. In the last chapter, it was emphasised that the field applied be sufficiently small in order for the linear and quadratic distortion effects to be decoupled. However, as is illustrated in figure 3.2, it is expected that as the field increases, dielectric distortions can influence ϕ. The curvature in ϕ as a function of applied field has a cubic-like functional form, and can be probed by considering the 3$^{\mathrm{rd}}$ harmonic, which is sensitive to such non-linearities in the transmission as a function of voltage, in a similar way that the linear and quadratic behaviour can be probed by considering the 1$^{\mathrm{st}}$ and 2$^{\mathrm{nd}}$ harmonics, as was described in chapter 2 (§2.3.5). A simulation of the 3$^{\mathrm{rd}}$ harmonic as a function of incident angle is shown in figure 3.3. Here, a numerical routine is used to determine the director structure under field application, and then a standard anisotropic optical modelling routine is used to extract the amplitude of the transmission at static field strengths of $E = E_0$ and $E = E_0/2$, where $E_0 = 0.3$ Vμm^{-1}. The 3$^{\mathrm{rd}}$ harmonic in the transmission relative to the driving frequency can then be approximated by using a central-finite-difference method to calculate the third differential, such that,

$$T'''(E_0) \approx \frac{1}{6}\left(-2T_{(E=E_0/2)} + T_{(E=E_0)} - T_{(E=-E_0)} + 2T_{(E=-E_0/2)}\right) \tag{3.8}$$

The 3$^{\mathrm{rd}}$ harmonic is given as a function of angle of incidence to increase the sensitivity with respect to experimental measurements, by providing a larger set of data. The results of numerical simulations in figure 3.3 show that when $\Delta\varepsilon = 0$, the third harmonic is negligible due to the near-linear relationship between ϕ and E. However, third harmonic is present when $\Delta\varepsilon \neq 0$, and as might be expected from the schematic illustrations in figures 3.1 and 3.2, its sign depends on the sign of $\Delta\varepsilon$. This shows that in this field regime $\Delta\varepsilon$ suppresses and enhances ϕ as expected.

Following the method discussed in detail in §2.3, figure 3.4 shows experimental transmission and 1$^{\mathrm{st}}$, 2$^{\mathrm{nd}}$ and 3$^{\mathrm{rd}}$ harmonic transmission amplitudes as a function of angle of incidence for a device filled with E7+3.5%R5011 chiral nematic liquid crystal (the same device was used in §2.3, and a description of the preparation of the device can be found in §2.3.1). A frequency of 1013 Hz is used to drive the liquid crystal. This frequency is large enough for the effects of ions on the field to be negligable (as discussed in §2.1.2). The ex-

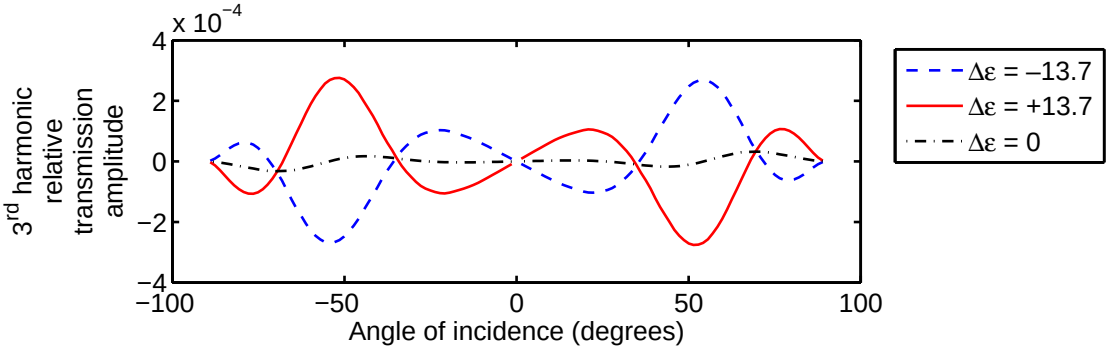

Figure 3.3: A numerical simulation of the 3rd Harmonic transmission amplitude as a function of the angle of incidence onto a cell, for a field of amplitude 0.3 Vμm^{-1}. The red line simulates the expected parameters for E7, while the blue line simulates the same parameters except for an inversion of $\Delta\varepsilon$ from positive to negative. The black line is for zero $\Delta\varepsilon$. The third harmonic is very sensitive to curvature in the transmission as a function of field strength, and so is a useful experimental tool for observing the dielectric influence on chiral flexoelectric switching.

Table 3.1: Fitting parameters used in the numerical simulation shown in figure 3.4. The simulated transmission is sensitive to small changes in these parameters, and so 3 significant figures have been given for these cases. However, this is not representative of the precision of measurements of these parameters, for which only the first two figures are significant.

Δnd (μm)	$\frac{\Delta\varepsilon\varepsilon_0}{K_2}$(FN^{-1}m^{-1})	$\frac{e_1-e_3}{K_1+K_3}$ (CN^{-1}m^{-1})	E (Vμm^{-1}	Pitch P (nm)
1.93	18.6	0.472	0.28	254

perimental harmonic amplitudes have been multiplied by factors that take into account the finite switching time of the liquid crystal, which is calculated using equation 2.12 in §2.3.4 of chapter 2. A numerical fit is shown for each harmonic, from which key liquid crystal parameters are determined through their use as fitting parameters. The transmission is used to determine the product of the material's optical birefringence and device thickness, Δnd. The 1st Harmonic is used to measure the flexo-elastic parameter $(e_1 - e_3)/(K_1 + K_3)$ and the 2nd Harmonic can be used to measure the dielectro-elastic parameter $\Delta\varepsilon\varepsilon_0/K_2$. Table 6.1 shows the parameters used in the simulation. The 3rd Harmonic does not require further fitting, but shows that the dielectric distortion is contributing to a non-linearity in ϕ exactly as expected.

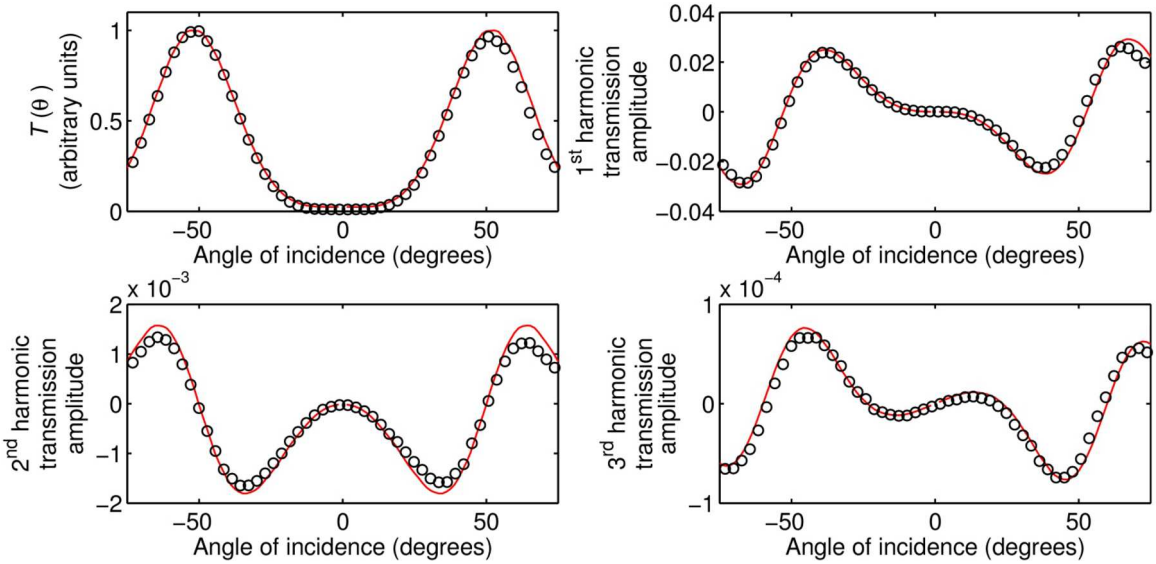

Figure 3.4: Transmission and 1st, 2nd and 3rd harmonic transmission amplitudes relative to a driving frequency of 1013 Hz, as a function of angle of incidence for E7+3.5%R5011 cholesteric mixture. The transmission is used to measure Δnd, and the 1st harmonic to measure the flexo-elastic parameter $(e_1 - e_3)/(K_1 + K_3)$. The 2nd harmonic is sensitive to the dielectro-elastic parameter related to the in-plane distortion due to the dielectric effect, $\Delta\varepsilon\varepsilon_0/K_2$. Once these parameters have been determined, the 3rd harmonic requires no further fitting, but shows that the dielectric distortion is contributing to a non-linearity in ϕ.

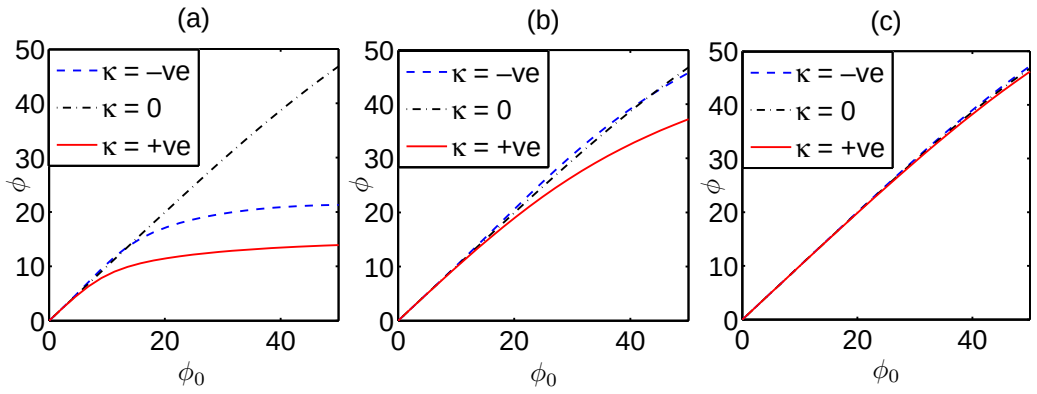

Figure 3.5: A numerical simulation of ϕ (in degrees) against the Patel and Meyer linear approximation of the flexoelectric tilt angle given in equation 3.1 (in degrees). The three plots show the behaviour for different magnitudes of the control parameter κ, for positive and negative cases. The $\kappa = 0$ case is also shown. (a) $|\kappa| = \kappa_{\mathrm{E7}} = 10.5$, (b) $|\kappa| = 1.05$, (c) $|\kappa| = 0.105$. The plots illustrate the influence of the dielectric anisotropy on ϕ. In cases where κ is negative, there is some enhancement of ϕ at some angles.

3.2.3 Maximising Director Tilt Enhancement

While the experimental data show that the case for E7+3.5%R5011 is well represented by the theory, it is important to investigate the negative $\Delta\varepsilon$ regime to explore the behaviour of any enhancement in the flexoelectric tilt. In order to do this, it will be useful to consider a dimensionless control parameter that describes the relative flexoelectric and dielectric distortions in a cholesteric liquid crystal. By combining equations 3.1 and 3.5, we can express a dimensionless dielectric- to flexoelectric-distortion ratio

$$\kappa = \frac{\theta_0}{\phi_0^2} = \frac{\Delta\varepsilon\varepsilon_0(K_1 + K_3)^2}{8K_2(e_1 - e_3)^2} \tag{3.9}$$

which gives the relative strength of the dielectric and flexoelectric distortions in a particular liquid crystal material.

Figure 3.5 shows results from a numerical simulation of ϕ (as defined in figure 3.1) against the Patel and Meyer linear approximation for the flexoelectric tilt angle, ϕ_0, given in equation 3.1, for three different values of κ. In figure 3.5 (a), κ is evaluated for the parameters of E7, and ϕ is determined numerically and shown as the solid red line. The dot-dashed black line corresponds to $\kappa = 0$, and the dashed blue line corresponds to $\kappa = -\kappa_{\mathrm{E7}}$. Note in figure 3.5 (a), that while a material with $\kappa = 0$ follows closely the linear relation given by the Patel and Meyer approximation, the dielectric distortion reduces the maximum tilt angle drastically for E7-like materials. Interestingly, a material with a negative value of κ of the same magnitude as E7 does indeed show a slight enhancement relative to when $\kappa = 0$ for tilt angles up to $\approx$ 10 degrees. However, the tilt angle is still reduced relative to when $\kappa = 0$ at larger angles. Figure 3.5 (c) shows a numerical simulation for where κ is evaluated with parameters associated with bimesogen materials, whose properties have been engineered for flexoelectric switching. These materials have very small $\Delta\varepsilon$ and hence a small κ compared with E7. There is only a small perturbation from the $\kappa = 0$ case. Figure 3.5 (b) illustrates an intermediate value of $|\kappa|$. In this intermediate case, there is a notable enhancement in the case that κ is negative, showing an enhancement of up to a degree at approximately 25 degrees.

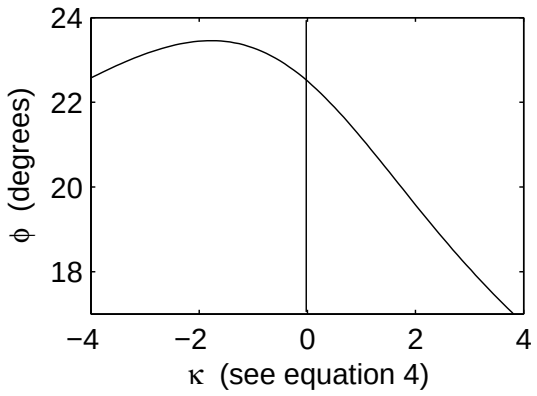

Figure 3.6: A numerical simulation of ϕ in the case where $\phi_0 = 22.5$ degrees, against the control parameter κ. For positive κ, the dielectric distortion always reduces ϕ relative to the $\kappa = 0$ case. However, a negative κ can enhance ϕ up to a degree. A further increase in the magnitude of a negative κ reduces ϕ. This means there is an optimal value of κ at which the tilt angle is maximised.

To explore the optimal value of κ, figure 3.6 shows ϕ as a function of κ, for the test case where the tilt angle at $\kappa = 0$ is 22.5 degrees. For positive κ, the tilt angle is reduced relative to the $\kappa = 0$ case. However, we see that for negative κ, the tilt angle can be enhanced by approximately a degree. A further increase in the magnitude of a negative κ, however, leads to a reduction in ϕ, with the result that there is a maximum enhancement possible for a given desired tilt angle.

3.2.4 Conclusion and Discussion

It has been shown that the dielectric distortion in cholesteric liquid crystals influences the magnitude of the flexoelectric tilt at the point where the director is perpendicular to the field. In particular, a negative dielectric anisotropy, $\Delta\varepsilon$, can in some situations enhance the flexoelectric tilt at this point. For example, a material with $\Delta\varepsilon = -3.3$, $K_1 + K_3 = 29.7$ pN, $K_2 = 6.0$ pN and $e_1 - e_3 = 18$ pCm^{-1} would result in $\kappa = -1.77$, and this would lead to an enhancement of 1 degree at $\phi_0 = 22.5$ degrees relative to a material with zero $\Delta\varepsilon$. This is a small difference, and so it is unlikely that it would be a major consideration when engineering materials for optimal flexoelectro-optic switching.

A usual concern when using negative $\Delta\varepsilon$ materials, is that they have a tendency to orient with the helicoidal axis parallel to the field to minimise the dielectric energy given in

equation 3.4, as has been described in §1.7.2. However, as will be described in detail in chapters 4 (§4.3.1) and 5 (§5.2.1), flexoelectric polarization can contribute to the dielectric permittivity perpendicular to the helicoidal axis, and will allow this component of the permittivity to be greater than the component parallel to the helicoidal axis if the liquid crystal parameters satisfy the condition,

$$\frac{\varepsilon_{\parallel}+\varepsilon_{\perp}}{2} < \varepsilon_{\perp} < \frac{\varepsilon_{\parallel}+\varepsilon_{\perp}}{2} + \frac{1}{\varepsilon_0}\left(\frac{(e_1-e_3)^2}{2(K_1+K_3)}\right) \tag{3.10}$$

In this case, the applied field will not reorient the negative $\Delta\varepsilon$ cholesteric material, and some enhancement of the flexoelectric switching is potentially possible.

In the next section, the effect of helix constraint on flexoelectric tilt is examined.

3.3 Using Constraint of the Cholesteric Pitch

In the last section, the effect of dielectric distortion on flexoelectric switching of cholesteric liquid crystals was explored. It was suggested that in the case of a negative dielectric anisotropy, the dielectric effect causes an increase in the local effective pitch, which in turn can enhance the flexoelectric switching angle by up to a degree in some situations. Because this enhancement is only small, it is unlikely to become an important engineering consideration. In this section, a completely different approach is taken. The influence on the flexoelectric switching of imposing a pitch on a cholesteric material other than its natural pitch is explored. First, the derivation of the flexoelectric tilt, ϕ_0, that was presented in §1.8.2 is generalised for the case in which the natural chirality, $q = 2\pi/P$, is different from a 'constrained' chirality, defined as, $q_{\mathrm{c}} = 2\pi/P_{\mathrm{imposed}}$, where P_{imposed} is the imposed pitch. It is found that for a given imposed pitch, a material with a longer natural pitch will result in a significantly larger tilt angle, calculated to be up to a factor of 2.3 for parameters corresponding to a bimesogenic liquid crystal. Suggestions are given as to how the effect may be measured and exploited.

3.3.1 Generalising ϕ_0 to Cases Where $q \neq q_c$

Adapting the derivation by Rudquist [51, 52] (c.f. the derivation given in §1.8.2), the director of a constrained helicoid, where the imposed pitch, P_{imposed}, is in general not equal to the natural pitch of the cholesteric material, with its helicoidal axis parallel to the z-axis, can be described by,

$$\hat{\mathbf{n}} = \begin{bmatrix} n_x \\ n_y \\ n_z \end{bmatrix} = \begin{bmatrix} \cos q_c z \cos\phi \\ \sin q_c z \\ -\cos q_c z \sin\phi \end{bmatrix} \tag{3.11}$$

where q_c is the constrained chirality, given by $q_c = 2\pi/P_{\text{imposed}}$, and ϕ is the angle of the director tilt about the y-axis (see figure 1.14 in chapter 1 for an illustration of the director and coordinate system). By using these components of $\hat{\mathbf{n}}$ in the free energy expression given in equation 3.2, and omitting the dielectric energy term, we get,

$$\begin{aligned} F =& \frac{1}{2}K_1 q_c^2 \sin^2 q_c z \sin^2\phi + \frac{1}{2}K_2(q - q_c\cos\phi)^2 + \frac{1}{2}K_3(q_c^2\cos^2 q_c z \sin^2\phi) \\ & - E(e_1 q_c \sin^2 q_c z \sin\phi - e_3 \cos^2 q_c z \sin\phi) \end{aligned} \tag{3.12}$$

Since we want to know the tilt angle ϕ when the total free energy of the whole system is minimum, we average over a whole number of pitches using the fact that,

$$\langle \sin^2 q_c z \rangle = \langle \cos^2 q_c z \rangle = \frac{1}{2} \tag{3.13}$$

and so the average volume energy density is,

$$\langle F \rangle = \frac{1}{4}(K_1 + K_3) q_c^2 \sin^2\phi + \frac{1}{2}K_2(q - q_c\cos\phi)^2 - \frac{1}{2}(e_1 - e_3)E q_c \sin\phi \tag{3.14}$$

In order to determine the value of ϕ that minimises the total energy (assuming a fixed q), we take the differential and minimise by setting equal to zero,

$$\frac{\partial\langle F\rangle}{\partial\phi} = \frac{1}{2}(K_1 - 2K_2 + K_3) q_c^2 \sin\phi\cos\phi + K_2 q q_c \sin\phi - \frac{1}{2}(e_1 - e_3)E q_c \cos\phi = 0 \tag{3.15}$$

which can be rearranged for $\tan\phi$,

$$\tan\phi = \frac{e_1 - e_3}{2K_2 q}E - \frac{(K_1 - 2K_2 + K_3)q_c}{2K_2 q}\sin\phi \tag{3.16}$$

Finally, for small angles we can make the approximation that $\tan\phi \approx \sin\phi \approx \phi$, and simplify the expression for the tilt angle,

$$\left(\frac{q}{q_c} - \frac{K_1 + K_3}{2K_2} + 1\right)\phi = \frac{(e_1 - e_3)E}{2K_2 q} \tag{3.17}$$

which can be written,

$$\phi_0(E) = \frac{e_1 - e_3}{K_1 + K_3}\frac{E}{q} \cdot \left\{1 + \frac{2K_2}{K_1 + K_3}\left(\frac{q}{q_c} - 1\right)\right\}^{-1} \tag{3.18}$$

which gives the flexoelectric tilt angle in the case that the natural and imposed pitches are not the same. This result has been previously derived by Parry-Jones [109, 110]. When $q_c = q$, we see that equation 3.18 will simplify back to the previous result for ϕ_0 from equation 3.1. Hence, we find that the tilt angle is expected to differ from the unconstrained case by a factor that is independent of E, which is given by the expression in the curly brackets in equation 3.18.

3.3.2 The Influence of Pitch Constraint and Different Elastic Parameters

It is interesting to look at the behaviour one might expect from equation 3.18. Figure 3.7(a) shows ϕ_0 as a function of the applied field strength, according to equation 3.18, in the case where parameters are those corresponding to E7, where $(e_1 - e_3)/(K_1 + K_3) = 0.46$ CN^{-1}m^{-1} (based on the measured value from chapter 2, §2.2) and $(2K_2)/(K_1 + K_3) = 0.48$ (based on values provided by the material supplier, Merck), for different values of the ratio q/q_c, at an imposed pitch of 250 nm. For comparison, 3.7(b) also shows $\phi_0(E)$, but using parameters corresponding to a bimesogenic material where $(e_1 - e_3)/(K_1 + K_3) = 1.1$ CN^{-1}m^{-1} (based on a measurement by Castles [111] of a bimesogenic material used in chapter 6), and $(2K_2)/(K_1 + K_3) = 0.56$ (based on a measurement of $(K_1 + K_3)$ in chapter 6 and a value of K_2 from the literature), also for an imposed pitch of 250 nm. The figures show that there is a significant increase in ϕ_0 when $q/q_c < 1$. In the case that $q/q_c = 0$, there is a factor of 1.9 enhancement in ϕ_0 compared with the $q/q_c = 1$ case for E7 parameters, and a factor of 2.3 enhancement for parameters corresponding to the bimesogenic material used in chapter 6.

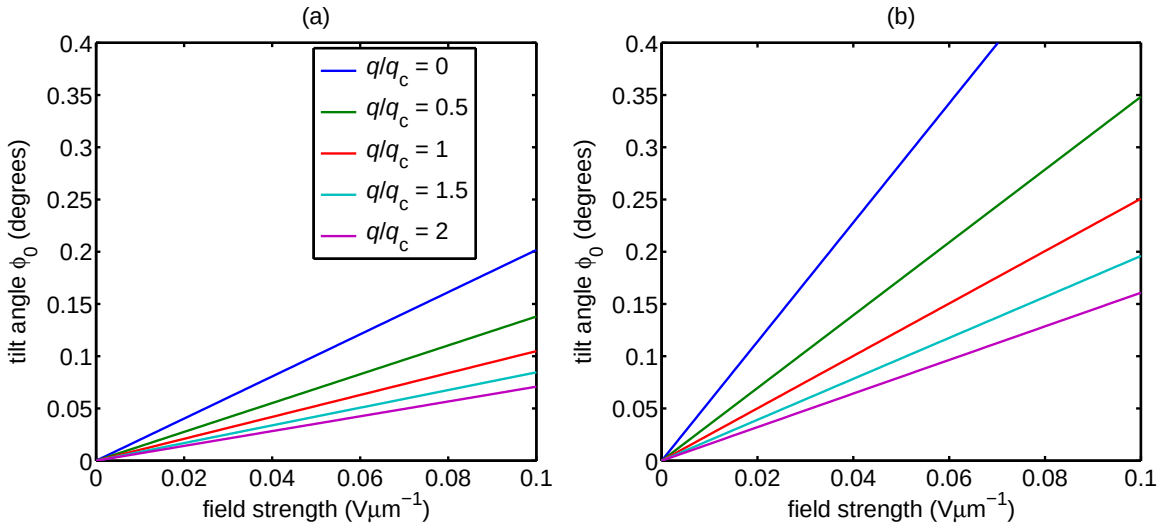

Figure 3.7: The flexoelectric tilt angle of the director in a cholesteric liquid crystal is shown as a function of the strength of a field applied perpendicular to the helicoidal axis, in cases where the natural cholesteric pitch is unequal to the imposed pitch, based on the analytically derived equation 3.18, where the imposed pitch is 250 nm, for cases where parameters correspond to those of (a) nematic E7 and (b) a bimesogenic material also used in chapter 6. There is a significant enhancement of the tilt angle as a function of applied field strength in the cases where the natural pitch is significantly longer than the imposed pitch, and the sensitivity of ϕ_0 to the ratio q/q_c is dependent upon the ratio $(2K_2)/(K_1 + K_3)$, which is further illustrated in figure 3.8.

The difference in the factors corresponding to E7 and the bimesogenic material are due to the sensitivity of ϕ_0 to the ratio $(2K_2)/(K_1 + K_3)$. Figure 3.8 shows ϕ_0 against the ratio q/q_c under the application of a constant field of 0.1 Vμm^{-1}, for different values of the ratio $(2K_2)/(K_1 + K_3)$. When $q/q_c = 1$, then the system is insensitive to differences in $(2K_2)/(K_1 + K_3)$, however, it can be seen in figure 3.8 that for values of q/q_c towards zero, the ratio $(2K_2)/(K_1 + K_3)$ has a larger influence on ϕ_0. Therefore, if we are to use pitch constraint in order to enhance the flexoelectric switching angle, then it is best to use materials with large K_2 and small $K_1 + K_3$, as can also be seen from equation 3.18.

To think intuitively about this result, we can imagine that as the director of the cholesteric tilts due to flexoelectricity, the pitch of the twist of the structure becomes longer such that,

$$P_{\text{twist}} = \frac{P_{\text{imposed}}}{\cos\phi} \tag{3.19}$$

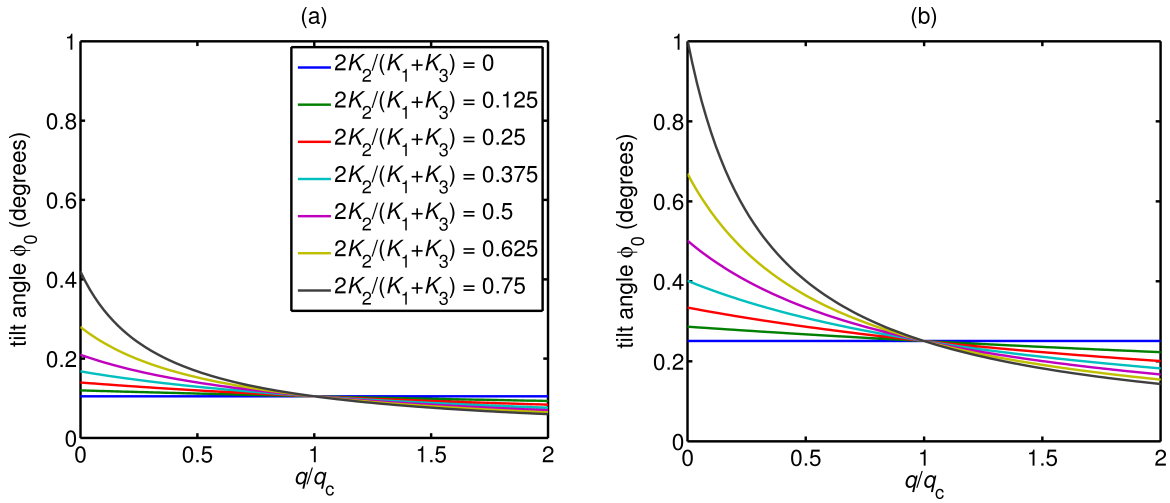

Figure 3.8: The flexoelectric tilt angle of the director in a cholesteric liquid crystal is shown for a fixed field strength of 0.1 Vμm^{-1}, as a function of the ratio of q/q_c, for a range of values of the elastic ratio $(2K_2)/(K_1 + K_3)$, for the case where the value of the flexoelastic parameter is given by (a) 0.46 CN^{-1}m^{-1} (corresponding to that of E7) and (b) 1.1 CN^{-1}m^{-1} (corresponding to that of a bimesogenic material also used in chapter 6.) Note that $(2K_2)/(K_1 + K_3)$ for E7 is 0.48 and for the bimesogen material is approximately 0.56, although a range of values are shown to illustrate the general behaviour. These plots show that in order to maximise the enhancement in the flexoelectric switching due to pitch constraint, then it is favourable to have a large K_2 relative to $K_1 + K_3$.

and the pitch of the bend-splay pattern gets shorter such that

$$P_{\text{bend-splay}} = \frac{P_{\text{imposed}}}{\sin\phi} \tag{3.20}$$

as illustrated in figure 3.9. Since $e_1 - e_3$ couples to bend-splay, the free energy due to flexoelectricity is minimised when $P_{\text{bend-splay}}$ is minimised, and hence when ϕ_0 is maximised. In contrast, the bend and splay elastic energy are minimised when $P_{\text{bend-splay}}$ is maximised, and hence when ϕ_0 is maximised. Ignoring for a moment the twist elastic free energy, referring to the free energy given in equation 3.2, for small angles, the flexoelectric free energy (the last two terms in the free energy) goes down linearly with increasing ϕ_0, while the bend-splay combined elastic energy (the first and third term) goes up quadratically with ϕ_0. Hence, in the absence of a twist energy term, at some value of ϕ_0, the flexoelectric and bend-splay elastic energy is balanced, and an equilibrium ϕ_0 is reached. The bend-splay elastic energy is reduced if $K_1 + K_3$ is reduced, therefore, a larger equilibrium ϕ_0 occurs if $K_1 + K_3$ is small.

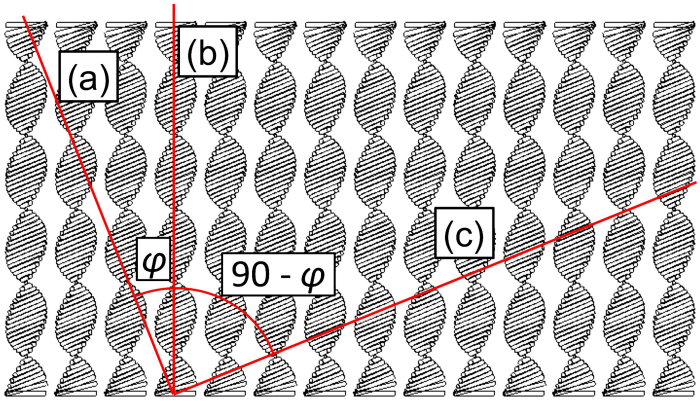

Figure 3.9: An illustration of a cholesteric structure with a uniform tilt ϕ in the director. (a) The axis normal to the director, and along which there is a twist in the director. The pitch of the twist is approximated by equation 3.19. (b) The helicoidal axis of the structure, which is defined as the axis normal to planes of uniform director. The planes of uniform director have a periodicity along the helicoidal axis with a characteristic pitch, P_{imposed}. (c) This line is a cross section of a plane of pure bend-splay in the director. The bend-splay director pattern has a periodicity along this axis approximated by equation 3.20.

In addition to this, the twist elastic energy also depends on ϕ_0. The twist energy is minimised when $P_{\text{twist}} = P$, i.e., when the twist in the structure is equal to the natural pitch. If the system is constrained such that the imposed pitch is shorter than the natural pitch, the twist energy can decrease as ϕ_0 increases. A larger value of K_2 will increase the free energy associated with a difference between P and P_{twist}, and hence, a larger K_2 will provide a larger enhancement in cases where $q/q_{\text{c}} < 1$.

In the case that the factor in curly brackets in equation 3.18 is zero, then the cholesteric structure without a field applied becomes unstable. For the cholesteric to remain stable, the parameters must satisfy the condition that,

$$\left\{1 + \frac{2K_2}{K_1 + K_3}\left(\frac{q}{q_{\text{c}}} - 1\right)\right\} > 0 \tag{3.21}$$

and we can rearrange this to write,

$$K_1 + K_3 > \left(1 - \frac{q}{q_{\text{c}}}\right) 2K_2 \tag{3.22}$$

If this condition is not met, then the reduction in twist elastic energy from increasing ϕ, is greater than the cost in bend-splay elastic energy, and a structure that is pure bend-splay is lower in energy than the twisted structure[1]. The twisted structure is therefore unstable.

[1]A similar threshold between bend-splay and twist structures has been considered in the pi-cell in order to

It should be noted that liquid crystal materials generally satisfy this inequality. In order to maximise the enhancement due to the helix constraint, the ratio $\frac{2K_2}{K_1+K_3}$ should be as large as possible, but still satisfy the inequality in equation 3.22.

3.3.3 The Use of Polymer Networks for Pitch Constraint

Of course, one may ask how realistic a scenario in which $q/q_c = 0$ is. In a recent paper [113], a polymer network was produced in a highly chiral system in which the remaining liquid crystal was removed using a solvent and then replaced with a non-chiral liquid crystal. The non-chiral liquid crystal was found to 'template' the structure of the polymer network, that is, to form the same structure and periodicity as the polymer network, whose structure had been taken from the chiral liquid crystal material. Hence, in this situation, the condition $q/q_c = 0$ was indeed realised, albeit in a blue phase rather than a cholesteric geometry. It would be interesting to repeat a similar process using a ULH device, such that one could observe the effect of the templated liquid crystal's natural pitch on the resultant flexoelectric switching characteristics.

It is known that polymer networks tend to reduce the flexoelectric switching angle in cholesteric materials [114, 115]. It is not known at present exactly how the polymer network will influence the elastic properties of the liquid crystal. It may be that in order to stabilise and impose a pitch that is significantly different from the natural pitch of the liquid crystal, a concentration of polymer network would be required that would be so large as to prohibitively reduce the flexoelectric switching capability. Without further experiments, or accommodating the influence of the network into the theory, it remains an open question for further work.

measure K_2 by Brimicombe [112]. The pi cell can be considered as a system in which the pitch is constrained due to the surface alignment condition. Since liquid crystals usually have a larger combination $K_1 + K_3$ than $2K_2$, then a twist state in a pi cell is lower in energy than a bend-splay state. However, there is a threshold at which a voltage applied parallel to the helicoidal axis will change the lowest energy state to the bend-splay state, due to the dielectric coupling. A combination of this threshold effect and the flexoelectric effect used in polymer stabilised cholesteric structures could potentially be used to create a unique electrooptic technology.

3.3.4 Summary and Discussion

In this section, the derivation of tilt in the director of a cholesteric under the application of a field applied perpendicular to the helicoidal axis has been generalised to the case where the pitch may be constrained to be other than the natural pitch. The result of the derivation suggests that there is a significant enhancement of up to a factor of 2.3 in the tilt angle as a function of applied field strength in cases where the natural pitch is significantly longer than the imposed pitch. The sensitivity of ϕ_0 to the ratio q/q_c is dependent upon the ratio $(2K_2)/(K_1 + K_3)$. In order to maximise the enhancement due to the constraint effect, a large ratio $(2K_2)/(K_1 + K_3)$ is favourable. These results should be taken with caution, however, as in order to produce a strong constraint condition, a polymer network may be required, whose additional influence on the switching angle has not been considered.

A constraint condition in which $q/q_c = 0$ has been demonstrated in blue phases via the use of polymer networks [113]. In chapter 6, the effect of flexoelectric switching in blue phase systems with no polymer networks is investigated. It is found in that chapter that flexoelectricity contributes to Kerr switching in blue phases. Enhancement of flexoelectric switching in templated blue phase systems in which $q/q_c = 0$ may therefore also be interesting to investigate in a further study.

3.4 Conclusion

In this chapter, the dielectric and twist-elastic energy terms in the free energy equation (equation 3.2) have been considered in the context of enhancing the flexoelectric switching of cholesteric liquid crystals. In §3.2, the effect of dielectric distortions on the flexoelectric tilt angle in the director was investigated, and it was found numerically that although a positive dielectric anisotropy always reduces the flexoelectric tilt, the tilt can be enhanced by up to a degree in some situations in which a negative dielectric anisotropy material is used. A technique for observing the coupling of dielectric and flexoelectric effects in cholesteric liquid crystals based on electrooptic measurements of Grandjean structures was developed and a numerical simulation of the liquid crystal electrooptic behaviour was shown to be

consistent with experimental electrooptic behaviour of chiral-doped E7 liquid crystal, in which a positive dielectric anisotropy reduces the flexoelectric tilt angle. The enhancement possible by using the dielectric coupling to the tilt angle is not large enough to be a serious consideration for technological application.

In §3.3, the derivation of the flexoelectric tilt in a cholesteric under the application of a field perpendicular to the helicoidal axis was generalised to cases where the natural pitch and imposed pitch are not equal. Such cases can exist where there is a polymer network formed with a pitch that is different from the liquid crystal pitch. It was found that theoretically a significant enhancement of the flexoelectric tilt could be achieved by imposing a pitch significantly shorter than the natural pitch of the liquid crystal. The sensitivity of the enhancement in the tilt with respect to such pitch constraint is strongly dependent on the ratio of twist and splay-bend elastic constants, $(2K_2)/(K_1 + K_3)$. In order to produce the greatest enhancement, this ratio should be maximised. However, a question remains as to the effect of a polymer network on the switching, as it is known that polymer networks reduce the flexoelectric switching angles in cholesteric liquid crystals [114, 115], and this effect has not been taken into account in the analysis.

While in this chapter, enhancement of chiral flexoelectric switching has been investigated, in the next chapter, a different aspect of chiral flexoelectric technology will be addressed: Uniform Lying Helix (ULH) alignment. The ULH is the most heavily researched potential method for exploiting the chiral flexoelectrooptic effect in display applications, but development is hindered because of the difficulty in forming, and making stable, ideal ULH structures. Chapter 4 will discuss the key problems, previous work on the subject, and the development of a series of new approaches to ULH alignment.

Chapter 4

Uniform Lying Helix Alignment

4.1 Introduction

As we saw in chapter 1, flexoelectric polarisation induces a tilt in the director about an electric field applied perpendicular to a cholesteric liquid crystal helicoidal axis. If the pitch is much less than the wavelength of light, then the liquid crystal acts as a uniaxial wave plate, whose optic axis orientation can be controlled with a field transverse to the film via a flexoelectrically induced rotation of the director. Since its conception, this high-speed, linear and in-plane electrooptic effect has elicited a great deal of research interest, especially when exploited in the Uniform Lying Helix (ULH) geometry [58, 116, 19, 117, 108], which was introduced in §1.8.4.

As noted earlier, the development of materials optimised for the flexoelectric effect mean that rotation angles of $\pm 22.5^{\circ}$ (and in some cases $\pm 45^{\circ}$[73]) can be readily obtained with switching times typically of microseconds [74, 56, 75, 76, 57]. This development would allow the possibility of large area, wide-viewing-angle, grey-scale, field-sequential colour, video rate and glasses-free multi-user time-multiplexed autostereoscopic 3D display technologies, however most methods for ULH alignment do not produce an adequate alignment quality, and new insights into this problem are in great need [54, 53, 118, 119, 120, 42, 121, 122]. The alignment quality has a direct impact on the blackest state of the liquid crystal between crossed polarizers, which is critical to a device's optical contrast between bright and dark states. Improvements to ULH alignment techniques are therefore of critical importance.

This chapter is therefore concerned with the key challenge of ULH alignment. Some important issues are discussed first, and how the ULH can be made stable with homeotropic surface alignment conditions is described. Previous methods for ULH alignment are reviewed, and inform a series of new approaches to ULH formation that produce stable ULH textures without any polymer stabilisation, which will be described in the rest of the chapter. The first method utilises periodic boundary conditions to uniformly align weakly-chiral nematic liquid crystal textures in §4.2. The use of in-plane switching fields is then commented upon in §4.3. In §4.4, a combination of homeotropic surface alignment and unidirectional nano-grooves made by a relatively simple and low-cost process is adopted. Finally, in §4.5 micron-scale channels are created using a replica-moulding technique, and shown experimentally and theoretically to promote a high quality ULH alignment with the helicoidal axis oriented parallel to the channels.

4.1.1 Surface Energy

Different alignment conditions can promote different alignments of cholesteric liquid crystals within devices (see figure 1.10 in §1.6.3). In devices with planar surface anchoring, the Grandjean texture, in which the helicoidal axis is perpendicular to the confining surfaces, is the most stable and lowest energy state. Planar anchoring was, for example, adopted in §2.3 to promote a Grandjean structure. The Grandjean structure is the lowest in energy because the director is uniformly in the plane of the liquid crystal cell, and can meet the planar alignment condition while remaining undistorted (assuming the cell thickness is an integer number of half-pitch lengths). The director of the ULH structure, however, is not uniformly in the plane of the cell, and distortion and/or defect lines occur near the surfaces due to the planar surface anchoring condition, resulting in a larger free energy density [123]. As a result, alignment of ULH structures on planar surfaces is not stable and quickly reverts back to a Grandjean alignment, which reduces the free energy.

In the case of homeotropic anchoring however, the situation is less clear. Homeotropic anchoring is not compatible with either Grandjean or ULH alignments, and so in both cases

elastic distortion and an increase in free energy density will occur. The total free energy per unit area is given by,

$$W_{\text{total}} = W_{\text{surface}} + W_{\text{bulk}} + W_{\text{defects}} \tag{4.1}$$

where W_{bulk} is the bulk energy per unit area, W_{defects} is the defect energy per unit area, and W_{surface} is the surface energy per unit area, where,

$$W_{\text{surface}} = \frac{W_0}{2}\left(1 - (\hat{\mathbf{n}} \cdot \hat{\mathbf{s}})^2\right) \tag{4.2}$$

where W_0 is the surface anchoring strength, $\hat{\mathbf{n}}$ is the unit magnitude director, and $\hat{\mathbf{s}}$ is a unit vector normal to the surface (see §1.2.2). In the limit of very weak homeotropic anchoring, there are no defects or elastic distortions due to interaction with the surface, and hence $W_{\text{bulk}} = W_{\text{defects}} = 0$ and $W_{\text{total}} = W_{\text{surface}}$. Furthermore, for the planar Grandjean geometry in this situation, $W_{\text{total}} = W_0/2$, because at all positions $\hat{\mathbf{n}} \cdot \hat{\mathbf{s}} = 0$. On the other hand, W_{surface} for the ULH is $W_0/4$, because in some places along the helix, the director is homeotropic and therefore compatible with the homeotropic condition. Hence, in the limit of weak homeotropic anchoring the ULH is lower in energy than the Grandjean geometry. In fact, for weak anchoring, the total free energy of the Grandjean increases at twice the rate with respect to W_0 as the ULH. Importantly, this means that the ULH can be made stable by employing weak homeotropic anchoring. Experimentally, it is well known that weak homeotropic anchoring tends to promote the finger-print or ULH textures in cholesteric materials [124, 125], and this effect is illustrated in figure 4.1.

Stronger surface anchoring causes director distortions and an associated elastic free energy cost, in both the cases of ULH and Grandjean geometries. In the limit of strong anchoring, the Grandjean will saturate when the defect-free director field is completely homeotropic at the surface interface. The ULH, however, is not directly topologically compatible with uniform homeotropic alignment, and in the limit of strong homeotropic anchoring defect lines form, which further contribute to the energy of the system, at which point the director in the ULH can also be completely homeotropic at the surface interface. Both the ULH and Grandjean structures on homeotropic alignment involve considerable elastic

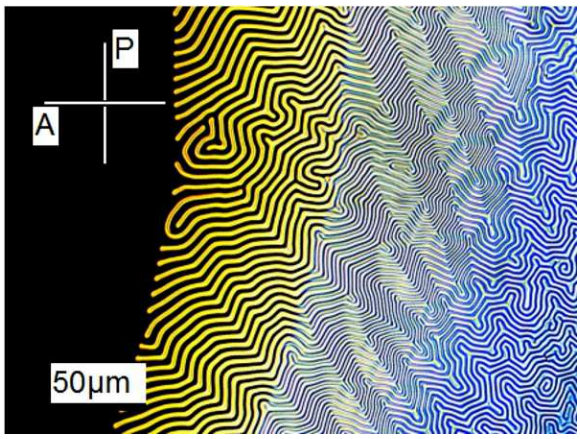

Figure 4.1: Non-chiral nematic liquid crystal E7 was allowed to mix with chiral-doped E7 within a cell that had been treated with weak homeotropic alignment layers on top and bottom substrate surfaces, resulting in a gradient in the concentration of chiral dopant increasing from left to right. The image shows a polarizing microscope image of the cell, and demonstrates that homeotropic alignment promotes a fingerprint texture over a range of helical pitch lengths.

distortion near the surfaces. In the Grandjean case this will be a reorientation from the homeotropic surface to the bulk planar state over the entire surface area. In the ULH case the distortion is less uniform, but is substantial in the vicinity of the defect. If we therefore assume that the elastic energy per unit area is similar in both ULH and Grandjean cases, then we might suggest that the additional energy of the defects in the ULH case means that the total energy of the ULH saturates at a higher level than the Grandjean, as illustrated in figure 4.2.

A second situation is in fact also possible that does not involve defects. Instead, the ULH structure can form a continuous distortion, involving a region of reverse twist, near the surface interface with a period equal to the pitch, and such that in some areas there is even a region in which the director twists in the opposite sense to the natural chirality [123]. Such a deformation has a large free energy density, and would also suggest that the ULH is more costly in energy than the Grandjean case [123, 121]. Curiously, there has not been any published experimental data to show a cross-over in energy of the two structures at larger anchoring strengths, as homeotropic alignments generally form ULH configurations on cooling from isotropic [124]. This may suggest that homeotropic anchoring agents

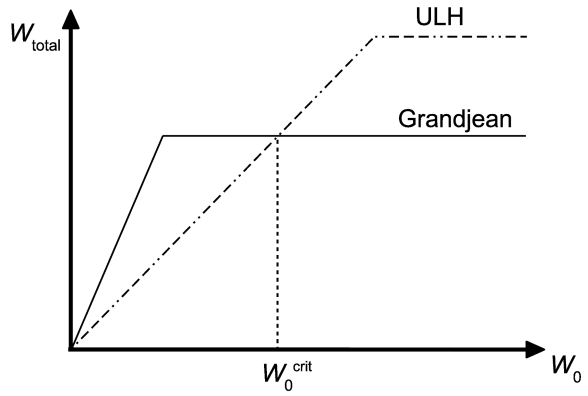

Figure 4.2: An illustration of the total energy per unit area W_{total} as a function of the homeotropic anchoring strength W_0 for ULH and Grandjean geometries. In the limit of small W_0, W_{total} is proportional to W_0. Due to its partial compatibility with homeotropic anchoring, W_{total} for the ULH rises slower than that for the Grandjean geometry, therefore in this region the ULH is lower in energy and stable relative to the Grandjean geometry. However, at large W_0, the ULH W_{total} saturates at a larger energy than that of the Grandjean due to distortion and the creation of defect lines. A critical W_0^{crit} occurs where both configurations are equal in energy. Note that the behaviour of W_{total} at intermediary values of W_0 are not well represented by the plot, but modelling of the behaviour in this region is beyond the scope of this work.

available are not strong enough for such a cross-over to be observed experimentally. We also generally observe that under flow, devices with homeotropic alignment conditions tend to form stable Grandjean-like textures. It may be the case that both Grandjean and ULH geometries are quasi-stable, and the history of the device (temperature or flow history) is more important than which state is the global energy minimum in determining which geometry is formed.

What is observed experimentally is consistent with the above discussion. Planar anchoring causes the Grandjean texture to form spontaneously on cooling (figure 4.3(a)), while a weak homeotropic anchoring surface treatment (created using lecithin) promotes a randomly oriented ULH (focal conic) texture (figure 4.3(b)). Here, a second problem that must be overcome in order to form a desired ULH texture can be seen: orientational degeneracy. Whilst the weak homeotropic anchoring favours ULH alignment, the observed texture has no preferred direction. To promote a single preferred ULH alignment direction,

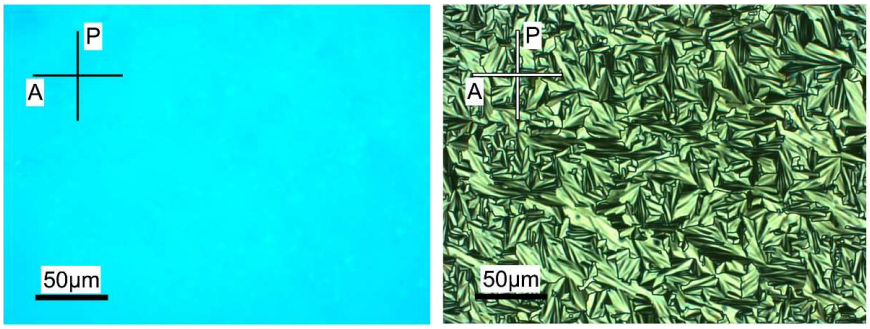

Figure 4.3: Polarizing microscope images of the Grandjean texture (left) which has been promoted with planar surface anchoring, and the focal conic texture (right) which arises on cooling a short pitch cholesteric from isotropic where the substrates have been treated with a weak homeotropic anchoring condition.

an orientational-degeneracy breaking agent or condition therefore must be employed.

Most of the alignment techniques described in this chapter rely on homeotropic alignment conditions to produce a ULH alignment. It should be noted, however, that liquid crystal materials designed to have large flexoelectric coefficients, namely bimesogenic and bent-core liquid crystals, do not respond well to homeotropic alignment conditions [126, 78], including lecithin, which is used throughout the work presented in this chapter, and that this problem has not been addressed. However, successful homeotropic alignment of bent-core liquid crystals using trichloroocta-decyl silane in heptane has been reported elsewhere [78].

In the next section, previous methods of ULH alignment are discussed. While in the work presented in subsequent sections, a homeotropic alignment condition is adopted in combination with a variety of methods for breaking the orientational degeneracy, this approach is in contrast to the most common method for ULH alignment in the literature, which adopts planar alignment conditions and exploits the dielectric reorientation of positive dielectric anisotropy materials under an applied field.

4.1.2 Previous Methods

Attempts at solving the problem of ULH alignment have been numerous but with varying and limited success. Many of the methods have produced reasonable alignment, however, for most technological applications, either the alignment has not been of sufficient quality,

or the complex surface treatments and processes involved are not suitable for economical mass production. Here, methods that have been tried in the past will be described, and the work in this chapter that attempts to address these problems will be introduced.

Planar Alignment Methods

The most common method for ULH alignment is to use planar alignment surface layers and cool from the isotropic phase in the presence of a transverse electric field. Due to the dielectric effect, the transverse field makes the ULH favoured over the Grandjean geometry (see §1.7.2) [127]. A more uniform alignment can also be obtained by exploiting the electrohydrodynamic effect [42]. However, as was discussed in the previous section, the ULH is not stable in cells with planar surface conditions, and rapidly reverts to a Grandjean geometry on field removal. To prevent this, polymer stabilisation is often employed [54]. A liquid-crystal host will have been mixed with a reactive mesogen, which can then be polymerised in-situ using ultra-violet radiation. The resultant polymer forms a network that stabilises the ULH from reverting to the more stable Grandjean structure after the field is removed. Polymer network can be formed throughout the liquid crystal or be localised to the surfaces to improve switching characteristics [53, 119]. This method is reliable, however forming the ULH using a transverse field prior to polymerisation does not yield a sufficient alignment quality. Furthermore, polymer networks have additional disadvantages, leading to larger switching voltages and potentially reducing the optical contrast by having residual birefringence [114, 115] and introducing light scatter [128, 129]. No polymer networks are used in this thesis.

In a related method, Gardiner used in-plane fields with planar anchoring to produce the ULH before polymerisation to stabilise against reverting to the Grandjean structure [122]. This method proves particularly effective, although again, the requirement of polymer network is sub-optimal. In §4.3, the method is repeated and the main issues discussed, before a modification to the method is demonstrated that allows the ULH to remain stable on removal of the field without polymer stabilisation. Experimentally it is shown that both the

flexoelectric and dielectric effects can be exploited to align the ULH with in-plane fields.

Homeotropic Alignment Methods

In work by Komitov, periodic boundary conditions were used, alternating between homeotropic and planar alignment [118, 120]. The idea is to match the topology of the periodic ULH directer orientation next to the alignment surface. Komitov suggests that as long as the planar regions are shorter than the pitch of the material, so that Grandjean does not form above them, then it is not vital that the periodicity of the boundary condition is commensurate with the material's pitch [118]. The planar regions act as a symmetry-breaking agent that promotes a single direction of ULH alignment. This general principle, of orientational symmetry breaking, is addressed in all work on ULH alignment. In order to understand Komitov's approach, in §4.2 a related approach using long-pitch materials is presented. Although long-pitch materials are not usually considered in flexoelectrooptic ULH technology, they have the advantage that the structure can be observed clearly using polarizing microscopy.

Carbone *et al* used periodic surface structures to encourage seeding lines of topological discontinuities, reducing the energy of the ULH relative to the Grandjean structures by reducing the energy of these lines [121]. The structures were fabricated using laser-scanning lithography; an effective but expensive technique that is inappropriate for mass production. In §4.4, nano-grooves are fabricated using a polishing compound to produce a ULH alignment by what may be a similar mechanism. The process is cheap and could be scaled for application.

In another study by Carbone *et al*. a highly ordered and stable ULH alignment was achieved using homeotropic alignment in polymer channels [55]. The channels break the in-plane orientational degeneracy, resulting in the unidirectional ULH being the lowest energy configuration. By far the most uniform ULH texture in the literature, the method also requires additional processing and complexity, making it unsuitable for industrial-scale production. In §4.5, similar channels are produced using a far simpler process involving surface

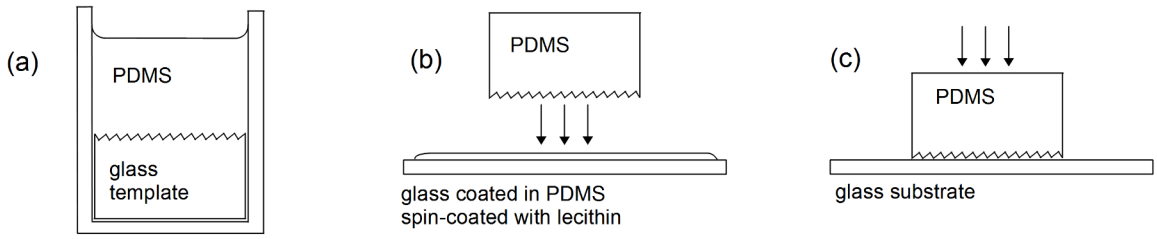

Figure 4.4: A schematic illustration of the stages involved in producing periodic surface alignment conditions (not to scale). (a) A cast is made of a blazed diffraction grating with a pitch of a 6.6 µm using polydimethylsiloxane (PDMS). (b) Glass that has been coated in PDMS is spin-coated at 3000 rpm for 30 seconds with 0.1 wt% lecithin disolved in propanol. The PDMS cast is lightly pressed against the PDMS coated glass, and lecithin is partially transfered onto the tips of the cast. (c) The blazed PDMS cast is pressed against a clean glass substrate, and the lecithin on the cast is transfered to the glass resulting in a striped periodic lecithin print. The process is repeated for a second substrate, and a liquid crystal cell is assembled using the substrates.

relief structures. Similar structures are already used in commercial displays, demonstrating the potential viability of the technology [130].

In the next section, a periodic-boundary printing technique is used with long pitch materials.

4.2 Printed Periodic Boundary Conditions in Long-Pitch Systems

While Komitov's work, in which periodic alignment conditions were created, was successful at producing a ULH texture, the alignment quality was not of a sufficient quality for most display applications. In the brief study described in this section, a print-transfer technique is adopted, illustrated in figure 4.4, to produce a periodic homeotropic boundary condition. A relatively large-pitch periodic print structure of 6.6 µm was chosen, with a chiral nematic material with a similar periodic length scale, to allow the helicoidal structure to be observable with polarizing microscopy. Although one should be careful when extrapolating results between very different scales of cholesteric pitch, the motivation for using long-pitch materials is to gain insight into alignment of liquid crystals on periodic substrates.

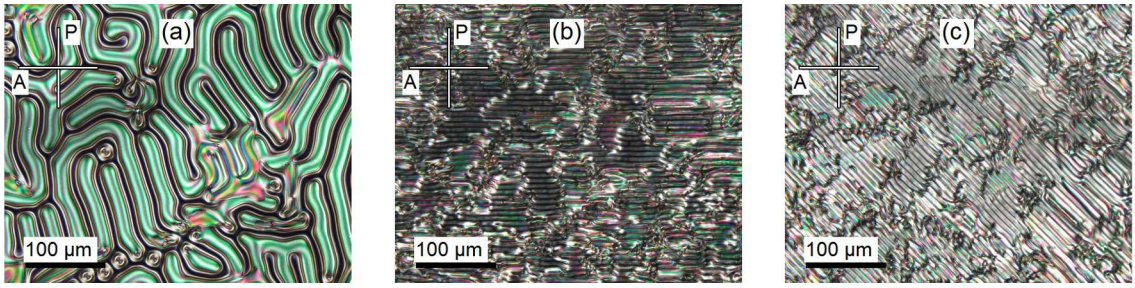

Figure 4.5: Polarizing microscope photographs of a cell with periodic homeotropic boundary conditions (pitch 6.6 µm) filled with chiral-doped nematic E7 whose pitch is approximately commensurate with the pitch of the boundary condition, at 60°C. (a) Some areas of the cell show a fingerprint texture consistent with homeotropic surface conditions. In other areas, the boundary conditions have aligned the liquid crystal helicoidal axis perpendicular to the lecithin stripes. (b) and (c) show such alignment where the lecithin stripes are parallel and at 45° to the analyser respectively.

Nematic liquid crystal E7 was doped with 0.7 wt% chiral addative R5011, resulting in a long pitch of 14.8 ± 0.8 µm at room temperature (corresponding to a 2π rotation of the director). The material was engineered to have a pitch roughly commensurate with the 6.6 µm printed lecithin substrates. A cell of thickness greater than 30 µm, with periodic boundary conditions on both top and bottom substrate surfaces made using the printing technique, was filled with the mixture. On cooling from the isotropic phase to 60°, some areas of the cell show a fingerprint texture, shown in figure 4.5(a). The fingerprint texture, in which the helicoidal axis is perpendicular to the substrates, is a consequence of homeotropic boundary conditions [124, 125], and has no prefered helicoidal axis orientation. In other areas of the cell, the liquid crystal has been influenced by the periodic boundary conditions, shown in 4.5(b) and (c). Discontinuous boundaries appear between regions of uniform alignment. These discontinuities might arise because the liquid crystal pitch and boundary-condition periodicity are not exactly commensurate.

A second cell, of thickness 20 µm made in the same way and filled with the same 14.8 µm pitch liquid crystal mixture, is shown in figure 4.6. A low magnification image shows a large region of aligned texture, with much larger distances between discontinuous boundaries. By holding the liquid crystal close to the nematic-isotropic transition temperature and varying the temperature slowly, the texture was found to become more uniform.

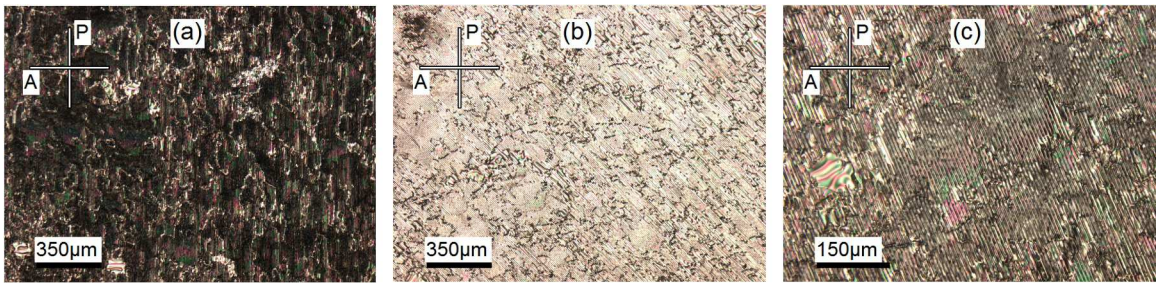

Figure 4.6: Low magnification polarizing microscope photographs of a second cell with periodic boundary conditions and filled with chiral-doped E7 ($P = 14.8$ µm) where (a) the periodic striped boundaries are parallel with the polarizer and (b) at 45°. (c) Shows a slightly higher magnification and a rotation of 22.5° to the polarizer.

Although the pitch was not measured for this material as a function of temperature, it is expected to vary slightly. The fluctuating pitch with variations in temperature may contribute to the alignment quality.

This study has shown that periodic homeotropic boundary conditions heavily influence the director orientation and can result in a uniformly oriented lying-helix texture. While detailed conclusions cannot be drawn from this limited study, defects have been observed in the ULH structures here. It is likely that shorter pitch systems would also contain alignment defects. This may suggest why the work by Komitov using short-pitch materials did not produce a high quality alignment, although more work is required to know with certainty.

In the next section, a different method for ULH alignment is examined, and we return to short-pitch systems.

4.3 In-Plane Switching Fields

In this section, Gardiner's method (reference [122]) for ULH alignment that relies on the application of in-plane switching (IPS) fields using interdigitated electrode structures is examined and extended. The method is demonstrated to work for both flexoelectric- and dielectric-dominated materials, and differences between the alignment mechanism in these two types of materials is commented upon. ULH structures made using the technique revert to the Grandjean texture on removal of the field in cells with planar alignment. It is

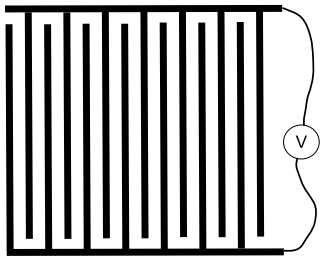

Figure 4.7: An illustration (not to scale) of the structure of In-Plane Switching (IPS) interdigitated electrodes, which are etched onto a glass substrate surface in order to produce an electric field in the plane of a liquid crystal cell. IPS electrodes used in this study are separated by 9 µm and are 5 µm wide.

demonstrated that this problem can be mitigated by using a weak homeotropic alignment condition, which destabilises the Grandjean in favour of the lying helix geometry, as was discussed in §4.1.1.

4.3.1 Theory

Fields Produced by Interdigitated Electrodes

In-Plane Switching (IPS) cells contain a series of interdigitated electrodes that are etched onto one glass substrate surface, as illustrated in figure 4.7. A voltage difference between alternating electrodes results in a non-uniform field with a large component in the plane of the device. A simulation of the electric potential and field, done using a commercial electrostatics finite-element software package (COMSOL multi-physics), is shown in figure 4.8, and shows several significant features. There is a large component of the field in the plane of the device between the electrodes, however, the field is non-uniform and much stronger near the electrode edges. The field also has an out-of-plane component, and is purely out-of-plane directly above the electrodes.

Dielectric Dominated Cholesteric Materials in Electric Fields

In the case of the positive dielectric anisotropy cholesteric material (ZLI-4792 + 2.7 wt% R5011), an electric field produces a reorienting torque that promotes the alignment of the helicoidal axis perpendicular to the field, which minimises the dielectric energy.

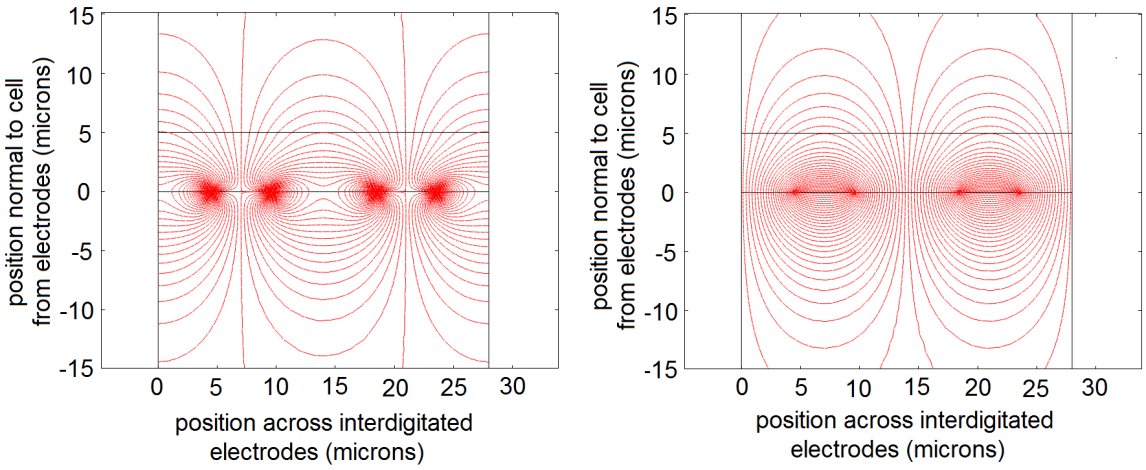

Figure 4.8: A numerical simulation of the electric field (left) and electric potential (right) in a 5 µm thick device with interdigitated electrodes. The simulation shows a cross-section of a single repeating unit of 28 µm, in which the electrodes are separated by 9 µm and are 5 µm wide. The simulations show that there is a large component of the field in the plane of the device, however, above the electrodes there is also a vertical component.

This effect is discussed in §1.7.2, where it was shown that the difference in energy between alignment of the helicoidal axis parallel and perpendicular to the field (ignoring any flexo-electric polarization) is given by,

$$\delta f_{\text{effective}} = \frac{1}{4}\Delta\varepsilon\varepsilon_0 E^2 \tag{4.3}$$

For typical material parameters for a mono-mesogenic liquid crystal ($\Delta\varepsilon = 10$) and a field of 10 Vµm^{-1}, we find that $\delta f_{\text{effective}} = 250$ µVm^{-3}.

The field that is produced by interdigitated electrodes, shown in figure 4.8, has in-plane and out-of-plane components. The only orientation that satisfies the condition that the helicoidal axis is perpendicular to the field at all positions is where the helicoidal axis is oriented parallel to the electrodes. However, if the field were uniformly in the plane of the device, then the helicoidal axis could take any orientation that is perpendicular to the field, which could also be out of the plane of the device. Therefore, the inhomogeneity of the field is a crucial feature of the device to allow a uni-directional ULH alignment. Indeed, in cells that have standard ITO electrodes on top and bottom in order to produce a uniform transverse field, a focal-conic with the ULH oriented randomly in the plane of the device

is commonly observed for materials with positive dielectric anisotropy and relatively small flexoelectric coefficients when a field is applied [41, 42, 43, 44, 45, 46].

Flexoelectric Dominated Cholesteric Materials in Electric Fields

The very small dielectric anisotropy of bimesogenic materials precludes the above mechanism for ULH alignment in fields produced by interdigitated fields. However, it has previously been demonstrated that fields produced by interdigitated electrodes can also be used to reorient the helicoidal axis of cholesteric materials with large flexoelectric parameters but small dielectric anisotropy [122]. In this case, a different mechanism of alignment is likely.

For a cholesteric material in which there is no flexoelectric polarization, the effective dielectric permittivity along the helicoidal axis is $\varepsilon_\perp$, and perpendicular to the helicoidal axis is $(\varepsilon_\parallel + \varepsilon_\perp)/2$. However, we will see in chapter 5 that flexoelectric polarization enhances the effective dielectric permittivity perpendicular to the helicoidal axis of a cholesteric (this result is derived in the main section on this topic in §5.2), by an amount,

$$\varepsilon_{\text{flexo}} = \frac{1}{\varepsilon_0}\left(\frac{(e_1 - e_3)^2}{2(K_1 + K_3)}\right) \tag{4.4}$$

Therefore, the difference between the effective permittivity parallel and perpendicular to the helicoidal axis is given by,

$$\Delta\varepsilon_{\text{effective}} = \varepsilon_\perp - \left(\frac{\varepsilon_\parallel + \varepsilon_\perp}{2} + \varepsilon_{\text{flexo}}\right) = -\left(\frac{\Delta\varepsilon}{2} + \varepsilon_{\text{flexo}}\right) \tag{4.5}$$

Bimesogenic materials have a very small dielectric anisotropy, but a large $e_1 - e_3$. For bimesogenic materials this enhancement in the effective permittivity due to flexoelectricity can make the helicoidal axis orientation perpendicular to the field lower in energy. Hence, a cholesteric bimesogenic material can be reoriented using a field whose frequency is sufficiently small to couple to flexoelectric polarization. The free energy difference between parallel and perpendicular alignment of the helicoidal axis with the field is given by,

$$\delta f = -\frac{1}{2}\Delta\varepsilon_{\text{effective}}\varepsilon_0 E^2 = \frac{1}{4}\left(\Delta\varepsilon\varepsilon_0 + \frac{(e_1 - e_3)^2}{K_1 + K_3}\right)E^2 \tag{4.6}$$

The flexoelectric interaction produces a term in the effective dielectric anisotropy of the material of the same form as the dielectric effect, and therefore can also be used to reorient the helicoidal axis. Since the bimesogenic material has $\Delta\varepsilon \approx 0$, only the second term is important. Estimating typical parameters for bimesogenic materials ($e_1 - e_3$ = 10 pCm^{-1}, $K_1 + K_3$ = 10 pN) then for a field strength of $E = 10$ Vμm^{-1}, we find, $\delta f = 25$ μVm^{-3}. This is ten times smaller than the $\delta f = 250$ μVm^{-3} in the previous case of a typical positive dielectric anisotropy, mono-mesogenic liquid crystal, and therefore we may expect that a larger field (by a factor of $\sqrt{10} = 3.16$) will be required to produced the reorienting effect in bimesogenic materials.

In cells with standard ITO electrodes on top and bottom substrate surfaces that produce a uniform transverse field, filled with a bimesogenic material, the application of a field that couples to the flexoelectric polarization results in a focal conic texture, in which the helicoidal axis is perpendicular to the field but randomly oriented in the plane of the cell. The behaviour is shown in chapter 5, figure 5.6(a) and (d). This behaviour is analogous to the same experiment using mono-mesogenic materials described in the last section. Again, this suggests that the inhomogeneity in the field produced by interdigitated electrodes is crucially important for ULH alignment in these devices.

Here, it has been shown that both the flexoelectric effect and the dielectric coupling to a positive $\Delta\varepsilon$ gives the cholesteric a negative effective dielectric anisotropy, in which the permittivity along the helicoidal axis is smaller than that perpendicular. In both cases, how the effective dielectric anisotropy resulting from the two effects could be used to uniformly orient the helicoidal axis in cells with interdigitated electrodes has been explained. In addition, the crucial role of the field inhomogeneity produced by interdigitated electrodes has been discussed. In the next section, interdigitated cells are prepared with mono-mesogenic and bimesogenic materials, and shown to exhibit the expected behaviour. The method is then further extended in order to promote stability of the ULH texture when the field is removed by the use of homeotropic alignment layers, which destabilise the Grandjean geometry relative to the ULH, as was discussed in §4.1.1.

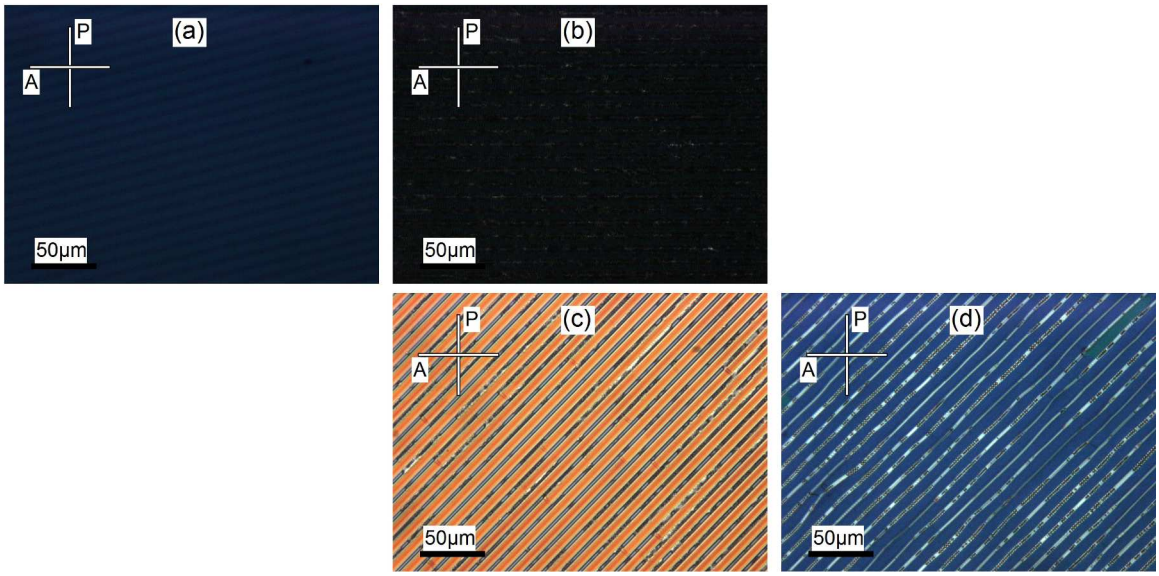

Figure 4.9: Polarizing optical microscope photographs of 5 µm planar IPS cells filled with cholesteric material ZLI-4792+2.7wt%R5011. (a) On cooling from the isotropic phase, the Grandjean texture forms. The application of 10 $V_{rms}\mu m^{-1}$ at 1 kHz results in a ULH texture, which is shown here with the helicoidal axis (b) parallel and (c) at 45° to the polarizer. (d) One second after the field is removed, the ULH reverts to a Grandjean texture, due to the planar surface alignment.

4.3.2 Experimental

Dielectric Dominated Mono-mesogenic Liquid Crystal

Figure 4.9 shows optical polarizing microscope photographs of a 5 µm thickness, planar-aligned IPS cell (electrode width 5 µm, gap between electrodes 9 µm), containing a positive dielectric anisotropy, mono-mesogenic cholesteric mixture ZLI-4792 doped with 2.7 wt% R5011. On cooling from isotropic, the planar Grandjean texture forms owing to the planar surface alignment. With the application of 10 $V_{rms}\mu m^{-1}$ at 1 kHz a ULH texture forms, in agreement with the theory. On removal of the field, the liquid crystal reverts to the Grandjean texture within approximately one second, shown in figure 4.9 (d).

Flexoelectric Dominated Bimesogenic Liquid Crystal

Figure 4.10 shows polarising microscope photographs of the same type of interdigitated electrode cell filled with low-dielectric-anisotropy bimesogen mixture MDA-4407 mixed with 1.8 wt% of chiral dopant R5011. On application of 20 $V\mu m^{-1}$, defects form and

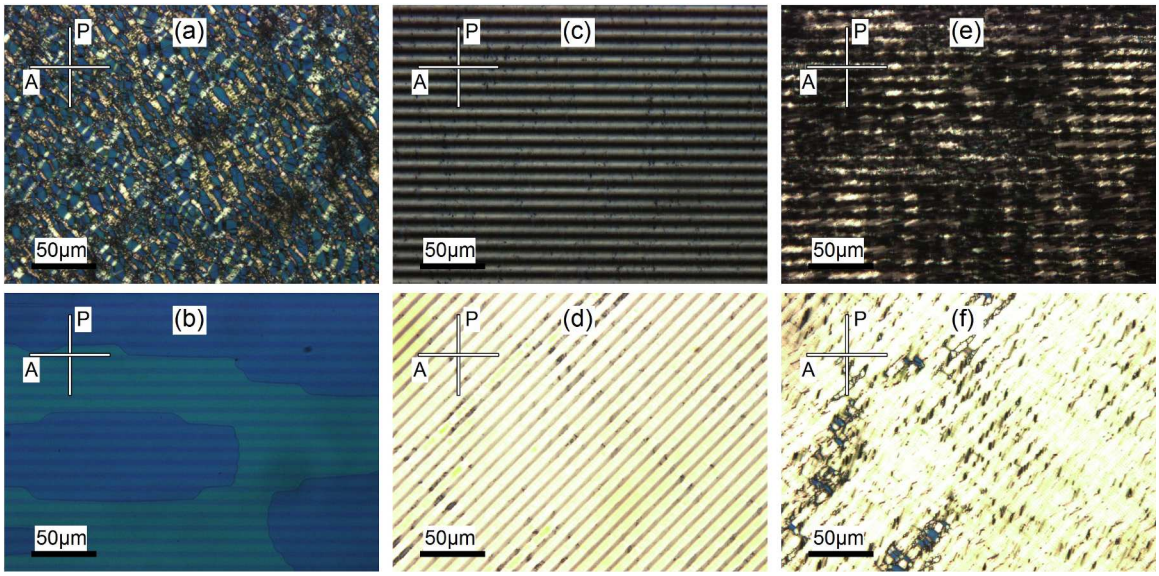

Figure 4.10: Polarizing optical microscope photographs showing a high-viscosity bimesogenic cholesteric mixture (a) forming just below the nematic-isotropic transition temperature, (b) having formed the Grandjean, which in the absence of any fields is the lowest energy state, (c) on application of 20 $V_{rms}\mu m^{-1}$ at 100 Hz, where the cell has been rotated such that the field is applied parallel with the polarizer, (d) with the same conditions as (c) but rotated by 45°, and (e) and (f) are taken immediately after the field is removed. The field promotes the ULH alignment, which remains for up to 60 seconds before reverting to the Grandjean structure.

a ULH texture forms, in agreement again with the above discussion. As suggested from the discussion in the theory, a larger field was indeed required to switch the liquid crystal, which corresponds to the estimates for the effective difference in free energy in the two systems between parallel and perpendicular alignment of the helicoidal axis with the field. A minimum field required to switch the liquid crystal into a uniform lying helix alignment in either dielectric or flexoelectric dominated materials was not measured, however.

On removal of the field, the ULH texture remains for some time. Because the bimesogenic mixture has a high viscosity, it takes a relatively long time to return to the Grandjean texture. This is illustrated in figure 4.11, which shows the same texture as in 4.10(e) and (f), rotated to 22.5°, just after and two minutes after the field was removed.

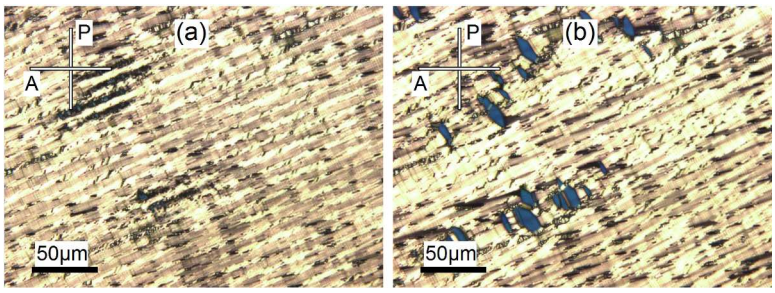

Figure 4.11: Polarizing optical microscope photographs showing the same texture as in 4.10(e) and (f). (a) On removal of the field, the ULH texture remains, however, (b) after 2 minutes, begins to revert to the Grandjean texture. This is evidenced by the small blue regions that grow over time.

Stabilising the ULH using Homeotropic Alignment Conditions

While the two examples and discussion above have shown that both flexoelectric and dielectric effects can be used to orient the ULH in cells with interdigitated electrodes, the resultant ULH geometry is not stable against reverting to the Grandjean geometry on removal of the field. In order to overcome this problem, Gardener suggested the use of polymer stabilisation. However, as was discussed in §4.1.1, a homeotropic alignment can stabilise the ULH from reverting to the Grandjean, and in this section, this alternative approach is adopted.

Figure 4.12 shows analogous polarizing microscope images to those in figure 4.9, of cells containing the mono-mesogenic ZLI-4792 mixture, but this time with a homeotropic alignment condition created using lecithin. In contrast to the case with planar alignment however, which returns to the Grandjean geometry within approximately one second after removing the field, in the case of homeotropic anchoring the ULH remains stable indefinitely. This is a poignant advantage, as it removes the requirement for a polymer network, making the method far less complicated, and this is the first time homeotropic alignment has been used to create a stable alignment after using an in-plane field to produce ULH alignment.

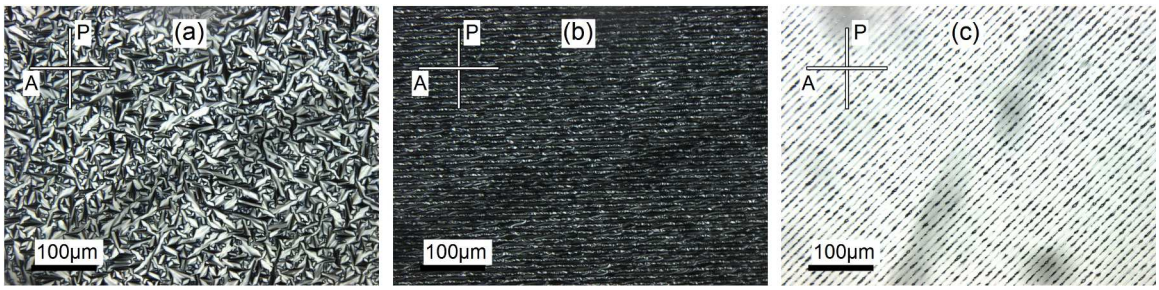

Figure 4.12: Polarizing optical microscope photographs of 5 µm homeotropic IPS cells filled with cholesteric material ZLI-4792+2.7wt%R5011. (a) On cooling from isotropic, a focal conic alignment, in which the helicoidal axis is in the plane of the cell within randomly oriented domains, forms spontaneously due to the homeotropic boundary condition. (b) On application and removal of 10 $V_{rms}\mu m^{-1}$ at 1 kHz, a reorientation of the helicoidal axis occurs that results in a ULH texture, which is dark between crossed polarizers in this case where the helicoidal axis is parallel to the polarizer, and (c) bright in the case where the cell is rotated by 45°. The texture is stable against reverting back to the Grandjean texture.

4.3.3 Conclusion

In this section, by considering the effective dielectric permittivity of the cholesteric structure, a theory of how interdigitated electrode structures can be used for ULH alignment using in-plane fields has been developed, both in materials whose field interactions are primarily flexoelectric- or dielectric-dominated, for the first time. It has been shown that the inhomogeneity of the field produced by interdigitated electrodes is critical to allow the formation of the ULH using this method. Devices have been demonstrated to exhibit the predicted behaviour using positive dielectric anisotropy, mono-mesogenic liquid crystal, and small dielectric anisotropy, highly flexoelectric bimesogenic liquid crystal mixtures. Further, a homeotropic alignment condition has been demonstrated to prevent the cholesteric from reverting to Grandjean alignment after the field is removed, without the requirement of polymer stabilisation.

However, the alignment quality produced by this method is unfortunately still inadequate for most applications, which require dark black states to allow for a large contrast between on and off states. In the next section, a different approach is taken based on the pinning of topological defects using surface structures to promote ULH alignment.

4.4 Nano-Grooved Surface Structures

In this section, ULH devices are described that exploit the use of homeotropic alignment layers (to destabilise the Grandjean relative to the ULH), and unidirectional nano-grooved relief structures (to break the orientational degeneracy of the ULH axis direction).

4.4.1 Device Preparation

To produce unidirectional nano-grooved relief structures, 1 mm thick slide glass substrates are polished by hand with 6 µm diamond lapping compound. Figure 4.13 is an Atomic Force Micrograph (AFM) of the resultant scratched surface profile from such a process, and shows a variation in depth of approximately 10 to 30 nm. The glass is washed using a series of stages: Decon to remove oil from the lapping compound, de-ionized water for 20 minutes, iso-propylalcohol for 20 minutes, acetone for 20 minutes, and finally de-ionized water again for 20 minutes, all at 50°C and under sonication. A solution of 0.1% lecithin in chloroform is spin-coated at 3000 rpm for 30 s onto the polished glass, which is known to promote a weak homeotropic surface anchoring condition [3]. The substrates are left for 5 minutes at room temperature before being assembled into a cell using ultra-violet-curable glue, which has been mixed with spacer balls in order to achieve a desired cell thickness. The cell's thickness is subsequently measured interferometrically using a spectrometer.

Nematic liquid-crystal mixture E7 ($\Delta\varepsilon = 13.7$) and the negative dielectric anisotropy nematic MLC-7029 ($\Delta\varepsilon = -3.66$), both from Merck, are doped with 3.5% by weight of high twisting-power, commercially available chiral additive R5011 (Merck), resulting in a cholesteric with a pitch of 250 nm for E7 and 270 nm for MLC-7029 at room temperature. The pitch is deduced from the Bragg reflection band in the transmission spectrum when aligned in the Grandjean geometry [27] (see §1.6.2). The materials are then capillary filled into cells while in the isotropic phase.

Note that negative dielectric anisotropy materials such as MLC-7029 are normally difficult to align in a ULH structure, because the common method of applying a transverse field while cooling into the cholesteric phase from the isotropic state cannot be used. The ten-

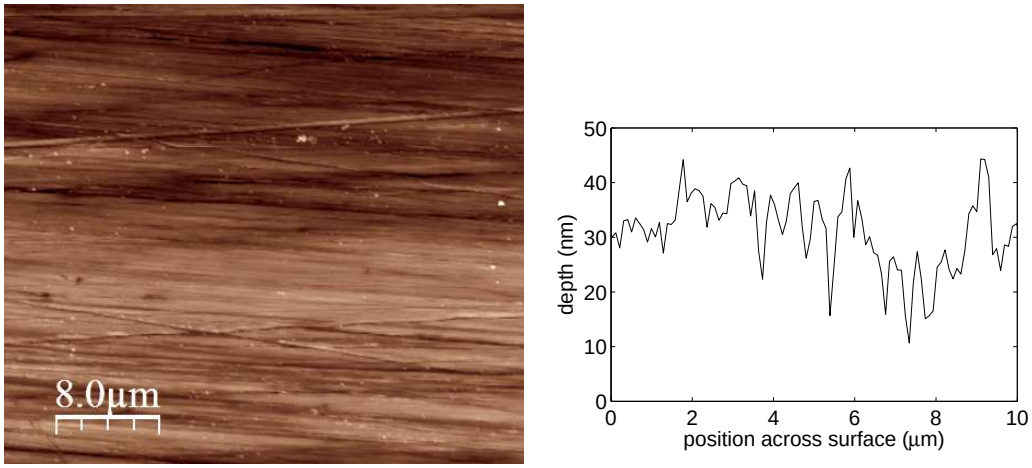

Figure 4.13: An AFM image of the grooved structure obtained by unidirectionally polishing a glass surface with 6 µm lapping compound (left), and the surface depth profile perpendicular to the polishing direction (right). The variation in depth is of the order of tens of nanometres.

dency in this scenario is to form the Grandjean state (see §1.7.2), and hence, ULH methods for measuring the flexoelectric response of negative dielectric materials have previously not been attempted.

4.4.2 Results and Discussion

ULH formation

The presence of a blue phase appears to be critical to the formation of ULH in the devices in this study. The liquid-crystal is slowly cooled from the isotropic into a blue phase (figure 4.14 (a)), which is present at 53°C in chiral-doped E7. On cooling to 52°C, a birefringent texture forms simultaneously and uniformly over the entire observational area (figure 4.14 (b)). This texture may be a wetting phenomenon, whereby a thin layer of ULH precipitates out from the blue phase on the alignment surface. On further cooling, the bulk ULH texture appears from seed-points before spreading over the entire film (figure 4.14 (c) to (f)). The apparent relation between a blue phase and ULH formation has before been commented upon by Coles *et al* [56].

The ease with which a ULH texture is obtained is dependent on cell thickness, with thinner cells forming ULH more readily. Cooling quickly results in a poor ULH texture,

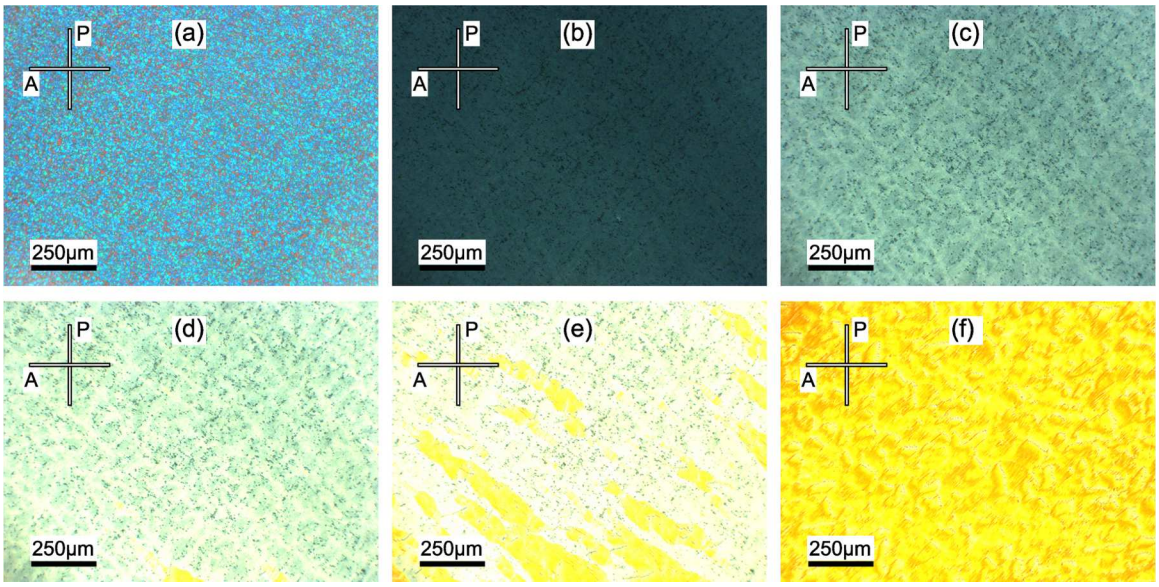

Figure 4.14: A series of 10× magnification polarizing microscope images showing the formation of the ULH as the cell is cooled from 54°C in the blue phase (a) to 52°C (f). The exposure time has been increased in (a) in order to observe the blue phase, which is relatively dark. The device thickness in this case is 6.5 µm (which is consistent with the final yellow colour of the ULH texture in (f)). The optic axis of the ULH texture is oriented at 45° with respect to the analyser.

except in extremely thin cells ($\approx$ 1 µm). However, a range of cells have been produced using this method that exhibit spontaneous ULH alignment, varying in thickness from 1 to 7 µm, that are stable over at least 3 weeks with no degradation in alignment quality.

Figure 4.15 shows polarizing microscope images of cells of thickness 2 µm and 6.5 µm containing E7+3.5% R5011 and of thickness 5.1 µm containing MLC-7029+3.5% R5011, at angles where the optic axis of the ULH is oriented at 0° and 45° with respect to the analyser. The images are consistent with a ULH liquid crystal structure that acts as a uniaxial layer whose transmission depends upon,

$$T = \sin^2(2\chi)\sin^2(\frac{\pi\Delta n_{\text{effective}}d}{\lambda}) \tag{4.7}$$

where χ is the angle of the optical axis with respect to the analyser, $\Delta n_{\text{effective}}$ is the effective birefringence, d is the layer thickness, and λ is the wavelength of incident light (see §1.8.4). Defects in the alignment reduce the optical contrast, especially by reducing the quality of the dark states shown in figure 4.15. Photographs shown in figure 4.16, not taken through

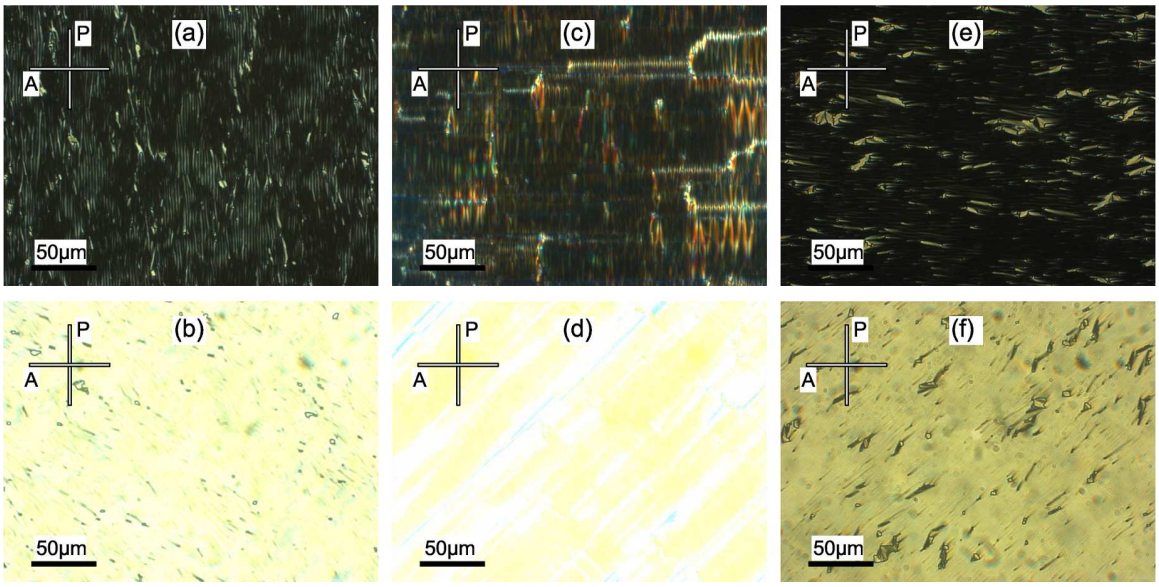

Figure 4.15: 50× magnification polarizing microscope images of ULH cells made using the method described in the text. Cells are of thickness 2 µm (a) and (b) and 6.5 µm (c) and (d), both filled with E7+3.5% R5011, and of thickness 5.1 µm filled with negative $\Delta\varepsilon$ material MLC-7029+3.5% R5011 (e) and (f). The optic axis is oriented at 0° ((a), (c) and (e)) and 45° ((b), (d) and (f)) to the analyser.

a microscope, of a 2 µm thick cell containing chiral-doped E7 between crossed polarizers show that the uniform texture can extend over a large area of the cell.

ULH Helicoidal Axis Orientation

The helicoidal axis direction relative to the groove direction was determined by comparing with textures of known helix orientation. The same E7+3.5wt%R5011 mixture was capillary filled into a 7 µm thick planar aligned cell. The cell was cooled from the isotropic phase under the application of a transverse electric field, below the unwinding threshold. The ULH texture obtained bares close resemblance to those obtained using the method described using nano-grooved surfaces, and the helicoidal direction was determined by increasing the field to the unwinding field. At this point, line defects that run perpendicular to the helicoidal direction form, and thereby reveal the helicoid direction. The result is that the helicoidal axis is perpendicular to the scratches in our cells. This result is further supported by conoscopic image data (see figure 4.17). The conoscopic data were obtained using a commercial conoscopic system (Eldim) by placing the test device between crossed polaris-

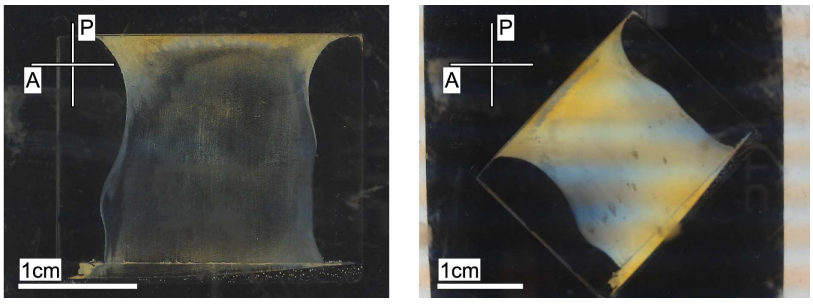

Figure 4.16: Photographs of ≈ 2µm thick cell filled with chiral-doped E7, rotated such that the optic axis of the ULH material is at 0° (left) and 45° (right) to the analyser. The ULH alignment extends over the majority of the cell.

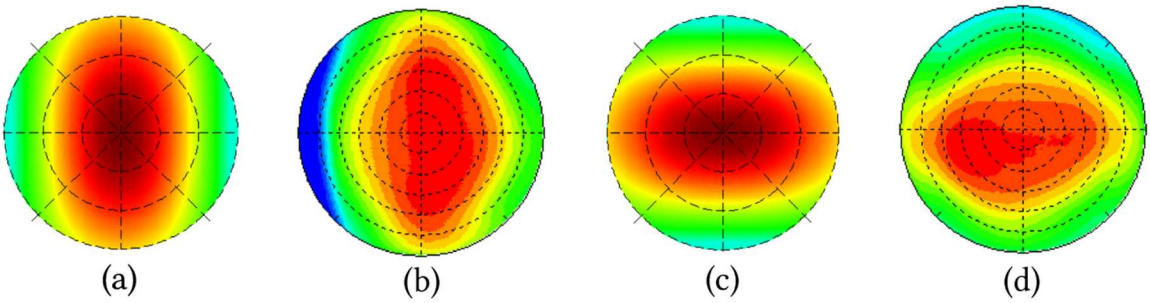

Figure 4.17: Simulated conoscopic transmission up to 60° off-axis transmission of a uniaxial slab with its axis oriented (a) vertically and (c) horizontally, used to determine the orientation of the helicoidal axis relative to the surface lapping direction. The simulated slab's Δnd is chosen to match that of the ULH device under investigation. (b) and (d) are corresponding experimental conoscopic transmission for the ULH device. The false colour corresponds to the normalised transmission, with red corresponding to a maximum. The data are consistent with the helicoidal axis running perpendicular to the grooves created through a lapping process, which is used to align and stabilise the ULH texture.

ers and illuminating it with an isotropic, homogeneous back-light taken from a commercial liquid crystal display. Corresponding simulations were carried out using the standard 4-by-4 Berreman optical modelling technique [15].

Lines of surface anchoring breaking, which are perpendicular to the helicoidal axis, are therefore parallel to the nano-grooves of the cells in this study. There are two hypotheses as to why this may be the case, and a combination of the two is also possible. The first hypothesis is that the scratches provide seeding sites that promote surface anchoring breaking in a single direction. This hypothesis is based on the numerical study in reference [121], that found that similar structures reduce the energy of the ULH at the liquid crystal glass

interface. The second hypothesis is that alignment of the ULH in a single direction results in a minimisation in the elastic frustration caused near an undulating surface profile. This phenomenon was first described by Berreman [131] in the case of the alignment of nematic liquid crystals on polished surfaces, where the theory is found to result in the nematic director aligning parallel to the grooves. Although the case of a ULH structure aligned on similar grooves that have been treated with a weak homeotropic alignment condition is different from the case demonstrated by Berreman, a similar principle could be in effect. The planar oriented regions of the ULH structure have a lower elastic energy when oriented parallel to the grooves (and therefore with the helicoidal axis orientation perpendicular to the grooves). In the case that the first hypothesis is correct, then it is interesting to point out that the periodicity of the scratches (being random in our case) is not required to be commensurate with the pitch of the material in order to promote a single orientation of ULH (an observation also made by Komitov in relation to ULH formation on periodic structures [118]).

Electro-optic Studies

In order to characterise the devices' electrooptic responses, the cells are placed in the path of a laser between crossed polarizers, such that the unperturbed optic axis is oriented at 22.5° to the analyser. This ensures maximum intensity modulation, and a linear optical switching regime (see §2.2). External indium-tin-oxide (ITO) electrodes are used to apply a transverse electric field to the ULH cells. This is because ITO cannot be used on glass substrates unless it is deposited after the polishing process, which is inconvenient and unnecessary for the purposes of this study. The transmitted intensity under the application of symmetric square and triangular voltage amplitudes are shown in figure 4.18 for a 6.5 µm thick cell filled with E7 + 3.5% R5011, measured using a photo diode. The cells all show a linear transmission amplitude with respect to the driving voltage, which is typical of the flexoelectric effect at small field strengths in these materials, and the characteristic switching time for E7 ($P = 250$ nm) at room temperature (measured as the time for the cell's transmission to reach $1/e$

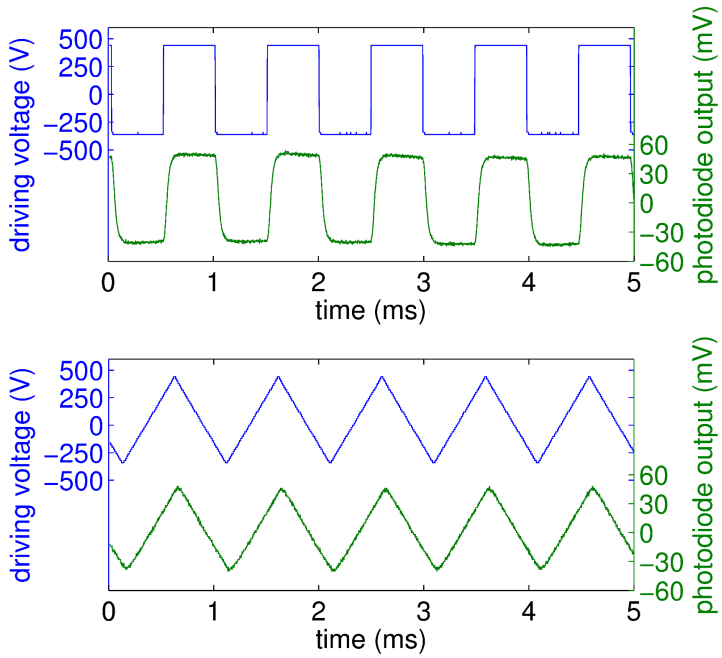

Figure 4.18: The electrooptic response of a 6.5 µm thick cell filled with cholesteric mixture E7 + 3.5% R5011, aligned in the ULH goemetry using a combination of surface polishing, weak homeotropic anchoring and slow cooling. The cell's time-dependent transmission modulation under the application of a 1 kHz square-modulated voltage (top), which is applied to the external surfaces of the cell, is used to measure the characteristic switching time of the device. The electro-optic switching under the application of a triangle-modulated driving voltage demonstrates a linear switching of the liquid crystal (bottom).

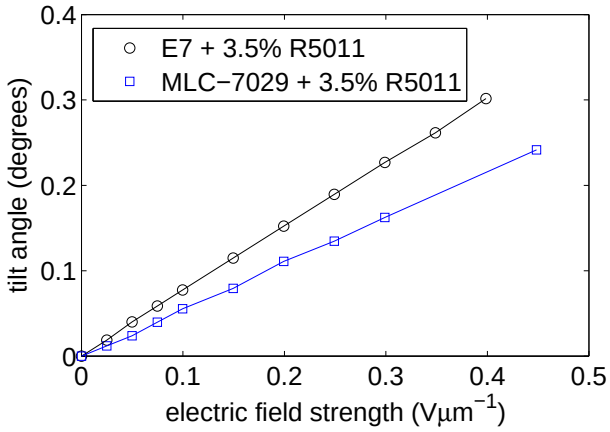

Figure 4.19: The tilt angle for doped E7 and MLC-7029 as a function of the field strength, calculated from electrooptic data. The response is linear in this field range, which is typical for the flexoelectrooptic effect.

of its equilibrium value after a field-polarity reversal) is 60 µs.

Measurement of Flexoelectric Properties

Figure 4.19 shows switching angles as a function of applied field strength for chiral-doped E7 ($P = 250$ nm) and the negative dielectric anisotropy material MLC-7029 ($P = 270$ nm). By considering equation 2.4, the data from figure 4.19 can be used to determine a value of the flexoelastic parameter $(e_1 - e_3)/(K_1 + K_3)$ of 0.46 $\mathrm{Cm^{-1}N^{-1}}$ for E7 (which is consistent with previous measurements of the parameter in the same material in §2.2 and §2.3) and 0.14 $\mathrm{Cm^{-1}N^{-1}}$ for MLC-7029 (see §2.2). Using values of $K_1 + K_3$ provided by the material supplier (Merck) of 26.9 pN for E7 and 31 pN for MLC-7029, $e_1 - e_3$ is determined to be $12.5 \pm 1.3 \times 10^{-12}$ $\mathrm{pCm^{-1}}$ for E7 and $4.3 \pm 0.4 \times 10^{-12}$ $\mathrm{pCm^{-1}}$ for MLC-7029. The dominant source of error is uncertainty in the field strength, which is calculated by considering the dielectric properties and thickness of the glass and liquid crystal layers, and the applied voltage.

This is the first measurement of $e_1 - e_3$ of a material with a negative dielectric anisotropy of this magnitude ever attempted using a ULH method, and demonstrates a useful feature of the ULH alignment technique here; that it does not require the application of a field.

4.4.3 Conclusion of Nano-Grooves Method

In this section, it has been demonstrated that by applying a weak homeotropic alignment layer to a unidirectionally scratched glass surface, the orientational degeneracy of the ULH alignment can be broken to promote a single preferred direction. ULH textures obtained in this work form spontaneously without an electric field or flow-induced alignment, are stable over long periods of time, repeatable, and may be used with negative dielectric anisotropy materials, which up until now have been very difficult to align. The cells display a linear and sub-millisecond flexoelectrooptic response.

Periodic surface line structures have been shown elsewhere to stabilise the ULH and promote a single direction by seeding the lines of surface anchoring breaking associated with the topological incompatibility of the ULH confined by homogeneous alignment layers

[121]. The quasi-random surface structure created by polishing the glass may act as the necessary line structures to seed a unidirectional ULH formation as the cells cool from the blue phase. Similar nano-grooved structures have been shown to align nematic liquid crystals via an alternative mechanism [131]. This alternative mechanism could also be important, which would suggest that planar regions of the ULH texture have a lower elastic deformation if they align with the director parallel to the grooves. The helicoidal axis is perpendicular to the grooved surface treatment, in support of these hypotheses.

It is interesting to note differences between the method described here in which scratched surfaces provide orientational bias for the ULH, and the work by Carbone *et al* which employed a method for creating polymer channels [55]. In the former, the ULH helicoidal axis aligns perpendicular to the scratches. In the latter, the helicoidal axis aligns parallel to the micro-channels. There may be an intermediary geometry, in which both mechanisms for ULH alignment are co-existent. If the alignment surface had grooves that were much larger than the nano-scale scratches in the present work, adjacent grooves on opposite substrates could effectively create micro-channels if the cell gap were small enough, and the helicoidal axis would then align parallel to the grooves, via the same mechanism of alignment as the polymer channels method employed by Carbone. In the next section, such channels are fabricated using a mould-templating technique and are shown to result in a high-quality ULH alignment.

4.5 Mould-Templated Micro-Channels

While the previous method was successful at producing ULH alignment, the quality of the alignment and ease with which it can be implemented limit its application potential. In this section, an altogether different approach is undertaken. As was discussed in the last section, there has been one method for ULH alignment described in the literature that has produced a particularly high quality alignment. Carbone *et al* produced a reliable ULH texture, which was stable under thermal cycling and required no field- or flow-induced alignment [55]. The work employed a method for creating micro-channels using a complicated process reported

elsewhere [132], however the technique employed was too complicated for commercial exploitation.

A key difference between the micro-channels method and other methods is the ratio of the surface in contact with the liquid crystal to the bulk volume of the liquid crystal. This is hypothesised to be an important characteristic of the device if it is to produce a high quality ULH alignment. It is likely that using less complicated methods could reproduce the quality of alignment in the work by Carbone, as long as these methods increase the surface relative to the bulk liquid crystal.

In this section, a relatively straight-forward moulding technique is employed to produce similar channels to the work by Carbone [55]. Replica-moulding techniques have long been applied to create small structures, and recently, the use of Polydimethylsiloxane (PDMS) has proved successful for use in surface relief structures designed for liquid crystal alignment applications, and especially to promote bistability [133, 134, 135]. Surface structures can provide greater functionality, in some cases allowing for multiple stable configurations, providing new possibilities for alignment. Moulding techniques can produce structures that increase the surface area in contact with the liquid crystal relative to the bulk, which may be a key characteristic to allow high-quality alignment in ULH devices where other techniques have failed. Furthermore, similar relief structures are already used in commercial bistable liquid crystal devices (notably the Zenithally Bistable Nematic Device (ZBND), which also exploits a flexoelectric effect [130]), which demonstrates their economic viability. By considering the case of weak homeotropic anchoring, it is explained how the channels promote a high-quality texture.

4.5.1 Theory

Square Channels

While it is known that weak homeotropic anchoring promotes a randomly oriented ULH texture [124, 125], it is not necessarily clear why channels with homeotropic anchoring would favour a single direction of the ULH. Consider a channel with a square cross-section

and with weak homeotropic anchoring on each surface interface within the channel. In the case of weak homeotropic anchoring, there are negligible elastic distortions or defects due to surface interactions with a cholesteric material, and the surface energy per unit area is given by,

$$W_{\text{surface}} = \frac{W_0}{2}\big(1 - (\hat{\mathbf{n}} \cdot \hat{\mathbf{s}})^2\big) \tag{4.8}$$

as was given previously in equation 4.2. Let us define the z-axis parallel to the channel. In the case of a cholesteric material whose helicoidal axis is parallel to the channel, the director can be expressed as,

$$\hat{\mathbf{n}}_{\text{parallel}} = \begin{bmatrix} n_x \\ n_y \\ n_z \end{bmatrix} = \begin{bmatrix} \cos\theta \\ \sin\theta \\ 0 \end{bmatrix} \tag{4.9}$$

where $\theta = qz$. A cross section of the channel at an arbitrary value of z reveals a plane in which the director orientation does not vary. The director makes an angle θ with two of the surfaces, and $90 - \theta$ with the other two, as illustrated in figure 4.20. Therefore, the average surface energy density per unit area (using equation 4.8) taken over all four bounding surfaces of the cross-section, is given by,

$$W_{\text{surface}}^{\text{parallel}} = \frac{W_0}{4}\left(1 - \cos^2\theta + 1 - \sin^2\theta\right) = \frac{W_0}{4} \tag{4.10}$$

This is true for all values of z due to the relation $\sin^2\theta + \cos^2\theta = 1$. Now let us consider a cholesteric material whose helicoidal axis lies perpendicular to the channels, along, for example, the x-axis, and whose director can be expressed,

$$\hat{\mathbf{n}}_{\text{perpendicular}} = \begin{bmatrix} n_x \\ n_y \\ n_z \end{bmatrix} = \begin{bmatrix} 0 \\ \sin\theta \\ \cos\theta \end{bmatrix} \tag{4.11}$$

where $\theta = qx$, as illustrated in figure 4.20(b). For surfaces parallel to the y-axis, we have $(\hat{\mathbf{n}} \cdot \hat{\mathbf{s}})^2 = 0$, and for surfaces parallel to the x-axis, we have $(\hat{\mathbf{n}} \cdot \hat{\mathbf{s}})^2 = \langle \sin^2(qx) \rangle$. Therefore the average surface energy density per unit area taken over all four bounding surfaces of the cross-section, using equation 4.8, is given by,

$$W_{\text{surface}}^{\text{perpendicular}} = \frac{1}{2}\left(\frac{W_0}{2} + \frac{W_0}{2}\big(1 - \langle \sin^2 qx \rangle\big)\right) = \frac{3W_0}{8} \tag{4.12}$$

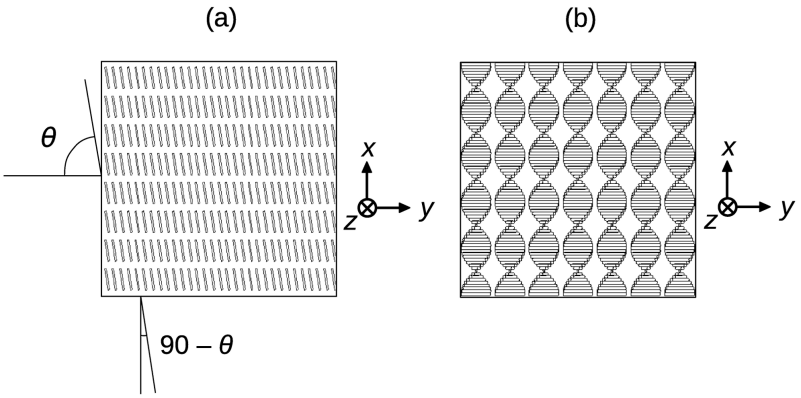

Figure 4.20: An illustration of a square cross-section of a channel filled with a cholesteric liquid crystal where the surfaces represent weak homeotropic boundaries. The director field is represented inside the cross-section for the cases where (a) $\theta = qz$ i.e. the helicoidal axis is parallel with the channel, and (b) $\theta = qx$ i.e. the helicoidal axis is perpendicular to the channel. By considering the surface energy in each case, it can be shown that case (a) has a smaller total surface energy.

Here, it has been assumed that the pitch is much less than the channel width, which allows the use of the average over an integer number of cholesteric pitch lengths.

Hence we find that $W_{\text{surface}}^{\text{perpendicular}}/W_{\text{surface}}^{\text{parallel}} = 1.5$, which means that in the case of a weak homeotropic anchoring, the surface energy is significantly lower for a cholesteric whose helicoidal axis is parallel to the channel than for one whose axis is perpendicular. The channels break the orientational degeneracy in ULH alignment energy, and therefore promote a spontaneous ULH alignment parallel to the channels.

Circular Channels

Incidentally, we can arrive at the same result for circular-cross-section channels. Circular channels are interesting because they are characteristic of capillary tubes and photonic band-gap fibres. Such structures filled with liquid crystal have been suggested for a variety of applications, including sensing [136], communications [137] and lasing [138]. DNA can form cholesteric phases, and there has been interest in being able to align the cholesteric structure to study the DNA [139, 140]. Alignment of chiral liquid crystal within circular channels has been studied before [141], although the regime in which the cholesteric pitch

is much smaller than the capillary diameter was not considered. For all of these reasons, it is interesting to consider the case of a short-pitch cholesteric within circular channels with homeotropic boundary conditions.

In the case of a circular capillary of diameter d, with its axis parallel to the z-axis, we can describe,

$$\hat{\mathbf{s}} = \begin{bmatrix} s_x \\ s_y \\ s_z \end{bmatrix} = \begin{bmatrix} \cos\left(\frac{\pi}{d}x\right) \\ \cos\left(\frac{\pi}{d}y\right) \\ 0 \end{bmatrix} \tag{4.13}$$

Now considering $\hat{\mathbf{n}}_{\text{parallel}}$ from equation 4.9, we find that,

$$\begin{aligned}(\hat{\mathbf{n}} \cdot \hat{\mathbf{s}})^2 = &\cos^2(qz)\cos^2\left(\frac{\pi}{d}x\right) + \sin^2(qz)\cos^2\left(\frac{\pi}{d}y\right) \\ &+ \cos(qz)\cos\left(\frac{\pi}{d}x\right)\sin(qz)\cos\left(\frac{\pi}{d}y\right)\end{aligned} \tag{4.14}$$

which, summing over x, y and z directions we find that,

$$\int_{z=0}^{\pi/q}\int_{x,y=0}^{d}(\hat{\mathbf{n}} \cdot \hat{\mathbf{s}})^2 dxdydz = \frac{1}{2} \tag{4.15}$$

Substituting into equation 4.8, we find that $W_{\text{surface}} = W_0/4$, which is the same result as for the square-cross-section channel in equation 4.10.

In the case that the helicoidal axis is perpendicular to the channel, we can consider $\hat{\mathbf{n}}_{\text{perpendicular}}$ in equation 4.9 and find that,

$$(\hat{\mathbf{n}} \cdot \hat{\mathbf{s}})^2 = \sin^2(qx)\cos^2\left(\frac{\pi}{d}y\right) \tag{4.16}$$

which, in this case, summing over x, y and z directions, gives 1/4. Substituting this into equation 4.8, we find that $W_{\text{surface}} = 3W_0/8$, which is the same result as for the square-cross-section channel in equation 4.10.

Hence, it has been shown that a circular cross section with homeotropic boundary conditions can also be used to align the helicoidal axis parallel to the channel.

4.5.2 Experimental

In contrast to the polymer channels in work by Carbone *et al* that were created post cell-assembly by UV exposure and subsequent polymerization of a reactive mesogen component

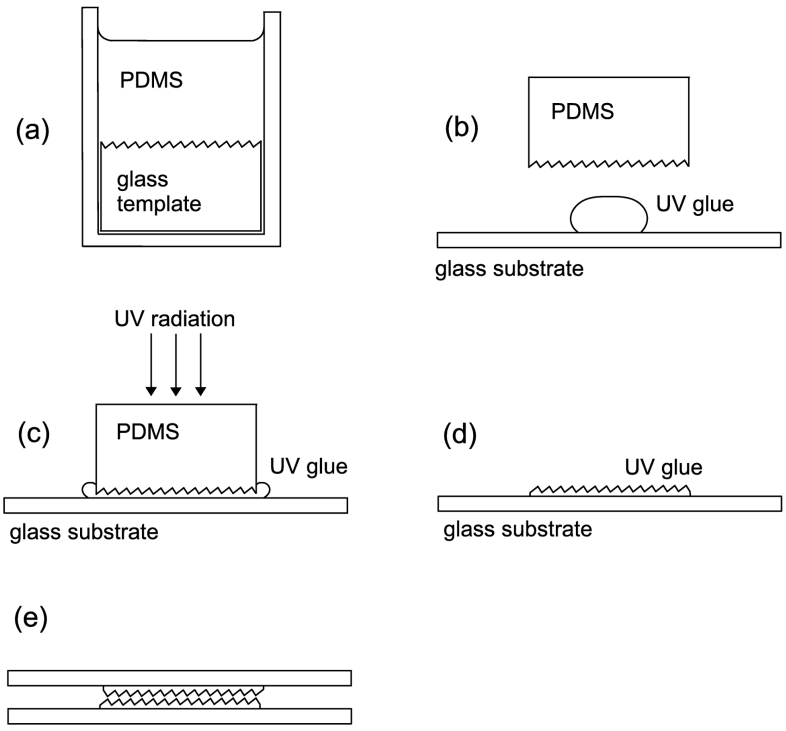

Figure 4.21: A schematic illustration of the process by which a micro-grooved substrate surface is produced (not to scale). (a) A mould of a blazed glass diffraction grating with pitch of 6.6 µm is made using polydimethylsiloxane (PDMS). (b) and (c) A drop of ultra-violet (UV) photo-curable glue is placed onto a glass substrate, and the PDMS mould is placed on top, such that the glue acquires the structure of the mould. (d) Once the glue is cured and the mould removed, the substrate is spin coated at 3000 rpm for 30 seconds with 0.1 w.t.% of lecithin in isopropyl alcohol, which is known to promote a homeotropic alignment [3]. (e) Finally, the cell is constructed using two of the micro-grooved substrates, creating the required polymer channels for ULH alignment.

in the liquid crystal mixture, here a periodic triangular relief pattern is produced on both top and bottom glass substrates prior to cell assembly, such that once assembled, the cell exhibits a similar polymer channel structure, with a roughly square cross-section. The procedure is illustrated and described in figure 4.21, and figure 4.22 shows a scanning electron micrograph of the resultant grooved surface structure. The grooved surface substrates are subsequently spin-coated for 30 seconds at 3000 rpm with 0.1w.t.% of lecithin disolved in isopropanol, which, as noted before, is known to provide a weak homeotropic alignment [3]. The cell is assembled without a spacer, and filled with a cholesteric mixture

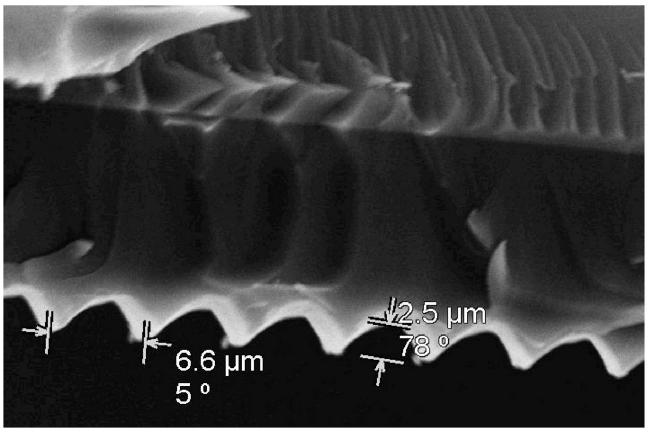

Figure 4.22: A scanning electron micrograph of a cross-section of the relief structure created using the method illustrated in figure 4.21. The cross-section is revealed after cleaving the glass substrate along a direction perpendicular to the grooved structure.

ZLI4792+2.7w.t.% R5011 chiral dopant (natural helicoidal pitch of mixture = 320 nm at room temperature) while heated to the isotropic phase. On cooling, the cholesteric material spontaneously adopts a ULH texture.

Figure 4.23 shows polarizing optical microscope images of a liquid-crystal cell prepared using the mould-templating technique. The cell shows a high level of extinction when the optic axis of the ULH is parallel to the polarizer (figure 4.23(a)), which results in a large contrast relative to when rotated to 45 degrees with respect to the polarizer (figure 4.23(b)). The apparent stripes from top-left to bottom-right visible in figure 4.23(b) are due to the grooves on the top and bottom surfaces not being exactly parallel to each other. The grooved pattern on top and bottom substrate surfaces therefore alternates between being aligned and in phase, and not aligned and out of phase, with a length scale determined by the groove width and the angle between top and bottom substrates. Only when the grooves on top and bottom are in phase does the resultant structure form a channel, which may explain the bands of light-leakage visible in figure 4.23(a). The grooves run from bottom-left to top-right in 4.23(b). The ULH texture returns on thermal cycling between isotropic and cholesteric phase, and does not require the presence of a field.

The cell gap thickness in cells with grooved structures is difficult to determine using the common method of analysing Fabry-Perot fringes of empty cells. This is due to the added

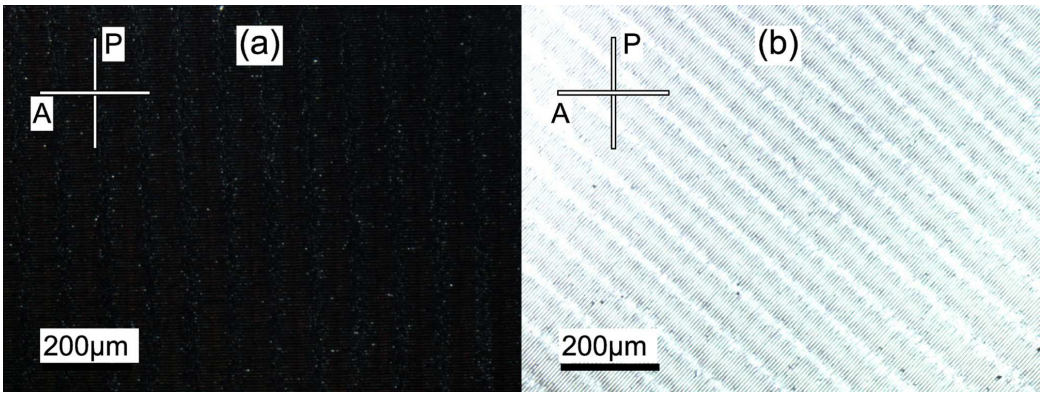

Figure 4.23: Optical polarizing microscope images (4X magnification, crossed polarizers) of a cell assembled from grooved substrates made using a mould-templating technique, and homeotropic surface anchoring. The cell is filled while the material is in the isotropic phase and allowed to cool into the ULH without any field application. The photographs show the same cell with the optic axis (a) parallel to the polarizer and (b) at 45 degrees rotation.

complexity of the grooved polymer structure. None-the-less, in cells that do spontaneously form a ULH texture, the white colour of the resultant birefringent structure when viewed between crossed polarizers with white illuminating light, suggests a cell thickness of less than 5 microns. In thicker cells, a ULH texture does not spontaneously form, and the liquid crystal often adopts a Grandjean state, as shown in figure 4.24.

In order to determine the optic axis orientation, and hence the orientation of the helicoidal axis relative to the channels, the device was observed with white light between crossed polarizers in series with a variable retarder (see §1.6.3). The colour of the transmitted light with the optical axis of the variable retarder parallel and perpendicular to the channels reveals the optic axis of the device by comparing the colour with a Michel-Levy chart [142] (see §1.6.3 for the method). This provided confirmation that the helicoidal axis runs parallel to the channels, supporting the discussion in §4.5.1.

Devices made using the technique exhibit the expected flexoelectrooptic response (a description of the electrooptic behaviour of ULH devices is given in §2.2), shown in figure 4.25. In order to apply a transverse field to the liquid crystal, ITO coated glass was used to make the liquid crystal cells. Note that in this case, a standard nematic has been used, which responds well to the homeotropic aligning lecithin layer. This means that the modulation is

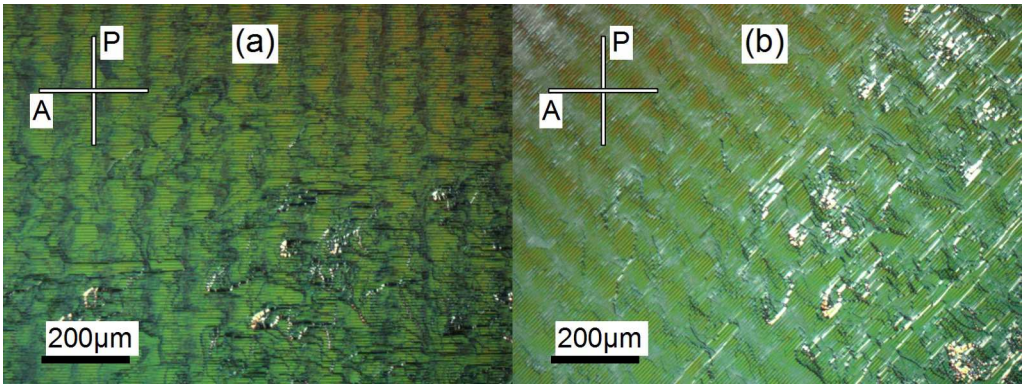

Figure 4.24: Optical polarizing microscope images (4X magnification, crossed polarizers) of a cell assembled from grooved substrates made using a mould-templating technique, and homeotropic surface anchoring. In this case, the cell is more than 20 µm thick, and a Grandjean structure forms. The photographs show the same cell with the micro-grooved structure (a) parallel to the polarizer and (b) at 45 degrees rotation.

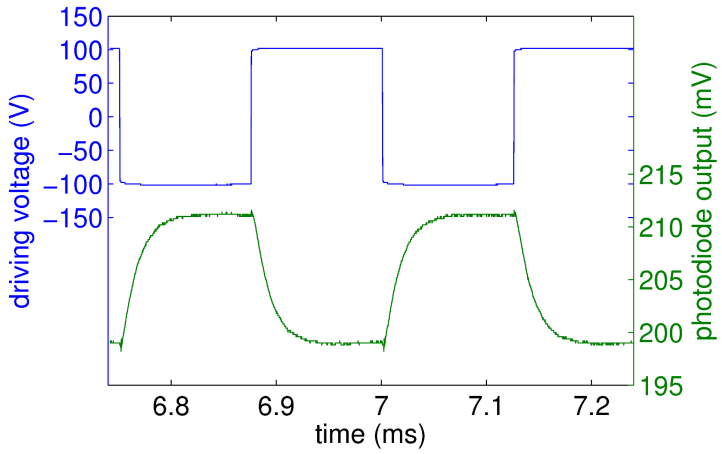

Figure 4.25: The electro-optic response of a Uniform Lying Helix device created using the replica-moulded surface relief structure substrates, as measured using a photo diode, is shown under the application of a square-wave driving voltage. The device is placed between crossed polarizers with the helicoidal axis of the ULH oriented at 22.5 degrees to the analyser. The electrooptic response is characteristic of the chiral flexoelectrooptic effect, with a response time of less than 100 µs. The large voltage amplitude of 100 V is used because the electrodes are positioned external to the cell, and so the field across the liquid crystal is small relative to the voltage.

small, compared with materials that have been optimised for flexoelectrooptic switching.

4.5.3 Conclusion of Micro-Channels Method

It has been shown how a replica-moulding technique can be used to create micro-channels, which align the helicoidal axis of a Uniform Lying Helix structure parallel with the channels by breaking the degeneracy in the surface energy of the helicoidal axis orientation. Cells made using the technique show a high level of extinction between crossed polarizers, providing the potential for greatly improved contrast for chiral-flexoelectrooptic technologies compared with other ULH alignment methods. Furthermore, the process is inexpensive, having the potential to be scaled for commercial applications. Closely related structures have already been commercially exploited in bistable liquid crystal devices, demonstrating their economic viability [130].

4.6 Conclusion

Summary

In this chapter, a methodological framework for successful ULH alignment has been developed in which a weak homeotropic anchoring is used to destabilise the Grandjean alignment relative to uniform lying helix alignment, allowing stable ULH alignment without the need for polymer networks, and an additional agent is used to break the degeneracy in the uniform lying helicoidal axis orientation in the plane of the cell. A series of different methods for ULH alignment within this framework have been investigated. First, Periodic homeotropic alignment conditions have been used to align cholesteric materials with relatively long pitches ($P = 14.8$ µm). Defects in the alignment were attributed to differences between the characteristic length scale of the printed structure and the cholesteric pitch. Second, in-plane switching fields were shown theoretically and experimentally to align the ULH via a combination of flexoelectric and dielectric field interactions, and it was shown how the inhomogeneity of the field produced by interdigitated electrodes is critical to the alignment method. The method was further extended to produce stable ULH alignment by

using homeotropic surface conditions. Third, nano-grooved surface structures were fabricated using a polishing compound, and found to break the orientational degeneracy in the ULH alignment orientation when used in cells with homeotropic alignment. Since the method does not rely on electric field to produce the alignment, it was possible to align a negative dielectric anisotropy cholesteric material, which allowed the first measurement of a negative dielectric anisotropy material's flexoelectric properties using a ULH method. Finally, it was shown theoretically how micro-channels of either circular of square cross section can produce ULH alignment by using surface energy considerations. A mould-templating technique was used to produce micro-grooved substrates that formed channels when assembled to make cells. Cholesteric liquid crystal filled into the cells was found to form a high-quality ULH alignment.

Final Remarks

Interest in the Uniform Lying Helix has waxed and waned in recent years as industry has tried and failed in cycles to solve the alignment problem, and research has moved to and fro between flexoelectricity in cholesteric structures and other potential fast-switching liquid crystal technologies, such as ferroelectric and blue phases [143]. With the work on ULH alignment presented here, there is now a serious case for taking development further. Relief structures similar to the ones used in this work, are a proven technology, having been used in over 5 million ZBD devices[1], and here, such structures have been shown to produce a highly reliable and stable ULH texture.

The remaining issue, which has thus far not been addressed, is that materials that exhibit the large flexoelastic ratios required for the technology tend to also be those that do not respond well to homeotropic alignment layers, which in this work are key to destabilising the Grandjean texture and allowing the ULH as the lowest energy configuration. One solution is to develop a homeotropic alignment and liquid crystal combination that works together and produces the required homeotropic alignment condition. In chapter 5, a bimesogen mixture is mixed with a mono-mesogenic material and is found to respond well to a homeotropic

[1] According to their website (`http://www.zbdsolutions.com/`).

alignment condition made using lecithin. Therefore, it may be that a combination of bimesogenic and mono-mesogenic materials will provide a good compromise between alignment and flexoelectrooptic switching. As has been mentioned previously, bent-core liquid crystals, which also do not typically respond to homeotropic alignment, have been found to respond well to trichloroocta-decyl silane in heptane [78]. Therefore, there is hope that a working combination of liquid crystal and homeotropic alignment method can be found.

In the next chapter, a method for exploiting dielectric and flexoelectric effects in helicoidal liquid crystals to allow state switching between Grandjean and ULH or focal conic configurations is described. The method relies on dispersion in the dielectric properties of a cholesteric material due to the contribution from the flexoelectric susceptibility. In addition, the application of the technique to reflective cholesteric technology is demonstrated.

Chapter 5

Flexoelectric Polarization Dispersion

5.1 Introduction

The previous chapters have been concerned with three key areas related to helicoidal liquid crystal systems: the measurement of liquid crystal parameters using electrooptic techniques; the enhancement of flexoelectric switching in cholesteric structures; and the alignment of the Uniform Lying Helix. There is a change of focus in this chapter, in which a new and versatile mechanism for allowing switching between states in cholesteric liquid crystals is described. The technique exploits the finite response time of the chiral flexoelectric effect and how this influences a material's frequency-dependent dielectric properties.

In the first half of the chapter, the contribution of flexoelectric polarisation to the dielectric susceptibility in helicoidal liquid crystals is formulated for the static equilibrium case, and further in the case of a time-varying field. The special case of a negative dielectric anisotropy nematic material is considered and experimentally shown to agree with the analytical theory. It is further demonstrated how relaxation of the flexoelectric contribution to the dielectric tensor in this special case can be exploited to switch between states in cholesteric liquid crystal structures by altering the applied time-dependent field amplitude under certain conditions. Counter examples are also given where the material's parameters are outside of the required constraints, and switching between states is not possible.

In the second half of the chapter, the exploitation of the effect in reflective cholesteric technology is demonstrated. Flexoelectric polarisation allows the device to be switched into a weakly-scattering focal-conic state at low frequencies, while at higher frequencies, the de-

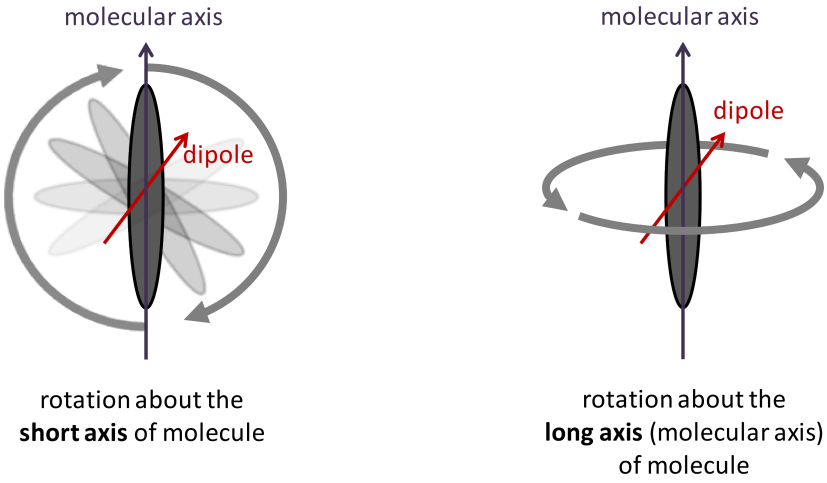

Figure 5.1: An illustration of possible rotations of molecules: (left) about the short axis and; (right) about the long axis. Rotation of the dipoles associated with the molecules contribute to the polarizability of liquid crystal materials. The polarization due to molecular rotation about the short axis takes a longer time to develop under the application of a field than the component due to rotations about the long axis, due to the difference in rotational viscosity about these axes.

vice is driven into the reflective Grandjean state. This non-conventional dual-frequency effect allows driving between states in both directions. A cross-over frequency as low as 300 Hz is demonstrated, orders of magnitude smaller than conventional dual-frequency effects, which typically have cross-over frequencies between 15 and 35 kHz [144, 145, 146]. Devices of various reflective colours are produced that have favourable contrast ratios, viewing angles, and switching behaviours at room temperature. The technique potentially affords a greater flexibility in surface alignment conditions, driving schemes, material parameters and use of polymer networks in reflective cholesteric devices than other switching methods.

5.2 Cholesteric State Switching using Flexoelectric Dispersion

5.2.1 Theory

Dielectric Dispersion in Liquid Crystals

Frequency-dependent dielectric relaxation in polar liquids has been extensively studied and results from a correlation between the mobilities of molecular dipole reorientations and

the time-dependence of macroscopic induced electric polarization [4, 5, 6]. As was briefly introduced in §1.3.2, in calamitic nematic liquid crystals, several dielectric relaxation phenomena have been studied [147, 148]. Since nematic materials are uniaxial, the dielectric permittivity is a tensor quantity, and the susceptibility can be considered as having several contributing mechanisms, each with respective time dependencies. In general, at optical frequencies, there is a complicated dispersion relation that depends on electron mobilities within molecules. However, at lower frequencies, the molecular dipoles can rotate and orient with an electric field. For uniaxial nematic materials, one can consider two such rotations; about the long and short axes of the molecule, as illustrated in figure 5.1. The rotation about the long axis is much faster, and in common room temperature thermotropic nematic liquid crystals, there is a relaxation at between 200 and 700 MHz due to this effect. This is in contrast to the rotation about the short axis, which relaxes typically between 10 kHz and 10 MHz [149, 150], and indeed materials have been engineered to relax at frequencies as low as 1 kHz [151]. The relaxation in the dielectric permittivity component parallel to the director can be described by,

$$\varepsilon_{\parallel} = \varepsilon_{\infty} + \frac{\varepsilon_{\mathrm{s}}}{1 + \omega^2 \tau_{\mathrm{s}}^2} \tag{5.1}$$

where ε_{∞} is in this case the permittivity at frequencies much greater than the relaxation frequency but lower than potential relaxation phenomena associated with contributions to the dielectric permittivity that are not related to the suppression of the rotation of dipoles about the short axis of the molecules, ε_{s} is the contribution to $\varepsilon_{\parallel}$ due to the rotation of dipoles about the short axis in the limit of low frequency, ω is the angular frequency of the driving electric field ($\omega = 2\pi f$ where f is the frequency), and τ_{s} is the characteristic time associated with the rotation of dipoles about the short axis. If ω is much greater than the relaxation frequency, then the denominator in equation 5.1 becomes much greater than 1, and the contribution to $\varepsilon_{\parallel}$ due to the rotation of dipoles about the short axis is suppressed. If as a result of the relaxation, $\varepsilon_{\parallel}$ becomes less than $\varepsilon_{\perp}$, then the dielectric anisotropy, $\Delta\varepsilon = \varepsilon_{\parallel} - \varepsilon_{\perp}$, changes sign. Since the dielectric energy is proportional to the dielectric

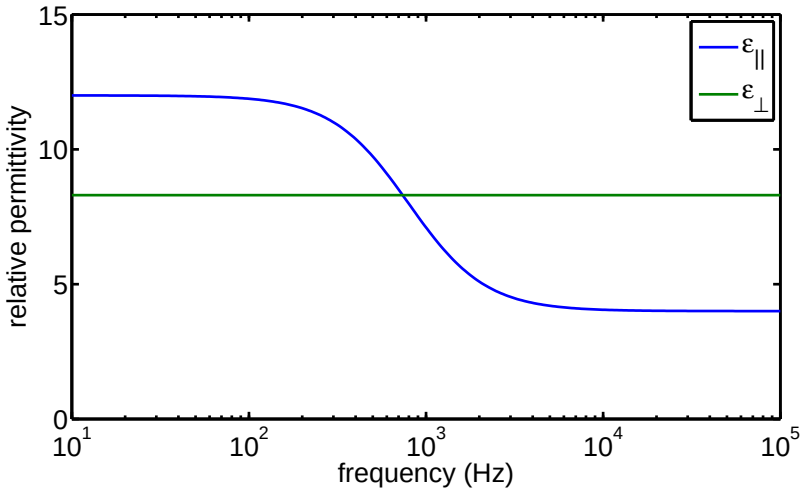

Figure 5.2: An illustrative plot showing an analytical model of the dielectric permittivity parallel and perpendicular to the liquid crystal director. A relaxation model of the form given in equation 5.1 is used, using parameters based on data presented in reference [151] for a dual-frequency liquid crystal. The relaxation in the dielectric permittivity parallel to the liquid crystal director causes $\Delta\varepsilon$ to change sign at the point at which $\varepsilon_{\parallel}$ and $\varepsilon_{\perp}$ cross over. There is no relaxation in $\varepsilon_{\perp}$ in the range of frequencies shown.

anisotropy by,

$$f_{\text{dielectric}} = -\frac{1}{2}\Delta\varepsilon\varepsilon_0(\hat{\mathbf{n}}\cdot\mathbf{E})^2 \tag{5.2}$$

then materials can be reoriented depending on the driving frequency as a result of the relaxation. Such materials are known as 'dual-frequency' liquid crystals, because they can be reoriented by applying different field frequencies [152]. The behaviour of $\varepsilon_{\parallel}$ and $\varepsilon_{\perp}$ is illustrated in figure 5.2, using models of the form given in 5.1. Parameters are based on data presented in reference [151] for a dual-frequency liquid crystal. The parallel permittivity has a relaxation at approximately 1 kHz, and crosses over the perpendicular permittivity.

Dielectric Dispersion due to Flexoelectricity in Cholesteric Systems

In cholesteric liquid crystals, the combination of a dipole and shape anisotropy of molecules leads to a chiral-flexoelectric polarization in the presence of an electric field [48] (see §1.3.4). This polarization contributes to the permittivity of the material, although it is not usually considered in this context. In this section, the chiral-flexoelectric contribution to the permittivity perpendicular to the helicoidal axis will be derived, and in §4.3.1, how this

contribution contributes to the free energy associated with the helicoidal axis orientation within a field was described. However, in this chapter, exploitation of the relaxation in the permittivity due to chiral flexoelectric polarization will also be considered, and exploited to produce a novel 'dual-frequency' effect in cholesteric liquid crystals.

The bend-splay distortion that is flexoelectrically coupled to the electric polarization is a macroscopic reorientation of the nematic director field, and takes a correspondingly large time, since it is dependent on a secondary coupling of the steric interactions of anisotropic molecules, and not on the primary statistical correlation function relating molecular dipole reorientations to polarization, which happens on a much shorter time scale. Indeed, the flexoelectric polarization typically relaxes out at between 100 Hz and 2 kHz, depending strongly on the chiral pitch and other material parameters.

We can consider the cholesteric as having a chiral but uniaxial symmetry where the axis of symmetry is the helicoidal axis. If the system is designed such that the difference in permittivity parallel and perpendicular to the helicoidal axis undergoes a sign reversal as a result of a frequency dependent relaxation of the flexoelectric contribution to the dielectric permittivity, then this system has the potential to be switched between states where the helicoidal axis is either parallel or perpendicular to the field. For example, the system may be switched between the so-called Uniform Lying Helix and Grandjean states, which were introduced in §1.6.3. The work presented here is the first time this switching ability has been considered or demonstrated, and provides a unique new functionality for technological applications.

In the next sections, the flexoelectric polarization is considered and its frequency -dependent contribution to the dielectric permittivity of the material is derived. The conditions that allow for state switching are described. Further, the relaxation is demonstrated experimentally in a material that has been engineered to have the necessary condition for state switching. Finally, the switching between Uniform Lying Helix and Grandjean states using a transverse field is demonstrated. The implications for various technological applications are commented upon, and include dual-mode and transflective displays. The

application to reflective display technology is developed in §5.3. Flexoelectric dispersion will also be considered in chapter 6, where it will be used to measure flexoelectric and dielectric contributions to the Kerr effect in blue phase liquid crystals.

Chiral Flexoelectric Effect

Consider, as we did in §1.8.2, a cholesteric liquid crystal whose director is described by,

$$\hat{\mathbf{n}} = \begin{bmatrix} n_x \\ n_y \\ n_z \end{bmatrix} = \begin{bmatrix} \cos qz \cos\phi \\ \sin qz \\ -\cos qz \sin\phi \end{bmatrix} \tag{5.3}$$

with a field applied perpendicular to its helicoidal axis. Recall from equation 1.77 in §1.8.2, that the free energy per unit length averaged over one pitch of the helicoid under the application of an electric field, after considering elastic and flexoelectric contributions to the free energy, for small angles, is approximated by,

$$\langle f \rangle \approx \frac{(K_1 + K_3)}{4} q^2 \phi^2 + E(e_1 - e_3)\frac{q\phi}{2} \tag{5.4}$$

where ϕ is the angle of the director about the applied field (where $\phi = 0$ when $E = 0$), e_1 and e_3 are the coefficients for flexoelectric polarization as originally defined by Meyer [8], K_1 and K_3 are the splay and bend elastic coefficients respectively, q is a wave number corresponding to the chirality of the cholesteric material, and E is the electric field component perpendicular to the helicoidal axis. Minimising this with respect to ϕ gives the well-known form for the tilt in the director about the component of the field perpendicular to the helicoid axis from §1.8.2, given by,

$$\phi = \frac{e_1 - e_3}{K_1 + K_3}\frac{E}{q} \tag{5.5}$$

This is the static equilibrium solution. Now, if we allow for a time varying field, and assume that the rate of change in ϕ is proportional to the change in $\langle f \rangle$, mediated by a viscous dissipation parameter, we can write,

$$-\gamma \frac{\partial \phi}{\partial t} = \frac{\partial \langle f \rangle}{\partial \phi} \tag{5.6}$$

where γ is the viscous dissipation parameter, which here we assume to be a constant. Substituting the free energy given in equation 5.4 into 5.6 we find that,

$$-\gamma\frac{\partial\phi}{\partial t} = \left(\frac{K_1+K_3}{2}q^2\phi + E(e_1-e_3)\frac{q}{2}\right) \tag{5.7}$$

For now, if we consider a time-varying field of the form $E = E_0e^{i\omega t}$ and a corresponding flexoelectric tilt of the form $\phi = \phi_0 e^{i\omega t}$, where i is the imaginary number and ω is an angular frequency, then we can substitute this into equation 5.7 and write,

$$\gamma i\omega\phi_0 + \frac{K_1+K_3}{2}q^2\phi_0 = -\frac{q}{2}(e_1-e_3)E_0 \tag{5.8}$$

which can be rearranged to arrive at the steady state oscillating response given by,

$$\phi_0 = E_0\frac{\left(\frac{(e_1-e_3)}{(K_1+K_3)q}\right)}{1+i\omega\left(\frac{2\gamma}{(K_1+K_3)q^2}\right)} \tag{5.9}$$

Note that for small frequency ω, the denominator tends towards unity and we recover the static equilibrium form given in equation 5.5. However, as $\omega \to \infty$, we find that $\phi_0 \to 0$. This means that the flexoelectric switching is suppressed at large enough driving frequencies.

Chiral Flexoelectric Polarization

The flexoelectric polarization is given by,

$$\mathbf{P}_{\text{flexoelectric}} = e_1\hat{\mathbf{n}}(\nabla\cdot\hat{\mathbf{n}}) + e_3(\nabla\times\hat{\mathbf{n}})\times\hat{\mathbf{n}} \tag{5.10}$$

where $\hat{\mathbf{n}}$ is the unit-magnitude local director [8]. By substituting the cholesteric director given in equation 5.3 into equation 5.10, taking the average over one pitch length and rearranging for ϕ, we find that,

$$\phi = -\frac{2\langle P\rangle}{q(e_1-e_3)} \tag{5.11}$$

where $\langle P\rangle$ is the component of the flexoelectric polarization that is parallel to the field, averaged over one pitch of the helicoid. We can again consider the case where there is a time-varying field, and hence find that,

$$\langle P\rangle(t) = E_0e^{i\omega t}\frac{\left(\frac{(e_1-e_3)^2}{2(K_1+K_3)}\right)}{1+i\omega\left(\frac{2\gamma}{(K_1+K_3)q^2}\right)} \tag{5.12}$$

Now, the relative dielectric permittivity is of the form,

$$\varepsilon_r(\omega) = \varepsilon_\infty + \frac{1}{\varepsilon_0}\frac{\partial\langle P\rangle}{\partial E} \tag{5.13}$$

where the second term on the right hand side is the extra contribution to the relative permittivity due to flexoelectricity. The ε_∞ for a field applied perpendicular to the helicoidal axis is given by,

$$\varepsilon_\infty = \frac{1}{2}(\varepsilon_\parallel + \varepsilon_\perp) \tag{5.14}$$

and is the dielectric permittivity contribution of the material at frequencies much higher than the relaxation frequency for the flexoelectric distortion (but for frequencies lower than any further relaxations in permittivity of $\varepsilon_\parallel$ or $\varepsilon_\perp$). Substituting the time-dependent expression for $\langle P\rangle$ given in equation 5.12, we find the relative permittivity, given by,

$$\varepsilon_{\mathrm{r}}(\omega) = \varepsilon_\infty + \frac{\varepsilon_{\text{flexo}}}{1 + i\omega\tau_{\text{flexo}}} \tag{5.15}$$

which has real (ε_r') and imaginary (ε_r'') components given by,

$$\varepsilon_{\mathrm{r}}' = \varepsilon_\infty + \frac{\varepsilon_{\text{flexo}}}{1 + (\omega\tau_{\text{flexo}})^2} \tag{5.16}$$

and,

$$\varepsilon_{\mathrm{r}}'' = \frac{\omega\tau_{\text{flexo}}\varepsilon_{\text{flexo}}}{1 + (\omega\tau_{\text{flexo}})^2} \tag{5.17}$$

respectively, where,

$$\varepsilon_{\text{flexo}} = \frac{1}{\varepsilon_0}\left(\frac{(e_1 - e_3)^2}{2(K_1 + K_3)}\right) \tag{5.18}$$

which is also the contribution to the relative permittivity due to the equilibrium flexoelectric polarization in the limit that $\omega \to 0$, and,

$$\tau_{\text{flexo}} = \frac{2\gamma}{(K_1 + K_3)q^2} \tag{5.19}$$

is the time constant corresponding to the flexoelectric contribution to the relative permittivity. The critical frequency, which defines the relaxation in $\varepsilon_r(f)$ due to flexoelectricity, is therefore given by,

$$f_{\mathrm{c}} = \frac{q^2}{4\pi\gamma}(K_1 + K_3) \tag{5.20}$$

Figure 5.3 illustrates the behaviour of ε_r' with typical liquid crystal parameters.

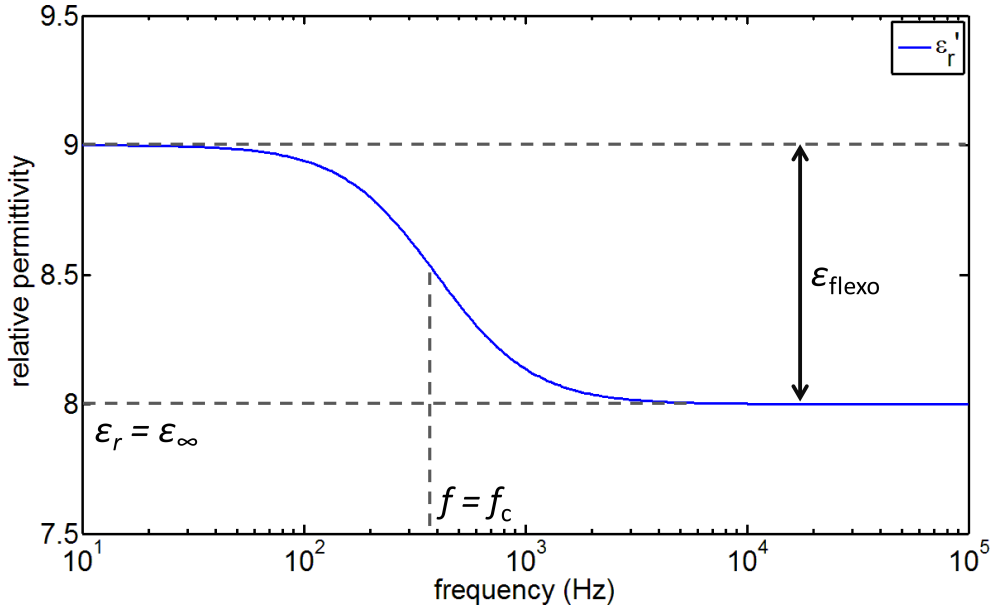

Figure 5.3: An illustrative plot showing the behaviour of the relative permittivity perpendicular to the helicoidal axis of a cholesteric material, of the form given in equation 5.16, using typical liquid crystal parameters. The contribution to the permittivity due to chiral flexoelectric polarization, $\varepsilon_{\text{flexo}}$, given in equation 5.18, relaxes at a frequency given by equation 5.20, and ε_∞ is given by equation 5.14.

Switching Between States

Now that key quantities related to the frequency dependent dielectric properties of the system have been derived, we can describe how the relaxation in the permittivity perpendicular to the helicoidal axis can be used to switch the helicoidal axis between being perpendicular and parallel with the electric field. In the case that the helicoidal axis is perpendicular to the field, we see from equation 5.16 that if $f \ll f_c$ then the relative permittivity is given by,

$$\varepsilon'_{\mathrm{r}(f \ll f_{\mathrm{c}})} = \varepsilon_\infty + \varepsilon_{\text{flexo}} \tag{5.21}$$

and for $f \gg f_c$, the relative permittivity is reduced to,

$$\varepsilon'_{\mathrm{r}(f \gg f_{\mathrm{c}})} = \varepsilon_\infty \tag{5.22}$$

where ε_∞ is given by equation 5.14. Furthermore, in the case that the helicoidal axis is parallel to the field, the relative permittivity is just $\varepsilon_\perp$, independent of the frequency. This

means that if the system is engineered in such a way that,

$$\varepsilon_\infty < \varepsilon_\perp < \varepsilon_\infty + \varepsilon_{\text{flexo}} \tag{5.23}$$

or, writing the expression out in full,

$$\frac{\varepsilon_\parallel + \varepsilon_\perp}{2} < \varepsilon_\perp < \frac{\varepsilon_\parallel + \varepsilon_\perp}{2} + \frac{1}{\varepsilon_0}\left(\frac{(e_1 - e_3)^2}{2(K_1 + K_3)}\right) \tag{5.24}$$

then we can ensure that by altering the frequency with which we address the liquid crystal, the lowest energy state will change between that with the helicoidal axis perpendicular, and that with the helicoidal axis parallel, to the field. By subtracting $\varepsilon_\perp$ from each part, it can be seen that a consequence of the above inequality is that $\Delta\varepsilon < 0$, where $\Delta\varepsilon = \varepsilon_\parallel - \varepsilon_\perp$. That is, the material must have a negative dielectric anisotropy. Further, we can extract the condition that,

$$\frac{(e_1 - e_3)^2}{(K_1 + K_3)} > -\Delta\varepsilon\varepsilon_0 \tag{5.25}$$

which constrains the relative strength of the dielectric and flexoelectric interactions.

As was discussed in chapter 4 (see §4.3.1), one can also give the difference in the free energy between the orientations of the helicoidal axis parallel and perpendicular to the field,

$$\delta f = \frac{1}{2}\Delta\varepsilon_{\text{effective}}\varepsilon_0 E^2 = \frac{1}{4}\left(\Delta\varepsilon\varepsilon_0 + \frac{(e_1 - e_3)^2}{K_1 + K_3}\right)E^2 \tag{5.26}$$

where $\Delta\varepsilon_{\text{effective}}$ is the effective macroscopic dielectric anisotropy of the cholesteric material (and δf is not to be confused with the driving frequency, f).

Finally, the frequency at which the states will cross over in energy will be where $\varepsilon_\perp$ is equal to the real part of ε_{r} given in equation 5.16, such that,

$$\varepsilon_\perp = \varepsilon_\infty + \frac{\varepsilon_{\text{flexo}}}{1 + (\omega\tau_{\text{flexo}})^2} \tag{5.27}$$

Using the relation $f = 2\pi\omega$, equation 5.27 can be rearranged for f to give an expression for the cross-over frequency,

$$f_{(\varepsilon_\perp = \varepsilon'_{\text{r}})} = \frac{1}{2\pi\tau_{\text{flexo}}}\sqrt{\frac{2\varepsilon_{\text{flexo}}}{-\Delta\varepsilon} - 1} \tag{5.28}$$

which, by substituting expressions for ε_∞, $\varepsilon_{\text{flexo}}$, and τ_{flexo} from equations 5.14, 5.18 and 5.19, can be written,

$$f_{(\varepsilon_\perp=\varepsilon'_{\text{r}})} = \frac{q^2}{4\pi\gamma}(K_1+K_3)\sqrt{\frac{(e_1-e_3)^2}{-\Delta\varepsilon\varepsilon_0(K_1+K_3)}-1} \tag{5.29}$$

Notice that this cross-over frequency is in general not equal to the critical frequency given in equation 5.20, and that $\Delta\varepsilon$ must be negative for there to be real solutions. In order for the cross-over frequency to be equal to the relaxation frequency of the flexoelectric switching, we must have,

$$\sqrt{\frac{(e_1-e_3)^2}{-\Delta\varepsilon\varepsilon_0(K_1+K_3)}-1} = 1 \tag{5.30}$$

which can be written as,

$$\varepsilon_{\text{flexo}} = -\Delta\varepsilon \tag{5.31}$$

In this section, how flexoelectricity contributes to the dielectric properties of cholesteric materials has been described. Further, it has been shown that by selecting a material with parameters that satisfy inequality 5.24, and by varying the driving frequency, one can control which state, either with the helicoid axis parallel or perpendicular to the applied field, has the lowest energy. In the next section, how this can be used to switch between states in a cholesteric liquid crystal device is demonstrated experimentally.

5.2.2 Experimental

In this section, measurements of the capacitance of a device as a function of frequency is used to show the relaxation in the permittivity due to flexoelectricity described in the last section. The flexoelectrooptic switching time while in the ULH geometry is shown to coincide with the characteristic relaxation frequency of the capacitance measurements. Finally, switching between Uniform Lying Helix and Grandjean geometries is demonstrated. Cases where the parameters of the liquid crystal do not allow switching between states are also demonstrated.

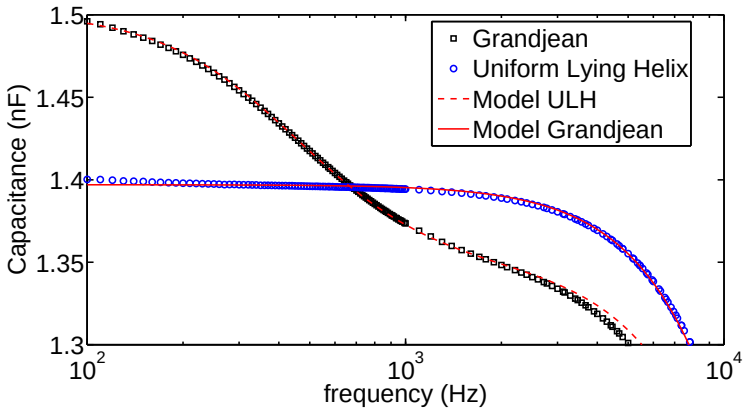

Figure 5.4: Capacitance measured as a function of frequency for a 5µm cell filled with a high $e_1 - e_3$, negative $\Delta\varepsilon$ material in both Uniform Lying Helix and Grandjean geometries. In the ULH geometry, the data show a relaxation in the effective dielectric properties of the material as the flexoelectric switching is suppressed at higher frequencies. Analytical relaxation models are also shown, and for the ULH is of the form given in equation 5.32, and for the Grandjean is of the form given in equation 5.33. The numerical values of the parameters determined are summarised in table 5.1.

Dielectric relaxation due to flexoelectricity

To prepare a suitable device, a liquid crystal mixture comprising 40% by weight of negative $\Delta\varepsilon$ nematic material MLC-7029 and 60% of high $e_1 - e_3$, low $\Delta\varepsilon$, chiral-doped bimesogen mixture MDA-1245 (both from Merck), having a pitch of approximately 600 nm, was capillary filled while in the isotropic phase into a cell with anti-parallel rubbed polyimide alignment layers. The cell is of thickness 5 µm, and has indium-tin-oxide on both substrate surfaces in order to apply a transverse field to the liquid crystal. A Uniform Lying Helix alignment was obtained by applying a 4 Vµm^{-1}, 100 Hz square wave driving field, which is thought to align the ULH by a combination of interaction with the alignment layer and an electrohydrodynamic effect [153, 42]. On removal of the field, the ULH is stable for several minutes before starting to revert to a Grandjean texture. A Grandjean geometry in the same cell was obtained with the application of 4 Vµm^{-1}, 2 kHz square wave driving field. Figure 5.4 shows the measured capacitance of the cell as a function of frequency for both ULH and Grandjean geometries. The amplitude of the signal used for the capacitance measurements was 100 mV, which is not large enough to switch the state of the cell. A relaxation model

Table 5.1: Parameters measured by fitting the analytical models given in equations 5.32 and 5.33 to the data, and converting capacitances into permittivities using the standard relation (see §1.3.3). The time constants and empty cell capacitance are also given.

$\varepsilon_{\text{flexo}}$	ε_∞	$\varepsilon_\perp$	τ_{F} (µs)	τ_{X} (µs)	C_0 (pF)
0.9	7.7	7.9	350	5.6	176

of the form,

$$C_{\text{ULH}}(f) = \frac{C_{\text{a}}}{1 + (2\pi f \tau_{\text{F}})^2} + \frac{C_{\text{b}}}{1 + (2\pi f \tau_{\text{X}})^2} \tag{5.32}$$

is used to fit the ULH capacitance data (c.f. equation 5.16). In equation 5.32, the parameter C_a is proportional to the low-frequency contribution to the relative dielectric permittivity due to flexoelectricity, $\varepsilon_{\text{flexo}}$, and τ_F corresponds to τ_{flexo}. The parameter C_{b} is proportional to ε_∞ from equation 5.14. The reason for the second relaxation, formulated in the denominator of the second term, is that the resistance of the ITO electrodes causes the measured capacitance to reduce to zero at very high frequencies ($\gtrsim$ 30 kHz). The parameter τ_X is the time constant associated with this effect.

From the theory, the Grandjean capacitance is not expected to vary with frequency, however, a model of the form,

$$C_{\text{Grandjean}}(f) = \frac{C_{\text{c}}}{1 + (2\pi f \tau_{\text{X}})^2} \tag{5.33}$$

is again used to account for the effect of the ITO resistance at high frequencies. The parameter C_{c} is proportional to $\varepsilon_\perp$. The values of C_{a}, C_{b} and C_{c} by converting to values of permittivity using $\varepsilon_r = C/C_0$, where C_0 is taken as the empty cell capacitance, are used to determine $\varepsilon_{\text{flexo}}$, ε_∞ and $\varepsilon_\perp$ respectively (see §1.3.3). The results are summarised in table 5.1, along with the time constants τ_{F} and τ_{X}.

The capacitance data show that for this material, there is a relaxation in the dielectric properties of the material when in the ULH geometry, such that the permittivity crosses over that of the Grandjean geometry at a frequency of approximately 700 Hz. Using the relaxation model, we find the characteristic time of the relaxation is 350 µs. This is supported by electrooptic measurements of switching in the ULH geometry, presented in fig-

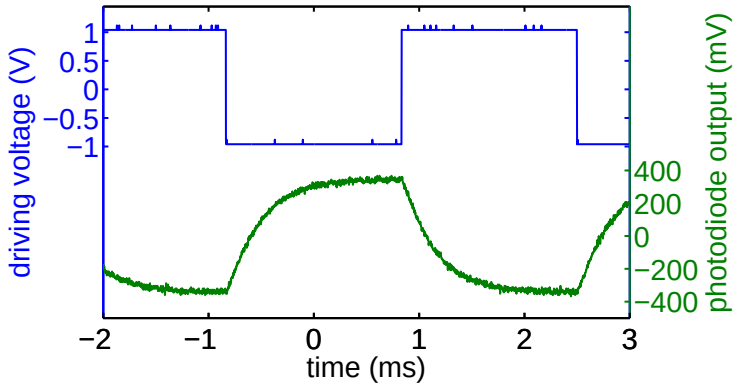

Figure 5.5: Electrooptic data of the ULH (bottom) being driven with a 1 V_{rms} square wave (top). The characteristic time of the switching is measured to be 330 µs, which is consistent with relaxation frequency observed in the capacitance of the device, and shows that the dispersion is due to flexoelectricity.

ure 5.5, which show a flexoelectric switching time constant of 330 µs. Using the values of τ_{flexo}, $\varepsilon_{\text{flexo}}$ and $\Delta\varepsilon$ determined, together with equation 5.29, would suggest a cross-over frequency of ≈ 750 Hz, in good agreement with the observed value in figure 5.4.

The capacitance data and electrooptic measurements have established that there is a relaxation in the relative permittivity of the cholesteric material, and that this relaxation is due to the suppression in the flexoelectric switching at high frequencies. It has further been demonstrated that the effective permittivity as a function of field frequency of the cholesteric material perpendicular to the helicoidal axis crosses over the permittivity parallel to the helicoidal axis. This allows a change in the lowest energy state of the liquid crystal at a cross-over frequency. Crucially, this change in the lowest energy configuration allows driving between lying helix and Grandjean configurations, opening up a previously unexploited method for switching between states that have considerable technological importance. In the next section, the ability to switch between states using the method is demonstrated.

Switching Between States

Figure 5.6 shows polarizing microscope images of the device for which capacitance and electrooptic characteristics have already been examined. The default state of the device,

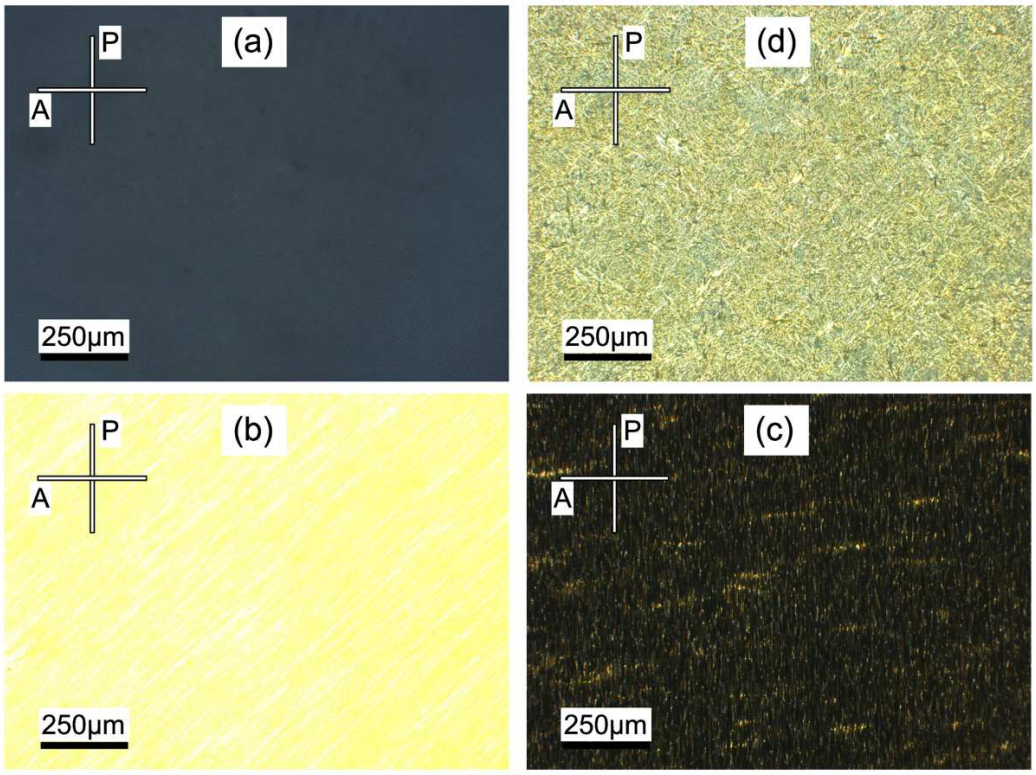

Figure 5.6: Polarizing optical micrographs taken at 10X magnification of the three textures that have been accessed in this work using the mechanism described. (a) The Grandjean texture, accessed using 2 kHz, 20 V_{rms} applied transverse to the liquid crystal film. The ULH texture, accessed by applying 100 Hz and 20 V_{rms} from either Grandjean or focal conic textures, with its optic axis at (b) 45°, and (c) 0° to the polarizer. (d) The focal conic texture, accessed by applying a 300 Hz, 20 V_{rms}.

shown in figure 5.6(a), is the Grandjean geometry. From this, there are two other states that are easily accessible. With the application of a 100 Hz square wave field of amplitude 4 $V\mu m^{-1}$, the cell will spontaneously form the ULH, shown in figure 5.6(b) and (c), if left with this driving regime for several seconds. Since the material has a negative dielectric anisotropy, the dielectric torque due to the microscopic dielectric anisotropy cannot be responsible for the reorientation of the helicoidal axis to be in the plane of the device, and therefore flexoelectricity must be responsible. It is thought that the ULH forms due to an electrohydrodynamic effect, in which flow is induced by the movement of charge carriers, and results in a uniform helix orientation alignment that is related to the direction of the planar surface treatment [153, 42]. Such electrohydrodynamic effects are not present at field

frequencies above approximately 200 Hz. On removal of the field, the texture will begin to revert slowly to the Grandjean texture after several minutes. Starting from the Grandjean texture, if a field of frequency 300 Hz is applied, then rather than form the ULH, the cell will form the focal conic texture, shown in figure 5.6(d). This may be because at this frequency electrohydrodynamic effects, which appear to be important in promoting a uniform helix axis orientation, are suppressed. By choosing a frequency between 100 and 300 Hz, it is possible to produce states that are intermediary between ULH and focal conic, with varying degrees of bias in the orientation of the helicoidal axis towards a uniform direction. From the ULH or focal conic, the cell can be driven back to the Grandjean geometry, with the application of a 2 kHz field (where $f > f_{\varepsilon_\perp = \varepsilon'_r}$). Hence, we have the ability to drive the liquid crystal between lying helix and Grandjean geometries.

The time taken to switch between the Grandjean and focal conic textures depends on field strength. In the case of an applied field of 8 $V_{rms}\mu m^{-1}$, switching in either direction by modulating the frequency involves a fast initial switch process that takes approximately 100 ms, and a longer settling of the texture as defect structures are formed or annihilate that takes up to a second. In §5.3.1, this switching is examined in more detail in a related device.

In this section, the ability to switching between Grandjean and ULH or focal conic states, in a time of approximately 100 ms, simply by altering the driving frequency, has been demonstrated in materials that have a negative dielectric anisotropy, and whose flexoelectric polarization contribution can increase the effective permittivity to be greater than $\varepsilon_\perp$. The values of the parameters of the liquid crystal that allow this switching, which is due to flexoelectric dispersion, must satisfy the inequality given in equation 5.24. In the next section, cases where the liquid crystal parameters do not satisfy this inequality are also considered for comparison.

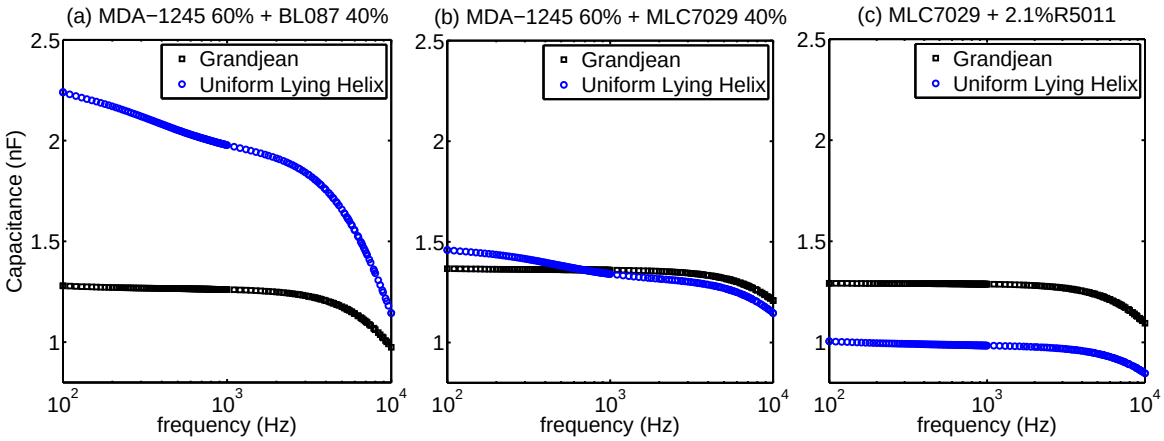

Figure 5.7: Capacitance as a function of frequency is shown for two control devices (left and right) that are filled with materials whose parameters do not satisfy the inequality in equation 5.24 and hence to do not have a switching capability. The ULH and Grandjean capacitances in these control cases do not cross over as a function of frequency. The central plot is from a device filled with a material whose parameters do satisfy the inequality, in which the capacitances do cross, and is presented for comparison.

Cases that Preclude Switching

In the previous sections, a single device that was filled with a material with parameters that satisfy equation 5.24 was examined. However, as controls, two further examples that are incapable of switching are provided here.

Figure 5.7 shows capacitance data for cells filled with three different mixtures. In the first case in 5.7(a), the mixture comprises 60 wt% MDA1245 and 40 wt% BL087. In this case, there is a large flexoelectric contribution at low frequencies in the Uniform Lying Helix (ULH) due to the MDA1245 (a requirement for switching). However, the BL087 has a positive dielectric anisotropy, which means that the Grandjean state always has a lower capacitance than the ULH state, and there is no possibility of switching because there is no change in which state has the lowest energy.

In the second case, shown in 5.7(b), the results from the same material whose capacitance is also shown in figure 5.4 are repeated here for comparison with the control cases. The material parameters satisfy equation 5.24; a 40 wt% MLC7029 component gives the material a negative dielectric anisotropy, and 60 wt% MDA1245 component allows a flexoelectric contribution to the dielectric properties that is sufficient to change which helicoidal

axis orientation has the lowest energy state, therefore allowing switching between states.

In the final case, shown in 5.7(c), the mixture comprises MLC7029 (negative dielectric anisotropy nematic) with 2.1 wt% R5011 chiral additive (to make the material a cholesteric). In this case, the material has a negative dielectric anisotropy (a requirement for switching), however it does not have a sufficient flexoelectric contribution to lift the capacitance of the ULH higher than the Grandjean state at low frequencies. Hence, there is no cross-over in dielectric properties as a function of frequency and no possibility of switching in this case.

These examples further illustrate that the capability to switch between Grandjean and lying states relies on choosing parameters that satisfy equation 5.24. The ability to switch between states has potential for application, and in §5.3, potential applications for such a switching capability are discussed.

5.2.3 Discussion

The states that are achievable using the switching mechanism described in this work are ones of considerable current and potential future application in display and other electrooptic technology. By selecting the pitch of the material, the Grandjean geometry has been proposed for ultra-fast transmissive displays [58, 19], and has also been commercialised as a reflective technology [28, 29, 30]. The focal conic texture is optically isotropic and weakly scattering, and has been suggested for use in reflective display technology, including bistable modes [42, 144, 145, 146, 41, 43, 44, 45, 46, 154, 155]. The ULH has long been developed for use as a transmissive display technology [53, 54, 55, 56, 57, 42], having major advantages over existing technology, including sub-millisecond switching times and the possibility of having an in-plane rotation of the optic axis without the need for complicated interdigitated electrode structures. Additionally, switching between states in cholesteric materials has been proposed for use in privacy windows and light shutters (using, for example, polymer dispersed cholesteric liquid crystals) [156], in switchable diffraction gratings [157] and in other optical components. The ability to switch between Grandjean and lying helix states, as demonstrated in this chapter, leads to the potential of adding value to

the body of research that has gone into the aforementioned cholesteric technologies by allowing the exploitation of multiple functionalities in a single device and providing a new mechanism for switching cholesteric liquid crystals.

In the next section, the use of switching based on flexoelectric dispersion in reflective cholesteric technologies is explored, and several devices are demonstrated and characterised.

5.3 Switching in Reflective Cholesteric Displays

Bistable reflective cholesteric liquid crystal display technology usually relies on two key states in its operation. The focal-conic state, in which the cholesteric helicoidal axis is non-uniform and forms randomly oriented domains, is weakly scattering. When used in front of a dark light-absorbing material, this state provides the dark, non-reflective state. The second state is the Grandjean geometry, in which the helicoidal axis is uniformly perpendicular to the cell normal. As was discussed in §1.6, the pitch can be chosen such that the material reflects light of wavelengths λ commensurate with the pitch P of a cholesteric material with average refractive index n, by the relation $\lambda = nP$, thereby producing a bright, reflective state.

Reflective displays that exploit these two states have been researched for some time and are commercially available [30, 28]. Typically, the cholesteric material will have a positive dielectric anisotropy, and with a transverse field a focal conic texture forms. A mechanism for recovering the Grandjean state is a key issue, and there have been three main ways in which this has been achieved: thermal cycling; dielectric helix unwinding followed by elastic relaxation; and utilising dual-frequency materials. By heating the material, the pitch can increase, making the Grandjean more stable, and allowing the device to be switched through an annealing process [154, 155]. The second method involves applying a large field that unwinds the helicoid into a uniformly homeotropic state [41, 42, 43, 44, 45, 46]. On removal of the field, the Grandjean state is recovered. This is often combined with a polymer network in order to provide bistability or to speed up the process [158]. Finally, by

using a dual-frequency material, in which the contribution to the material's polarisability due to the longitudinal molecular dipole component relaxes at a sufficiently small frequency (usually about 15 to 35 kHz), the cholesteric material can be switched to the Grandjean state by driving at a frequency at which the material has a negative dielectric anisotropy [144, 145, 146].

In this section, the mechanism described in §5.2 is exploited for the first time to produce the necessary switching between Grandjean and focal conic states for use in reflective display technology. Capacitance measurements are used again to demonstrate the effect of flexoelectric dispersion and how it is affected by pitch. Measurements of transmission spectra, switching times, contrast ratios and photographs of the cells in both states accessible using the technique are presented. The advantages of exploiting flexoelectric polarization over existing switching methods, which include permitting a greater flexibility in choice of surface alignment conditions, driving schemes, material parameters and use of polymer networks, are commented on. Finally, some suggestions are provided for improving the devices' performance.

5.3.1 Experimental

A liquid crystal mixture comprising 40% by weight of a commercially available negative dielectric anisotropy room-temperature nematic MLC-7029 and 60% by weight of high flexoelectricity, bimesogenic MDA-10-4409 liquid crystal, was doped with small amounts of high-twisting-power chiral additive R5011, in order to obtain a range of desired pitch lengths. The material has the parameters necessary for state switching, that were described in §5.2.1. Three mixtures were filled into planar-aligned cells and allowed to form the Grandjean texture, and their Bragg reflection maxima, as measured on a spectrometer, are centered on 480, 540 and 590 nm (see §1.6.2). The mixtures were then capilliary filled in the isotropic phase into 5 micron thick cells, with homeotropic surface alignment conditions, that had been produced with conducting indium-tin-oxide electrodes on top and bottom substrate surfaces in order to apply an electric field. This is in contrast to most reflective

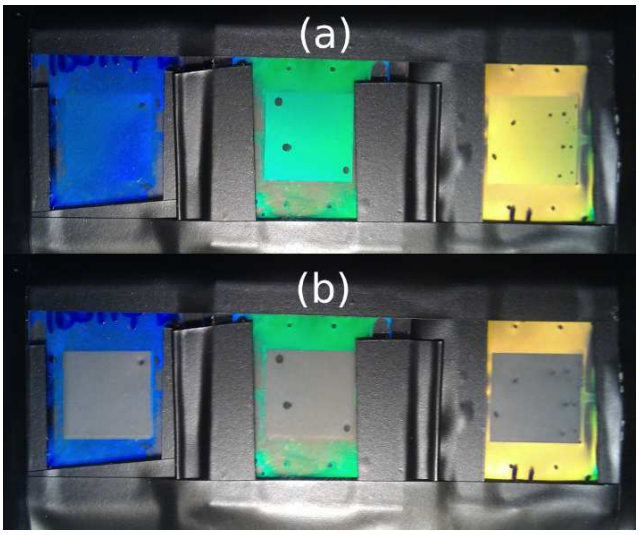

Figure 5.8: Photographs taken of three cells filled with materials with different proportions of chiral dopant that can be switched by exploiting flexoelectric dispersion between (a) the Grandjean state, accessed by driving the cell with 5 kHz, 10 V_{rms} µm^{-1}, and (b) the weakly scattering focal conic state, after the application of 10 V_{rms} µm^{-1} at 100 Hz. The textures are stable on removal of the field.

cholesteric technologies, which commonly use planar surface alignment conditions to allow the planar Grandjean state to be accessed via an elastic interaction with the surface [41, 42, 43, 44, 45, 46]. Here, however, because this mechanism for switching is not relied upon, a homeotropic anchoring has been chosen to demonstrate the technology, which increases the viewing angle without the need for a polymer network. All of the following measurements were taken at 25°C.

On application of 5 kHz, 10 V_{rms} µm^{-1}, the material is driven into the Grandjean texture. This is because at this frequency, the flexoelectric contribution to the dielectric properties is suppressed, and the component of the effective permittivity parallel to the helicoidal axis of the cholesteric material is larger than the component perpendicular. Consider the relative free energy of the cholesteric within the field, given by,

$$\delta f = \frac{1}{2}\Delta\varepsilon_{\text{effective}}\varepsilon_0 E^2 = \frac{1}{4}\left(\Delta\varepsilon\varepsilon_0 + \frac{(e_1 - e_3)^2}{K_1 + K_3}\right)E^2 \tag{5.34}$$

which was also given in §5.2.1. For the free energy given by equation 5.34 to be minimised, ignoring the flexoelectric term that includes $(e_1 - e_3)$ (because it is suppressed at high frequency due to the finite switching time of the flexoelectric polarization) and considering

that $\Delta\varepsilon$ is negative, the helicoidal axis must be parallel to the field. The Grandjean state is stable for long periods once the field is removed. This is because the surface interaction is weak, and causes minimal reorientation of the liquid crystal. Photographs of the devices in figure 5.8(a) show a range of colours of the Bragg-reflected light that can be achieved in the Grandjean state.

On application of 100 Hz, 10 V_{rms} μm^{-1}, the devices are driven into the focal conic state, shown in figure 5.8(b), which is also stable for long periods. Again, referring to equation 5.34, at low frequencies, the flexoelectric polarization contribution to the effective dielectric anisotropy of the cholesteric material is larger than the magnitude of the contribution arising from the contribution from term that includes $\Delta\varepsilon$, and so the free energy is minimised when the helicoidal axis is perpendicular to the applied field.

Since the materials have pitches that are commensurate with optical wavelengths, they reflect visible light while in the Grandjean state, as was discussed in §1.6.2. The Bragg behaviour in the Grandjean state and scattering efficiency in the focal conic state is illustrated by transmission spectra of the devices, shown in figure 5.9. Under the application of 5 kHz, the three devices show dips in transmission consistent with a Bragg reflecting Grandjean texture, and the Bragg behaviour is completely absent once the cells are driven into the focal conic state, where they have almost identical transmission characteristics, consistent with a weakly scattering focal conic state. The states are confirmed with polarizing microscopy. These cells therefore demonstrate switching between reflective and transmitting states across a range of possible wavelengths.

To demonstrate the cross-over in the dielectric properties of the two stable states due to dispersion in the flexoelectric polarisation, frequency-dependent capacitance, in the vicinity of the cross-over frequency, is shown in figure 5.10. The cross-over frequency was derived in §5.2.1 and given in equations 5.28 and 5.29. At frequencies below the cross-over frequency, for a given material, the focal conic state has a larger capacitance than the Grandjean state, and at frequencies above the cross-over frequency, the focal conic capacitance is lower than the Grandjean. A larger capacitance implies a larger effective dielectric

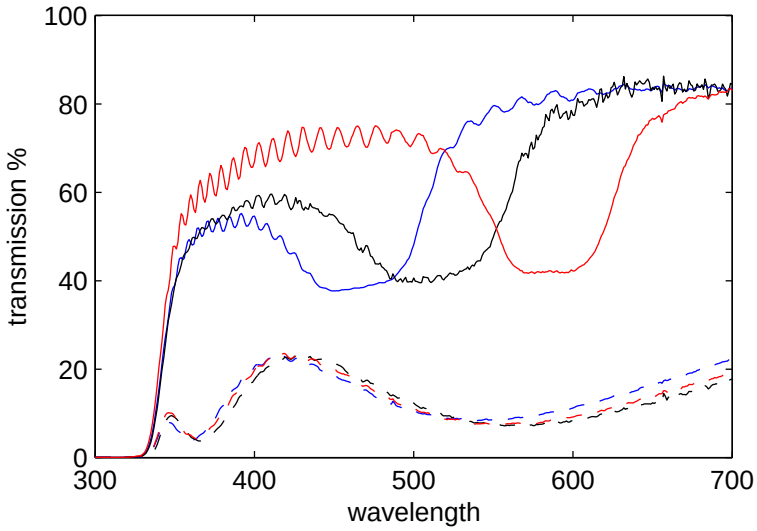

Figure 5.9: The transmission spectrum of the devices under the application of 10 V_{rms} µm^{-1} at 5 kHz (solid lines) and 100 Hz (dashed lines). The spectra are consistent with a Bragg reflecting Grandjean state when driven with 5 kHz, and with a weakly scattering focal conic state when driven with 100 Hz. Blue, black and red lines correspond to cells with measured Bragg peaks of 480, 540 and 590 nm respectively.

permittivity, and the larger component of the permittivity will have a tendency to reorient parallel to the applied field, in order to minimise the electric potential energy. Materials with different pitches show slightly different cross-over frequencies of 460, 370 and 300 Hz for materials with Bragg reflection peaks centred on 480, 540 and 590 nm respectively. Recall from equation 5.29, that the cross-over frequency $f_{(\varepsilon_\perp=\varepsilon'_r)} \propto 1/P^2$. Therefore, we expect that $f_{(\varepsilon_\perp=\varepsilon'_r)}(nP)^2 = \text{constant}$, where nP is the Bragg reflection peak frequency. The three pitch cases shown in figure 5.10 all have $f_{(\varepsilon_\perp=\varepsilon'_r)}(nP)^2 = 1.05 \times 10^8$ Hz(nm)^2, within 2% of one another.

Note that while the cross-over frequency is pitch dependent, the inequality that describes the constraints on the liquid crystal parameters that allow for state switching via flexoelectric dispersion, given in equation 5.24, does not involve the pitch, and therefore the ability to switch between states is unaffected by pitch variation. Moreover, the cross-over frequency in these cells is between 300 and 500 Hz, orders of magnitude smaller than the typical $\varepsilon_\parallel$ relaxation frequency in specially engineered dual-frequency materials used in this context [145, 146].

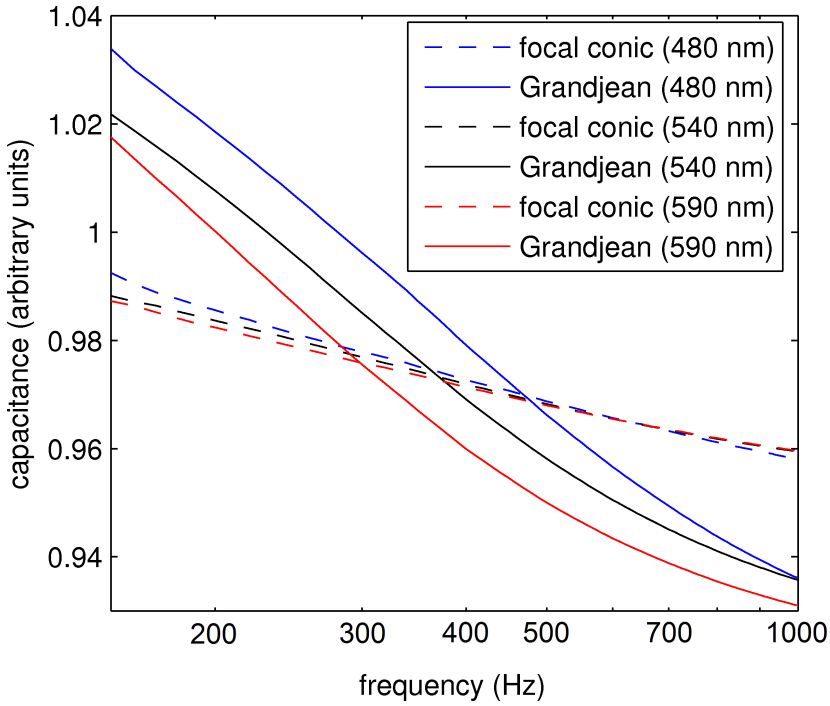

Figure 5.10: Capacitance as a function of frequency (using 100 mV test voltage) for cells filled with mixtures whose Bragg reflection maxima centre on 480, 540 and 590 nm, while in stable focal conic and Grandjean states. The capacitance is related to the dielectric permittivity via $C = C_0\varepsilon_{\text{effective}}$ where $\varepsilon_{\text{effective}}$ is given by equation 5.16 in the case of the focal conic and by equation 5.14 in the case of the Grandjean states. Dispersion in the flexoelectric polarisability causes a cross-over in the frequency-dependent dielectric properties of the focal conic and Grandjean states at a frequency that depends on pitch (see equation 5.29) at between 300 and 500 Hz, enabling a frequency-addressed switching between the two states.

To demonstrate further the relationship between the switching behaviour and the cholesteric pitch, a planar surface treated cell was capillary filled simultaneously from each side with different two liquid crystal mixtures, each comprising of 40 wt% MLC-7029 and 60 wt% of MDA-10-4409 liquid crystal, and therefore having the appropriate condition for switching via flexoelectric dispersion, but differing in chiral dopant concentration so as to have Bragg reflection maxima at 940 and 480 nm. Filling the cell simultaneously with two different mixtures from opposite sides results in an interficial region in which the two materials mix, and the concentration of chiral dopant and resultant pitch varies over the cell. Polarizing microscope images of this cell are shown in figure 5.11. The cell shows a pitch variation that results in discrete pitch jumps in the Grandjean state, due to the planar surface

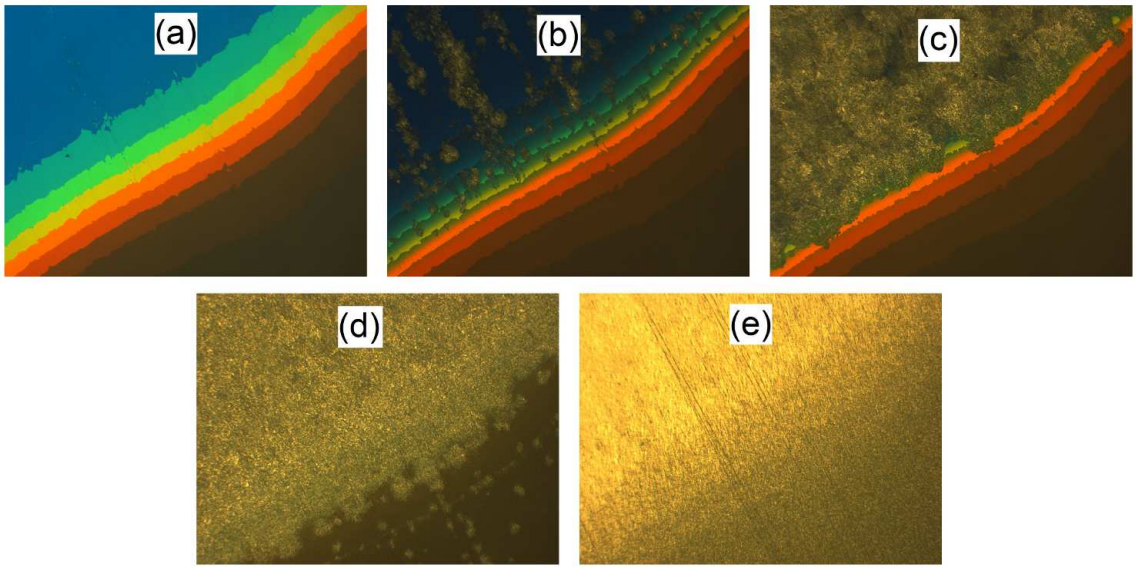

Figure 5.11: Optical polarizing microscope photographs of a cell in which there is a gradient in the chiral dopant, which results in discrete pitch jumps while the liquid crystal is in the Grandjean state. An applied field of 32 V_{rms} μm^{-1} is applied with a frequency of (a) 5 kHz, (b) 200 Hz and (c) 200 Hz a moment later, (d) 110 Hz, and (e) 50 Hz. The field switches the Grandjean into a focal conic state when the frequency is below the cross-over frequency, which depends upon the pitch.

constraint, which only allows half-integer numbers of pitches across the cell thickness. As the driving frequency is decreased from 5 kHz to 50 Hz, the cross-over frequency is passed and switching to the lying-helix state occurs, first for the short-pitch region in which the cross-over frequency is high, and then the shorter pitch regions, until the entire cell has switched to the lying helix state at 50 Hz.

To study the electrooptic characteristic of the switching, a light emitting diode with a peak frequency of 525 nm was used to illuminate at normal incidence the liquid-crystal device with a Bragg reflection peak centred on 540 nm. The experimental arrangement is shown in figure 5.12. A black, light-attenuating structure was positioned behind the device, which was driven between focal conic and Grandjean states with the application of 10 $V_{rms}\mu m^{-1}$ that cycled between 100 Hz and 5 kHz. The cell pixel was imaged onto a photo diode in order to measure the reflected intensity at a test-angle of approximately 15 degrees, which was chosen to avoid directly reflected light from the glass-air interface of the cell reaching the photo diode. The normalised reflection intensity as a function of time is

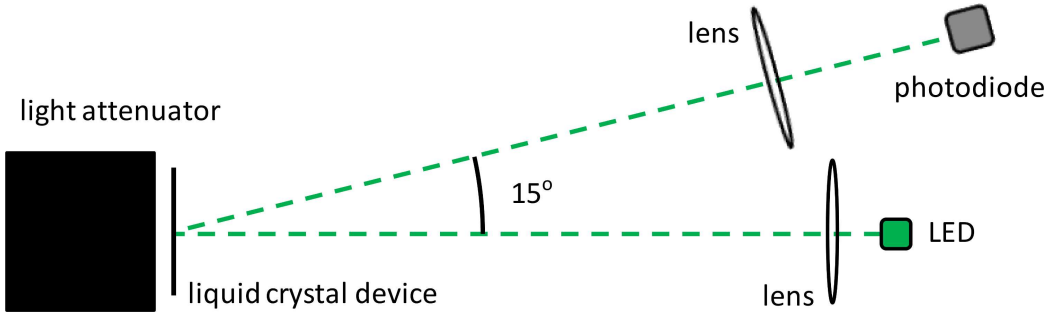

Figure 5.12: A schematic diagram of the experimental arrangement used to measure the electrooptic characteristics of the device with a Bragg reflection peak centred on 540 nm. Light from a light emitting diode (LED), columnated by a lens, is incident at 0 degrees onto the liquid crystal device. An image of the device is focused onto a photo diode, such that the photo diode, device, and LED make an angle of 15°. The green line illustrates the path of the light taken from the LED to the photo diode, however, the device while in the Grandjean geometry reflects light over a wide range of angles (not shown).

shown in figure 5.13. The transition from Grandjean to focal conic state is remarkably fast at under 5 ms, however the focal conic to Grandjean transition has a characteristic switching time (the time for the intensity to reach $1/e$ of its value after a change in the driving frequency) of 520 ms. These times are typical of switching between focal conic to Grandjean states reported elsewhere using other switching mechanisms. For example, switching from the focal conic to the Grandjean via an intermediary unwound homeotropic state takes about 300 ms or more [159], and traditional dual frequency materials have been reported to allow switching from focal conic to Grandjean states of between 240 and 450 ms, depending on surface alignment treatments [146]. Switching from Grandjean to focal conic has been reported to be of the order of milliseconds, using both alternative switching mechanisms [159, 146], similar to the switching time of 5 ms in our systems. The reflected intensities of Grandjean and focal conic states provide a reasonable contrast ratio of 5:1.

Measurements of the reflected intensity at angles other than 15° have not been taken. However, from inspection of the cells under illumination, it can be seen that the devices reflect light over relatively wide viewing angle. The wide angle observed in devices with homeotropic surface alignment is in contrast to devices with planar alignment, which only show strong reflection at angles equal to the incident angle of the illumination.

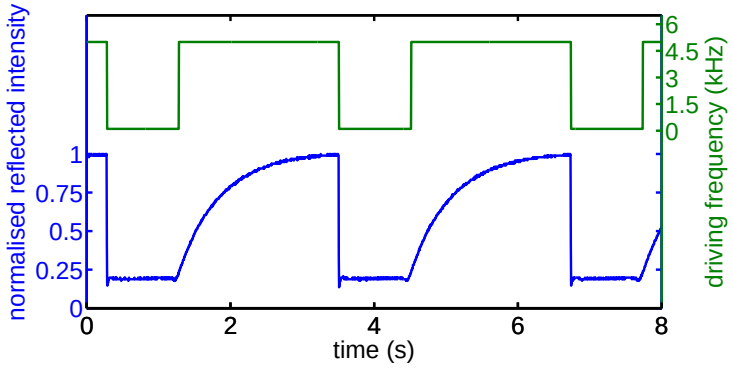

Figure 5.13: The normalised intensity of reflected light, which is normally incident on the device, at a reflection angle of 15 degrees (see figure 5.12), for the cell with a Bragg reflection peak of 540 nm, as a function of time. The cell is addressed with 10 $V_{rms}\mu m^{-1}$ that cycled between 100 Hz and 5 kHz.

In the next section are some suggestions to further improve the devices' performance.

5.3.2 Discussion

Improving Switching Times

Whilst it has been demonstrated that flexoelectric dispersion can be exploited in reflective cholesteric display technology, there are many ways that the devices studied in this work could be improved upon.

The switching time from focal conic to Grandjean states is very slow, for example. Consistent with the discussion in §1.7.2, it is suggested that this switching time is related to the restoring torque on the director, which is related to the dielectric energy given by,

$$F_{\text{dielectric}} = -\frac{1}{2}\Delta\varepsilon\varepsilon_0 E^2 \tag{5.35}$$

The switching time is therefore dependent on field strength and dielectric anisotropy. The speed with which the device switches from the Grandjean to the focal conic state, on the other hand, is fast at under 5 ms. It may be possible to reduce the flexoelectric bimesogenic component of the mixture in order to provide a greater negative dielectric anisotropy without compromising dual-frequency switching functionality, in order to mitigate this on-off-on switching asymmetry, as long as the inequality in equation 5.24 remains satisfied.

Furthermore, the bimesogenic component of the mixtures used has a very large viscosity, which further increases the switching time.

There have also been a variety of techniques reported in the literature to improve switching times in reflective cholesteric technologies, including the use of polymer networks and recently, the exploitation of Helfrich instabilities [160]. It may well be that the use of one or more of these techniques in combination with the present technology will produce the best performance, and this provides a platform for further investigation. Indeed, within this work (although not presented here), Helfrich-like states (possibly flexoelectrically rather than dielectrically induced, since in this work a negative dielectric anisotropy material is used) have been observed to exist in cells with planar alignment conditions, and may also be accessed in devices that can exploit flexoelectric dispersion for state switching in cholesteric systems. These states have been shown to provide switching times in reflective cholesteric cells of the order of 10 ms.

Summary

In this section, a new method for driving between focal conic and Grandjean states in reflective, bistable cholesteric display technology has been demonstrated. The technique exploits the dispersion in the dielectric properties of the material due to the relaxation in flexoelectric polarisability, which enables the selection of focal conic or Grandjean states using appropriate driving frequencies. The dual-frequency effect has a cross-over frequency of between 300 and 500 Hz in cells demonstrated here, dependent on the pitch of the material, orders of magnitude lower than other dual-frequency effects. Devices made using the technique show bistability, a contrast ratio of reflected intensity of 5:1, a switching time from focal conic to Grandjean of 520 ms, and from Grandjean to focal conic of under 5 ms, and wide viewing angles, without any polymer networks. The technique allows a much greater flexibility in the choice of other parameters, including surface alignment condition, driving scheme, material parameters (in comparison with dual-frequency materials) and polymer network stabilisation. The technique shows potential for development and application, po-

tentially in combination with techniques reported in related literature, such as the use of polymer networks. A reduction in the viscosity would greatly reduce the switching time.

5.4 Conclusion

By considering the contribution to the dielectric permittivity of cholesteric liquid crystals, which has before been neglected from consideration in the literature, a novel and versatile mechanism for controlling twisted liquid crystal structures based on dispersion in flexoelectric polarization has been described; applications include transmissive, reflective, multifunctional and bistable displays, electrooptics in telecommunications, scientific electrooptic components, novel meta-materials and photonics.

Helicoidal liquid crystal systems have secured a strong market position in reflective (e.g. Magink) and transmissive (e.g. Twisted Nematic) display technologies. Furthermore, helicoidal systems have long been touted within the field as providing the functionalities required for the next generation of displays including colour-sequential, video rate, reflective and auto-stereoscopic 3D, and the commercial potential of these functionalities has thus far been unexploited. The new and versatile method for switching between states in helicoidal liquid crystal systems presented in this chapter potentially affords a substantial flexibility in device parameters and associated cost reduction of existing technologies, and unlocks novel technologies by providing a previously impossible functionality.

A key component of any liquid crystal technology is switching between one or more states. Up until now, there is an almost exclusive utilisation of a liquid crystal's dielectric anisotropy to effect state switching, which is intrinsically independent of field polarity and therefore cannot be field-driven in both directions. The technique presented in this chapter exploits flexoelectricity, allowing field-driven switching between multiple and potentially stable states. This added functionality unlocks the value within a vast body of technology research related to helicoidal liquid crystal systems, and provides a key mechanism to be incorporated into the arsenal of tools available to a liquid crystal device engineer. The Key advantages are: a cost reduction of existing technologies, for example, by potentially

avoiding the need for polymer networks; unlocking the widely-reported yet untapped potential of helicoidal systems, including ultra-fast switching, wide viewing angles, cheaper electrode structures, reduced power consumption, increased resolution, reflective, bistable and multifunctional technologies; and providing a new mechanism for field-driven switching between multiple transmissive or reflective states, affording flexibility in design and previously impossible functionality.

Flexoelectric dispersion, which in this chapter has been exploited to switch between states in cholesteric liquid crystal cells, will in the next chapter instead be exploited to measure independently the flexoelectric and dielectric contributions to electro-optic switching in blue phase liquid crystals. Blue phase liquid crystals, which are currently being heavily researched for their unique application potential, are closely related to the cholesteric structures that this thesis has been concerned with thus far. However, the flexoelectrooptic effect in blue phases has up until now been neglected in the literature, as the symmetry of the blue phase does not allow polar switching as it does in the cholesteric phase. We will see in the next chapter that flexoelectric dispersion can allow the electrooptic effects arising from dielectric and flexoelectric interactions in the blue phase to be decoupled and measured independently.

Chapter 6

Dielectric and Flexoelectric Kerr Effects in Blue Phases

6.1 Introduction

The liquid crystal mesophases are a quintessential disruptive technology, having completely eradicated the market for cathode-ray tubes in displays. However, as was discussed in §2.1, fast-switching liquid crystal devices could potentially enable a variety of new functionalities in displays and other technologies. In §1.8.3 there was a description of how short pitch cholesteric liquid crystals could potentially provide faster electro-optic switching. Cholesteric materials have been suggested for use in display technology by exploiting either dielectric distortions in a Grandjean arrangement [58, 19] or flexoelectric distortions within a Uniform Lying Helix arrangement [53, 54, 55, 56, 57, 42].

However, the Kerr effect in Blue Phase Liquid Crystals (BPLCs) has also been reported as potentially enabling fast-switching technologies [161, 162]. The Kerr effect is a field-squared dependent induced birefringence, and the Kerr constant of a material is defined as,

$$K = \frac{\delta n}{\lambda E^2} \tag{6.1}$$

where δn is the induced birefringence and λ is the wavelength of incident light, and E is the field strength. BPLCs, which were introduced in §1.5.2, are thermodynamically stable mesophases that exist between chiral-nematic and isotropic phases. Three such phases are known to exist; BPI, PBII and BPIII have body-centered cubic, simple cubic

and amorphously arranged periodic defect-line structures respectively [21, 22]. Short pitch BPLCs have several desirable qualities with regard to display technology. They are optically isotropic with relatively large Kerr constants compared to solid-state or isotropic liquid materials. Because they are optically isotropic with zero field applied, rich black display states with wide-viewing-angles and minimal optical compensation can be achieved between crossed polarizers. Presently, in order to achieve favourable viewing angle properties, displays require multiple domains of liquid crystal material oriented in orthogonal directions, and this requires expensive patterned alignment and electrode structures. BPLCs, on the other hand, require no alignment layers since they are optically isotropic and the optical axis of the Kerr birefringence is determined by the applied field direction [26]. This is a distinct advantage, because as was discussed in chapter 4, alignment in other potential fast switching liquid crystal technologies, such as uniform lying helix alignment, has proved particularly problematic. Furthermore, BPLCs can produce a polarization-independent electrically-tunable phase retardation, which is required for high-efficiency holographic imaging and optical communications applications [163, 164]. These electrooptic phenomena all occur with sub-millisecond switching times [165]. In addition, BPI and BPII, due to the cubic symmetry, act as self-organizing three-dimensional photonic band-gap devices, which have been suggested for a variety of applications including wavelength tunable lasers [166, 167, 32].

There remain a number of significant issues precluding the exploitation of blue phases in technology. The Kerr constants of BPLCs, although larger than many other materials, are currently too small to allow full light modulation at voltages suitable for use with commercially available thin-film-transistors [161]. Adapted from Gerber [168], the Kerr constant in liquid crystals can be estimated by,

$$K_{\mathrm{d}} \approx \frac{\Delta n}{\lambda q^2}\left(\frac{\Delta\varepsilon\varepsilon_0}{K_2}\right) \tag{6.2}$$

The subscript of K_{d} has been added here to emphasize that this estimate does not take account of flexoelectricity (the ‘d’ standing for ‘dielectric contribution’). The normal method of increasing the Kerr constant is to engineer materials with large dielectric anisotropies,

which increases the dielectric coupling to the field, or with large Δn. However, such materials tend to have high viscosity, which severely increases the switching time of the materials [169].

Curiously, flexoelectrooptic phenomena in blue phases are not much discussed in the literature [170]. In the cholesteric phase, the flexoelectric effect causes a rotation in the director about a field applied perpendicular to the helicoidal axis, as was discussed in §1.8.4. In short-pitch cholesteric liquid crystals, the optic axis is parallel to the helicoidal axis, and a rotation in the director due to flexoelectricity causes a rotation in the optical axis. However, due to the cubic or amorphous symmetry, the blue phase is optically isotropic. For every local region in which the helicoidal axis is oriented in a particular direction, there is a second region oriented orthogonally, resulting in a net optical isotropy. Hence, a rotation in the director due to flexoelectricity in one region of the BLCS is optically compensated by a second region with the same structure but at 90 degrees to the first, and so no polar flexoelectrooptic effect is possible [23]. However, the flexoelectric effect still couples to director curvature distortion in blue phase systems, and can produce a Kerr effect. Kerr effects arising from flexoelectricity are not considered in equation 6.2, but may provide a valuable approach to engineering BPLCs with larger Kerr constants.

In this chapter, by examining blue phase materials with very different flexoelectric and dielectric properties, experimentally it is demonstrated that: *i*) both flexoelectric and dielectric effects contribute to BPLC Kerr switching; *ii*) both effects are found to have a similar influence on the magnitude of the Kerr effect; and *iii*) that the flexoelectric and dielectric Kerr contributions combine constructively in the case where the dielectric anisotropy is positive; *iv*) and destructively in the case where the dielectric anisotropy is negative. The flexoelectric and dielectric contributions are measured by exploiting the suppression in the flexoelectric switching at high frequencies; an effect that was also exploited in the last chapter to achieve control of state switching in cholesteric systems. An analytical model for flexoelectric Kerr switching in BPLCs is developed in analogy to Gerber's equation (equation 6.2) in §6.5.2. Furthermore, these analytical models are developed further by the

inclusion of empirically determined geometric factors, that relate the dimensionally consistent combination of liquid crystal parameters to the experimentally measured flexoelectric and dielectric contributions to the Kerr constant.

In addition, the different approaches to the thermostability of the wide-temperature-range BPLCs used in this study are discussed, and important parameters relating to flexoelectric and dielectric Kerr effects are characterised. Finally, the consequence of these new insights into PBLC Kerr switching for the engineering of materials for the next generation of electro-optic technologies is discussed. The potential influence of order-electricity and gradient-flexoelectricity on Kerr switching in BPLCs is also remarked upon.

6.2 Comparison of Wide-Temperature Blue Phase Materials

In order to study the flexoelectric and dielectric contributions to Kerr switching, two very different wide-temperature-range BPLC materials are compared: a high-viscosity flexoelectric-dominated bimesogenic mixture (mixture F) having a large flexo-elastic ratio, $(e_1 - e_3)/(K_1 + K_3)$, of 1.1 $\mathrm{CN}^{-1}\mathrm{m}^{-1}$ and a very small, negative dielectric anisotropy of -0.083 is compared to a dielectric-dominated mixture having a low viscosity, extremely small flexo-elastic ratio of 0.011 $\mathrm{CN}^{-1}\mathrm{m}^{-1}$ and a positive dielectric anisotropy of 1.6. In this section, the different approaches to producing a wide thermostability in BPLCs used in this study are discussed and key parameters related to flexoelectric and dielectric Kerr switching are characterised using a variety of techniques.

6.2.1 Flexoelectric-Dominated Blue Phase

The flexoelectric-dominated BPLC used in this study is a mixture, supplied by the University of Cambridge, of five components; a chiral dopant 4.2 wt% BDH1281 [171], and 24 wt% each of FFO5OFF, FFO7OFF, FFO9OFF and FFO11OFF, where the structure of FFO-n-OFF is given in reference [25], which has a cholesteric pitch of $\approx$ 250 nm at room temperature. This material, which here will be refered to as mixture F, undergoes a phase

transition on cooling from isotropic to an unidentified blue phase at 51°C that is stable over a wide temperature range. The bimesogenic components give the mixture a high flexoelectric susceptibility, which is thought to provide thermostability of the blue phases by reducing the free energy near defects [172]. The high viscosity of bimesogenic mixtures also improves the metastability of blue phases outside of their thermodynamically stable temperature range.

The flexo-elastic ratio of mixture F was measured by F. Castles (University of Cambridge) using a standard Uniform Lying Helix method (see §2.2) to be 1.1 $\mathrm{CN^{-1}m^{-1}}$ at 40°C and does not vary significantly with temperature.

Here, the dielectric properties were calculated from frequency-dependent capacitance measurements at 40°, shown in figure 6.1 (a). The dielectric properties can be deduced by considering that a cell's capacitance is given by $C = \varepsilon_r \varepsilon_0 V/d$, where ε_r is the effective relative permittivity of the liquid crystal (see §1.3.3). The relative permittivity is assumed to be equal to $\varepsilon_\perp$ when the cell is in the Grandjean state. As was discussed in more detail in §5.2.2, while in the ULH state, the effective relative permittivity is a combination of $\bar{\varepsilon} = (\varepsilon_\perp + \varepsilon_\parallel)/2$ and an additional contribution due to the flexoelectric polarizability of the material. The flexoelectric effect is suppressed at higher frequencies, resulting in a relaxation in the capacitance as a function of frequency that is evident in figure 6.1. By dividing the capacitances of the cell in these states by the empty cell capacitance, in which it is assumed that for air, $\varepsilon_r = 1$, and using a model of the form given in equation 5.32 in chapter 5, one can determine the dielectric anisotropy of the liquid crystal, $\Delta\varepsilon = \varepsilon_\parallel - \varepsilon_\perp$. For mixture F, $\Delta\varepsilon = -0.083$, and $\bar{\varepsilon} = 5.7$ at 40°C. Because $\Delta\varepsilon = -0.083$ is small, its relative magnitude may be highly sensitive to changes in temperature [126].

Incidentally, the capacitance data also allow for the measurement of the flexoelectric contribution to the permittivity of the ULH at low frequency, which for material F is found to be $\varepsilon_{\mathrm{flexo}} = 0.51$. As was discussed in §5.2.1, $\varepsilon_{\mathrm{flexo}}$ is related to flexoelectric and elastic parameters by the relation,

$$\varepsilon_{\mathrm{flexo}} = \frac{1}{\varepsilon_0}\left(\frac{(e_1 - e_3)^2}{2(K_1 + K_3)}\right) \tag{6.3}$$

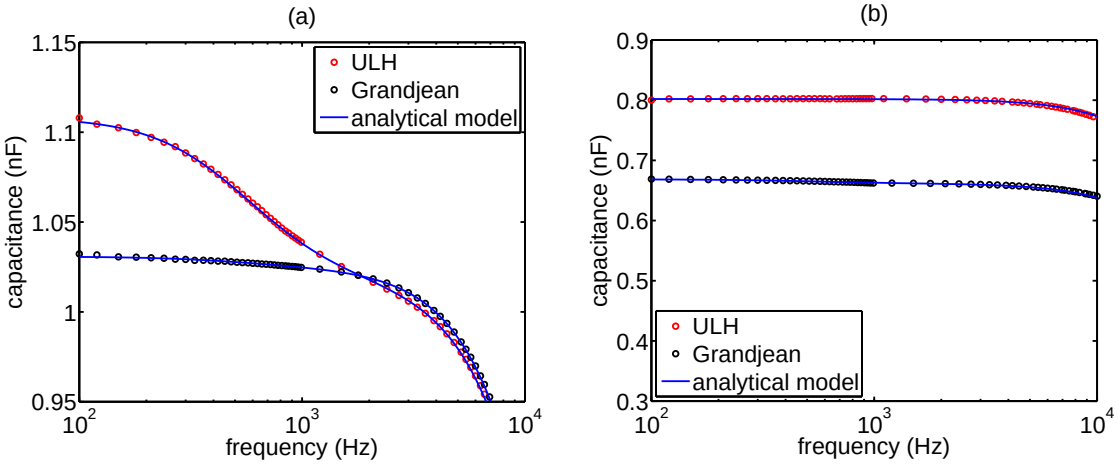

Figure 6.1: The capacitance as a function of frequency for cells (empty cell capacitance 0.18 nF) filled with (a) material F at 40°C and (b) material D at 25°C. An analytical model of the form given in equation 5.32 (solid lines) is used to determine the dielectric and flexoelectric properties of the materials, including $\Delta\varepsilon$. A relaxation in the capacitance in (a) when in the ULH configuration is consistent with the suppression of the flexoelectric polarization at higher frequencies. In the case of (b), there is no such relaxation, and thus no evidence of substantial flexoelectric polarization.

By considering the value of e/K measured using the ULH method, one can therefore infer that $e_1 - e_3 = 7.8$ pCN^{-1} and that $K_1 + K_3 = 7.1$ pN. The large value of e/K is therefore due to a relatively small value of $K_1 + K_3$ in this mixture (c.f. for mono-mesogenic E7, $K_1 + K_3 = 27$ pN). This may be due to a small K_3, which is characteristic of bimesogenic liquid crystals [173].

6.2.2 Dielectric-Dominated Blue Phase

The dielectric-dominated BPLC used in this study is a mixture, provided by Feng Chia University, Taiwan, of a nematic host liquid crystal FCU-LCM10 and a relatively weak left-hand chiral dopant FCU-NYCL, whose helical twisting power is ~ 20 µm^{-1}. The dielectric anisotropy of the pure nematic host is 2.7 at room temperature, with a birefringence of 0.1 at $\lambda = 550$ nm (both measured by Feng Chia University [174]). The rotational viscosity of the nematic host is estimated to be less than 100 mPa·s [174]. After adding 8 wt% chiral dopant, the mixture exhibits a cubic blue phase in a very narrow temperature range [174]. The temperature range of the blue phases become wider with increasing chiral-

dopant concentration, and with 21 wt% and 24 wt% chiral dopant, the mixtures exhibit phase sequences (all in °C) Isotropic 35 BPIII 28 BPI 21.1 N* and Isotropic 32 BPIII 16 BPI < 20, respectively [174]. The approach to producing a large blue phase temperature range for this dielectric-dominated material is in contrast to that adopted for the flexoelectric-dominated material F. The thermostability of blue phases has been shown to correlate with a reduction in the dielectric anisotropy and an increase in the elastic constants [175]. In addition, a chiral dopant with good solubility can extend the temperature range of the blue phase [176]. The chiral dopant used in this mixture reduces the viscosity of the nematic host [174]. The viscosity is correlated with the order parameter, and a reduction in the order parameter might reduce the free energy around the disclination. In this study, the 21 wt% chiral-doped mixture ($P \sim 250$ nm), which here will be refered to as mixture D, is used because it has a favourable phase sequence including the cubic blue phases. However, in some cases, data are also presented for the 24 wt% mixture, which is refered to as mixture D2.

The flexoelectric response of mixture D is too small to measure using a standard ULH technique, and so was measured using the Grandjean rotation method with a quarter-wave plate (the method and data for mixture D is presented in §2.3.6). The mixture exhibits an extremely small flexo-elastic ratio of 0.011 $\text{CN}^{-1}\text{m}^{-1}$ at room temperature. The dielectric properties of mixture D were determined from the capacitance as a function of frequency shown in figure 6.1 (b), with the result that $\Delta\varepsilon = 1.6$ and $(\varepsilon_\perp + \varepsilon_\parallel)/2 = 4.5$ at 25°C. The chiral dopant dilutant in this mixture reduces $\Delta\varepsilon$ relative to the pure host material. Note that the capacitance of the cell in the ULH state does not show a noticeable relaxation as a function of frequency, which is consistent with the material's small flexo-elastic ratio.

6.2.3 The Relative Distortion due to Dielectric and Flexoelectric Field Interactions

While it is expected that the two materials in this study, F and D, behave very differently in electric fields due to being either dielectric or flexoelectric dominated, it will be useful to quantify this difference. To achieve this, consider the relative flexoelectric and dielectric

distortions in a cholesteric liquid crystal. A field applied perpendicular to the helicoidal axis causes a rotation of the director about the field direction due to flexoelectricity given by (see §1.8.2),

$$\phi_0(E) = \frac{e_1 - e_3}{K_1 + K_3}\frac{E}{q} \tag{6.4}$$

The dielectric interaction also causes a director rotation, although the rotation is not uniform (being a function of position along the helicoidal axis) and is in the plane of the director. The maximum in-plane rotation due to the dielectric distortion, as was derived in §1.7.1, is given by,

$$\theta_0(E) = \frac{\Delta\varepsilon\varepsilon_0}{8K_2}\left(\frac{E}{q}\right)^2 \tag{6.5}$$

By combining equations 6.5 and 6.4, we can express a dimensionless dielectric- to flexoelectric-distortion ratio,

$$\kappa = \frac{\theta_0}{\phi_0^2} = \frac{\Delta\varepsilon\varepsilon_0(K_1 + K_3)^2}{8K_2(e_1 - e_3)^2} \tag{6.6}$$

which gives the relative strength of the dielectric and flexoelectric distortions in a particular liquid crystal material (this quantity was also considered in the context of the coupling of dielectric and flexoelectric effects in cholesteric liquid crystals in chapter 3). The values of κ for material D and F are 7×10^3 and -4×10^{-2} respectively. Here it has been assumed that for the bimesogenic material F, $K_2 = 2$ pN, which is taken from measured and calculated values of similar materials [177, 173, 19]. Thus, these blue phase materials' dielectric- to flexoelectric-distortion ratios differ by a factor of 10^5, making them particularly suited to comparing the contribution to Kerr switching arising from the two field-distortion effects.

6.3 Measurement of the Kerr Constant

In order to determine the materials' Kerr constants, the field-squared dependence of the birefringence was measured using cells within the experimental arrangement shown in figure 6.2. Cells were made using an ITO electrode on one of the substrate surfaces, in which a 2 mm gap had been etched in order to apply a uniform in-plane field. The same electrode structure was adopted in chapter 2 to investigate flexoelectric switching in Grandjean and

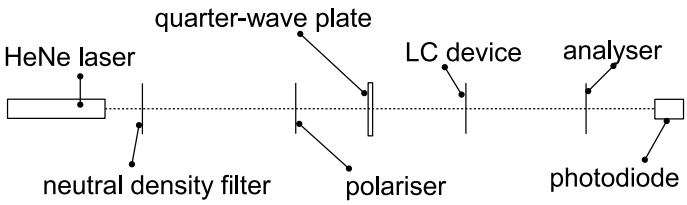

Figure 6.2: A schematic of the experimental arrangement, used to measure both the magnitude of the Kerr constant and the individual contributions to the Kerr constant due to flexoelectric and dielectric field distortions. A circular polarization is generated using a linear polarizer and quarter-wave plate. A liquid crystal cell with IPS-type electrodes is followed by an analyser set at 45 degrees to the applied electric field direction, and a photo-diode detects the transmitted intensity.

twisted nematic cells. A numerical study in §2.3.2 found that such an electrode structure produces a highly uniform field. The cell is positioned such that the in-plane field direction makes an angle of 45 degrees to the analyser.

The normalised transmission is given by,

$$T = \sin^2\left(\frac{\pi}{4} + \frac{\pi\delta n d}{\lambda}\right) \tag{6.7}$$

where the $\pi/4$ is the retardation due to the quarter-wave plate, and δn is the induced birefringence. For small δn, this can be approximated as,

$$T = \frac{1}{2} + \frac{\pi\delta n d}{\lambda} \tag{6.8}$$

where d is the device thickness. The cell was driven with a sine-modulated field (with a frequency well below the relaxation frequency of the flexoelectric switching) of the form $E = E_0 \sin(\omega t)$. From equation 6.1, and substituting for E, we find that,

$$\delta n = \lambda K E_0^2 \sin^2(\omega t) \tag{6.9}$$

Substituting this into equation 6.8 and using a double-angle formula, we find that,

$$T = \frac{1}{2} + \frac{\pi d}{2} K E_0^2 \left(1 - \cos(2\omega t)\right) \tag{6.10}$$

In order to extract this component formally, we can perform a Fourier series calculation for the 2ω component, i.e. we can multiply by $\cos(2\omega t)$,

$$T\cos(2\omega t) = \frac{1}{2}\cos(2\omega t) + \frac{\pi d}{2}KE_0^2\left(\cos(2\omega t) - \cos^2(2\omega t)\right) \tag{6.11}$$

From equation 6.10, we know that the transmission is a function that includes a term $-T_0\cos(2\omega t)$, where T_0 is the transmission amplitude at an angular frequency of 2ω. Substituting this for T in the above expression and taking the time average, we find that,

$$T_0 = \frac{\pi d}{2}KE_0^2 \tag{6.12}$$

which is the amplitude of the 2ω frequency component of the transmission. This can be rearranged for K,

$$K = \frac{2T_0}{\pi d E_0^2} \tag{6.13}$$

which puts K in terms of measurable and known quantities. To determine T_0, the output of the photo diode in the experimental arrangement in figure 6.2 is analysed using a lock-in amplifier, which can measure the amplitude of the 2ω frequency component of the photo diode output, V_0, to a high level of accuracy. From equation 6.8, it can be seen that when there is no field-induced birefringence (at $E = 0$) then the transmission is equal to 0.5. The transmission amplitude T_0 can thus be determined by,

$$T_0 = \frac{V_0}{2V_{E=0}} \tag{6.14}$$

where V_0 is the amplitude of the 2ω frequency component of the photo diode output voltage, and $V_{E=0}$ is the photo diode output voltage when $E = 0$. The cell thickness, d, is measured by analysing Fabry-Perot fringes in a transmission spectrum of cells before filling with liquid crystal.

The birefringence is shown as a function of λE^2 in figure 6.3. The values of the Kerr constants are then the slopes of these lines (see equation 6.1), and are summarised in table 6.1 for materials D and F, which have $K = 0.13$ nmV^{-2} and $K = 0.022$ nmV^{-2} respectively.

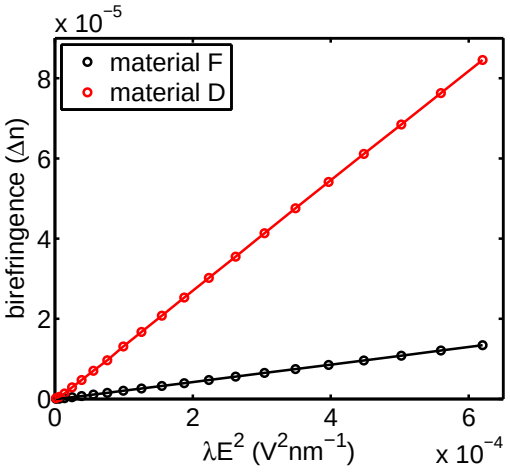

Figure 6.3: The induced birefringence is shown as a function of λE^2 for materials D and F. The slopes correspond to the Kerr constants. The birefringence was determined by analysing the transmission between crossed polarizers of devices with uniform in-plane fields in series with a quarter-wave plate, as shown in figure 6.2.

Table 6.1: A summary of the physical parameters of the BPLC materials used in this study. The Kerr constant for the materials, which have been measured using the method described in §6.3, are given in the final column.

	$\Delta\varepsilon$	$\frac{e_1-e_3}{K_1+K_3}$	κ	γ	τ	K
Material F	-0.083	1.1	-4×10^{-2}	≈ 0.6	185 (T=50°C)	0.022
Material D	1.6	0.011	7×10^{3}	≈ 0.1	23 (T=34°C)	0.13
Unit		$\mathrm{CN^{-1}m^{-1}}$		Pa·s	µs	$\mathrm{nmV^{-2}}$

In this section, a technique for measuring the Kerr constant, K, has been described, and the method has been used to measure K in both flexoelectric and dielectric dominated blue phase materials. In the next section, a technique is developed and applied to measure the independent contributions to K arising from the flexoelectric and dielectric interactions.

6.4 Flexoelectric and Dielectric Contributions to the Kerr Effect

6.4.1 Frequency Dependence of Flexoelectric Switching in Blue Phases

In chapter 5, the suppression of flexoelectric switching in cholesteric materials as a function of frequency was described in detail. In §5.2, it was found that in cholesteric materials,

there is a relaxation in the flexoelectric tilt angle as a function of driving frequency at a characteristic frequency given by,

$$f_{\text{flexoelectric}} = \frac{q^2}{4\pi\gamma}(K_1 + K_3) \tag{6.15}$$

where γ is a viscosity.

The lattice parameter of blue phase systems is roughly the same as the pitch in the cholesteric phase at the same temperature [178, 179]. Therefore, flexoelectric distortion in blue phase systems is likely to have a similar relaxation frequency to the analogous cholesteric phase,

$$f^{\text{b}}_{\text{flexoelectric}} \approx \frac{q^2}{4\pi\gamma}(K_1 + K_3) \tag{6.16}$$

although it may be slightly different due to the different structure of the blue phase. In the rest of this chapter, the assumption will be made that $f^{\text{b}}_{\text{flexoelectric}} = f_{\text{flexoelectric}}$, and that τ_{f} is equal to the time constant associated with the suppression of flexoelectric switching in blue phases.

We may expect that the contribution of flexoelectric distortion to the Kerr effect in BPLCs will be absent at frequencies in excess of $f_{\text{flexoelectric}}$. On the other hand, the dielectric polarization, as was also discussed in chapter 5, is typically not suppressed below frequencies of MHz [149, 150]. Hence, the dielectric contribution to the Kerr effect in BPLCs will not be suppressed at frequencies well above the relaxation frequency of the flexoelectric contribution. This is the key to distinguish between the two contributions experimentally. By observing Kerr switching as a function of frequency, a relaxation in the flexoelectric contribution is observed, and at driving frequencies much greater than $f_{\text{flexoelectric}}$, only the dielectric contribution remains.

Let us express the Kerr constant as a sum of flexoelectric and dielectric contributions,

$$K(\omega) = K^0_{\text{f}} + K_{\text{d}} \tag{6.17}$$

where K_{d} is the Kerr constant associated with the dielectric effect, and K^0_{f} is the frequency-dependent Kerr constant associated with the flexoelectric effect. From §5.2.1, we found that

the flexoelectric tilt angle is frequency dependent, and that the amplitude of the tilt angle in a sine-modulated field is given by,

$$\phi_0 = \frac{\phi}{1 + \omega^2 \tau_{\mathrm{f}}^2} \tag{6.18}$$

where ϕ is the flexoelectric tilt in the static field case, ω is the driving frequency and $\tau_f = 1/2\pi f_{\mathrm{flexoelectric}}$ (c.f. equation 5.9). We might expect that the flexoelectric contribution to Kerr switching in blue phases depends upon the flexoelectric switching, and so in a similar fashion we can write,

$$K_{\mathrm{f}}^0 = \frac{K_{\mathrm{f}}}{1 + \omega^2 \tau_{\mathrm{f}}^2} \tag{6.19}$$

and hence, we can write,

$$K(\omega) = \frac{K_{\mathrm{f}}}{1 + \omega^2 \tau_{\mathrm{f}}^2} + K_{\mathrm{d}} \tag{6.20}$$

which gives the frequency-dependent Kerr constant in terms of flexoelectric and dielectric contributions.

The flexoelectric contribution to Kerr switching results from flexoelectric distortion, and while the resultant induced birefringence is independent of the polarity of the field, the underlying distortion is field polarity dependent. At frequencies larger than the flexoelectric-switching relaxation frequency, the magnitude of the flexoelectric distortion is proportional to the time-average of the field, which for an AC field with zero DC component is zero. Hence, the flexoelectric distortion, and associated flexoelectric contribution to Kerr switching, is suppressed at large driving frequencies. On the other hand, the dielectric contribution to Kerr switching results from distortion due to the dielectric effect, which is the same for positive and negative fields. At large frequencies, the dielectric distortion amplitude is proportional to the time-average of the square of the field, or the mean-squared field. Hence, the distortion due to the dielectric effect, and associated Kerr switching, will not be suppressed at large field frequencies. There will be a relaxation in the time-averaged transmission as a function of the driving frequency of a BPLC device between crossed polarizers due to the relaxation in the flexoelectric contribution to the Kerr switching, however the dielectric contribution will not produce such a relaxation. In order to probe this behaviour, the

frequency ω of a driving voltage signal is varied, and the driving signal's amplitude is modulated using a relatively low modulation frequency ω_{m}; one that is well below the relaxation frequency. A lock-in amplifier measures the amplitude of the transmission at the modulation frequency, which is effectively equal to the time-averaged transmission if the driving signal were not modulated. Using a lock-in amplifier to measure the amplitude of the modulated signal allows a much greater level of precision than measuring the time-average of the photo diode output directly, since the lock-in amplifier can detect amplitudes as small as tens of microvolts or less. Using this method, it is possible to measure the transmission amplitude at the modulation frequency as a function of driving frequency, and from this to determine the independent flexoelectric and dielectric contributions to Kerr switching in blue phases. In the next section, a mathematical treatment of the above discussion will be presented.

6.4.2 Determining Flexoelectric and Dielectric Kerr Contributions

Using a Modulated Driving Signal

Let us take a field described by,

$$E = E_0 \sin(\omega t) \sin^2\left(\frac{\omega_{\mathrm{m}}}{2} t\right) \tag{6.21}$$

in which ω is a test angular frequency that will be varied, and ω_{m} is a fixed modulating frequency where $\omega_{\mathrm{m}} \ll 2\pi f_{\text{flexoelectric}}$. If this field is applied to a liquid crystal whose Kerr behaviour is described by $\delta n = \lambda K E^2$, then the birefringence is given by,

$$\delta n = \lambda K E_0^2 \sin^2(\omega t) \sin^4\left(\frac{\omega_{\mathrm{m}}}{2} t\right) \tag{6.22}$$

which, using suitable double-angle formulae, can be expressed,

$$\delta n = \lambda K E_0^2 \sin^2(\omega t) \left(\frac{3}{8} - \frac{1}{2}\cos(\omega_{\mathrm{m}} t) + \frac{1}{8}\cos(2\omega_{\mathrm{m}} t)\right) \tag{6.23}$$

From equation 6.23, it can be seen that δn will have frequency components at ω, ω_{m} and $2\omega_{\mathrm{m}}$. From equation 6.20, it is also clear that the flexoelectric contribution to K depends upon ω. Therefore, by varying ω, it is possible to analyse the magnitude of the Kerr birefringence as a function of frequency by measuring the amplitude of either the ω_{m} or $2\omega_{\mathrm{m}}$

frequency component of the birefringence, if ω_{m} and $2\omega_{\mathrm{m}}$ are well below the relaxation frequency associated in the suppression in flexoelectric contribution to the Kerr switching.

In order to study the birefringence, the liquid crystal can be placed between crossed polarizers with a quarter-wave plate as shown in figure 6.2. The transmission, assuming δn is small, is again given by,

$$T = \frac{1}{2} + \frac{\pi \delta n d}{\lambda} \tag{6.24}$$

From equation 6.23, it can be seen that the ω_{m} frequency component has a larger amplitude ($\frac{1}{2}$ compared to $\frac{1}{8}$ for the $2\omega_{\mathrm{m}}$ component). Experimentally, it will be possible to measure this component using a lock-in amplifier, which can accurately measure a given frequency component of a photo diode output signal. After substituting δn from equation 6.23 into equation 6.24 to find the transmission under the application of a field of the form in equation 6.21, we can again perform a Fourier series calculation, this time for the ω_{m} component, by multiplying by $\cos(\omega_{\mathrm{m}} t)$,

$$T\cos(\omega_{\mathrm{m}} t) = \frac{1}{2}\cos(\omega_{\mathrm{m}} t) + \pi d K E_0^2 \sin^2(\omega t)\left(\frac{3}{8}\cos(\omega_{\mathrm{m}} t) - \frac{1}{2}\cos^2(\omega_{\mathrm{m}} t) + \frac{1}{8}\cos(2\omega_{\mathrm{m}} t)\cos(\omega_{\mathrm{m}} t)\right) \tag{6.25}$$

By considering equation 6.23 and 6.24, we know that T includes a term $-T_0^m \cos(\omega_{\mathrm{m}} t)$, where T_0^m is the amplitude of the ω_{m} component of the transmission. Therefore, if we take the time-average of equation 6.25, such that $\sin^2(\omega t) = \cos^2(\omega_{\mathrm{m}} t) = 1/2$, we get,

$$T_0^{\mathrm{m}} = \frac{\pi d}{4}\left(\frac{K_{\mathrm{f}}}{1+\omega^2\tau_{\mathrm{f}}^2} + K_{\mathrm{d}}\right) E_0^2 \tag{6.26}$$

where T_0^{m} is the amplitude of the transmission at the modulation frequency ω_{m}, and the full form of K given in equation 6.20 has been used. The key difference between equation 6.26 and the result in equation 6.12, is that the modulation frequency at which the measurement is being made, ω_{m}, is independent of the frequency that is varied, ω, allowing the precise measurement of transmission at a range of frequencies over which flexoelectric switching is suppressed. By varying ω and measuring the amplitude of the ω_{m} frequency component of the transmission, we can therefore observe a relaxation in the Kerr switching due to

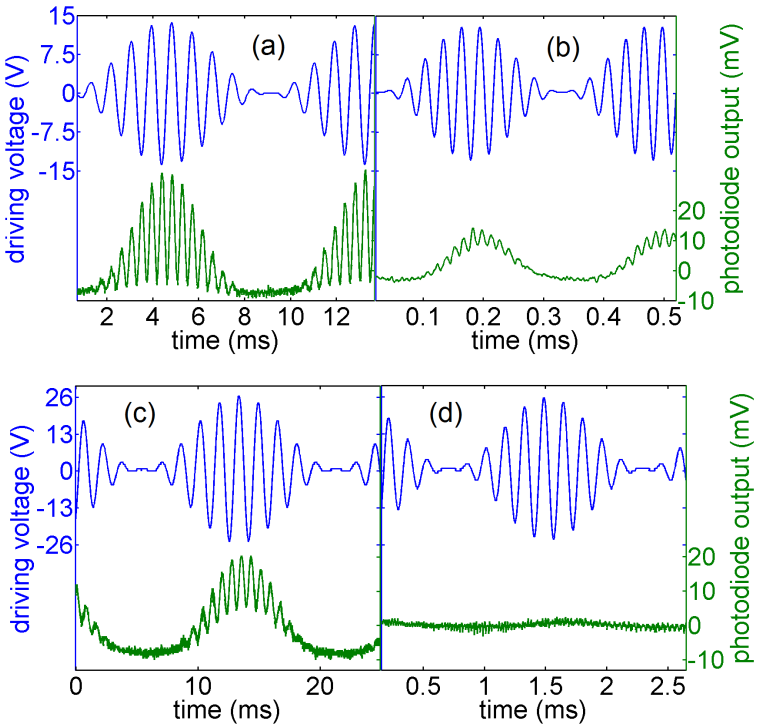

Figure 6.4: The response of devices with interdigitated electrodes under the application of sine-modulated AC fields of the form in equation 6.21 showing the difference between the Kerr behaviour of flexoelectric- and dielectric-dominated blue phase liquid crystals. Material D where (a) $\omega = 1.1$kHz, $\omega_{\mathrm{m}} = 110$ Hz, (b) $\omega = 11$kHz, $\omega_{\mathrm{m}} = 1.1$kHz. Material F where (c) $\omega = 630$ Hz, $\omega_{\mathrm{m}} = 63$ Hz, (d) $\omega = 6.3$ kHz and $\omega_{\mathrm{m}} = 630$ Hz. For illustration, the ratio of ω to ω_{m} has been kept constant in order to observe both frequency components in the plots. When $\omega/2\pi$ is greater than $f_{\mathrm{flexoelectric}}$, the flexoelectric-dominated material has a suppressed Kerr response due to the finite switching time of the flexoelectric effect, as can be seen in (d). Dielectric-dominated materials however continue to show a Kerr response that depends on V^2 even at high frequencies, as can be seen in (b).

flexoelectricity. From equation 6.26, if we take the ratio between the transmission amplitude at low and high values of ω, we can rearrange for the ratio of $K_{\mathrm{f}}/K_{\mathrm{d}}$, to get,

$$\frac{K_{\mathrm{f}}}{K_{\mathrm{d}}} = \frac{T_0^{\mathrm{m}}(2\pi\omega \ll f_{\mathrm{flexoelectric}})}{T_0^{\mathrm{m}}(2\pi\omega \gg f_{\mathrm{flexoelectric}})} - 1 \tag{6.27}$$

Hence, by measuring the transmitted intensity at frequencies greater than and less than $f_{\mathrm{flexoelectric}}$, we can determine the ratio $K_{\mathrm{f}}/K_{\mathrm{d}}$. In practice, rather than taking measurements of the transmission amplitude at only two driving frequencies, equation 6.26 will instead be used as an analytical model to compare with experimental transmission as a function of ω, and the ratio $K_{\mathrm{f}}/K_{\mathrm{d}}$ and τ_{f} will be introduced as fitting parameters.

Interdigitated Versus Wide-Electrode-Gap IPS Cells

In order to investigate experimentally the Kerr relaxation behaviour as a function of frequency, it must be possible in the experimental arrangement to apply a range of frequencies, including large frequencies, since the relaxation in the flexoelectric switching is expected to occur at several kHz. However, the maximum frequency that an amplifier is capable of at a particular voltage is determined by its slew rate – that is, the greatest rate of change of voltage, $\partial V/\partial t$. Wide-electrode-gap cells used in the measurement of the total Kerr constant, K – which can also be considered as the Kerr constant in the low-frequency limit – require very large voltages for modest field strengths, because $E \propto V/a$, where a here is the electrode gap. By using interdigitated electrodes, which were introduced in §4.3.1, a smaller voltage is required to produce the same field strength because the gap between electrodes is small ($\approx$ 10 μm), and the device behaviour can therefore be studied at much greater field frequencies.

However, interdigitated electrode cells, while convenient for allowing the application of large field frequencies, are inappropriate for measuring the absolute Kerr constants, K, using the arrangement in figure 6.2. The relationship between the transmission and the birefringence, given in equation 6.8, assumes that the entire region of the device on which light is incident has the same induced birefringence. Interdigitated cells, however, only switch liquid crystal between electrodes, and above the electrodes little or no birefringence is induced. Therefore, in order for the birefringence to be determined from the transmission of a device with interdigitated electrodes, a 'fill-factor' – the ratio of switched to unswitched area – would have to be included. However, this factor is not known. Furthermore, the non-uniformity of the field due to interdigitated electrodes (see §4.3.1) could complicate the measurement further, since the Kerr constant is defined in relation to a uniform field strength in equation 6.1. For these reasons, cells with single, wide 2 mm electrode gaps were used to measure the absolute value of K in §6.3, which produce a uniform field and allow the entire region of the cell on which the laser is incident to experience the same field strength. On the other hand, when observing the Kerr behaviour as a function of frequency, since

we are only interested in the relative transmission at low and high frequencies, we do not require to know the fill-factor that relates the transmission to the birefringence, and hence, interdigitated electrodes, which allow for the application of much greater field frequencies, may be used.

6.4.3 Experiment and Analysis

The photo-diode response of a device with interdigitated electrodes, within the experimental arrangement shown in figure 6.2, under the application of a field of the form in equation 6.21 is shown in figure 6.4. When the frequency is much greater than the flexoelectric relaxation frequency, the flexoelectric contribution is suppressed. In material F, the Kerr response is almost completely suppressed in figure 6.4 (d), because K_{f} is dominant and the dielectric contribution, K_{d}, is small. However, in the dielectric-dominated mixture D, although the high-frequency ω component of the transmission is suppressed, the amplitude of the photo-diode response at the modulation frequency is unchanged between figure 6.4 (a) and (b), because K_{f} is very small.

To determine the ratio $K_{\mathrm{f}}/K_{\mathrm{d}}$, a lock-in amplifier was used to measure T_0^{m} as a function of ω for BPLC materials F, D and D2, shown in figure 6.5. As discussed, fitting an analytical model of the form in equation 6.26 allows the ratio $K_{\mathrm{f}}/K_{\mathrm{d}}$ to be determined, and thus allows the relative dielectric and flexoelectric contributions to the Kerr switching to be studied, which has not previously been possible. The measured $K_{\mathrm{f}}/K_{\mathrm{d}}$ is shown in table 6.2.

The characteristic switching time of the Kerr effect in material D and D2 was measured independently by observing transmission under the application of bursts of 200 kHz AC (an example is shown in figure 6.6), to be 23 µs at 34°C and 320 µs at 25°C for material D and 23 µs for material D2 at 31°C. However, as is expected, there are no relaxations corresponding to these characteristic times in figure 6.5. This shows that the dielectric response does indeed depend on the square of the time-averaged high-frequency (ω) component of the field, in contrast to the flexoelectric Kerr response that is suppressed at high frequency. Material D does not exhibit a significant relaxation due to the suppression of the flexoelectric

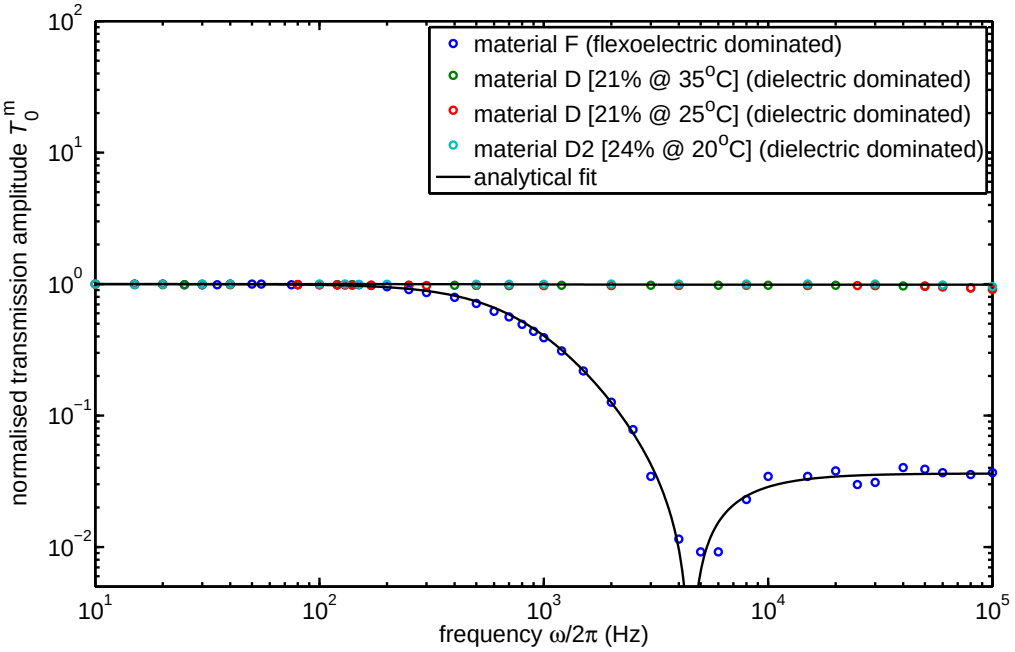

Figure 6.5: The normalised transmission amplitude at the modulation frequency, T_0^{m}, is shown as a function of the driving frequency ω, under the application of a field of the form $E = E_0 \sin(\omega t) \sin^2\left(\frac{\omega_{\mathrm{m}}}{2} t\right)$, in both flexoelectric and dielectric dominated BPLC materials, on a log-log scale. A relaxation model of the form given in equation 6.26 (solid line) is used to determine the ratio of the flexoelectric and dielectric contributions to the Kerr switching, $K_{\mathrm{f}}/K_{\mathrm{d}}$. A point at which the flexoelectric and dielectric contributions combine to give $K = 0$, and therefore at which $T_0^{\mathrm{m}} = 0$, is evident in the model at between 4 and 5 kHz.

switching, which corresponds to its small $e_1 - e_3$. The sensitivity of the lock-in amplifier provides an upper limit on the ratio $K_{\mathrm{f}}/K_{\mathrm{d}}$ in material D of 0.01 (summarised in table 6.2).

In the case of the flexoelectric dominated material, the small, negative dielectric anisotropy leads to a negative induced birefringence, and therefore a negative value of K_{d}. On the other hand, the flexoelectric response contributes positively to K, and K_{f} is positive. Material F shows a strong relaxation in the Kerr switching with a time constant $\tau_f = 185\mu$s, determined from fitting the model of the form in equation 6.26. As the frequency increases and the flexoelectric contribution is suppressed, there is a frequency at which the total frequency-dependent Kerr constant is equal to zero. This point is evident in the log-log plot by the downward spike in the model. By setting K from equation 6.20 equal to zero, and rearranging, we can determine the frequency at which flexoelectric and dielectric con-

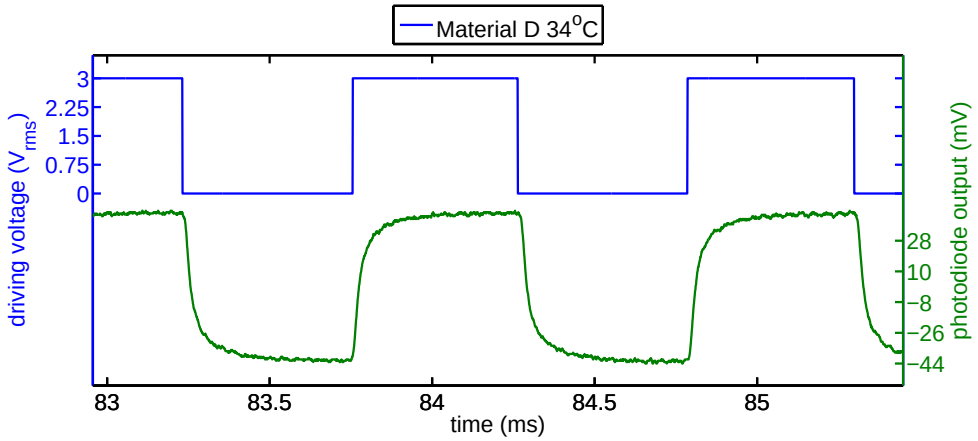

Figure 6.6: The output of a photo diode is shown for a cell filled with material D within the experimental arrangement shown in figure 6.2, under the application of pulses of AC at 200 kHz. The photo diode response is used to determine the characteristic response time of the Kerr effect in the dielectric-dominated blue phase systems.

Table 6.2: The ratios of contributions to the Kerr switching due to flexoelectric and dielectric effects in blue phase materials D and F, measured using the experiment described in §6.4. The total Kerr constant, measured using the experiment described in §6.3, is also given. The values of the flexoelectric and dielectric contributions, K_f and K_d, are deduced by combining results from both experiments.

	$K_\mathrm{f}/K_\mathrm{d}$	$K(\mathrm{nmV}^{-2})$	K_d (nmV^{-2})	K_f (nmV^{-2})
material F	-31.1	0.022	-0.00074	0.023
material D	<0.01	0.13	0.13	<0.001

tributions combine to give zero Kerr switching,

$$f_{\mathrm{K}=0} = \frac{1}{2\pi\tau_\mathrm{flexo}}\sqrt{-\frac{K_\mathrm{f}}{K_\mathrm{d}} - 1} \tag{6.28}$$

Using the measured value of τ_flexo and $K_\mathrm{f}/K_\mathrm{d}$, we find that $f_{\mathrm{K}=0} = 4.7$ kHz. At frequencies greater than this, K is negative. However, in this experiment, the lock-in amplifier measures only the absolute amplitude of the transmission at the modulation frequency, and so the measured amplitude of the transmission is a positive number, as shown in figure 6.5.

Rearranging equation 6.17, we get,

$$K_{\mathrm{d}} = \frac{K}{1 + \frac{K_{\mathrm{f}}}{K_{\mathrm{d}}}} \qquad\qquad K_{\mathrm{f}} = \frac{K}{1 + \left[\frac{K_{\mathrm{f}}}{K_{\mathrm{d}}}\right]^{-1}} \tag{6.29}$$

From the measurement of the total Kerr constant K using wide-electrode-gap devices (discussed in §6.3) and the ratio of $K_{\mathrm{f}}/K_{\mathrm{d}}$ using interdigitated devices, absolute Kerr contributions arising due to dielectric and flexoelectric effects can therefore be determined. For mixture F, $K_{\mathrm{d}} = -7.4 \times 10^{-4}$ nmV^{-2} and $K_{\mathrm{f}} = 2.3 \times 10^{-2}$ nmV^{-2}; for mixture D, $K_{\mathrm{d}} = 0.13$ nmV^{-2} and $K_{\mathrm{f}} < 1 \times 10^{-3}$ nmV^{-2} (these values are summarised in table 6.2 and later in table 6.3). Mixture F's negative value of K_{d} is consistent with a material with a negative dielectric anisotropy [180].

6.4.4 Summary

In this section, a method for measuring the independent contributions to Kerr switching in BPLCs arising from flexoelectric and dielectric effects has been described. The total Kerr effect was first measured using cells with wide electrode spacing. Secondly, the ratio of the flexoelectric and dielectric contributions to Kerr switching was determined using devices with interdigitated electrodes by measuring transmission as a function of driving field frequency, using an amplitude modulated driving signal. When the frequency $f \ll f_{\mathrm{flexoelectric}}$, the flexoelectric polarization contributes to the Kerr effect, and when $f \gg f_{\mathrm{flexoelectric}}$ the flexoelectric switching is suppressed due to dispersion in the flexoelectric polarization and only the dielectric effect remains. The method has been used to determine the Kerr constants, K_{d} and K_{f}, arising from dielectric and flexoelectric field interactions respectively, in both flexoelectric- and dielectric-dominated BPLCs. It has been demonstrated that in the case of a negative dielectric anisotropy, the total Kerr constant, K, is less than K_{f}. In the next section, the results are discussed in relation to analytical estimates of K_{d} and K_{f}, and the flexoelectric and dielectric effects are found to have a similar influence on the magnitude of the Kerr effect. Additionally, the consequence of these new insights for the development of BPLC materials is commented upon.

6.5 Semi-Empirical Models of Flexoelectric and Dielectric Kerr Contributions

6.5.1 Dielectric Contribution to Kerr Switching

Values of K_{d} calculated using Gerber's estimation in equation 6.2 are shown alongside the experimentally determined values for material F and D in table 6.3. To calculate the estimates, Δn was estimated to be 0.07 for both materials by inspecting the width of the Bragg reflection bands of transmission spectra while in the cholesteric phase in a Grandjean geometry (see §1.6.2). For material D, the Gerber estimate of K_{d} is a factor of 10 greater than the measured value. This discrepancy is likely a result of a geometric factor that is absent in the estimation. The Gerber estimate for the Kerr constant in equation 6.2 was deduced by considering that the induced birefringence depends on an energy balance between elastic distortions and director reorientation due to the field [168]. Relevant parameters were then organised into a dimensionally consistent combination, without taking account of geometric factors. If one includes a geometric factor, we may modify 6.2 to write

$$K_{\mathrm{d}} \approx G_{\mathrm{d}} \left[\frac{\Delta n}{\lambda q^2} \left(\frac{\Delta \varepsilon \varepsilon_0}{K_2} \right) \right] \tag{6.30}$$

where G_{d} is the geometric factor. The measured K_{d} of material D suggests that G_{d} is approximately 0.1, however, it is interesting to compare this with other blue phase Kerr measurements from the literature. Figure 6.7 shows measured Kerr constants of several polymer-stabilised blue phase systems reported in [169] against the value of the Gerber estimate calculated using equation 6.2. To calculate estimated Kerr constants, typical values were taken for the pitch (250 nm), wavelength of incident light (633 nm) and elastic constant (6 pN), as these are not provided in the paper [169]. The slope of a linear regression of the measured Kerr values against the estimated ones provides an estimate of G_{d}, giving a value of 0.026. This estimation is a factor of 4 smaller than that estimated by the measurement of mixture D given in table 6.3.

However, it is known that polymer networks increase the effective elastic constants of the liquid crystal [169]. Since the Kerr switching is inversely proportional to K_2 (equation

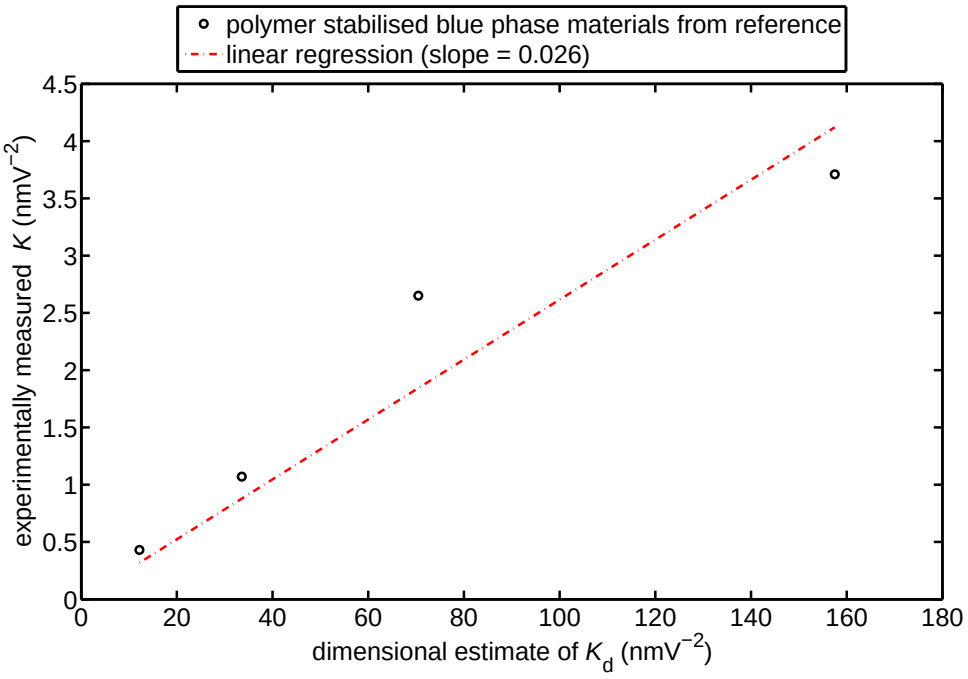

Figure 6.7: Experimentally measured values of the Kerr constant, K, for a series of polymer stabilised blue phase systems, taken from reference [169], against estimates based on Gerber's approximation to Kerr switching, which does not take account of geometric factors [168]. The slope of the linear regression provides an estimate of the geometric factor G_{d}. The estimate of G_{d} is likely to be smaller than in systems without polymer network stabilisation, due to the influence of the polymer network on the effective elastic constants of the material.

6.30), an increase in the effective value of K_2 would reduce the slope of the line in the plot in figure 6.7 and therefore reduce the determined value of G_{d} in polymer stabilised systems, since the dimensional estimate is made based on the value of K_2 of the liquid crystal without a polymer network. Polymer stabilised blue phase systems are therefore expected to have a smaller value of G_{d}, which could explain the difference between the value of G_{d} deduced from the polymer stabilised systems in the reference and the G_{d} determined for material D, which does not have a polymer network.

For material F, there is a large discrepancy between the value of K_{d} calculated using Gerber's estimation, and the experimentally determined value of K_{d}. The dielectric anisotropy measured at 40° in a Grandjean geometry using capacitance measurements was used in the calculation for the estimate, however K_{d} was experimentally determined in the

Table 6.3: Experimental values and corresponding estimates using dimensional considerations for flexoelectric and dielectric Kerr constants are summarised. Estimated values, ignoring geometric factors, are calculated using equations 6.30 and 6.32. The values emphasized with red boxes are those from which the geometric factors, G_{f} and G_{d}, are determined.

	Material F	Material D	Unit
K_{d} (experimental)	-0.00074	0.13	nmV^{-2}
K_{d} (estimated)	-0.063	1.2	nmV^{-2}
K_{f} (experimental)	0.023	<0.001	nmV^{-2}
K_{f} (estimated)	0.21	0.00021	nmV^{-2}

blue phase at 50°C. Since $\Delta\varepsilon$ is close to zero for Material F, changes in the temperature may have a large effect on the relative magnitude of $\Delta\varepsilon$. The dielectric anisotropy in bimesogenic materials is known to increase with increasing temperature, and can even undergo a change of sign near the nematic-to-isotropic transition temperature [126]. An absolute change in the value of $\Delta\varepsilon$ of the order of 0.1 over 10°, as reported in reference [126] for a similar bimesogenic liquid crystal, can account for the discrepancy between the measured and estimated values in table 6.3.

6.5.2 Flexoelectric Contribution to Kerr Switching

To provide a similar analysis of the flexoelectric contributions, an estimated value of K_{f} can be formulated using a similar process undertaken by Gerber [168]. One can immediately produce a dimensionally consistent estimate of K_{f} by considering the definition of the dimensionless quantity κ given in equation 6.6. Rearranging equation 6.6 we can write,

$$\kappa = \frac{\left\{\frac{\Delta\varepsilon\varepsilon_0}{K_2}\right\}}{8\left\{\frac{e_1-e_3}{K_1+K_3}\right\}^2} \tag{6.31}$$

where the terms on the top and bottom relate to the dielectric and flexoelectric distortion. Comparison with equation 6.2, and replacing the dielectric distortion terms with the flexoelectric distortion terms, we then arrive at a dimensionally consistent estimate for the Kerr

contribution from flexoelectric distortion,

$$K_{\mathrm{f}} = G_{\mathrm{f}} \left[\frac{\Delta n}{\lambda q^2} \left(\frac{e_1 - e_3}{K_1 + K_3} \right)^2 \right] \tag{6.32}$$

where G_{f} is again a geometric factor (and absorbs the factor of 8 in equation 6.31). The experimentally determined values of K_{f} are summarised along with estimates based on 6.32 (but ignoring the geometric factor) for material D and F in table 6.3. From the ratio of the experimental value to the estimated value of material F, we find that G_{f} is also approximately 0.1[1].

Interestingly, this result suggests that flexoelectric and dielectric effects have a similar influence on the magnitude of the Kerr effect in blue phases. This could have important implications for the engineering of large-Kerr-constant blue phase materials. There is a trade-off between a material's dielectric or optical anisotropy and the liquid crystal viscosity, which results in a trade-off between electrooptic response and switching time. However, here it has been demonstrated that the Kerr response can potentially also be improved by exploiting flexoelectricity. Therefore materials may be engineered that exploit both dielectric and flexoelectric effects in order to maximise the Kerr response, although it should also be noted that bimesogenic liquid crystals, while having a large flexo-elastic ratio, are also relatively viscous. We may summarise the combined flexoelectric and dielectric contribution to the Kerr effect in blue phases by the expression,

$$K = \frac{\Delta n}{\lambda q^2} \left[G_{\mathrm{d}} \frac{\Delta \varepsilon \varepsilon_0}{K_2} + G_{\mathrm{f}} \left(\frac{e_1 - e_3}{K_1 + K_3} \right)^2 \right] \tag{6.33}$$

which provides an expression for the total Kerr constant of blue phase liquid crystals due to both dielectric and flexoelectric distortions, and provides an entirely new insight for the engineering of Kerr-optimised blue phase materials.

Finally, the estimated value of K_{f} for material D, shown in table 6.3, is tiny, owing to the very low flexoelectric response in this material. The estimate is consistent with the upper limit on K_{f} found experimentally.

[1]Preliminary numerical simulations undertaken by Elston [181] of the a BPI structure using a director continuum model with Berreman optics has suggested that the geometric factors G_{f} and G_{d} are similar to one another in magnitude and substantially less than 1, consistent with the experimentally determined values.

6.5.3 Other Field Effects

So far we have considered the effect of flexoelectricity and the dielectric interaction on Kerr switching in blue phase liquid crystals. However, other phenomena may be important. BPLCs are materials whose dielectric properties and director orientation have a cubic or amorphous symmetry, and include a network of topological defect lines [21, 22]. As such, gradient flexoelectricity may influence the Kerr response. Gradient flexoelectric polarization is proportional to $e_1 + e_3$ and gradients in E (see §1.3.4), but there has been no attempt to separate the effects of $e_1 - e_3$ and $e_1 + e_3$ on the Kerr constant in this study.

The presence of a network of defects, in which the order parameter of the liquid crystal changes dramatically, allow for field effects that involve the order parameter, known as 'order electricity' [182, 183, 184]. These field effects may also contribute to the Kerr effect in blue phase systems and have not been considered in this study.

Finally, the present study has not addressed differences in Kerr behaviour between BPI, PBII or PBIII. It is likely that the geometric factors, G_{f} and G_{d}, may have some dependence on the type of blue phase geometry.

6.6 Conclusion

In this chapter, flexoelectric and dielectric contributions to Kerr switching in blue phase liquid crystals have been considered. An electro-optic technique has been developed to determine the individual contributions to the Kerr constant of the two effects, which have been denoted K_{f} and K_{d}. It has been shown that the influence on the blue phase Kerr constant of flexoelectric and dielectric effects combine constructively in the case where the dielectric anisotropy is positive, and destructively in the case of negative dielectric anisotropy. Further, analytical estimates of Kerr switching based on dimensional considerations have been considered for both flexoelectric and dielectric field interactions, and experimental results have been used to infer 'geometric' factors that relate these estimates to the Kerr constant. The results suggest that both flexoelectricity and the dielectric interaction have a similar influence on the magnitude of the Kerr effect in blue phase systems, which will inform

the development of large-Kerr-constant blue phase materials for electro-optic technologies. The development of blue phase materials with large Kerr constants could enable a variety of new technologies, including field-sequential colour and stereoscopic displays and projectors [26, 185], high-speed optical communications components [164] and liquid-crystal-over-silicon (LCOS) devices including adaptive optics and holographic projectors [186, 163]. Furthermore, with the new insight that flexoelectricity contributes to Kerr switching, novel devices that utilise both Kerr switching in the blue phase in one mode of operation, and the flexoelectrooptic effect in the cholesteric phase in a second mode of operation, could potentially be developed, adding to the possibilities available to the liquid crystal device engineer.

The next and final chapter concludes by summarising and drawing together the work in this thesis.

Chapter 7

Conclusions

This thesis has been concerned with flexoelectric and dielectric phenomena in a wide range of helicoidal liquid crystal systems, including non-chiral, cholesteric and blue phases. The dielectric and flexoelectric effects both involve the reorientation of the dipole moments of liquid crystal molecules by the action of electric fields, however, their individual behaviours are unique: Flexoelectric distortion depends on the field polarity, dielectric distortion does not; The dielectric energy is proportional to the square of the field and is minimised when the angle between the director and the field is minimised or maximised (depending on the sign of the dielectric anisotropy), while the flexoelectric energy is proportional to the field and is minimised when the director curvature distortion is maximised; In helicoidal liquid crystals, the dielectric effect results in a distortion in the director about the helicoidal axis, while the flexoelectric effect results in a distortion about the field axis. These differences produce a rich set of phenomena, which this thesis has explored, and that provide a unique tool-set for the engineer, inviting innovation and application.

In long pitch and non-chiral liquid crystal systems, the flexoelectric tilt in helicoidal twisted nematic structures allows the measurement of flexoelectric parameters in these systems. The in-plane rotation due to the dielectric effect, provides an alternative way to deduce the internal field in the twisted nematic structure, without relying on knowledge of the applied voltage. In a similar way, the approximate independence of the flexoelectric and dielectric distortions in cholesteric structures allows a unique measurement opportunity, as one can extract information about both flexoelectric and dielectric liquid crystal properties

simultaneously. In cholesteric materials, the flexoelectric rotation of the director about the applied field provides a fast optic axis rotation that is proportional to the field, potentially allowing a multitude of new display and other electrooptic functionalities that rely on fast-switching. Similarly, the dielectric distortion causes a cholesteric material to become optically biaxial, and may provide another potential fast-switching technology. In blue phase liquid crystals, both dielectric and flexoelectric distortions, due to the blue phase's cubic or amorphous symmetry, contribute to a Kerr effect that is much greater in these systems than in non-liquid crystalline systems, and could provide yet another potential fast-switching technology.

As well producing a distortion and resultant electrooptic switching, the flexoelectric and dielectric effects also contribute to the dielectric properties of liquid crystal materials. Cholesteric liquid crystals tend to reorient with the helicoidal axis parallel to the field when the liquid crystal has a negative dielectric anisotropy, and perpendicular to the field when they have a positive dielectric anisotropy. In the past this has been exploited to align the Uniform Lying Helix, for example, by applying a field across a liquid crystal device such that the helicoidal axis of the initial Grandjean state changes its orientation to be perpendicular to the field. The opposite situation has also been exploited, whereby a material with a negative dielectric anisotropy can be forced into a Grandjean geometry with the application of a field across the device. By considering the dielectric effect only, switching the helicoidal axis in only one direction has been possible without resorting to other reorienting effects such as elastic interactions with polymer networks or alignment surfaces. However, by considering the flexoelectric polarization in terms of its contribution to the dielectric properties of the cholesteric liquid crystal for the first time, the flexoelectric effect has provided a way to switch between orthogonal orientations of the helicoidal axis. Due to the dependence of the flexoelectric effect on the polarity of the field, at large enough frequencies only the dielectric effect remains, as the flexoelectric effect is suppressed, resulting in a dispersion in the effective dielectric permittivity perpendicular to the helicoidal axis. By selecting appropriate dielectric and flexoelectric properties, this dispersion allows a dual

frequency effect, in which states can be selected by changing the frequency of the addressing voltage signal. This has allowed a new method for switching between states in reflective cholesteric technology, permitting a greater flexibility in the choice of material parameters, and is likely to have many other technological applications. The states that can be accessed using the dual frequency effect based on flexoelectric dispersion are ones of considerable technological interest, that have not yet been fully exploited. This new switching functionality could add value to the body of technology research related to these states, by allowing multifunctional devices that can be used in multiple states for different purposes, such as devices that can operate in both transmissive and reflective display modes.

The contribution to the effective permittivity of flexoelectricity has been exploited not only in reflective cholesteric technology, but also in alignment of the Uniform Lying Helix using interdigitated electrodes that produce fields in the plane of liquid crystal devices. It has been demonstrated that both the dielectric and flexoelectric contributions to the effective permittivity of the cholesteric material can be used to orient the structure in the Uniform Lying Helix geometry. In the past, the assumption has generally been that the dielectric effect is required to provide an orienting torque. This is a problem if one is to align materials with very small dielectric anisotropy, which do not couple strongly to the dielectric effect. Exploiting the flexoelectric contribution to the permittivity circumvents this problem.

In blue phase liquid crystals, the Kerr effect has until now been considered a consequence of only dielectric distortion. It has even been suggested in the literature that flexoelectrooptic effects cannot occur in blue phases, including linear and Kerr-type effects [23]. This neglect of flexoelectricity in the literature is further demonstrated by an often expressed analytical approximation based on dimensional considerations that expresses the received conceptions as to the parameters that are important in Kerr switching in blue phases; Gerber's approximation. While this approximation does take into consideration that the Kerr constant of blue phase liquid crystals is proportional to dielectric anisotropy, it does not consider at all flexoelectric effects. By considering the unique property of the field-polarity dependence of the flexoelectric distortion, and by considering the resultant suppression in

flexoelectric switching at large frequencies, it has been possible to measure independent contributions to the Kerr constant of blue phases by probing the switching behaviour as a function of frequency. This technique has allowed the measurement of flexoelectric and dielectric contributions, and inspired an additional term to the analytical approximation of the Kerr constant in blue phases due to flexoelectricity that is proportional to the square of the flexoelectric parameter, which will inform the engineering of new blue phase materials. The analysis further inspired a suggestion of other field effects that may be unique to blue phase systems compared with other liquid crystal systems, such as order electricity and gradient flexoelectricity, which provides a platform for further investigation into blue phase Kerr switching.

In exploring these flexoelectric and dielectric phenomena in helicoidal liquid crystal systems, several techniques have been developed and applied. The crystal rotation method, in which the transmission of devices is observed as a function of the angle of incidence, is sensitive to flexoelectric distortions in helicoidal structures, which cause rotations of the optic axis in the plane of incidence. The method has been exploited in the measurement of flexoelectricity in twisted nematic and Grandjean cholesteric structures. In addition, the use of a lock-in amplifier to study frequency components of the transmission of chiral systems relative to a driving field has been used to provide sensitive measurements of subtle electrooptic effects. In the case of a Grandjean geometry, the first harmonic of the transmission, which is the component of the transmission that is proportional to the field, is sensitive to flexoelectric distortions and has enabled the measurement of flexoelectric parameters. The frequency component of the transmission at twice the driving frequency is sensitive to electrooptic effects that depend on the square of the field. Analysing this frequency component of the transmission has allowed the measurement of the dielectric-distortion induced optical biaxiality of Grandjean structures with in-plane fields, and measurement of Kerr switching in blue phases. Lock-in amplifier techniques have additionally been used to analyse more subtle behaviour of liquid crystal switching, such as the interaction of dielectric and flexoelectric distortion effects in cholesterics, which can result in enhancement of flexoelectric

switching, and the details of flexoelectric and dielectric contributions to Kerr switching in blue phases. Exploring how lock-in amplifier techniques can be extended to study electrooptic effects in other systems, such as elastomers and other liquid crystal phases, could lead to the discovery of novel electrooptic and electro-elastic phenomena.

The role of surface energy in the spontaneous alignment of uniform lying helix structures has been explored. A methodological framework for inducing uniform lying helix alignment has been developed, based upon the use of weak homeotropic alignment to destabilise Grandjean alignment relative to uniform lying helix alignment, in conjunction with a method to break the degeneracy in the uniform lying helicoidal axis orientation in the plane of the cell. A series of different approaches within this framework have been investigated, including the use of nano-grooved surface profiles, in-plane electric fields, periodic boundary conditions and micron-scale polymer channels fabricated using a mould-templating technique. The latter approach was found to provide a high level of alignment quality. The approach could be a commercially viable way to exploit the uniform lying helix in display and other electrooptic technology, given the success of available bistable liquid crystal displays that already exploit structures made using a similar method. The technique deserves further development, considering the potential benefits from sub-millisecond switching liquid crystal technology.

Finally, additional theoretical studies have found that flexoelectric switching in cholesteric, and potentially blue phase, liquid crystals could be enhanced by constraining a helicoidal pitch to be other than the natural pitch of the liquid crystal. This could potentially be achieved through the use of a polymer network that is either formed at a different temperature to the temperature at which the liquid crystal device will be operated (since pitch is temperature dependent), or by removing the liquid crystal after polymer network polymerisation and refilling with a liquid crystal with a different natural pitch. A threshold effect, in which the liquid crystal will spontaneously adopt a bend-splay rather than a twisted structure, has been explored theoretically, which is dependent on the ratio of bend, splay and twist elastic constants. It was noted that this threshold effect between bend-splay

and twist geometries is analogous to an effect in pi-cells, in which the dielectric effect is exploited to reduce the energy of the bend-splay state and cross the twist-to-bend-splay threshold in order to measure the twist elastic constant, and it was further noted that the dielectric effect could therefore potentially be used to induce the analogous threshold effect in constrained cholesteric structures. However, the effect of any polymer network used to constrain the liquid crystal has not been taken into account. A theoretical investigation into the influence of a polymer network and an experimental investigation to explore potential enhancement in switching or threshold switching effects, will provide a platform for further research.

In summary, the primary contributions of this work have been: to apply the crystal rotation method and lock-in amplifier techniques to investigate liquid crystal behaviour and develop new methods to measure key parameters in both chiral and non-chiral liquid crystals; to identify novel ways to enhance flexoelectrooptic switching in cholesterics, either by constraining pitch or via the coupling of the flexoelectric tilt to the dielectric distortion in materials with negative dielectric anisotropy; to describe for the first time the flexoelectric polarization contribution to the effective permittivity of cholesteric materials, the consequence of which has been the invention of a new and versatile switching mechanism in cholesteric systems, including bistable reflective display technology, and a new alignment technique for cholesteric technologies; to develop a methodological framework for successful uniform lying helix formation, which has led to the development of a technique that potentially could be developed for commercial application due to the quality of alignment that can be achieved and the already proven commercial viability of the technique in related technologies; and for the first time, to demonstrate experimentally the existence of, and develop a semi-empirical model for, the flexoelectric contribution to Kerr switching in blue phases, which is the first example of a non-polar flexoelectrooptic effect, and the work will inform the design of new blue phase materials and could potentially lead to new possibilities for device engineering.

References

[1] F.C. Frank. On the theory of liquid crystals. *Discussions of the Faraday Society*, 25:997, 1958.

[2] Frederic J Kahn, Gary N Taylor, and Harold Schonhorn. Surface-produced alignment of liquid crystals. *Proceedings of the IEEE*, 61(7):823–828, 1973.

[3] J. Cognard. Alignment of nematic liquid crystals and their mixtures. *Gorden & Breach Science Publishers; London & New York*, 1982.

[4] AD Buckingham and AD Buckingham. A theory of the dielectric polarization of polar substances. *Proceedings of the Royal Society of London. Series A. Mathematical and Physical Sciences*, 238(1213):235–244, 1956.

[5] S.H. Glarum. Dielectric relaxation of polar liquids. *The Journal of Chemical Physics*, 33:1371, 1960.

[6] R.H. Cole. Correlation function theory of dielectric relaxation. *The Journal of Chemical Physics*, 42:637, 1965.

[7] Stephen W Morris, P Palffy-Muhoray, and DA Balzarini. Measurements of the bend and splay elastic constants of octyl-cyanobiphenyl. *Molecular Crystals and Liquid Crystals*, 139(3-4):263–280, 1986.

[8] R.B. Meyer. Piezoelectric effects in liquid crystals. *Physical Review Letters*, 22:319, 1969.

[9] W Helfrich. Inherent bounds to the elasticity and flexoelectricity of liquid crystals. *Molecular Crystals and Liquid Crystals*, 26(1-2):1–5, 1974.

[10] H.P. Hinov and Y. Marinov. An electro-magneto-optical resonance method for determination of the value and sign of the flexoelectric coefficients in nematics. *Journal of optoelectronics and advanced materials*, 9:435, 2007.

[11] A.G. Petrov. Measurement and interpretation of flexoelectricity. *Chapter in the book Physical Properties of Liquid Crystals: Nematics edited by D.A. Dunmar, A. Fukuda, G.R. Luckhurst, published by INSPEC*, 2001.

[12] C. Fan. Comments on piezoelectric effect in liquid crystals. *Molecular crystals and liquid crystals*, 13:9, 1971.

[13] A. Derzhanski, A.G. Petrov, and M.D. Mitov. One-dimensional dielectric-flexoelectric deformations in nematic layers. *Journal de Physique*, 39:273, 1978.

[14] P Yeh and C. Gu. *The Optics of Liquid Crystal displays*. Wiley, 1999.

[15] D.W. Berreman. Optics in stratified and anisotropic media: 4 x 4-matrix formulation. *Journal of the Optical Society of America*, 62:502, 1972.

[16] Dwight W Berreman. Optics in smoothly varying anisotropic planar structures: application to liquid-crystal twist cells. *JOSA*, 63(11):1374–1380, 1973.

[17] DW Berreman and TJ Scheffer. Bragg reflection of light from single-domain cholesteric liquid-crystal films. *Physical Review Letters*, 25(9):577–581, 1970.

[18] MF Grandjean. Comptes rendus acad. *Sci*, 172:71, 1921.

[19] F. Castles, S. M. Morris, and H. J. Coles. Flexoelectro-optic properties of chiral nematic liquid crystals in the uniform standing helix configuration. *Phys. Rev. E*, 80:031709, 2009.

[20] P. Rudquist, M. Buivydas, L. Komitov, and S. T. Lagerwall. Linear electro-optic effect based on flexoelectricity in a cholesteric with sign change of dielectric anisotropy. *Journal of Applied Physics*, 76:7778, 1994.

[21] David C Wright and N David Mermin. Crystalline liquids: the blue phases. *Reviews of Modern physics*, 61(2):385, 1989.

[22] H Stegemeyer, Th Blümel, K Hiltrop, H Onusseit, and F Porsch. Thermodynamic, structural and morphological studies on liquid-crystalline blue phases. *Liquid Crystals*, 1(1):3–28, 1986.

[23] H-S Kitzerow. Blue phases: prior art, potential polar effects, challenges. *Ferroelectrics*, 395(1):66–85, 2010.

[24] Heinz Kitzerow and Christian Bahr. *Chirality in liquid crystals*. Springer Verlag, 2001.

[25] Harry J Coles and Mikhail N Pivnenko. Liquid crystal blue phases with a wide temperature range. *Nature*, 436(7053):997–1000, 2005.

[26] Hirotsugu Kikuchi, Masayuki Yokota, Yoshiaki Hisakado, Huai Yang, and Tisato Kajiyama. Polymer-stabilized liquid crystal blue phases. *Nature Materials*, 1(1):64–68, 2002.

[27] P. Kassubek and G. Meier. Optical studies on grandjean planes in cholesteric liquid crystals. *Molecular Crystals and Liquid Crystals*, 8(1):305–314, 1969.

[28] D. Coates. Low power large-area cholesteric displays. *Info. Display*, page 18, 2009.

[29] B.G. Wu, H. Zhou, and Y.D. Ma. Ultra fast response, multistable reflective cholesteric liquid crystal displays, August 26 1997. US Patent 5,661,533.

[30] AM Green, E. Montbach, N. Miller, D. Davis, A. Khan, T. Schneider, and W. Doane. Energy efficient flexible reflex displays. *Proc. IDRC*, 8:55–59, 2008.

[31] VI Kopp, B Fan, HKM Vithana, and AZ Genack. Low-threshold lasing at the edge of a photonic stop band in cholesteric liquid crystals. *Optics letters*, 23(21):1707–1709, 1998.

[32] Harry Coles and Stephen Morris. Liquid-crystal lasers. *Nature Photonics*, 4(10):676–685, 2010.

[33] Yuhua Huang, Ying Zhou, and Shin-Tson Wu. Spatially tunable laser emission in dye-doped photonic liquid crystals. *Applied physics letters*, 88(1):011107–011107, 2006.

[34] Masanori Ozaki, Masahiro Kasano, Tetsuro Kitasho, Dirk Ganzke, Wolfgang Haase, and Katsumi Yoshino. Electro-tunable liquid-crystal laser. *Advanced Materials*, 15(12):974–977, 2003.

[35] Pascal Hubert, Pontus Jägemalm, Claudio Oldano, and Mauro Rajteri. Optic models for short-pitch cholesteric and chiral smectic liquid crystals. *Physical Review E*, 58(3):3264, 1998.

[36] BI Outram and SJ Elston. Flexoelectric and dielectric in-plane switching behaviour of grandjean liquid-crystal structures. *EPL (Europhysics Letters)*, 99(3):37007, 2012.

[37] Damian J. Gardiner, Stephen M. Morris, Flynn Castles, Malik M. Qasim, Wook-Sung Kim, Su Seok Choi, Hyun-Jin Park, In-Jae Chung, and Harry J. Coles. Polymer stabilized chiral nematic liquid crystals for fast switching and high contrast electro-optic devices. *Applied Physics Letters*, 98(26):263508, 2011.

[38] Stephen M. Morris, Damian J. Gardiner, Flynn Castles, Philip J. W. Hands, Timothy D. Wilkinson, and Harry J. Coles. Fast-switching phase gratings using in-plane addressed short-pitch polymer stabilized chiral nematic liquid crystals. *Applied Physics Letters*, 99(25):253502–253502, 2011.

[39] R.B. Meyer. Distortion of a cholesteric structure by a magnetic field. *Applied Physics Letters*, 14:208, 1969.

[40] P.G. de Gennes. Calculation of distortion in a cholesteric structure by magnetic field. *Solid State Communications*, 6:163, 1968.

[41] C.T. Wang and T.H. Lin. Vertically integrated transflective liquid crystal display using multi-stable cholesteric liquid crystal film. 2012.

[42] C.T. Wang, W.Y. Wang, and T.H. Lin. A stable and switchable uniform lying helix structure in cholesteric liquid crystals. *Applied Physics Letters*, 99(4):041108–041108, 2011.

[43] D.K. Yang, JL West, L.C. Chien, and JW Doane. Control of reflectivity and bistability in displays using cholesteric liquid crystals. *Journal of applied physics*, 76(2):1331–1333, 1994.

[44] T. Yamaguchi, H. Yamaguchi, and Y. Kawata. Driving voltage of reflective cholesteric liquid crystal displays. *Journal of applied physics*, 85(11):7511–7516, 1999.

[45] K.H. Kim, H.J. Jin, K.H. Park, J.H. Lee, J.C. Kim, and T.H. Yoon. Long-pitch cholesteric liquid crystal cell for switchable achromatic reflection. *Optics Express*, 18(16):16745–16750, 2010.

[46] C.T. Wang and T.H. Lin. Bistable reflective polarizer-free optical switch based on dye-doped cholesteric liquid crystal [invited]. *Optical Materials Express*, 1(8):1457–1462, 2011.

[47] Y. Bouligand. Sur l'existence de" pseudomorphoses cholesteriques" chez divers organismes vivants. *Journal de Physique (France)*, 30:C4–90, 1969.

[48] J.S. Patel and R. B. Meyer. Flexoelectric electro-optics of a cholesteric liquid crystal. *Physical Review Letters*, 58:1538, 1987.

[49] J.S. Patel and S.D. Lee. Fast linear electro-optic effect based on cholesteric liquid crystals. *Journal of Applied Physics*, 66:1879, 1989.

[50] S.D. Lee, J.S. Patel, and R.B. Meyer. Effect of flexoelectric coupling on helix distortions in cholesteric liquid crystals. *Journal of Applied Physics*, 67:1293, 1990.

[51] P. Rudquist. *The flexoelectro-optic effect in cholesteric liquid crystals*. PhD thesis, Chalmers University of Technology, Goteborg, 1997.

[52] P. Rudquist, T. Carlsson, L. Komitov, and ST Lagerwall. The flexoelectro-optic effect in cholesterics. *Liquid crystals*, 22(4):445–449, 1997.

[53] S.H. Kim, L.C. Chien, and L. Komitov. Short pitch cholesteric electro-optical device stabilized by nonuniform polymer network. *Applied Physics Letters*, 86(16):161118–161118, 2005.

[54] B.J. Broughton, M.J. Clarke, S.M. Morris, A.E. Blatch, and H.J. Coles. Effect of polymer concentration on stabilized large-tilt-angle flexoelectro-optic switching. *Journal of Applied Physics*, 99:23511, 2006.

[55] G. Carbone, P. Salter, S.J. Elston, P. Raynes, L. De Sio, S. Ferjani, G. Strangi, C. Umeton, and R. Bartolino. Short pitch cholesteric electro-optical device based on periodic polymer structures. *Applied Physics Letters*, 95:011102, 2009.

[56] H.J. Coles, B. Musgrave, M.J. Coles, and J. Willmott. The effect of the molecular structure on flexoelectric coupling in the chiral nematic phase. *Journal of Materials Chemistry*, 11:2709, 2001.

[57] B. Musgrave, M.J. Coles, S.P. Perkins, and H.J. Coles. Enhanced flexoelectric switching behaviour in the chiral nematic phase. *Molecular Crystals and Liquid Crystals*, 366(1):735–742, 2001.

[58] B.J. Broughton, M.J. Clarke, A.E. Blatch, and H.J. Coles. Optimized flexoelectric response in a chiral liquid-crystal phase device. *Journal of Applied Physics*, 98:34109, 2005.

[59] Z. Zhang and H. Guo. The phase behavior, structure, and dynamics of rodlike mesogens with various flexibility using dissipative particle dynamics simulation. *The Journal of Chemical Physics*, 133:144911, 2010.

[60] J.L. Ericksen. Conservation laws for liquid crystals. *Transaction of the Society of Rheology*, 5:23, 1961.

[61] F.M. Leslie. Some constitutive equations for liquid crystals. *Archive for Rational Mechanics and Analysis*, 28:265, 1968.

[62] O. Parodi. Stress tensor for a nematic liquid crystal. *Journal de Phisique*, 31:581, 1970.

[63] S.A. Jewell, TS Taphouse, and J.R. Sambles. Rapid switching in a dual-frequency hybrid aligned nematic liquid crystal cell. *Applied Physics Letters*, 87:021106, 2005.

[64] J.C. Jones. New calculus for the treatment of optical systems. *Journal of the Optical Society of America*, 31:488, 1941.

[65] T. Scharf. *Polarized light in liquid crystals and polymers*. Wiley, 2007.

[66] D.W. Berreman. Liquid-crystal twist cell dynamics with backflow. *Journal of Applied Physics*, 46(9):3746–3751, 1975.

[67] NJ Mottram and C. Newton. Introduction to Q-tensor theory. *University of Strathclyde, Department of Mathematics, Research Report*, 10, 2004.

[68] Hiroyuki Mori, Eugene Gartland, Jack Kelly, Philip Bos, et al. Multidimensional director modeling using the q tensor representation in a liquid crystal cell and its application to the pi cell with patterned electrodes. *Japanese journal of applied physics*, 38:135, 1999.

[69] Xuemei Zhang and Joyce E Farrell. Sequential color breakup measured with induced saccades. In *Proc. SPIE*, volume 5007, pages 210–217, 2003.

[70] Andrew J Woods. Crosstalk in stereoscopic displays: a review. *Journal of Electronic Imaging*, 21(4):040902–040902, 2012.

[71] Marc TM Lambooij, Wijnand A IJsselsteijn, Ingrid Heynderickx, et al. Visual discomfort in stereoscopic displays: a review. *Stereoscopic Displays and Virtual Reality Systems XIV*, 6490(1), 2007.

[72] Gordon D Love, David M Hoffman, Philip JW Hands, James Gao, Andrew K Kirby, and Martin S Banks. High-speed switchable lens enables the development of a volumetric stereoscopic display. *Optics express*, 17(18):15716, 2009.

[73] H.J. Coles, M.J. Clarke, S.M. Morris, B.J. Broughton, and A.E. Blatch. Strong flexoelectric behaviour in bimesogenic liquid crystals. *Journal of Applied Physics*, 99:34104, 2006.

[74] C. Noot, MJ Coles, B. Musgrave, SP Perkins, and HJ Coles. The flexoelectric behaviour of a hypertwisted chiral nematic liquid crystal. *Molecular Crystals and Liquid Crystals*, 366(1):725–733, 2001.

[75] S. M. Morris, M. J. Clarke, A. E. Blatch, and H. J. Coles. Structure-flexoelastic properties of bimesogenic liquid crystals. *Physical Review E*, 75(4, Part 1), 2007.

[76] Andrew E Blatch, Marcus J Coles, Bronje Musgrave, and Harry J Coles. Flexoelectric liquid crystal bimesogens. *Molecular Crystals and Liquid Crystals*, 401(1):47–55, 2003.

[77] PS Salter, C Kischka, SJ Elston, and EP Raynes. The influence of chirality on the difference in flexoelectric coefficients investigated in uniform lying helix, grandjean and twisted nematic structures. *Liquid Crystals*, 36(12):1355–1364, 2009.

[78] S Kaur, J Addis, C Greco, A Ferrarini, V Görtz, JW Goodby, and HF Gleeson. Understanding the distinctive elastic constants in an oxadiazole bent-core nematic liquid crystal. *Physical Review E*, 86(4):041703, 2012.

[79] S Kaur, L Tian, H Liu, C Greco, A Ferrarini, J Seltmann, M Lehmann, and HF Gleeson. The elastic and optical properties of a bent-core thiadiazole nematic liquid crystal: the role of the bend angle. *Journal of Materials Chemistry C*, 2013.

[80] R Amaranatha Reddy and Carsten Tschierske. Bent-core liquid crystals: polar order, superstructural chirality and spontaneous desymmetrisation in soft matter systems. *Journal of materials chemistry*, 16(10):907–961, 2006.

[81] Hideo Takezoe and Yoichi Takanishi. Bent-core liquid crystals: their mysterious and attractive world. *Japanese journal of applied physics*, 45:597, 2006.

[82] Abdelhak Belaissaoui, Stephen J Cowling, and John W Goodby. Spontaneous formation of chiral macrostructures in achiral hockey-stick liquid crystals. *Liquid Crystals*, (ahead-of-print):1–9, 2013.

[83] HF Gleeson. *Private Communication*.

[84] H.J. Deuling. On a method to measure the flexo-electric coefficients of nematic liquid crystals. *Solid State Communications*, 14(11):1073–1074, 1974.

[85] LM Blinov, LA Beresnev, SA Davidyan, SG Kononov, and SV Yablonsky. Flexoelectric effects in liquid crystals. *Ferroelectrics*, 84(1):365–377, 1988.

[86] J. Harden, B. Mbanga, N. Eber, K. Fodor-Csorba, S. Sprunt, J.T. Gleeson, and A. Jakli. Giant flexoelectricity of bent-core nematic liquid crystals. *Physical review letters*, 97(15):157802, 2006.

[87] S. Ponti, P. Ziherl, C. Ferrero, and S. Zumer. Flexoelectro-optic effect in a hybrid nematic liquid crystal cell. *Liquid Crystals*, 26(8):1171–1177, 1999.

[88] B. Musgrave, P. Lehmann, and HJ Coles. A new series of chiral nematic bimesogens for the flexoelectro-optic effect. *Liquid crystals*, 26(8):1235–1249, 1999.

[89] F Castles, SC Green, DJ Gardiner, SM Morris, and HJ Coles. Flexoelectric coefficient measurements in the nematic liquid crystal phase of 5cb. *AIP Advances*, 2(2):022137–022137, 2012.

[90] G. Baur, V. Wittwer, and D.W. Berreman. Determination of the tilt angles at surfaces of substrates in liquid crystal cells* 1. *Physics Letters A*, 56(2):142–144, 1976.

[91] B.I. Outram and S.J. Elston. Determination of flexoelectric coefficients in nematic liquid crystals using the crystal rotation method. *Liquid Crystals*, 39(2):149–156, 2012.

[92] Benjamin I Outram and Steve J Elston. A novel method for measuring the difference in flexoelectric coefficients of nematic liquid crystals. *Solid State Phenomena*, 181:26–32, 2012.

[93] Eugene Fredericq and Claude Houssier. *Electric dichroism and electric birefringence*. Clarendon Press Oxford, 1973.

[94] A.A.T. Smith, C.V. Brown, and N.J. Mottram. Theoretical analysis of the magnetic freedericksz transition in the presence of flexoelectricity and ionic contamination. *Physical Review E*, 75(4):041704, 2007.

[95] I. Dozov, P. Martinot-Lagarde, and G. Durand. Flexoelectrically controlled twist of texture in a nematic liquid crystal. *Journal de Physique Lettres*, 43(10):365–369, 1982.

[96] P.R.M. Murthy, VA Raghunathan, and NV Madhusudana. Experimental determination of the flexoelectric coefficients of some nematic liquid crystals. *Liquid Crystals*, 14(2):483–496, 1993.

[97] DR Link, M Nakata, Y Takanishi, K Ishikawa, and H Takezoe. Flexoelectric polarization in hybrid nematic films. *Physical Review E*, 65(1, Part 1), 2002.

[98] J. Prost and PS Pershan. Flexoelectricity in nematic and smectic-A liquid crystals. *Journal of Applied Physics*, 47(6):2298–2312, 1976.

[99] R.A. Ewings, C. Kischka, L.A. Parry-Jones, and S.J. Elston. Measurement of the difference in flexoelectric coefficients of nematic liquid crystals using a twisted nematic geometry. *Physical Review E*, 73:011713, 2006.

[100] EK Tidey, LA Parry-Jones, and SJ Elston. Determination of the difference of flexoelectric coefficients in a nematic liquid crystal using a conoscopic technique. *Liquid Crystals*, 34(2):251–255, 2007.

[101] C. Kischka, L.A. Parry-Jones, S.J. Elston, and E.P. Raynes. Measurement of the flexoelectric coefficients e_1 and e_3 in nematic liquid crystals. *Molecular Crystals and Liquid Crystals*, 480:103–110, 2008.

[102] George H Heilmeier and Philip M Heyman. Note on transient current measurements in liquid crystals and related systems. *Physical Review Letters*, 18(15):583–585, 1967.

[103] HY Chen, KX Yang, and ZY Lin. Electrodynamic behaviour of nematic liquid crystal in a relaxation process. *Journal of Physics D: Applied Physics*, 43(31):315103, 2010.

[104] Hui-Yu Chen. *Electrodynamic Investigations of Ion Charge Transport in Liquid-Crystal Cell*. PhD thesis, Ph. D. Dissertation, Chung Yuan Christian University, Chung-Li, Taiwan, 2007.

[105] Hiroyoshi Naito, Masahiro Okuda, and Akihiko Sugimura. Transient discharging processes in nematic liquid crystals. *Physical Review A*, 44(6):R3434–R3437, 1991.

[106] Akihiko Sugimura, Nobuyuki Matsui, Yutaka Takahashi, Hajimu Sonomura, Hiroyoshi Naito, and Masahiro Okuda. Transient currents in nematic liquid crystals. *Physical Review B*, 43(10):8272, 1991.

[107] Hui-Yu Chen, Kai-Xian Yang, and Wei Lee. Transient behavior of the polarity-reversal current in a nematic liquid-crystal device. *Optics express*, 12(16):3806–3813, 2004.

[108] DR Corbett and SJ Elston. Modeling the helical flexoelectro-optic effect. *Physical Review E*, 84(4):041706, 2011.

[109] L.A. Parry-Jones, S.J. Elston, and G.P. Alexander. Theoretical investigation of the chiral flexoelectro-optic effect in cholesteric liquid crystals. *Proceedings for 21st International Liquid Crystal Conference, Keystone, Colorado USA*, 2006.

[110] L.A. Parry-Jones, S.J. Elston, and G.P. Alexander. Theoretical investigation of the chiral flexoelectro-optic effect. *Unpublished*.

[111] F Castles. *Private Communication*.

[112] PD Brimicombe, C Kischka, SJ Elston, and EP Raynes. Measurement of the twist elastic constant of nematic liquid crystals using pi-cell devices. *Journal of applied physics*, 101(4):043108–043108, 2007.

[113] F Castles, FV Day, SM Morris, DH Ko, DJ Gardiner, MM Qasim, S Nosheen, PJW Hands, SS Choi, RH Friend, et al. Blue-phase templated fabrication of three-dimensional nanostructures for photonic applications. *Nature Materials*, 11(7):599–603, 2012.

[114] RAM Hikmet. Electrically induced light scattering from anisotropic gels. *Journal of applied physics*, 68(9):4406–4412, 1990.

[115] I. Dierking. Polymer network-stabilized liquid crystals. *Advanced Materials*, 12:167–181, 2000.

[116] AJ Davidson, SJ Elston, and EP Raynes. Investigation into chiral active waveplates. *Journal of applied physics*, 99:093109, 2006.

[117] P. Rudquist, L. Komitov, and S.T. Lagerwall. Linear electro-optic effect in a cholesteric liquid crystal. *Physical Review E*, 50:4735, 1994.

[118] L. Komitov, G.P. Bryan-Brown, E.L. Wood, and A.B. Smout. Alignment of cholesteric liquid crystals using periodic anchoring. *Journal of Applied Physics*, 86:3508, 1999.

[119] S.H. Kim, L. Shi, and L.C. Chien. Fast flexoelectric switching in a cholesteric liquid crystal cell with surface-localized polymer network. *Journal of Physics D: Applied Physics*, 42:195102, 2009.

[120] G. Hegde and L. Komitov. Periodic anchoring condition for alignment of a short pitch cholesteric liquid crystal in uniform lying helix texture. *Applied Physics Letters*, 96:113503, 2010.

[121] G. Carbone, D. Corbett, S.J. Elston, P. Raynes, A. Jesacher, R. Simmonds, and M. Booth. Uniform lying helix alignment on periodic surface relief structure generated via laser scanning lithography. *Molecular Crystals and Liquid Crystals*, 544(1):37–49, 2011.

[122] D.J. Gardiner, S.M. Morris, P.J.W. Hands, F. Castles, M.M. Qasim, W.S. Kim, S. Seok Choi, T.D. Wilkinson, and H.J. Coles. Spontaneous induction of the uniform lying helix alignment in bimesogenic liquid crystals for the flexoelectro-optic effect. *Applied Physics Letters*, 100(6):063501–063501, 2012.

[123] P.S. Salter, G. Carbone, S.A. Jewell, S.J. Elston, and P. Raynes. Unwinding of the uniform lying helix structure in cholesteric liquid crystals next to a spatially uniform aligning surface. *Physical Review E*, 80(4):041707, 2009.

[124] PE Cladis and M. Kleman. The cholesteric domain texture. *Molecular Crystals and Liquid Crystals*, 16(1-2):1–20, 1972.

[125] GS Chilaya and LN Lisetski. Cholesteric liquid crystals: physical properties and molecular-statistical theories. *Molecular Crystals and Liquid Crystals*, 140(2-4):243–286, 1986.

[126] Cecile Schott, Steven P Perkins, and Harry J Coles. Physical properties of some novel nematic bimesogens for the flexoelectric effect. *Molecular Crystals and Liquid Crystals*, 366(1):715–724, 2001.

[127] Patrick S Salter, Steve J Elston, Peter Raynes, and Lesley A Parry-Jones. Alignment of the uniform lying helix structure in cholesteric liquid crystals. *Japanese Journal of Applied Physics*, 48(10):1302, 2009.

[128] Michael J Escuti, Chris C Bowley, Gregory P Crawford, and Slobodan Zumer. Enhanced dynamic response of the in-plane switching liquid crystal display mode through polymer stabilization. *Applied physics letters*, 75(21):3264–3266, 1999.

[129] Rifat AM Hikmet. Anisotropic gels in liquid crystal devices. *Advanced Materials*, 4(10):679–683, 1992.

[130] LA Parry-Jones and SJ Elston. Flexoelectric switching in a zenithally bistable nematic device. *Journal of applied physics*, 97(9):093515–093515, 2005.

[131] Dwight W Berreman. Solid surface shape and the alignment of an adjacent nematic liquid crystal. *Physical Review Letters*, 28(26):1683–1686, 1972.

[132] Roberto Caputo, Luciano De Sio, Alessandro Veltri, Cesare Umeton, and Andrey V. Sukhov. Development of a new kind of switchable holographic gratingmade of liquid-crystal films separated by slices of polymericmaterial. *Optics Letters*, 29(11):1261–1263, Jun 2004.

[133] C. Park, M.K. Park, K.I. Joo, J.S. Park, K.W. Park, Y. Han, S.W. Kang, and H.R. Kim. Liquid crystal anchoring utilizing surface topological effects of self-structured dual-groove patterns. *Journal of Physics D: Applied Physics*, 45(37):375101, 2012.

[134] Jin Seog Gwag, Jun ichi Fukuda, Makoto Yoneya, and Hiroshi Yokoyama. In-plane bistable nematic liquid crystal devices based on nanoimprinted surface relief. *Applied Physics Letters*, 91(7):073504, 2007.

[135] W. Zheng and M.-C. Lee. Attainment of planarly aligned liquid crystal using vertical alignment polymer walls. *Molecular Crystals and Liquid Crystals*, 553(1):28–35, 2012.

[136] Tomasz R Wolinski, Aleksandra Czapla, Sławomir Ertman, Marzena Tefelska, Andrzej W Domanski, Jan Wójcik, Edward Nowinowski-Kruszelnicki, and Roman Dabrowski. Photonic liquid crystal fibers for sensing applications. *Instrumentation and Measurement, IEEE Transactions on*, 57(8):1796–1802, 2008.

[137] Thomas Larsen, Anders Bjarklev, David Hermann, and Jes Broeng. Optical devices based on liquid crystal photonic bandgap fibres. *Optics Express*, 11(20):2589–2596, 2003.

[138] V Barna, S Ferjani, A De Luca, R Caputo, N Scaramuzza, C Versace, and G Strangi. Band edge and defect modes lasing due to confinement of helixed liquid crystals in cylindrical microcavities. *Applied Physics Letters*, 87(22):221108–221108, 2005.

[139] Rolf Brandes and David R Kearns. Magnetic ordering of DNA liquid crystals. *Biochemistry*, 25(20):5890–5895, 1986.

[140] Joanna Olesiak-Banska, Halina Mojzisova, Dominique Chauvat, Marcin Zielinski, Katarzyna Matczyszyn, Patrick Tauc, and Joseph Zyss. Liquid crystal phases of DNA: Evaluation of DNA organization by two-photon fluorescence microscopy and polarization analysis. *Biopolymers*, 95(6):365–375, 2011.

[141] H-S Kitzerow, B Liu, F Xu, and PP Crooker. Effect of chirality on liquid crystals in capillary tubes with parallel and perpendicular anchoring. *Physical Review E*, 54(1):568, 1996.

[142] P.F. Kerr and A.F. Rogers. *Optical mineralogy*. McGraw-Hill, 1977.

[143] Sven T Lagerwall. Linear and non-linear polar effects in liquid crystals. *Molecular Crystals and Liquid Crystals*, 543(1):3–769, 2011.

[144] C.Y. Huang, K.Y. Fu, K.Y. Lo, and M.S. Tsai. Bistable transflective cholesteric light shutters. *Optics Express*, 11(6):560–565, 2003.

[145] Y.C. Hsiao, C.Y. Wu, C.H. Chen, V.Y. Zyryanov, and W. Lee. Electro-optical device based on photonic structure with a dual-frequency cholesteric liquid crystal. *Optics letters*, 36(14):2632–2634, 2011.

[146] P. Kumar, S.W. Kang, and S.H. Lee. Advanced bistable cholesteric light shutter with dual frequency nematic liquid crystal. *Optical Materials Express*, 2(8):1121–1134, 2012.

[147] P.L. Nordio, G. Rigatti, and U. Segre. Dielectric relaxation theory in nematic liquids. *Molecular physics*, 25(1):129–136, 1973.

[148] G. Meier and A. Saupe. Dielectric relaxation in nematic liquid crystals. *Molecular Crystals and Liquid Crystals*, 1(4):515–525, 1966.

[149] TK Bose, B. Campbell, S. Yagihara, and J. Thoen. Dielectric-relaxation study of alkylcyanobiphenyl liquid crystals using time-domain spectroscopy. *Physical Review A*, 36:5767–5773, 1987.

[150] MT Viciosa, AM Nunes, A. Fernandes, PL Almeida, MH Godinho, and MD Dionísio. Dielectric studies of the nematic mixture e7 on a hydroxypropylcellulose substrate. *Liquid crystals*, 29(3):429–441, 2002.

[151] M. Schadt. Low-frequency dielectric relaxations in nematics and dual-frequency addressing of field effects. *Molecular crystals and liquid crystals*, 89(1-4):77–92, 1982.

[152] H. Xianyu, S.T. Wu, and C.L. Lin. Dual frequency liquid crystals: a review. *Liquid Crystals*, 36(6-7):717–726, 2009.

[153] Lev Michajlovič Blinov and Vladimir G Čigrinov. *Electrooptic effects in liquid crystal materials*. Springer Verlag, 1996.

[154] H.H. Liang, C.C. Wu, P.H. Wang, and J.Y. Lee. Electro-thermal switchable bistable reverse mode polymer stabilized cholesteric texture light shutter. *Optical Materials*, 33(8):1195–1202, 2011.

[155] J. Geng, C. Dong, L. Zhang, Z. Ma, L. Shi, H. Cao, and H. Yang. Electrically addressed and thermally erased cholesteric cells. *Applied physics letters*, 89(8):081130–081130, 2006.

[156] D.K. Yang, L.C. Chien, and JW Doane. Cholesteric liquid crystal/polymer dispersion for haze-free light shutters. *Applied physics letters*, 60(25):3102–3104, 1992.

[157] RL Sutherland, VP Tondiglia, LV Natarajan, TJ Bunning, and WW Adams. Electrically switchable volume gratings in polymer-dispersed liquid crystals. *Applied physics letters*, 64(9):1074–1076, 1994.

[158] I Dierking, LL Kosbar, AC Lowe, and GA Held. Polymer network structure and electro-optic performance of polymer stabilized cholesteric textures i. the influence of curing temperature. *Liquid crystals*, 24(3):387–395, 1998.

[159] Ki-Han Kim, Dong Han Song, Zheng-Guo Shen, Byung Wok Park, Kyoung-Ho Park, Joun-Ho Lee, and Tae-Hoon Yoon. Fast switching of long-pitch cholesteric liquid crystal device. *Optics Express*, 19(11):10174–10179, 2011.

[160] H. Nemati, D.K. Yang, K.L. Cheng, C.C. Liang, J.W. Shiu, C.C. Tsai, and RS Zola. Effect of surface alignment layer and polymer network on the helfrich deformation in cholesteric liquid crystals. *Journal of Applied Physics*, 112(12):124513–124513, 2012.

[161] Linghui Rao, Zhibing Ge, Shin-Tson Wu, and Seung Hee Lee. Low voltage blue-phase liquid crystal displays. *Applied Physics Letters*, 95(23):231101–231101, 2009.

[162] Meizi Jiao, Yan Li, and Shin-Tson Wu. Low voltage and high transmittance blue-phase liquid crystal displays with corrugated electrodes. *Applied Physics Letters*, 96(1):011102–011102, 2010.

[163] TD Wilkinson, CD Henderson, D Gil Leyva, and WA Crossland. Phase modulation with the next generation of liquid crystal over silicon technology. *Journal of Materials Chemistry*, 16(33):3359–3365, 2006.

[164] Yi-Hsin Lin, Hung-Shan Chen, Hung-Chun Lin, Yu-Shih Tsou, Hsu-Kuan Hsu, and Wang-Yang Li. Polarizer-free and fast response microlens arrays using polymer-stabilized blue phase liquid crystals. *Applied Physics Letters*, 96(11):113505–113505, 2010.

[165] HF Gleeson and HJ Coles. Dynamic properties of blue-phase mixtures. *Liquid Crystals*, 5(3):917–926, 1989.

[166] Wenyi Cao, Antonio Muñoz, Peter Palffy-Muhoray, and Bahman Taheri. Lasing in a three-dimensional photonic crystal of the liquid crystal blue phase ii. *Nature materials*, 1(2):111–113, 2002.

[167] Shiyoshi Yokoyama, Shinro Mashiko, Hirotsugu Kikuchi, Kiminori Uchida, and Toshihiko Nagamura. Laser emission from a polymer-stabilized liquid-crystalline blue phase. *Advanced Materials*, 18(1):48–51, 2006.

[168] Paul R Gerber. Electro-optical effects of a small-pitch blue-phase system. *Molecular Crystals and Liquid Crystals*, 116(3-4):197–206, 1985.

[169] Jin Yan, Yuan Chen, Shin-Tson Wu, and Xiaolong Song. Figure of merit of polymer-stabilized blue phase liquid crystals. *Journal of Display Technology*, 9(1):24–29, 2013.

[170] Peter J Collings and Jay S Patel. *Handbook of liquid crystal research*. Oxford University Press New York, 1997.

[171] Harry Coles, Mykhaylo Pivnenko, and Jonathan Hannington. Liquid crystal materials, November 24 2009. US Patent 7,623,214.

[172] F Castles, SM Morris, EM Terentjev, and HJ Coles. Thermodynamically stable blue phases. *Physical review letters*, 104(15):157801, 2010.

[173] AJ Jin, MR Fisch, MP Mahajan, KA Crandall, P Chu, C-Y Huang, V Percec, RG Petschek, and C Rosenblatt. Highly anisotropic elasticity of a dendrimeric liquid crystal. *The European Physical Journal B-Condensed Matter and Complex Systems*, 5(2):251–255, 1998.

[174] Hui-Yu Chen. *Private Communication*.

[175] Hui-Yu Chen, Hsin-Hung Liu, Jia-Liang Lai, Chih-Hao Chiu, and Ji-Yi Chou. Relation between physical parameters and thermal stability of liquid-crystal blue phase. *Applied Physics Letters*, 97(18):181919–181919, 2010.

[176] Hui-Yu Chen, Sheng-Feng Lu, and Yi-Chun Hsieh. Unusual electro-optical behavior in a wide-temperature BPiii cell. *Optics express*, 21(8):9774–9779, 2013.

[177] Mirko Cestari, Elisa Frezza, Alberta Ferrarini, and Geoffrey R Luckhurst. Crucial role of molecular curvature for the bend elastic and flexoelectric properties of liquid crystals: mesogenic dimers as a case study. *Journal of Materials Chemistry*, 21(33):12303–12308, 2011.

[178] S Meiboom and M Sammon. Structure of the blue phase of a cholesteric liquid crystal. *Physical Review Letters*, 44(13):882–885, 1980.

[179] DL Johnson, JH Flack, and PP Crooker. Structure and properties of the cholesteric blue phases. *Physical Review Letters*, 45(8):641–644, 1980.

[180] Yan Li, Yuan Chen, Jin Yan, Yifan Liu, JP Cui, QH Wang, and Shin-Tson Wu. Polymer-stabilized blue phase liquid crystal with a negative kerr constant. *Opt. Mater. Express*, 2(8):1135–1140, 2012.

[181] SJ Elston. *Private Communication*.

[182] G Durand. Order electricity in liquid crystals. *Physica A: Statistical Mechanics and its Applications*, 163(1):94–100, 1990.

[183] Tine Porenta, Miha Ravnik, and Slobodan Zumer. Effect of flexoelectricity and order electricity on defect cores in nematic droplets. *Soft Matter*, 7(1):132–136, 2011.

[184] HR Brand. Static effects of electric fields near the nematic and cholesteric to isotropic transitions. *Molecular crystals and liquid crystals. Letters section*, 3(5):147–153, 1986.

[185] Sihui He, Jiun-Haw Lee, Hui-Chuan Cheng, Jin Yan, and Shin-Tson Wu. Fast-response blue-phase liquid crystal for color-sequential projection displays. *Display Technology, Journal of*, 8(6):352–356, 2012.

[186] Jing Chen, Stephen M Morris, Timothy D Wilkinson, Jon P Freeman, and Harry J Coles. High speed liquid crystal over silicon display based on the flexoelectro-optic effect. *Optics Express*, 17(9):7130–7137, 2009.